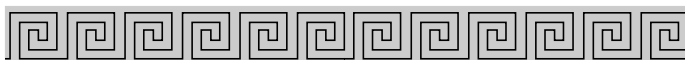


# CHAPTER 12



## Aperture Antennas

### 12.1 INTRODUCTION

Aperture antennas are most common at microwave frequencies. There are many different geometrical configurations of an aperture antenna with some of the most popular shown in Figure 1.4. They may take the form of a waveguide or a horn whose aperture may be square, rectangular, circular, elliptical, or any other configuration. Aperture antennas are very practical for space applications, because they can be flush mounted on the surface of the spacecraft or aircraft. Their opening can be covered with a dielectric material to protect them from environmental conditions. This type of mounting does not disturb the aerodynamic profile of the craft, which in high-speed applications is critical.

In this chapter, the mathematical tools will be developed to analyze the radiation characteristics of aperture antennas. The concepts will be demonstrated by examples and illustrations. Because they are the most practical, emphasis will be given to the rectangular and circular configurations. Due to mathematical complexities, the observations will be restricted to the far-field region. The edge effects, due to the finite size of the ground plane to which the aperture is mounted, can be taken into account by using diffraction methods such as the Geometrical Theory of Diffraction, better known as GTD. This is discussed briefly and only qualitatively in Section 12.10.

The radiation characteristics of wire antennas can be determined once the current distribution on the wire is known. For many configurations, however, the current distribution is not known exactly and only physical intuition or experimental measurements can provide a reasonable approximation to it. This is even more evident in aperture antennas (slits, slots, waveguides, horns, reflectors, lenses). It is therefore expedient to have alternate methods to compute the radiation characteristics of antennas. Emphasis will be placed on techniques that for their solution rely primarily not on the current distribution but on reasonable approximations of the fields on or in the vicinity of the antenna structure. One such technique is the *Field Equivalence Principle*.

### 12.2 FIELD EQUIVALENCE PRINCIPLE: HUYGENS' PRINCIPLE

The *field equivalence* is a principle by which actual sources, such as an antenna and transmitter, are replaced by equivalent sources. The fictitious sources are said to be

*equivalent within a region because they produce the same fields within that region.* The formulations of scattering and diffraction problems by the equivalence principle are more suggestive to approximations.

The field equivalence was introduced in 1936 by S. A. Schelkunoff [1], [2], and it is a more rigorous formulation of Huygens' principle [3] which states that "*each point on a primary wavefront can be considered to be a new source of a secondary spherical wave and that a secondary wavefront can be constructed as the envelope of these secondary spherical waves* [4]." The equivalence principle is based on the *uniqueness theorem* which states that "*a field in a lossy region is uniquely specified by the sources within the region plus the tangential components of the electric field over the boundary, or the tangential components of the magnetic field over the boundary, or the former over part of the boundary and the latter over the rest of the boundary* [2], [5]." The field in a lossless medium is considered to be the limit, as the losses go to zero, of the corresponding field in a lossy medium. Thus if the tangential electric and magnetic fields are completely known over a closed surface, the fields in the source-free region can be determined.

By the equivalence principle, the fields outside an imaginary closed surface are obtained by placing over the closed surface suitable electric- and magnetic-current densities which satisfy the boundary conditions. The current densities are selected so that the fields inside the closed surface are zero and outside they are equal to the radiation produced by the actual sources. Thus the technique can be used to obtain the fields radiated outside a closed surface by sources enclosed within it. The formulation is exact but requires integration over the closed surface. The degree of accuracy depends on the knowledge of the tangential components of the fields over the closed surface.

In most applications, the closed surface is selected so that most of it coincides with the conducting parts of the physical structure. This is preferred because the vanishing of the tangential electric field components over the conducting parts of the surface reduces the physical limits of integration.

The equivalence principle is developed by considering an actual radiating source, which electrically is represented by current densities  $\mathbf{J}_1$  and  $\mathbf{M}_1$ , as shown in Figure 12.1(a). The source radiates fields  $\mathbf{E}_1$  and  $\mathbf{H}_1$  everywhere. However, it is desired to develop a method that will yield the fields outside a closed surface. To accomplish this, a closed surface  $S$  is chosen, shown dashed in Figure 12.1(a), which encloses the current densities  $\mathbf{J}_1$  and  $\mathbf{M}_1$ . The volume within  $S$  is denoted by  $V_1$  and outside  $S$  by  $V_2$ . *The primary task will be to replace the original problem, shown in Figure 12.1(a), by an equivalent one which yields the same fields  $\mathbf{E}_1$  and  $\mathbf{H}_1$  outside  $S$  (within  $V_2$ ).* The formulation of the problem can be aided eminently if the closed surface is judiciously chosen so that fields over most, if not the entire surface, are known *a priori*.

An equivalent problem of Figure 12.1(a) is shown in Figure 12.1(b). The original sources  $\mathbf{J}_1$  and  $\mathbf{M}_1$  are removed, and we assume that there exist fields  $\mathbf{E}$  and  $\mathbf{H}$  inside  $S$  and fields  $\mathbf{E}_1$  and  $\mathbf{H}_1$  outside of  $S$ . For these fields to exist within and outside  $S$ , they must satisfy the boundary conditions on the tangential electric and magnetic field components. Thus on the imaginary surface  $S$  there must exist the *equivalent sources*

$$\mathbf{J}_s = \hat{\mathbf{n}} \times [\mathbf{H}_1 - \mathbf{H}] \quad (12-1)$$

$$\mathbf{M}_s = -\hat{\mathbf{n}} \times [\mathbf{E}_1 - \mathbf{E}] \quad (12-2)$$

and they radiate into an *unbounded space* (same medium everywhere). *The current densities of (12-1) and (12-2) are said to be equivalent only within  $V_2$ , because they*

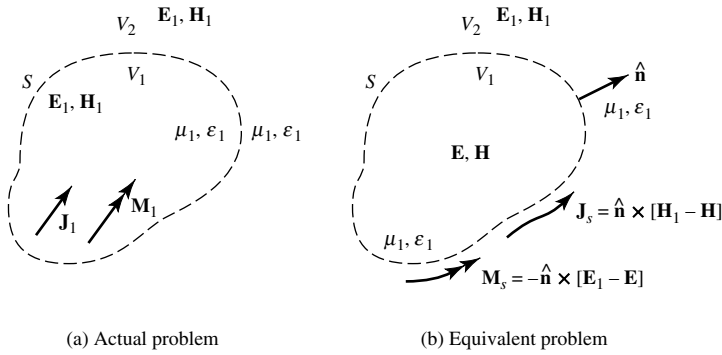


**Figure 12.1** Actual and equivalent models.

produce the original fields  $(\mathbf{E}_1, \mathbf{H}_1)$  only outside  $S$ . Fields  $\mathbf{E}, \mathbf{H}$ , different from the originals  $(\mathbf{E}_1, \mathbf{H}_1)$ , result within  $V_1$ . Since the currents of (12-1) and (12-2) radiate in an unbounded space, the fields can be determined using (3-27)–(3-30a) and the geometry of Figure 12.2(a). In Figure 12.2(a),  $R$  is the distance from any point on the surface  $S$ , where  $\mathbf{J}_s$  and  $\mathbf{M}_s$  exist, to the observation point.

So far, the tangential components of *both*  $\mathbf{E}$  and  $\mathbf{H}$  have been used in setting up the equivalent problem. From electromagnetic uniqueness concepts, it is known that the tangential components of only  $\mathbf{E}$  or  $\mathbf{H}$  are needed to determine the fields. It will be demonstrated that equivalent problems can be found which require only the magnetic-current densities (tangential  $\mathbf{E}$ ) or only electric current densities (tangential  $\mathbf{H}$ ). This requires modifications to the equivalent problem of Figure 12.1(b).

Since the fields  $\mathbf{E}, \mathbf{H}$  within  $S$  can be anything (this is not the region of interest), it can be assumed that they are zero. In that case the equivalent problem of Figure 12.1(b) reduces to that of Figure 12.3(a) with the equivalent current densities being equal to

$$\mathbf{J}_s = \hat{\mathbf{n}} \times (\mathbf{H}_1 - \mathbf{H})|_{\mathbf{H}=0} = \hat{\mathbf{n}} \times \mathbf{H}_1 \quad (12-3)$$

$$\mathbf{M}_s = -\hat{\mathbf{n}} \times (\mathbf{E}_1 - \mathbf{E})|_{\mathbf{E}=0} = -\hat{\mathbf{n}} \times \mathbf{E}_1 \quad (12-4)$$

This form of the field equivalence principle is known as *Love's Equivalence Principle* [2], [6]. Since the current densities of (12-3) and (12-4) radiate in an unbounded medium (same  $\mu, \epsilon$  everywhere), they can be used in conjunction with (3-27)–(3-30a) to find the fields everywhere.

Love's Equivalence Principle of Figure 12.3(a) produces a null field within the imaginary surface  $S$ . Since the value of the  $\mathbf{E} = \mathbf{H} = 0$  within  $S$  cannot be disturbed if the properties of the medium within it are changed, let us assume that it is replaced by a perfect electric conductor ( $\sigma = \infty$ ). The introduction of the perfect conductor will have an effect on the equivalent source  $\mathbf{J}_s$ , and it will prohibit the use of (3-27)–(3-30a) since the current densities no longer radiate into an unbounded medium. Imagine that the geometrical configuration of the electric conductor is identical to the profile of the imaginary surface  $S$ , over which  $\mathbf{J}_s$  and  $\mathbf{M}_s$  exist. As the electric conductor takes its place, as shown in Figure 12.3(b), the electric current density  $\mathbf{J}_s$ , which is tangent to the surface  $S$ , is short-circuited by the electric conductor. Thus the equivalent problem of Figure 12.3(a) reduces to that of Figure 12.3(b). There exists only a magnetic current

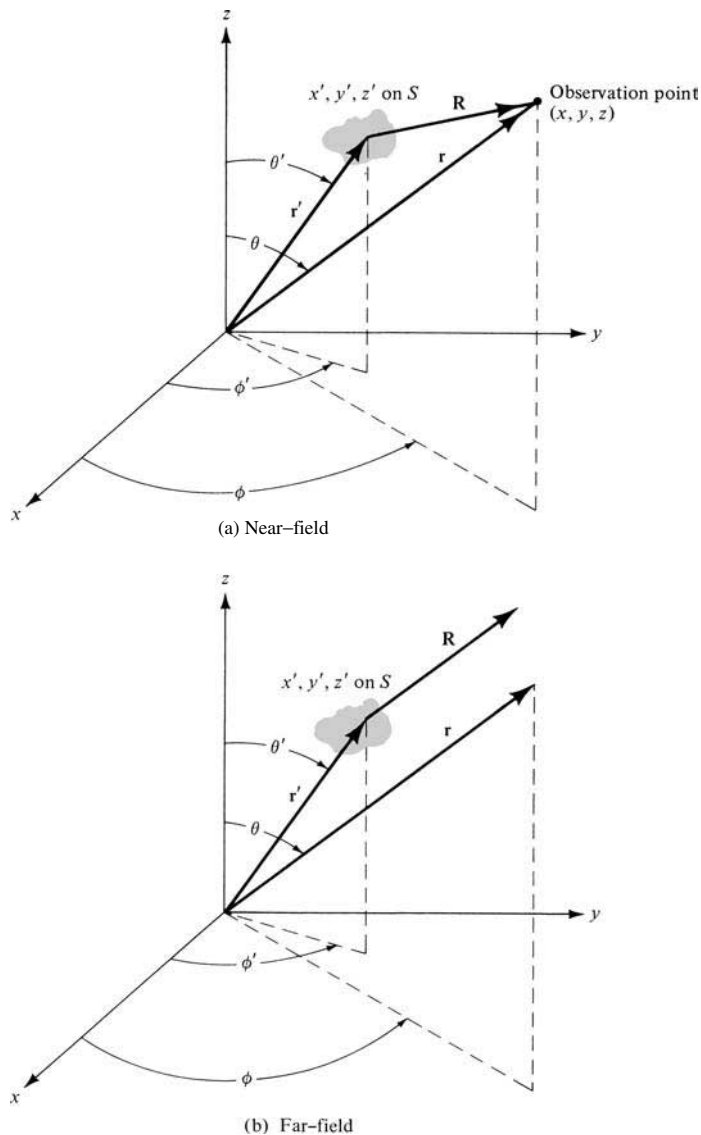


**Figure 12.2** Coordinate system for aperture antenna analysis.

density  $\mathbf{M}_s$  over  $S$ , and it radiates in the presence of the electric conductor producing outside  $S$  the original fields  $\mathbf{E}_1, \mathbf{H}_1$ . Within  $S$  the fields are zero but, as before, this is not a region of interest. The difficulty in trying to use the equivalent problem of Figure 12.3(b) is that (3-27)–(3-30a) cannot be used, because the current densities do not radiate into an unbounded medium. The problem of a magnetic current density radiating in the presence of an electric conducting surface must be solved. So it seems that the equivalent problem is just as difficult as the original problem itself.

Before some special simple geometries are considered and some suggestions are made for approximating complex geometries, let us introduce another equivalent problem. Referring to Figure 12.3(a), let us assume that instead of placing a perfect electric

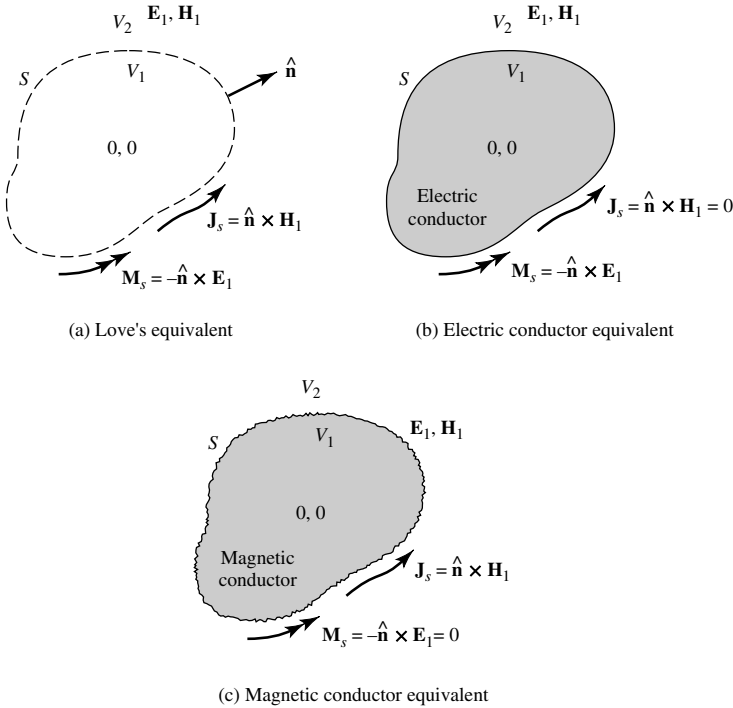


**Figure 12.3** Equivalence principle models.

conductor within  $S$  we introduce a perfect magnetic conductor which will short out the magnetic current density and reduce the equivalent problem to that shown in Figure 12.3(c). As was with the equivalent problem of Figure 12.3(b), (3-27)–(3-30a) cannot be used with Figure 12.3(c) and the problem is just as difficult as that of Figure 12.3(b) or the original of Figure 12.1(a).

To begin to see the utility of the field equivalence principle, especially that of Figure 12.3(b), let us assume that the surface of the electric conductor is flat and extends to infinity as shown in Figure 12.4(a). For this geometry, the problem is to determine how a magnetic source radiates in the presence of a flat electric conductor. From image theory, this problem reduces to that of Figure 12.4(b) where an imaginary magnetic source is introduced on the side of the conductor and takes its place (remove conductor). Since the imaginary source is in the same direction as the equivalent source, the equivalent problem of Figure 12.4(b) reduces to that of Figure 12.4(c). The magnetic current density is doubled, it radiates in an unbounded medium, and (3-27)–(3-30a) can be used. The equivalent problem of Figure 12.4(c) yields the correct  $\mathbf{E}$ ,  $\mathbf{H}$  fields to the right side of the interface. If the surface of the obstacle is not flat and infinite, but its curvature is large compared to the wavelength, a good approximation is the equivalent problem of Figure 12.3(c).

## SUMMARY

In the analysis of electromagnetic problems, many times it is easier to form equivalent problems that yield the same solution within a region of interest. This is the case for

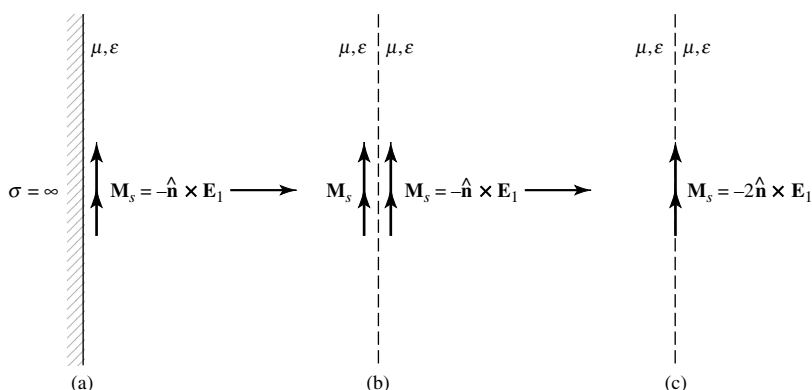


**Figure 12.4** Equivalent models for magnetic source radiation near a perfect electric conductor.

scattering, diffraction, and aperture antenna problems. In this chapter, the main interest is in aperture antennas. The concepts will be demonstrated with examples.

The steps that must be used to form an equivalent and solve an aperture problem are as follows:

1. Select an imaginary surface that encloses the actual sources (the aperture). The surface must be judiciously chosen so that the tangential components of the electric and/or the magnetic field are known, exactly or approximately, over its entire span. In many cases this surface is a flat plane extending to infinity.
2. Over the imaginary surface form equivalent current densities  $\mathbf{J}_s$ ,  $\mathbf{M}_s$  which take one of the following forms:
  - a.  $\mathbf{J}_s$  and  $\mathbf{M}_s$  over  $S$  assuming that the  $\mathbf{E}$ - and  $\mathbf{H}$ -fields within  $S$  are not zero.
  - b. or  $\mathbf{J}_s$  and  $\mathbf{M}_s$  over  $S$  assuming that the  $\mathbf{E}$ - and  $\mathbf{H}$ -fields within  $S$  are zero (Love's theorem)
  - c. or  $\mathbf{M}_s$  over  $S$  ( $\mathbf{J}_s = 0$ ) assuming that within  $S$  the medium is a perfect electric conductor
  - d. or  $\mathbf{J}_s$  over  $S$  ( $\mathbf{M}_s = 0$ ) assuming that within  $S$  the medium is a perfect magnetic conductor.
3. Solve the equivalent problem. For forms (a) and (b), (3-27)–(3-30a) can be used. For form (c), the problem of a magnetic current source next to a perfect electric conductor must be solved [(3-27)–(3-30a) cannot be used directly, because the current density does not radiate into an unbounded medium]. If the electric conductor is an infinite flat plane the problem can be solved exactly by image theory. For form (d), the problem of an electric current source next to a perfect magnetic conductor must be solved. Again (3-27)–(3-30a) cannot be used directly. If the magnetic conductor is an infinite flat plane, the problem can be solved exactly by image theory.

To demonstrate the usefulness and application of the field equivalence theorem to aperture antenna theory, an example is considered.

**Example 12.1**

A waveguide aperture is mounted on an infinite ground plane, as shown in Figure 12.5(a). Assuming that the tangential components of the electric field over the aperture are known, and are given by  $\mathbf{E}_a$ , find an equivalent problem that will yield the same fields  $\mathbf{E}$ ,  $\mathbf{H}$  radiated by the aperture to the right side of the interface.

*Solution:* First an imaginary closed surface is chosen. For this problem it is appropriate to select a flat plane extending from minus infinity to plus infinity, as shown in Figure 12.5(b). Over the infinite plane, the equivalent current densities  $\mathbf{J}_s$  and  $\mathbf{M}_s$  are formed. Since the tangential components of  $\mathbf{E}$  do not exist outside the aperture, because of vanishing boundary conditions, the magnetic current density  $\mathbf{M}_s$  is only nonzero over the aperture. The electric current density  $\mathbf{J}_s$  is nonzero everywhere and is yet unknown. Now let us assume that an imaginary flat electric conductor approaches the surface  $S$ , and it shorts out the current density  $\mathbf{J}_s$  everywhere.  $\mathbf{M}_s$  exists only over the space occupied originally by the aperture, and it radiates in the presence of the conductor [see Figure 12.5(c)]. By image theory, the conductor can be removed and replaced by an imaginary (equivalent) source  $\mathbf{M}_s$  as shown in Figure 12.5(d), which is analogous to Figure 12.4(b). Finally, the equivalent problem of Figure 12.5(d) reduces to that of Figure 12.5(e), which is analogous to that of Figure 12.4(c). The original problem has been reduced to a very simple equivalent and (3-27)–(3-30a) can be utilized for its solution.

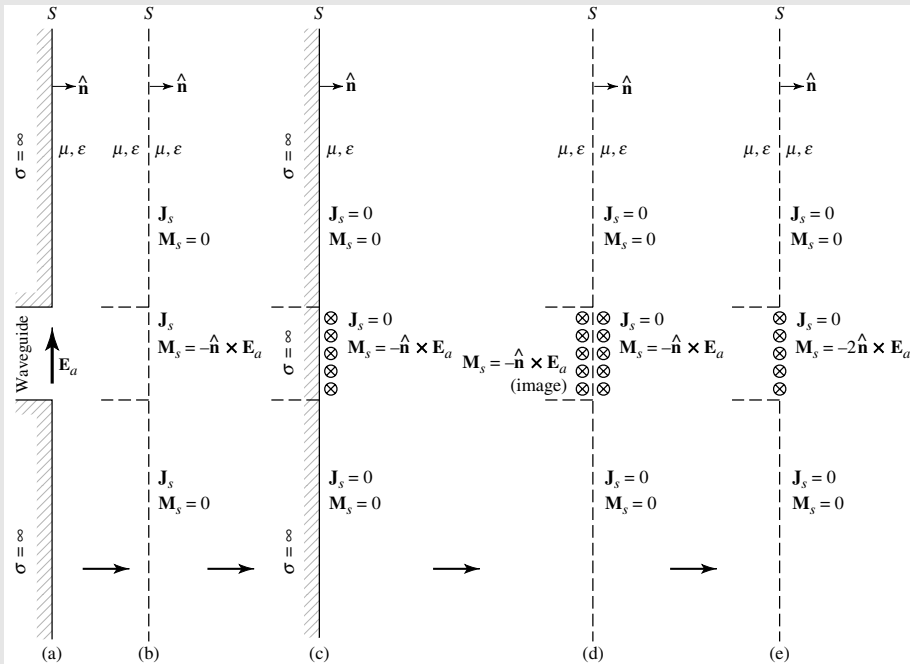


**Figure 12.5** Equivalent models for waveguide aperture mounted on an infinite flat electric ground plane.

In this chapter the theory will be developed to compute the fields radiated by an aperture, like that shown in Figure 12.5(a), making use of its equivalent of Figure 12.5(e). For other problems, their equivalent forms will not necessarily be the same as that shown in Figure 12.5(e).

## 12.3 RADIATION EQUATIONS

In Chapter 3 and in the previous section it was stated that the fields radiated by sources  $\mathbf{J}_s$  and  $\mathbf{M}_s$  in an unbounded medium can be computed by using (3-27)–(3-30a) where the integration must be performed over the entire surface occupied by  $\mathbf{J}_s$  and  $\mathbf{M}_s$ . These equations yield valid solutions for all observation points [2], [7]. For most problems, the main difficulty is the inability to perform the integrations in (3-27) and (3-28). However for far-field observations, the complexity of the formulation can be reduced.

As was shown in Section 4.4.1, for far-field observations  $R$  can most commonly be approximated by

$$R \simeq r - r' \cos \psi \quad \text{for phase variations} \quad (12-5a)$$

$$R \simeq r \quad \text{for amplitude variations} \quad (12-5b)$$

where  $\psi$  is the angle between the vectors  $\mathbf{r}$  and  $\mathbf{r}'$ , as shown in Figure 12.2(b). The primed coordinates ( $x'$ ,  $y'$ ,  $z'$ , or  $r'$ ,  $\theta'$ ,  $\phi'$ ) indicate the space occupied by the sources  $\mathbf{J}_s$  and  $\mathbf{M}_s$ , over which integration must be performed. The unprimed coordinates ( $x$ ,  $y$ ,  $z$  or  $r$ ,  $\theta$ ,  $\phi$ ) represent the observation point. Geometrically the approximation of (12-5a) assumes that the vectors  $\mathbf{R}$  and  $\mathbf{r}$  are parallel, as shown in Figure 12.2(b).

Using (12-5a) and (12-5b), (3-27) and (3-28) can be written as

$$\mathbf{A} = \frac{\mu}{4\pi} \iint_S \mathbf{J}_s \frac{e^{-jkR}}{R} ds' \simeq \frac{\mu e^{-jkr}}{4\pi r} \mathbf{N} \quad (12-6)$$

$$\mathbf{N} = \iint_S \mathbf{J}_s e^{jkr' \cos \psi} ds' \quad (12-6a)$$

$$\mathbf{F} = \frac{\epsilon}{4\pi} \iint_S \mathbf{M}_s \frac{e^{-jkR}}{R} ds' \simeq \frac{\epsilon e^{-jkr}}{4\pi r} \mathbf{L} \quad (12-7)$$

$$\mathbf{L} = \iint_S \mathbf{M}_s e^{jkr' \cos \psi} ds' \quad (12-7a)$$

In Section 3.6 it was shown that in the far-field only the  $\theta$  and  $\phi$  components of the  $\mathbf{E}$ - and  $\mathbf{H}$ -fields are dominant. Although the radial components are not necessarily zero, they are negligible compared to the  $\theta$  and  $\phi$  components. Using (3-58a)–(3-59b), the  $\mathbf{E}_A$  of (3-29) and  $\mathbf{H}_F$  of (3-30) can be written as

$$(E_A)_\theta \simeq -j\omega A_\theta \quad (12-8a)$$

$$(E_A)_\phi \simeq -j\omega A_\phi \quad (12-8b)$$



$$(H_F)_\theta \simeq -j\omega F_\theta \quad (12-8c)$$

$$(H_F)_\phi \simeq -j\omega F_\phi \quad (12-8d)$$

and the  $\mathbf{E}_F$  of (3-29) and  $\mathbf{H}_A$  of (3-30), with the aid of (12-8a)–(12-8d), as

$$(E_F)_\theta \simeq +\eta(H_F)_\phi = -j\omega\eta F_\phi \quad (12-9a)$$

$$(E_F)_\phi \simeq -\eta(H_F)_\theta = +j\omega\eta F_\theta \quad (12-9b)$$

$$(H_A)_\theta \simeq -\frac{(E_A)_\phi}{\eta} = +j\omega\frac{A_\phi}{\eta} \quad (12-9c)$$

$$(H_A)_\phi \simeq +\frac{(E_A)_\theta}{\eta} = -j\omega\frac{A_\theta}{\eta} \quad (12-9d)$$

Combining (12-8a)–(12-8d) with (12-9a)–(12-9d), and making use of (12-6)–(12-7a) the total  $\mathbf{E}$ - and  $\mathbf{H}$ -fields can be written as

$$E_r \simeq 0 \quad (12-10a)$$

$$E_\theta \simeq -\frac{jke^{-jkr}}{4\pi r}(L_\phi + \eta N_\theta) \quad (12-10b)$$

$$E_\phi \simeq +\frac{jke^{-jkr}}{4\pi r}(L_\theta - \eta N_\phi) \quad (12-10c)$$

$$H_r \simeq 0 \quad (12-10d)$$

$$H_\theta \simeq \frac{jke^{-jkr}}{4\pi r}\left(N_\theta - \frac{L_\theta}{\eta}\right) \quad (12-10e)$$

$$H_\phi \simeq -\frac{jke^{-jkr}}{4\pi r}\left(N_\phi + \frac{L_\phi}{\eta}\right) \quad (12-10f)$$

The  $N_\theta$ ,  $N_\phi$ ,  $L_\theta$ , and  $L_\phi$  can be obtained from (12-6a) and (12-7a). That is,

$$\mathbf{N} = \iint_S \mathbf{J}_s e^{+jkr' \cos \psi} ds' = \iint_S (\hat{\mathbf{a}}_x J_x + \hat{\mathbf{a}}_y J_y + \hat{\mathbf{a}}_z J_z) e^{+jkr' \cos \psi} ds' \quad (12-11a)$$

$$\mathbf{L} = \iint_S \mathbf{M}_s e^{+jkr' \cos \psi} ds' = \iint_S (\hat{\mathbf{a}}_x M_x + \hat{\mathbf{a}}_y M_y + \hat{\mathbf{a}}_z M_z) e^{+jkr' \cos \psi} ds' \quad (12-11b)$$

Using the rectangular-to-spherical component transformation, obtained by taking the inverse (in this case also the transpose) of (4-5), (12-11a) and (12-11b) reduce for the

$\theta$  and  $\phi$  components to

$$N_\theta = \iint_S [J_x \cos \theta \cos \phi + J_y \cos \theta \sin \phi - J_z \sin \theta] e^{+jkr' \cos \psi} ds' \quad (12-12a)$$

$$N_\phi = \iint_S [-J_x \sin \phi + J_y \cos \phi] e^{+jkr' \cos \psi} ds' \quad (12-12b)$$

$$L_\theta = \iint_S [M_x \cos \theta \cos \phi + M_y \cos \theta \sin \phi - M_z \sin \theta] e^{+jkr' \cos \psi} ds' \quad (12-12c)$$

$$L_\phi = \iint_S [-M_x \sin \phi + M_y \cos \phi] e^{+jkr' \cos \psi} ds' \quad (12-12d)$$

## SUMMARY

To summarize the results, the procedure that must be followed to solve a problem using the radiation integrals will be outlined. Figures 12.2(a) and 12.2(b) are used to indicate the geometry.

1. Select a closed surface over which the total electric and magnetic fields  $\mathbf{E}_a$  and  $\mathbf{H}_a$  are known.
2. Form the equivalent current densities  $\mathbf{J}_s$  and  $\mathbf{M}_s$  over  $S$  using (12-3) and (12-4) with  $\mathbf{H}_1 = \mathbf{H}_a$  and  $\mathbf{E}_1 = \mathbf{E}_a$ .
3. Determine the  $\mathbf{A}$  and  $\mathbf{F}$  potentials using (12-6)–(12-7a) where the integration is over the closed surface  $S$ .
4. Determine the radiated  $\mathbf{E}$ - and  $\mathbf{H}$ -fields using (3-29) and (3-30).

The above steps are valid for all regions (near-field and far-field) outside the surface  $S$ . If, however, the observation point is in the far-field, steps 3 and 4 can be replaced by 3' and 4'. That is,

- 3'. Determine  $N_\theta$ ,  $N_\phi$ ,  $L_\theta$  and  $L_\phi$  using (12-12a)–(12-12d).
- 4'. Determine the radiated  $\mathbf{E}$ - and  $\mathbf{H}$ -fields using (12-10a)–(12-10f).

Some of the steps outlined above can be reduced by a judicious choice of the equivalent model. In the remaining sections of this chapter, the techniques will be applied and demonstrated with examples of rectangular and circular apertures.

## 12.4 DIRECTIVITY

The directivity of an aperture can be found in a manner similar to that of other antennas. The primary task is to formulate the radiation intensity  $U(\theta, \phi)$ , using the far-zone

electric and magnetic field components, as given by (2-12a) or

$$U(\theta, \phi) = \frac{1}{2} \text{Re}[(\hat{\mathbf{a}}_\theta E_\theta + \hat{\mathbf{a}}_\phi E_\phi) \times (\hat{\mathbf{a}}_\theta H_\theta + \hat{\mathbf{a}}_\phi H_\phi)^*] = \frac{1}{2\eta} (|E_\theta^0|^2 + |E_\phi^0|^2) \quad (12-13)$$

which in normalized form reduces to

$$U_n(\theta, \phi) = (|E_\theta^0(\theta, \phi)|^2 + |E_\phi^0(\theta, \phi)|^2) = B_0 F(\theta, \phi) \quad (12-13a)$$

The directive properties can then be found using (2-19)–(2-22).

Because the radiation intensity  $U(\theta, \phi)$  for each aperture antenna will be of a different form, a general equation for the directivity cannot be formed. However, a general MATLAB and FORTRAN computer program, designated as **Directivity**, has been written to compute the directivity of any antenna, including an aperture, once the radiation intensity is specified. The program is based on the formulations of (12-13a), (2-19)–(2-20), and (2-22), and it is included in Chapter 2. In the main program, it requires the lower and upper limits on  $\theta$  and  $\phi$ . The radiation intensity for the antenna in question must be specified in the subroutine  $U(\theta, \phi, F)$  of the program.

Expressions for the directivity of some simple aperture antennas, rectangular and circular, will be derived in later sections of this chapter.

## 12.5 RECTANGULAR APERTURES

In practice, the rectangular aperture is probably the most common microwave antenna. Because of its configuration, the rectangular coordinate system is the most convenient system to express the fields at the aperture and to perform the integration. Shown in Figure 12.6 are the three most common and convenient coordinate positions used for the solution of an aperture antenna. In Figure 12.6(a) the aperture lies on the  $y$ - $z$  plane, in Figure 12.6(b) on the  $x$ - $z$  plane, and in Figure 12.6(c) on the  $x$ - $y$  plane. For a given field distribution, the analytical forms for the fields for each of the arrangements are not the same. However the computed values will be the same, since the physical problem is identical in all cases.

For each of the geometries shown in Figure 12.6, the only difference in the analysis is in the formulation of

1. the components of the equivalent current densities ( $J_x, J_y, J_z, M_x, M_y, M_z$ )
2. the difference in paths from the source to the observation point ( $r' \cos \psi$ )
3. the differential area  $ds'$

In general, the nonzero components of  $\mathbf{J}_s$  and  $\mathbf{M}_s$  are

$$J_y, J_z, M_y, M_z \quad [\text{Figure 12.6(a)}] \quad (12-14a)$$

$$J_x, J_z, M_x, M_z \quad [\text{Figure 12.6(b)}] \quad (12-14b)$$

$$J_x, J_y, M_x, M_y \quad [\text{Figure 12.6(c)}] \quad (12-14c)$$

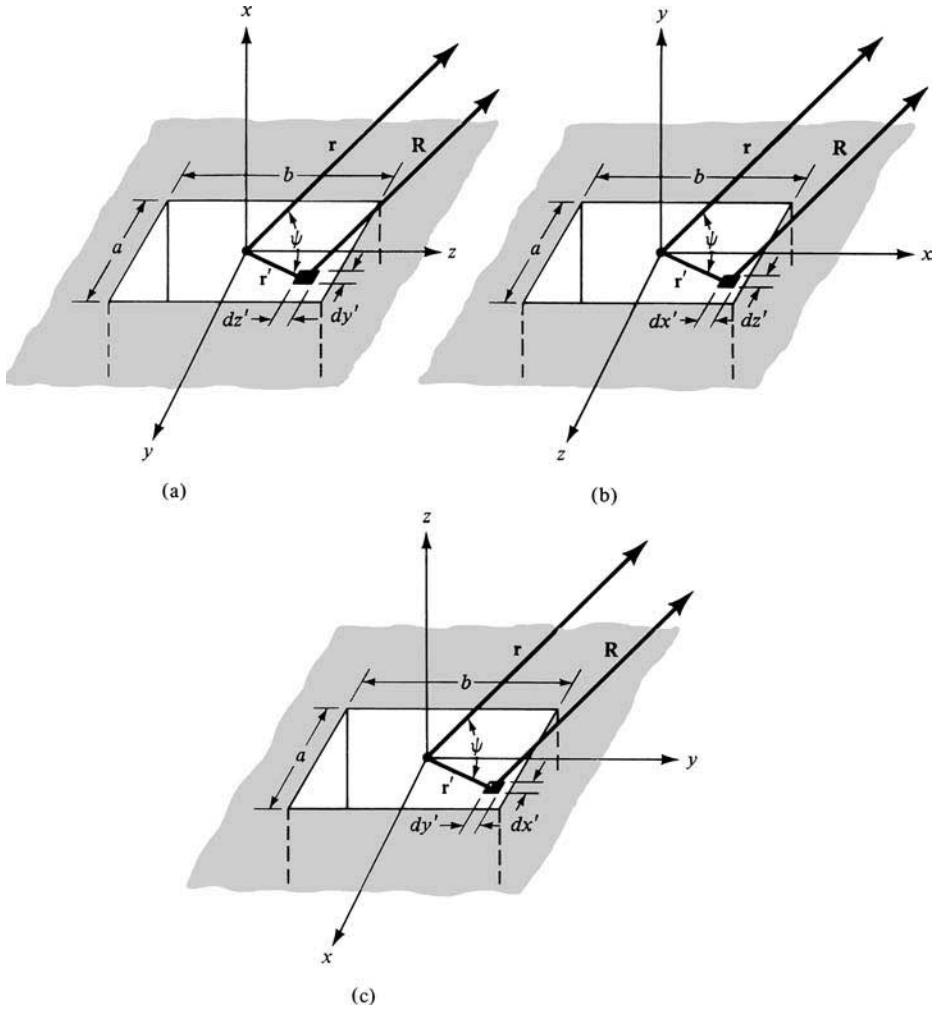


**Figure 12.6** Rectangular aperture positions for antenna system analysis.

The differential paths take the form of

$$\begin{aligned}
 r' \cos \psi &= \mathbf{r}' \cdot \hat{\mathbf{a}}_r = (\hat{\mathbf{a}}_y y' + \hat{\mathbf{a}}_z z') \cdot (\hat{\mathbf{a}}_x \sin \theta \cos \phi + \hat{\mathbf{a}}_y \sin \theta \sin \phi + \hat{\mathbf{a}}_z \cos \theta) \\
 &= y' \sin \theta \sin \phi + z' \cos \theta \quad [\text{Figure 12.6(a)}]
 \end{aligned} \tag{12-15a}$$

$$\begin{aligned}
 r' \cos \psi &= \mathbf{r}' \cdot \hat{\mathbf{a}}_r = (\hat{\mathbf{a}}_x x' + \hat{\mathbf{a}}_z z') \cdot (\hat{\mathbf{a}}_x \sin \theta \cos \phi + \hat{\mathbf{a}}_y \sin \theta \sin \phi + \hat{\mathbf{a}}_z \cos \theta) \\
 &= x' \sin \theta \cos \phi + z' \cos \theta \quad [\text{Figure 12.6(b)}]
 \end{aligned} \tag{12-15b}$$

$$\begin{aligned}
 r' \cos \psi &= \mathbf{r}' \cdot \hat{\mathbf{a}}_r = (\hat{\mathbf{a}}_x x' + \hat{\mathbf{a}}_y y') \cdot (\hat{\mathbf{a}}_x \sin \theta \cos \phi + \hat{\mathbf{a}}_y \sin \theta \sin \phi + \hat{\mathbf{a}}_z \cos \theta) \\
 &= x' \sin \theta \cos \phi + y' \sin \theta \sin \phi \quad [\text{Figure 12.6(c)}]
 \end{aligned} \tag{12-15c}$$



Figure 12.5(a), its equivalents are those of Figures 12.5(a)–(e). Using the equivalent of Figure 12.5(e)

$$\begin{aligned} \mathbf{M}_s &= \begin{cases} -2\hat{\mathbf{n}} \times \mathbf{E}_a = -2\hat{\mathbf{a}}_z \times \hat{\mathbf{a}}_y E_0 = +\hat{\mathbf{a}}_x 2E_0 & -a/2 \leq x' \leq a/2 \\ 0 & -b/2 \leq y' \leq b/2 \\ & \text{elsewhere} \end{cases} \quad (12-18) \\ \mathbf{J}_s &= 0 \quad \text{everywhere} \end{aligned}$$

### B. Radiation Fields: Element and Space Factors

The far-zone fields radiated by the aperture of Figure 12.7 can be found by using (12-10a)–(12-10f), (12-12a)–(12-12d), (12-14c), (12-15c), (12-16c), and (12-18). Thus,

$$N_\theta = N_\phi = 0 \quad (12-19)$$

$$L_\theta = \int_{-b/2}^{+b/2} \int_{-a/2}^{+a/2} [M_x \cos \theta \cos \phi] e^{jk(x' \sin \theta \cos \phi + y' \sin \theta \sin \phi)} dx' dy'$$

$$\boxed{L_\theta = \cos \theta \cos \phi \left[ \int_{-b/2}^{+b/2} \int_{-a/2}^{+a/2} M_x e^{jk(x' \sin \theta \cos \phi + y' \sin \theta \sin \phi)} dx' dy' \right]} \quad (12-19a)$$

In (12-19a), the integral within the brackets represents the *space factor* for a two-dimensional distribution. It is analogous to the space factor of (4-58a) for a line source (one-dimensional distribution). For the  $L_\theta$  component of the vector potential  $\mathbf{F}$ , the *element factor* is equal to the product of the factor outside the brackets in (12-19a) and the factor outside the brackets in (12-10c). The total field is equal to the product of the element and space factors, as defined by (4-59), and expressed in (12-10b) and (12-10c).

Using the integral

$$\int_{-c/2}^{+c/2} e^{j\alpha z} dz = c \left[ \frac{\sin\left(\frac{\alpha}{2}c\right)}{\frac{\alpha}{2}c} \right] \quad (12-20)$$

(12-19a) reduces to

$$L_\theta = 2abE_0 \left[ \cos \theta \cos \phi \left( \frac{\sin X}{X} \right) \left( \frac{\sin Y}{Y} \right) \right] \quad (12-21)$$

where

$$X = \frac{ka}{2} \sin \theta \cos \phi \quad (12-21a)$$

$$Y = \frac{kb}{2} \sin \theta \sin \phi \quad (12-21b)$$

Similarly it can be shown that

$$L_\phi = -2abE_0 \left[ \sin \phi \left( \frac{\sin X}{X} \right) \left( \frac{\sin Y}{Y} \right) \right] \quad (12-22)$$

Substituting (12-19), (12-21), and (12-22) into (12-10a)–(12-10f), the fields radiated by the aperture can be written as

$$E_r = 0 \quad (12-23a)$$

$$E_\theta = j \frac{abkE_0e^{-jkr}}{2\pi r} \left[ \sin \phi \left( \frac{\sin X}{X} \right) \left( \frac{\sin Y}{Y} \right) \right] \quad (12-23b)$$

$$E_\phi = j \frac{abkE_0e^{-jkr}}{2\pi r} \left[ \cos \theta \cos \phi \left( \frac{\sin X}{X} \right) \left( \frac{\sin Y}{Y} \right) \right] \quad (12-23c)$$

$$H_r = 0 \quad (12-23d)$$

$$H_\theta = -\frac{E_\phi}{\eta} \quad (12-23e)$$

$$H_\phi = +\frac{E_\theta}{\eta} \quad (12-23f)$$

Equations (12-23a)–(12-23f) represent the three-dimensional distributions of the far-zone fields radiated by the aperture. Experimentally only two-dimensional plots can be measured. To reconstruct experimentally a three-dimensional plot, a series of two-dimensional plots must be made. In many applications, however, only a pair of two-dimensional plots are usually sufficient. These are the principal  $E$ - and  $H$ -plane patterns whose definition was stated in Section 2.2.3 and illustrated in Figure 2.3.

For the problem in Figure 12.7, the  $E$ -plane pattern is on the  $y$ - $z$  plane ( $\phi = \pi/2$ ) and the  $H$ -plane is on the  $x$ - $z$  plane ( $\phi = 0$ ). Thus

#### **$E$ –Plane ( $\phi = \pi/2$ )**

$$E_r = E_\phi = 0 \quad (12-24a)$$

$$E_\theta = j \frac{abkE_0e^{-jkr}}{2\pi r} \left[ \frac{\sin \left( \frac{kb}{2} \sin \theta \right)}{\frac{kb}{2} \sin \theta} \right] \quad (12-24b)$$

#### **$H$ –Plane ( $\phi = 0$ )**

$$E_r = E_\theta = 0 \quad (12-25a)$$

$$E_\phi = j \frac{abkE_0e^{-jkr}}{2\pi r} \left\{ \cos \theta \left[ \frac{\sin \left( \frac{ka}{2} \sin \theta \right)}{\frac{ka}{2} \sin \theta} \right] \right\} \quad (12-25b)$$

To demonstrate the techniques, three-dimensional patterns have been plotted in Figures 12.8 and 12.9. The dimensions of the aperture are indicated in each figure. Multiple lobes appear, because the dimensions of the aperture are greater than one wavelength. The number of lobes increases as the dimensions increase. For the aperture whose dimensions are  $a = 3\lambda$  and  $b = 2\lambda$  (Figure 12.8), there are a total of five lobes in the principal  $H$ -plane and three lobes in the principal  $E$ -plane. The pattern

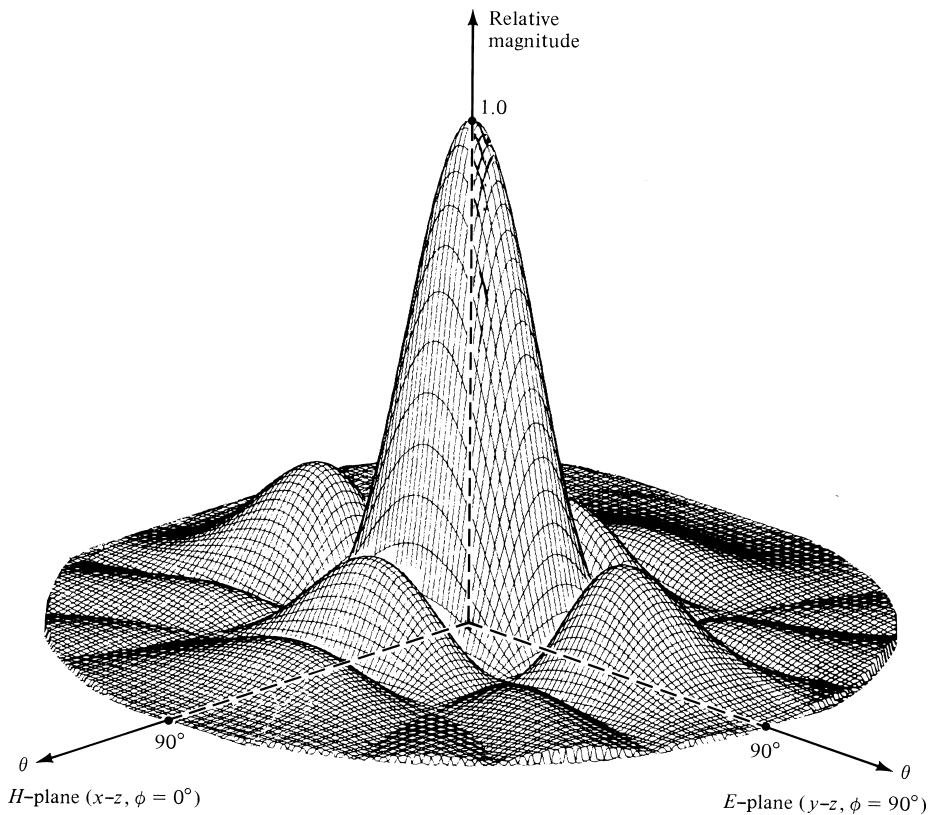


**Figure 12.8** Three-dimensional field pattern of a constant field rectangular aperture mounted on an infinite ground plane ( $a = 3\lambda$ ,  $b = 2\lambda$ ).

in the  $H$ -plane is only a function of the dimension  $a$  whereas that in the  $E$ -plane is only influenced by  $b$ . In the  $E$ -plane, the side lobe formed on each side of the major lobe is a result of  $\lambda < b \leq 2\lambda$ . In the  $H$ -plane, the first minor lobe on each side of the major lobe is formed when  $\lambda < a \leq 2\lambda$  and the second side lobe when  $2\lambda < a \leq 3\lambda$ . Additional lobes are formed when one or both of the aperture dimensions increase. This is illustrated in Figure 12.9 for an aperture with  $a = b = 3\lambda$ .

The two-dimensional principal plane patterns for the aperture with  $a = 3\lambda$ ,  $b = 2\lambda$  are shown in Figure 12.10. For this, and for all other size apertures mounted on an infinite ground plane, the  $H$ -plane patterns along the ground plane vanish. This is dictated by the boundary conditions. The  $E$ -plane patterns, in general, do not have to vanish along the ground plane, unless the dimension of the aperture in that plane (in this case  $b$ ) is a multiple of a wavelength.

The patterns computed above assumed that the aperture was mounted on an infinite ground plane. In practice, infinite ground planes are not realizable, but they can be approximated by large structures. Edge effects, on the patterns of apertures mounted on finite size ground planes, can be accounted for by diffraction techniques. They will be introduced and illustrated in Section 12.9. Computed results, which include diffractions, agree extremely well with measurements [8]–[10].



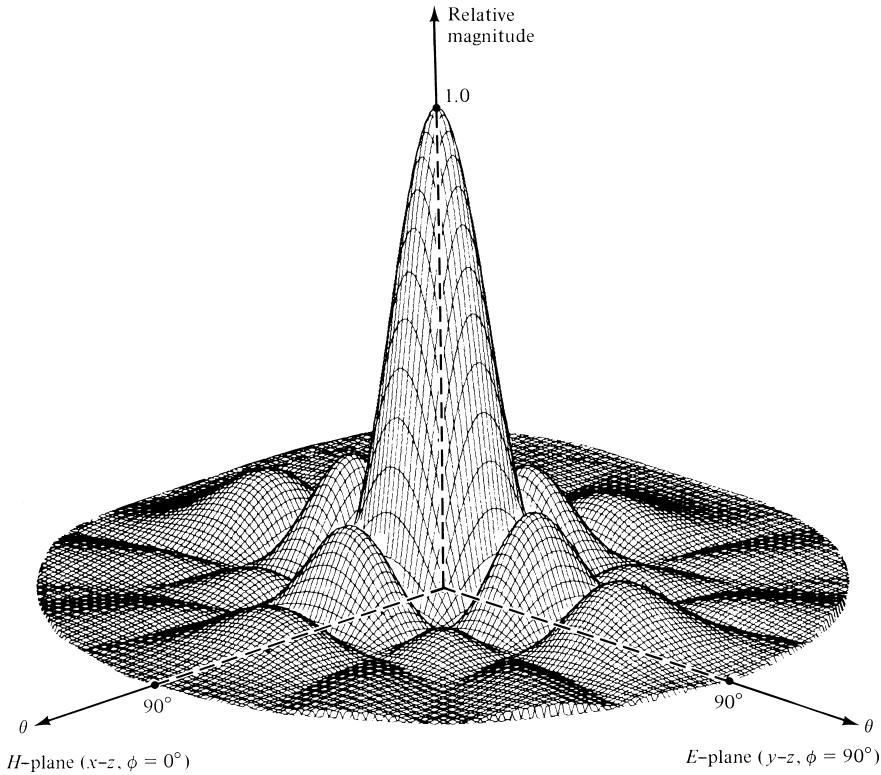


**Figure 12.9** Three-dimensional field pattern of a constant field square aperture mounted on an infinite ground plane ( $a = b = 3\lambda$ ).

### C. Beamwidths

For the  $E$ -plane pattern given by (12-24b), the maximum radiation is directed along the  $z$ -axis ( $\theta = 0$ ). The nulls (zeros) occur when

$$\frac{kb}{2} \sin \theta|_{\theta=\theta_n} = n\pi, \quad n = 1, 2, 3, \dots \quad (12-26)$$

or at the angles of

$$\begin{aligned} \theta_n &= \sin^{-1} \left( \frac{2n\pi}{kb} \right) = \sin^{-1} \left( \frac{n\lambda}{b} \right) \text{ rad} \\ &= 57.3 \sin^{-1} \left( \frac{n\lambda}{b} \right) \text{ degrees}, \quad n = 1, 2, 3, \dots \end{aligned} \quad (12-26a)$$

If  $b \gg n\lambda$ , (12-26a) reduces approximately to

$$\theta_n \simeq \frac{n\lambda}{b} \text{ rad} = 57.3 \left( \frac{n\lambda}{b} \right) \text{ degrees}, \quad n = 1, 2, 3, \dots \quad (12-26b)$$

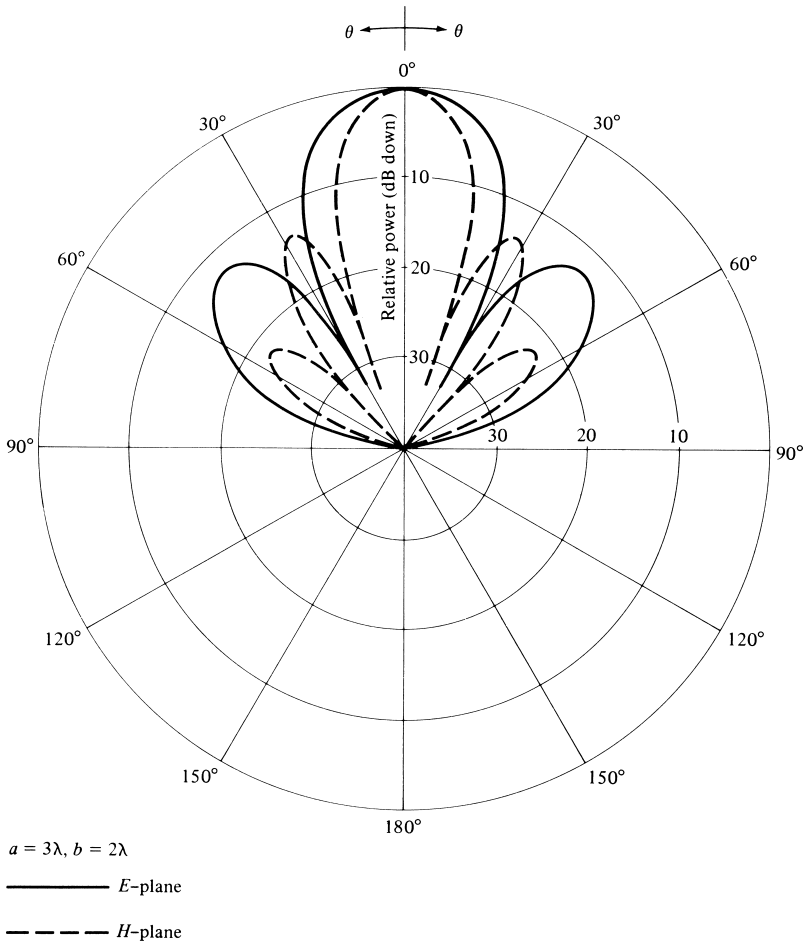


**Figure 12.10**  $E$ - and  $H$ -plane amplitude patterns for uniform distribution aperture mounted on an infinite ground plane ( $a = 3\lambda, b = 2\lambda$ ).

The total *beamwidth between nulls* is given by

$$\begin{aligned}\Theta_n &= 2\theta_n = 2 \sin^{-1} \left( \frac{n\lambda}{b} \right) \text{ rad} \\ &= 114.6 \sin^{-1} \left( \frac{n\lambda}{b} \right) \text{ degrees, } n = 1, 2, 3, \dots\end{aligned}\tag{12-27}$$

or approximately (for large apertures,  $b \gg n\lambda$ ) by

$$\Theta_n \simeq \frac{2n\lambda}{b} \text{ rad} = 114.6 \left( \frac{n\lambda}{b} \right) \text{ degrees, } n = 1, 2, 3, \dots\tag{12-27a}$$

The *first-null beamwidth* (FNBW) is obtained by letting  $n = 1$ .

The half-power point occurs when (see Appendix I)

$$\frac{kb}{2} \sin \theta|_{\theta=\theta_h} = 1.391 \quad (12-28)$$

or at an angle of

$$\begin{aligned} \theta_h &= \sin^{-1} \left( \frac{2.782}{kb} \right) = \sin^{-1} \left( \frac{0.443\lambda}{b} \right) \text{ rad} \\ &= 57.3 \sin^{-1} \left( \frac{0.443\lambda}{b} \right) \text{ degrees} \end{aligned} \quad (12-28a)$$

If  $b \gg 0.443\lambda$ , (12-28a) reduces approximately to

$$\theta_h \simeq \left( 0.443 \frac{\lambda}{b} \right) \text{ rad} = 25.38 \left( \frac{\lambda}{b} \right) \text{ degrees} \quad (12-28b)$$

Thus the total *half-power beamwidth* (HPBW) is given by

$$\Theta_h = 2\theta_h = 2 \sin^{-1} \left( \frac{0.443\lambda}{b} \right) \text{ rad} = 114.6 \sin^{-1} \left( \frac{0.443\lambda}{b} \right) \text{ degrees} \quad (12-29)$$

or approximately (when  $b \gg 0.443\lambda$ ) by

$$\Theta_h \simeq \left( 0.886 \frac{\lambda}{b} \right) \text{ rad} = 50.8 \left( \frac{\lambda}{b} \right) \text{ degrees} \quad (12-29a)$$

The maximum of the first side lobe occurs when (see Appendix I)

$$\frac{kb}{2} \sin \theta|_{\theta=\theta_s} = 4.494 \quad (12-30)$$

or at an angle of

$$\theta_s = \sin^{-1} \left( \frac{8.988}{kb} \right) = \sin^{-1} \left( \frac{1.43\lambda}{b} \right) \text{ rad} = 57.3 \sin^{-1} \left( \frac{1.43\lambda}{b} \right) \text{ degrees} \quad (12-30a)$$

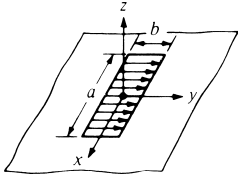
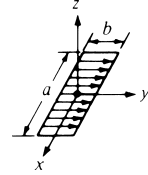
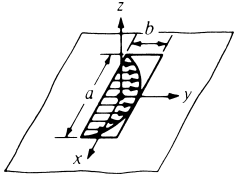
If  $b \gg 1.43\lambda$ , (12-30a) reduces to

$$\theta_s \simeq 1.43 \left( \frac{\lambda}{b} \right) \text{ rad} = 81.9 \left( \frac{\lambda}{b} \right) \text{ degrees} \quad (12-30b)$$

The total beamwidth between first side lobes (FSLBW) is given by

$$\Theta_s = 2\theta_s = 2 \sin^{-1} \left( \frac{1.43\lambda}{b} \right) \text{ rad} = 114.6 \sin^{-1} \left( \frac{1.43\lambda}{b} \right) \text{ degrees} \quad (12-30c)$$

TABLE 12.1 Equivalents, Fields, Beamwidths, Side Lobe Levels, and Directivities of Rectangular Apertures

	Uniform Distribution Aperture on Ground Plane	Uniform Distribution Aperture in Free-Space	TE <sub>10</sub> -Mode Distribution Aperture on Ground Plane
Aperture distribution of tangential components (analytical)	$\mathbf{E}_a = \hat{\mathbf{a}}_y E_0 \left\{ \begin{array}{l} -a/2 \leq x' \leq a/2 \\ -b/2 \leq y' \leq b/2 \end{array} \right.$	$\left. \begin{array}{l} \mathbf{E}_a = \hat{\mathbf{a}}_y E_0 \\ \mathbf{H}_a = -\hat{\mathbf{a}}_x \frac{E_0}{\eta} \end{array} \right\} \left\{ \begin{array}{l} -a/2 \leq x' \leq a/2 \\ -b/2 \leq y' \leq b/2 \end{array} \right.$	$\mathbf{E}_a = \hat{\mathbf{a}}_y E_0 \cos\left(\frac{\pi}{a}x'\right) \left\{ \begin{array}{l} -a/2 \leq x' \leq a/2 \\ -b/2 \leq y' \leq b/2 \end{array} \right.$
Aperture distribution of tangential components (graphical)			
Equivalent	$\mathbf{M}_s = \left\{ \begin{array}{l} -2\hat{\mathbf{n}} \times \mathbf{E}_a \\ 0 \end{array} \right\} \left\{ \begin{array}{l} -a/2 \leq x' \leq a/2 \\ -b/2 \leq y' \leq b/2 \\ \text{elsewhere} \end{array} \right.$ $\mathbf{J}_s = 0$ everywhere	$\left. \begin{array}{l} \mathbf{M}_s = -\hat{\mathbf{n}} \times \mathbf{E}_a \\ \mathbf{J}_s = \hat{\mathbf{n}} \times \mathbf{H}_a \end{array} \right\} \left\{ \begin{array}{l} -a/2 \leq x' \leq a/2 \\ -b/2 \leq y' \leq b/2 \end{array} \right.$ $\mathbf{M}_s \simeq \mathbf{J}_s \simeq 0$ elsewhere	$\mathbf{M}_s = \left\{ \begin{array}{l} -2\hat{\mathbf{n}} \times \mathbf{E}_a \\ 0 \end{array} \right\} \left\{ \begin{array}{l} -a/2 \leq x' \leq a/2 \\ -b/2 \leq y' \leq b/2 \\ \text{elsewhere} \end{array} \right.$ $\mathbf{J}_s = 0$ everywhere
Far-zone fields $X = \frac{ka}{2} \sin \theta \cos \phi$ $Y = \frac{kb}{2} \sin \theta \sin \phi$ $C = j \frac{abkE_0 e^{-jkr}}{2\pi r}$	$E_r = H_r = 0$ $E_\theta = C \sin \phi \frac{\sin X}{X} \frac{\sin Y}{Y}$ $E_\phi = C \cos \theta \cos \phi \frac{\sin X}{X} \frac{\sin Y}{Y}$ $H_\theta = -E_\phi / \eta$ $H_\phi = E_\theta / \eta$	$E_r = H_r = 0$ $E_\theta = \frac{C}{2} \sin \phi (1 + \cos \theta) \frac{\sin X}{X} \frac{\sin Y}{Y}$ $E_\phi = \frac{C}{2} \cos \phi (1 + \cos \theta) \frac{\sin X}{X} \frac{\sin Y}{Y}$ $H_\theta = -E_\phi / \eta$ $H_\phi = E_\theta / \eta$	$E_r = H_r = 0$ $E_\theta = -\frac{\pi}{2} C \sin \phi \frac{\cos X}{(X)^2 - \left(\frac{\pi}{2}\right)^2} \frac{\sin Y}{Y}$ $E_\phi = -\frac{\pi}{2} C \cos \theta \cos \phi \frac{\cos X}{(X)^2 - \left(\frac{\pi}{2}\right)^2} \frac{\sin Y}{Y}$ $H_\theta = -E_\phi / \eta$ $H_\phi = E_\theta / \eta$

Half-power beamwidth (degrees)	$E$ -plane $b \gg \lambda$	$\frac{50.6}{b/\lambda}$	$\frac{50.6}{b/\lambda}$	$\frac{50.6}{b/\lambda}$
	$H$ -plane $a \gg \lambda$	$\frac{50.6}{a/\lambda}$	$\frac{50.6}{a/\lambda}$	$\frac{68.8}{a/\lambda}$
First null beamwidth (degrees)	$E$ -plane $b \gg \lambda$	$\frac{114.6}{b/\lambda}$	$\frac{114.6}{b/\lambda}$	$\frac{114.6}{b/\lambda}$
	$H$ -plane $a \gg \lambda$	$\frac{114.6}{a/\lambda}$	$\frac{114.6}{a/\lambda}$	$\frac{171.9}{a/\lambda}$
First side lobe max. (to main max.) (dB)	$E$ -plane	-13.26	-13.26	-13.26
	$H$ -plane	$-13.26$ $a \gg \lambda$	$-13.26$ $a \gg \lambda$	$-23$ $a \gg \lambda$
Directivity $D_0$ (dimensionless)		$\frac{4\pi}{\lambda^2}(\text{area}) = 4\pi \left( \frac{ab}{\lambda^2} \right)$	$\frac{4\pi}{\lambda^2}(\text{area}) = 4\pi \left( \frac{ab}{\lambda^2} \right)$	$\frac{8}{\pi^2} \left[ 4\pi \left( \frac{ab}{\lambda^2} \right) \right] = 0.81 \left[ 4\pi \left( \frac{ab}{\lambda^2} \right) \right]$

or approximately (when  $b \gg 1.43\lambda$ ) by

$$\Theta_s \simeq 2.86 \left( \frac{\lambda}{b} \right) \text{ rad} = 163.8 \left( \frac{\lambda}{b} \right) \text{ degrees} \quad (12-30d)$$

#### D. Side Lobe Level

The maximum of (12-24b) at the first side lobe is given by (see Appendix I)

$$|E_\theta(\theta = \theta_s)| = \left| \frac{\sin(4.494)}{4.494} \right| = 0.217 = -13.26 \text{ dB} \quad (12-31)$$

which is 13.26 dB down from the maximum of the main lobe.

An approximate value of the maximum of the first side lobe can be obtained by assuming that the maximum of (12-24b) occurs when its numerator is maximum. That is, when

$$\frac{kb}{2} \sin \theta|_{\theta=\theta_s} \simeq \frac{3\pi}{2} \quad (12-32)$$

Thus,

$$|E_\theta(\theta = \theta_s)| \simeq \frac{1}{3\pi/2} = 0.212 = -13.47 \text{ dB} \quad (12-33)$$

These values are very close to the exact ones given by (12-31).

A similar procedure can be followed to find the nulls, 3-dB points, beamwidth between nulls and 3-dB points, angle where the maximum of first side lobe occurs, and its magnitude at that point for the  $H$ -plane pattern of (12-25b). A comparison between the  $E$ - and  $H$ -plane patterns of (12-24b) and (12-25b) shows that they are similar in form except for the additional  $\cos \theta$  term that appears in (12-25b). An examination of the terms in (12-25b) reveals that the  $\cos \theta$  term is a much slower varying function than the  $\sin(ka \sin \theta/2)/(ka \sin \theta/2)$  term, especially when  $a$  is large.

As a first approximation, (12-26)–(12-33), with  $b$  replaced by  $a$ , can also be used for the  $H$ -plane. More accurate expressions can be obtained by also including the  $\cos \theta$  term. In regions well removed from the major lobe, the inclusion of the  $\cos \theta$  term becomes more essential for accurate results.

#### E. Directivity

The directivity for the aperture can be found using (12-23a)–(12-23c), (12-13)–(12-13a), and (2-19)–(2-22). The analytical details using this procedure, especially the integration to compute the radiated power ( $P_{\text{rad}}$ ), are more cumbersome.

Because the aperture is mounted on an infinite ground plane, an alternate and much simpler method can be used to compute the radiated power. The average power density is first formed using the fields at the aperture, and it is then integrated over the physical bounds of the opening. The integration is confined to the physical bounds of the

opening. Using Figure 12.7 and assuming that the magnetic field at the aperture is given by

$$\mathbf{H}_a = -\hat{\mathbf{a}}_x \frac{E_0}{\eta} \quad (12-34)$$

where  $\eta$  is the intrinsic impedance, the radiated power reduces to

$$P_{\text{rad}} = \iint_S \mathbf{W}_{\text{av}} \cdot d\mathbf{s} = \frac{|E_0|^2}{2\eta} \iint_{S_a} ds = ab \frac{|E_0|^2}{2\eta} \quad (12-35)$$

The maximum radiation intensity ( $U_{\text{max}}$ ), using the fields of (12-23a)–(12-23b), occurs toward  $\theta = 0^\circ$  and it is equal to

$$U_{\text{max}} = \left( \frac{ab}{\lambda} \right)^2 \frac{|E_0|^2}{2\eta} \quad (12-36)$$

Thus the directivity is equal to

$$D_0 = \frac{4\pi U_{\text{max}}}{P_{\text{rad}}} = \frac{4\pi}{\lambda^2} ab = \frac{4\pi}{\lambda^2} A_p = \frac{4\pi}{\lambda^2} A_{em} \quad (12-37)$$

where

$A_p$  = physical area of the aperture

$A_{em}$  = maximum effective area of the aperture

Using the definition of (2-110), it is shown that *the physical and maximum effective areas of a constant distribution aperture are equal.*

The beamwidths, side lobe levels, and directivity of this and other apertures are summarized in Table 12.1.

### Example 12.2

A rectangular aperture with a constant field distribution, with  $a = 3\lambda$  and  $b = 2\lambda$ , is mounted on an infinite ground plane. Compute the

- FNBW in the  $E$ -plane
- HPBW in the  $E$ -plane
- FSLBW in the  $E$ -plane
- FSLMM in the  $E$ -plane
- directivity using (12-37)
- directivity using the **Directivity** computer program at the end of Chapter 2, the fields of (12-23a)–(12-23f), and the formulation of Section 12.4

*Solution:*

a. Using (12-27)

$$\Theta_1 = 114.6 \sin^{-1}\left(\frac{1}{2}\right) = 114.6(0.524) = 60^\circ$$

b. Using (12-29)

$$\Theta_h = 114.6 \sin^{-1}\left(\frac{0.443}{2}\right) = 114.6(0.223) = 25.6^\circ$$

c. Using (12-30c)

$$\Theta_s = 2\theta_s = 114.6 \sin^{-1}\left(\frac{1.43}{2}\right) = 114.6(0.796) = 91.3^\circ$$

d. Using (12-31)

$$|E_\theta|_{\theta=\theta_s} = 0.217 \simeq -13.26 \text{ dB}$$

e. Using (12-37)

$$D_0 = 4\pi(3)(2) = 75.4 = 18.77 \text{ dB}$$

f. Using the computer program at the end of Chapter 2

$$D_0 \simeq 80.4 = 19.05 \text{ dB}$$

The difference in directivity values using (12-37) and the computer program is not attributed to the accuracy of the numerical method. The main contributor is the aperture tangential magnetic field of (12-34), which was assumed to be related to the aperture tangential electric field by the intrinsic impedance. Although this is a good assumption for large size apertures, it is not exact. Therefore the directivity value computed using the computer program should be considered to be the more accurate.

### 12.5.2 Uniform Distribution in Space

The second aperture examined is that of Figure 12.7 when it is *not* mounted on an infinite ground plane. The field distribution is given by

$$\left. \begin{aligned} \mathbf{E}_a &= \hat{\mathbf{a}}_y E_0 \\ \mathbf{H}_a &= -\hat{\mathbf{a}}_x \frac{E_0}{\eta} \end{aligned} \right\} \begin{aligned} -a/2 &\leq x' \leq a/2 \\ -b/2 &\leq y' \leq b/2 \end{aligned} \quad (12-38)$$

where  $E_0$  is a constant. The geometry of the opening for this problem is identical to the previous one. However the equivalents and radiated fields are different, because this time the aperture is not mounted on an infinite ground plane.



### A. Equivalent

To form the equivalent, a closed surface is chosen which again extends from  $-\infty$  to  $+\infty$  on the  $x$ - $y$  plane. Over the entire surface  $\mathbf{J}_s$  and  $\mathbf{M}_s$  are formed. The difficulty encountered in this problem is that both  $\mathbf{J}_s$  and  $\mathbf{M}_s$  are not zero outside the opening, and expressions for them are not known there. The replacement of the semi-infinite medium to the left of the boundary (negative  $z$ ) by an imaginary electric or magnetic conductor only eliminates one or the other current densities ( $\mathbf{J}_s$  or  $\mathbf{M}_s$ ) but not both. Thus, even though an exact equivalent for this problem exists in principle, it cannot be used practically because the fields outside the opening are not known *a priori*. We are therefore forced to adopt an approximate equivalent.

The usual and most accurate relaxation is to assume that both  $\mathbf{E}_a$  and  $\mathbf{H}_a$  (and in turn  $\mathbf{M}_s$  and  $\mathbf{J}_s$ ) exist over the opening but are zero outside it. It has been shown, by comparison with measurements and other available data, that this approximate equivalent yields the best results.

### B. Radiated Fields

Using a procedure similar to that of the previous section, the radiation characteristics of this aperture can be derived. A summary of them is shown in Table 12.1.

*The field components of this aperture are identical in form to those of the aperture when it is mounted on an infinite ground plane if the  $(1 + \cos \theta)$  term in each component is replaced by 2.* Thus for small values of  $\theta$  (in the main lobe and especially near its maximum), the patterns of the two apertures are almost identical. This procedure can be used, in general, to relate the fields of an aperture when it is and it is not mounted on an infinite ground plane. However, the coordinate system chosen must have the  $z$ -axis perpendicular to the aperture.

A three-dimensional pattern for an aperture with  $a = 3\lambda$ ,  $b = 2\lambda$  was computed, and it is shown in Figure 12.11. The dimensions of this aperture are the same as those of Figure 12.8. However the angular limits over which the radiated fields now exist have been extended to  $0^\circ \leq \theta \leq 180^\circ$ . Although the general structures of the two patterns are similar, they are not identical. Because of the enlarged space over which fields now exist, additional minor lobes are formed.

### C. Beamwidths and Side Lobe Levels

To find the beamwidths and the angle at which the maximum of the side lobe occurs, it is usually assumed that the  $(1 + \cos \theta)$  term is a much slower varying function than the  $\sin(ka \sin \theta/2)/(ka \sin \theta/2)$  or the  $\sin(kb \sin \theta/2)/(kb \sin \theta/2)$  terms. This is an approximation, and it is more valid for large apertures (large  $a$  and/or  $b$ ) and for angles near the main maximum. More accurate results can be obtained by considering the  $(1 + \cos \theta)$  term. Thus (12-26)–(12-33) can be used, to a good approximation, to compute the beamwidths and side lobe level. A summary is included in Table 12.1.

### D. Directivity

Although the physical geometry of the opening of this problem is identical to that of Section 12.5.1, their directivities are not identical. This is evident by examining their far-zone field expressions or by realizing that the fields outside the aperture along the  $x$ - $y$  plane are not exactly the same.

To derive an exact expression for the directivity of this aperture would be a very difficult task. Since the patterns of the apertures are nearly the same, especially at the main lobe, their directivities are almost the same. To verify this, an example is taken.

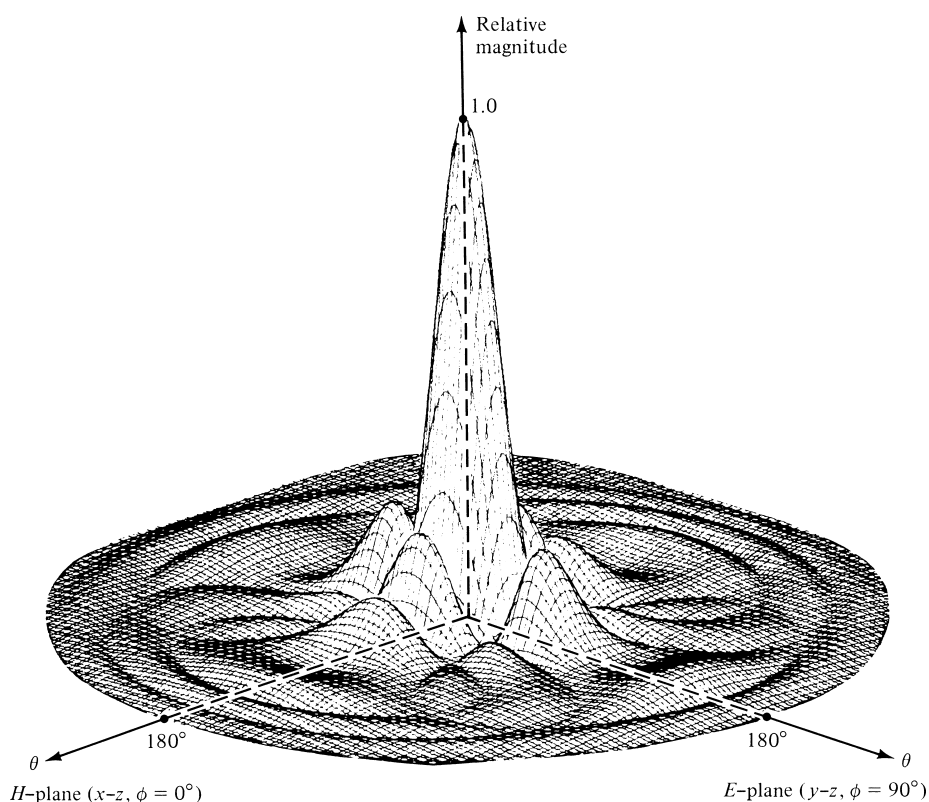


**Figure 12.11** Three-dimensional field pattern of a constant field rectangular aperture ( $a = 3\lambda$ ,  $b = 2\lambda$ ).

### Example 12.3

Repeat the problem of Example 12.2 for an aperture that is not mounted on an infinite ground plane.

*Solution:* Since the  $E$ -plane patterns of the two apertures are identical, the FNBW, HPBW, FSLBW, and FSLMM are the same. The directivities as computed by (12-37), are also the same. Since the fields radiated by the two apertures are not identical, their directivities computed using the far-zone fields will not be exactly the same. Therefore for this problem

$$D_0 \simeq 81.16(\text{dimensionless}) = 19.09 \text{ dB}$$

As with Example 12.2, the directivities computed using (12-37) and the computer program do not agree exactly. For this problem, however, neither one is exact. For (12-37), it has been assumed that the aperture tangential magnetic field is related to the aperture tangential electric field by the intrinsic impedance  $\eta$ . This relationship is good but not exact. For the computer program, the formulation is based on the equivalent of this section where the fields outside the aperture were assumed to be negligible. Again this is a good assumption for some problems, but it is not exact.

A summary of the radiation characteristics of this aperture is included in Table 12.1 where it is compared with that of other apertures.

### 12.5.3 TE<sub>10</sub>-Mode Distribution on an Infinite Ground Plane

In practice, a commonly used aperture antenna is that of a rectangular waveguide mounted on an infinite ground plane. At the opening, the field is usually approximated by the dominant TE<sub>10</sub>-mode. Thus

$$\mathbf{E}_a = \hat{\mathbf{a}}_y E_0 \cos\left(\frac{\pi}{a}x'\right) \begin{cases} -a/2 \leq x' \leq +a/2 \\ -b/2 \leq y' \leq +b/2 \end{cases} \quad (12-39)$$

#### A. Equivalent, Radiated Fields, Beamwidths, and Side Lobe Levels

Because the physical geometry of this antenna is identical to that of Figure 12.7, their equivalents and the procedure to analyze each one are identical. They differ only in the field distribution over the aperture.

The details of the analytical formulation are not included. However, a summary of its radiation characteristics is included in Table 12.1. The *E*-plane pattern of this aperture is identical in form (with the exception of a normalization factor) to the *E*-plane of the aperture of Section 12.5.1. This is expected, since the TE<sub>10</sub>-mode field distribution along

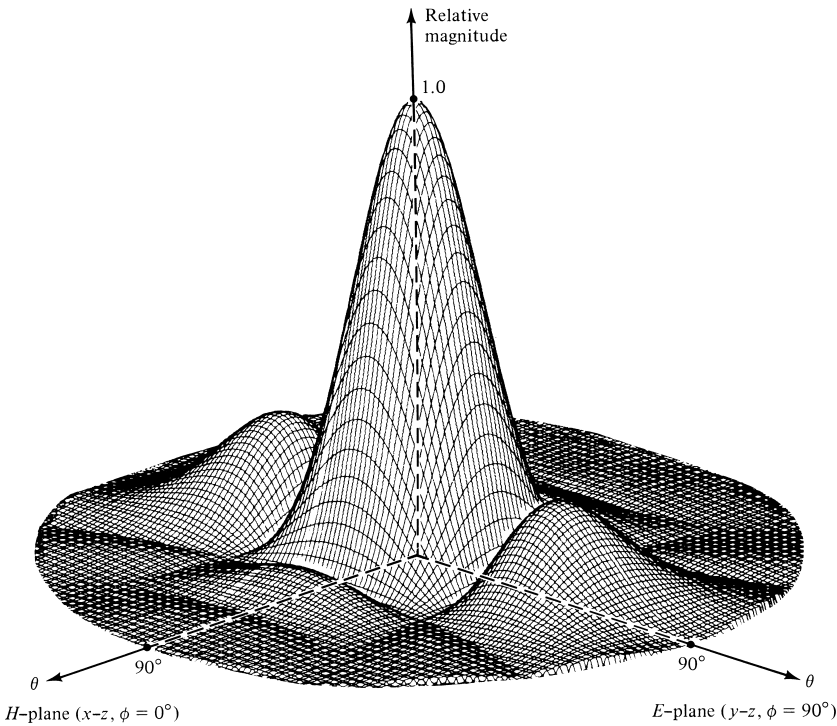


**Figure 12.12** Three-dimensional field pattern of a TE<sub>10</sub>-mode rectangular waveguide mounted on an infinite ground plane ( $a = 3\lambda$ ,  $b = 2\lambda$ ).

the  $E$ -plane ( $y$ - $z$  plane) is also a constant. That is not the case for the  $H$ -plane or at all other points removed from the principal planes. To demonstrate that, a three-dimensional pattern for the  $TE_{10}$ -mode aperture with  $a = 3\lambda$ ,  $b = 2\lambda$  was computed and it is shown in Figure 12.12. This pattern should be compared with that of Figure 12.8.

The expressions for the beamwidths and side lobe level in the  $E$ -plane are identical to those given by (12-26)–(12-33). However those for the  $H$ -plane are more complex, and a simple procedure is not available. Computations for the HPBW, FNBW, FSLBW, FSLMM in the  $E$ - and  $H$ -planes were made, and they are shown graphically in Figures 12.13 and 12.14.

When the same aperture is not mounted on a ground plane, the far-zone fields do not have to be re-derived but rather can be written by inspection. This is accomplished by introducing appropriately, in each of the field components ( $E_\theta$  and  $E_\phi$ ) of the fourth column of Table 12.1, a  $(1 + \cos \theta)/2$  factor, as is done for the fields of the two apertures in the second and third columns. This factor is appropriate when the  $z$ -axis is perpendicular to the plane of the aperture. Other similar factors will have to be used when either the  $x$ -axis or  $y$ -axis is perpendicular to the plane of the aperture.

### B. Directivity and Aperture Efficiency

The directivity of this aperture is found in the same manner as that of the uniform distribution aperture of Section 12.5.1. Using the aperture electric field of (12-39), and

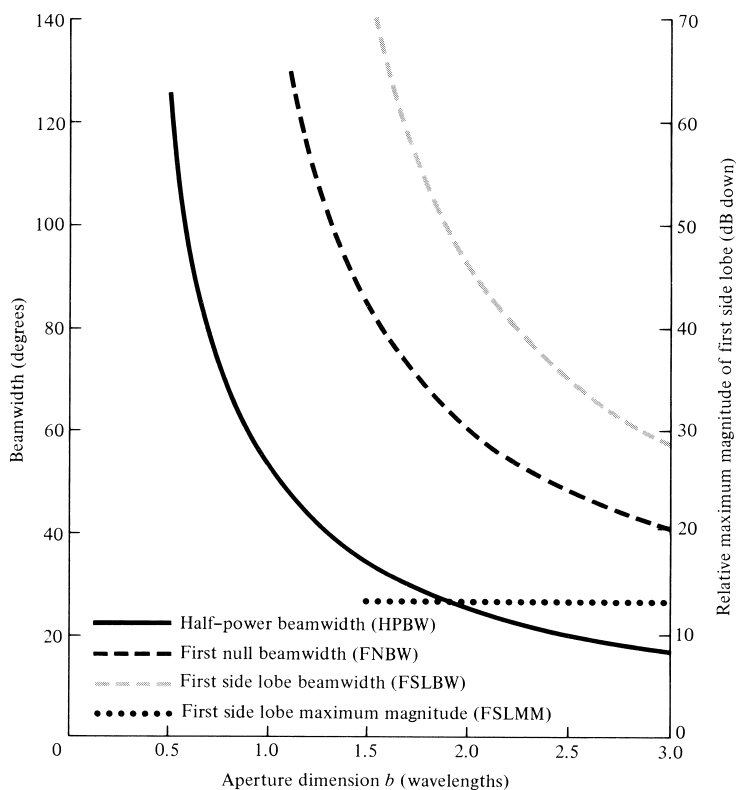


**Figure 12.13**  $E$ -plane beamwidths and first side lobe relative maximum magnitude for  $TE_{10}$ -mode rectangular waveguide mounted on an infinite ground plane.

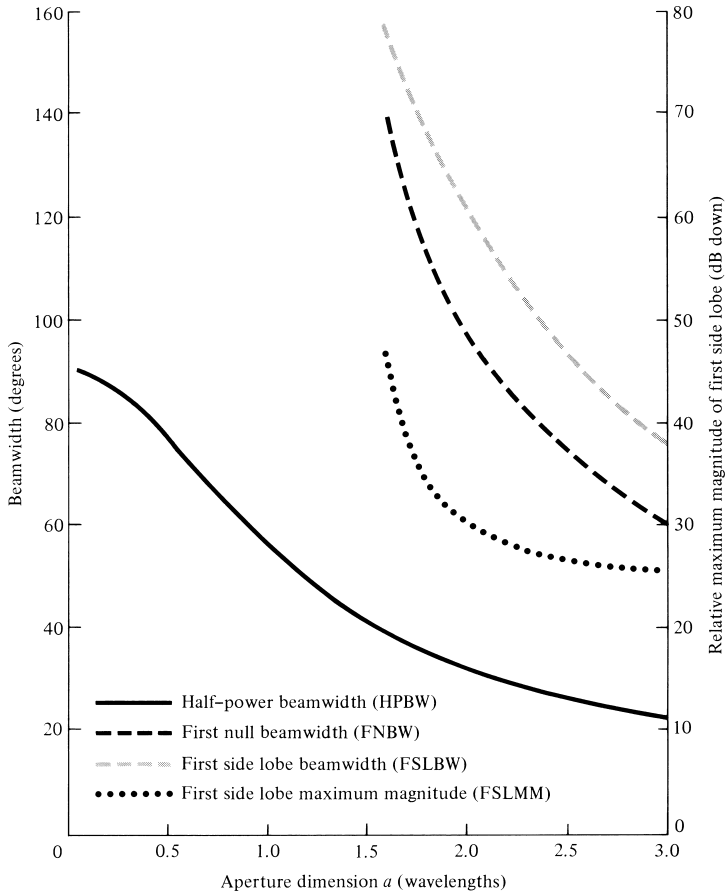


**Figure 12.14**  $H$ -plane beamwidths and first side lobe relative maximum magnitude for  $TE_{10}$ -mode rectangular waveguide mounted on an infinite ground plane.

assuming that the aperture magnetic field is related to the electric field by the intrinsic impedance  $\eta$ , the radiated power can be written as

$$P_{\text{rad}} = \iint_S \mathbf{W}_{\text{av}} \cdot d\mathbf{s} = ab \frac{|E_0|^2}{4\eta} \quad (12-39a)$$

The maximum radiation intensity occurs at  $\theta = 0^\circ$ , and it is given by

$$U_{\text{max}} = \frac{8}{\pi^2} \left( \frac{ab}{\lambda} \right)^2 \frac{|E_0|^2}{4\eta} \quad (12-39b)$$

Thus the directivity is equal to

$$D_0 = \frac{8}{\pi^2} \left[ ab \left( \frac{4\pi}{\lambda^2} \right) \right] = 0.81 \left[ ab \left( \frac{4\pi}{\lambda^2} \right) \right] = 0.81 A_p \left( \frac{4\pi}{\lambda^2} \right) = A_{em} \left( \frac{4\pi}{\lambda^2} \right) \quad (12-39c)$$

In general, the maximum effective area  $A_{em}$  is related to the physical area  $A_p$  by

$$A_{em} = \epsilon_{ap} A_p, \quad 0 \leq \epsilon_{ap} \leq 1 \quad (12-40)$$

where  $\epsilon_{ap}$  is the aperture efficiency. For this problem  $\epsilon_{ap} = 8/\pi^2 \simeq 0.81$ . The aperture efficiency is a figure of merit which indicates how efficiently the physical area of the antenna is utilized. Typically, aperture antennas have aperture efficiencies from about 30% to 90%, horns from 35% to 80% (optimum gain horns have  $\epsilon_{ap} \simeq 50\%$ ), and circular reflectors from 50% to 80%.

For reflectors, the aperture efficiency is a function of many factors. The most prominent are the spillover, amplitude taper, phase distribution, polarization uniformity, blockage, and surface random errors. These are discussed in detail in Section 15.4.1 of Chapter 15.

### 12.5.4 Beam Efficiency

The beam efficiency for an antenna was introduced in Section 2.10 and was defined by (2-53). When the aperture is mounted on the  $x$ - $y$  plane, the beam efficiency can be calculated using (2-54). The beam efficiency can be used to judge the ability of

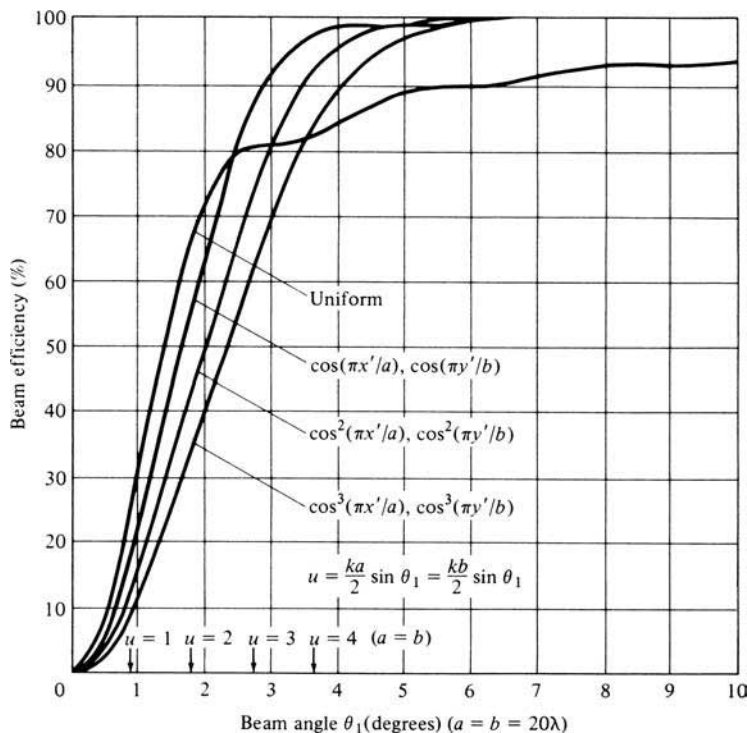


**Figure 12.15** Beam efficiency versus half-cone angle  $\theta_1$ , for a square aperture with different field distributions. The aperture is not mounted on an infinite ground plane. (SOURCE: D. G. Fink (ed.), *Electronics Engineers' Handbook*, Section 18 (by W. F. Croswell), McGraw-Hill, New York, 1975)

the antenna to discriminate between signals received through its main lobe and those through the minor lobes. Beam efficiencies for rectangular apertures with different aperture field distributions are plotted, versus the half-cone angle  $\theta_1$ , in Figure 12.15 [11]. The uniform field distribution aperture has the least ability to discriminate between main lobe and minor lobe signals. The aperture radiates in an unbounded medium, and it is not mounted on an infinite ground plane. The lower abscissa scale is in terms of  $\theta_1$  (in degrees), and it should be used only when  $a = b = 20\lambda$ . The upper abscissa scale is in terms of  $u[u = (ka/2) \sin \theta_1 = (kb/2) \sin \theta_1]$ , and it should be used for any square aperture.

#### Example 12.4

Determine the beam efficiency, within a cone of half-angle  $\theta_1 = 10^\circ$ , for a square aperture with uniform field distribution and with

- a.  $a = b = 20\lambda$
- b.  $a = b = 3\lambda$

*Solution:* The solution is carried out using the curves of Figure 12.15.

- a. When  $a = b = 20\lambda$ , the lower abscissa scale can be used. For  $\theta_1 = 10^\circ$ , the efficiency for the uniform aperture is about 94%.
- b. For  $a = b = 3\lambda$  and  $\theta_1 = 10^\circ$

$$u = \frac{ka}{2} \sin \theta_1 = 3\pi \sin(10^\circ) = 1.64$$

Using the upper abscissa scale, the efficiency for the uniform aperture at  $u = 1.64$  is about 58%.

An antenna array of slotted rectangular waveguides used for the AWACS airborne system is shown in Figure 6.27. It utilizes waveguide sticks, with slits on their narrow wall.

A MATLAB computer program, designated as *Aperture*, has been developed to compute and display different radiation characteristics of rectangular and circular apertures. The description of the program is found in the corresponding READ ME file included in the CD attached to the book.

## 12.6 CIRCULAR APERTURES

A widely used microwave antenna is the circular aperture. One of the attractive features of this configuration is its simplicity in construction. In addition, closed form expressions for the fields of all the modes that can exist over the aperture can be obtained.

The procedure followed to determine the fields radiated by a circular aperture is identical to that of the rectangular, as summarized in Section 12.3. The primary differences lie in the formulation of the equivalent current densities ( $J_x$ ,  $J_y$ ,  $J_z$ ,  $M_x$ ,  $M_y$ ,  $M_z$ ), the

differential paths from the source to the observation point ( $r' \cos \psi$ ), and the differential area ( $ds'$ ). Before an example is considered, these differences will be reformulated for the circular aperture.

Because of the circular profile of the aperture, it is often convenient and desirable to adopt cylindrical coordinates for the solution of the fields. In most cases, therefore, the electric and magnetic field components over the circular opening will be known in cylindrical form; that is,  $E_\rho, E_\phi, E_z, H_\rho, H_\phi$ , and  $H_z$ . Thus the components of the equivalent current densities  $\mathbf{M}_s$  and  $\mathbf{J}_s$  would also be conveniently expressed in cylindrical form ( $M_\rho, M_\phi, M_z, J_\rho, J_\phi, J_z$ ). In addition, the required integration over the aperture to find  $N_\theta, N_\phi, L_\theta$ , and  $L_\phi$  of (12-12a)–(12-12d) should also be done in cylindrical coordinates. It is then desirable to reformulate  $r' \cos \psi$  and  $ds'$ , as given by (12-15a)–(12-16c).

The most convenient position for placing the aperture is that shown in Figure 12.16 (aperture on  $x$ - $y$  plane). The transformation between the rectangular and cylindrical components of  $\mathbf{J}_s$  is given by (see Appendix VII)

$$\begin{bmatrix} J_x \\ J_y \\ J_z \end{bmatrix} = \begin{bmatrix} \cos \phi' & -\sin \phi' & 0 \\ \sin \phi' & \cos \phi' & 0 \\ 0 & 0 & 1 \end{bmatrix} \begin{bmatrix} J_\rho \\ J_\phi \\ J_z \end{bmatrix} \quad (12-41a)$$

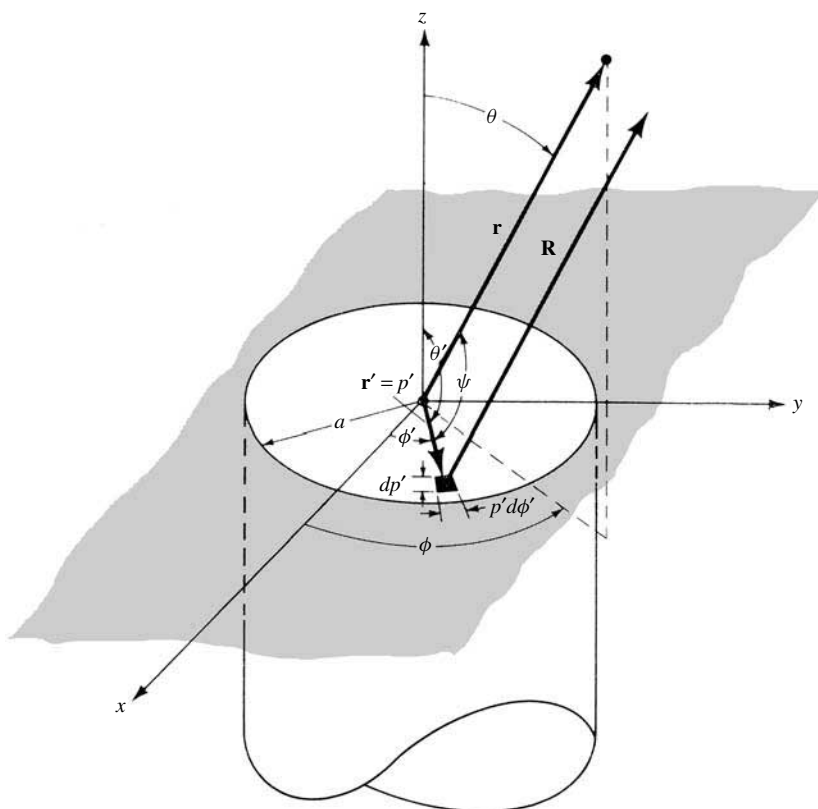


**Figure 12.16** Circular aperture mounted on an infinite ground plane.



A similar transformation exists for the components of  $\mathbf{M}_s$ . The rectangular and cylindrical coordinates are related by (see Appendix VII)

$$\begin{aligned}x' &= \rho' \cos \phi' \\y' &= \rho' \sin \phi' \\z' &= z'\end{aligned}\tag{12-41b}$$

Using (12-41a), (12-12a)–(12-12d) can be written as

$$\begin{aligned}N_\theta &= \iint_S [J_\rho \cos \theta \cos(\phi - \phi') + J_\phi \cos \theta \sin(\phi - \phi') - J_z \sin \theta] \\&\quad \times e^{+jkr' \cos \psi} ds'\end{aligned}\tag{12-42a}$$

$$N_\phi = \iint_S [-J_\rho \sin(\phi - \phi') + J_\phi \cos(\phi - \phi')] e^{+jkr' \cos \psi} ds' \tag{12-42b}$$

$$\begin{aligned}L_\theta &= \iint_S [M_\rho \cos \theta \cos(\phi - \phi') + M_\phi \cos \theta \sin(\phi - \phi') - M_z \sin \theta] \\&\quad \times e^{+jkr' \cos \psi} ds'\end{aligned}\tag{12-42c}$$

$$L_\phi = \iint_S [-M_\rho \sin(\phi - \phi') + M_\phi \cos(\phi - \phi')] e^{+jkr' \cos \psi} ds' \tag{12-42d}$$

where  $r' \cos \psi$  and  $ds'$  can be written, using (12-15c) and (12-41b), as

$$r' \cos \psi = x' \sin \theta \cos \phi + y' \sin \theta \sin \phi = \rho' \sin \theta \cos(\phi - \phi') \tag{12-43a}$$

$$ds' = dx' dy' = \rho' d\rho' d\phi' \tag{12-43b}$$

In summary, for a circular aperture antenna the fields radiated can be obtained by *either* of the following:

1. If the fields over the aperture are known in *rectangular components*, use the same procedure as for the rectangular aperture with (12-43a) and (12-43b) substituted in (12-12a)–(12-12d).
2. If the fields over the aperture are known in *cylindrical components*, use the same procedure as for the rectangular aperture with (12-42a)–(12-42d), along with (12-43a) and (12-43b), taking the place of (12-12a)–(12-12d).

### 12.6.1 Uniform Distribution on an Infinite Ground Plane

To demonstrate the methods, the field radiated by a circular aperture mounted on an infinite ground plane will be formulated. To simplify the mathematical details, the field

over the aperture is assumed to be constant and given by

$$\mathbf{E}_a = \hat{\mathbf{a}}_y E_0 \quad \rho' \leq a \quad (12-44)$$

where  $E_0$  is a constant.

#### A. Equivalent and Radiation Fields

The equivalent problem of this is identical to that of Figure 12.7. That is,

$$\begin{aligned} \mathbf{M}_s &= \begin{cases} -2\hat{\mathbf{n}} \times \mathbf{E}_a = \hat{\mathbf{a}}_x 2E_0 & \rho' \leq a \\ 0 & \text{elsewhere} \end{cases} \\ \mathbf{J}_s &= \begin{cases} 0 & \text{everywhere} \end{cases} \end{aligned} \quad (12-45)$$

Thus,

$$N_\theta = N_\phi = 0 \quad (12-46)$$

$$L_\theta = 2E_0 \cos \theta \cos \phi \int_0^a \rho' \left[ \int_0^{2\pi} e^{+jk\rho' \sin \theta \cos(\phi-\phi')} d\phi' \right] d\rho' \quad (12-47)$$

Because

$$\int_0^{2\pi} e^{+jk\rho' \sin \theta \cos(\phi-\phi')} d\phi' = 2\pi J_0(k\rho' \sin \theta) \quad (12-48)$$

(12-47) can be written as

$$L_\theta = 4\pi E_0 \cos \theta \cos \phi \int_0^a J_0(k\rho' \sin \theta) \rho' d\rho' \quad (12-49)$$

where  $J_0(t)$  is the Bessel function of the first kind of order zero. Making the substitution

$$\begin{aligned} t &= k\rho' \sin \theta \\ dt &= k \sin \theta d\rho' \end{aligned} \quad (12-49a)$$

reduces (12-49) to

$$L_\theta = \frac{4\pi E_0 \cos \theta \cos \phi}{(k \sin \theta)^2} \int_0^{ka \sin \theta} t J_0(t) dt \quad (12-49b)$$

Since

$$\int_0^\beta z J_0(z) dz = z J_1(z) \Big|_0^\beta = \beta J_1(\beta) \quad (12-50)$$

where  $J_1(\beta)$  is the Bessel function of order one, (12-49b) takes the form of

$$L_\theta = 4\pi a^2 E_0 \left\{ \cos \theta \cos \phi \left[ \frac{J_1(ka \sin \theta)}{ka \sin \theta} \right] \right\} \quad (12-51)$$

Similarly

$$L_\phi = -4\pi a^2 E_0 \sin \phi \left[ \frac{J_1(ka \sin \theta)}{ka \sin \theta} \right] \quad (12-52)$$

Using (12-46), (12-51), and (12-52), the electric field components of (12-10a)–(12-10c) can be written as

$$E_r = 0 \quad (12-53a)$$

$$E_\theta = j \frac{ka^2 E_0 e^{-jkr}}{r} \left\{ \sin \phi \left[ \frac{J_1(ka \sin \theta)}{ka \sin \theta} \right] \right\} \quad (12-53b)$$

$$E_\phi = j \frac{ka^2 E_0 e^{-jkr}}{r} \left\{ \cos \theta \cos \phi \left[ \frac{J_1(ka \sin \theta)}{ka \sin \theta} \right] \right\} \quad (12-53c)$$

In the principal  $E$ - and  $H$ -planes, the electric field components simplify to

**$E$ -Plane ( $\phi = \pi/2$ )**

$$E_r = E_\phi = 0 \quad (12-54a)$$

$$E_\theta = j \frac{ka^2 E_0 e^{-jkr}}{r} \left[ \frac{J_1(ka \sin \theta)}{ka \sin \theta} \right] \quad (12-54b)$$

**$H$ -Plane ( $\phi = 0$ )**

$$E_r = E_\theta = 0 \quad (12-55a)$$

$$E_\phi = j \frac{ka^2 E_0 e^{-jkr}}{r} \left\{ \cos \theta \left[ \frac{J_1(ka \sin \theta)}{ka \sin \theta} \right] \right\} \quad (12-55b)$$

A three-dimensional pattern has been computed for the constant field circular aperture of  $a = 1.5\lambda$ , and it is shown in Figure 12.17. The pattern of Figure 12.17 seems to be symmetrical. However closer observation, especially through the two-dimensional  $E$ - and  $H$ -plane patterns, will reveal that not to be the case. It does, however, possess characteristics that are almost symmetrical.

***B. Beamwidth, Side Lobe Level, and Directivity***

Exact expressions for the beamwidths and side lobe levels cannot be obtained easily. However approximate expressions are available, and they are shown tabulated in Table 12.2. More exact data can be obtained by numerical methods.

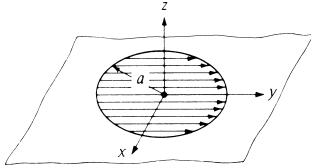
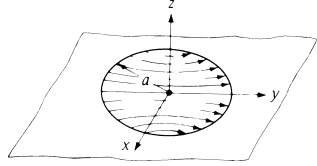
Since the field distribution over the aperture is constant, the directivity is given by

$$D_0 = \frac{4\pi}{\lambda^2} A_{em} = \frac{4\pi}{\lambda^2} A_p = \frac{4\pi}{\lambda^2} (\pi a^2) = \left( \frac{2\pi a}{\lambda} \right)^2 = \left( \frac{C}{\lambda} \right)^2 \quad (12-56)$$

since the maximum effective area  $A_{em}$  is equal to the physical area  $A_p$  of the aperture [as shown for the rectangular aperture in (12-37)].

A summary of the radiation parameters of this aperture is included in Table 12.2.

TABLE 12.2 Equivalents, Fields, Beamwidths, Side Lobe Levels, and Directivities of Circular Apertures

	Uniform Distribution Aperture on Ground Plane	$TE_{11}$ -Mode Distribution Aperture on Ground Plane
Aperture distribution of tangential components (analytical)	$\mathbf{E}_a = \hat{\mathbf{a}}_y E_0 \quad \rho' \leq a$	$\left. \begin{aligned} \mathbf{E}_a &= \hat{\mathbf{a}}_\rho E_\rho + \hat{\mathbf{a}}_\phi E_\phi \\ E_\rho &= E_0 J_1(\chi'_{11} \rho' / a) \sin \phi' / \rho' \\ E_\phi &= E_0 J_1'(\chi'_{11} \rho' / a) \cos \phi' \end{aligned} \right\} \begin{aligned} \rho' &\leq a \\ \chi'_{11} &= 1.841 \\ ' &= \frac{\partial}{\partial \rho'} \end{aligned}$
Aperture distribution of tangential components (graphical)		
Equivalent	$\mathbf{M}_s = \begin{cases} -2\hat{\mathbf{n}} \times \mathbf{E}_a & \rho' \leq a \\ 0 & \text{elsewhere} \end{cases}$ $\mathbf{J}_s = 0 \quad \text{everywhere}$	$\mathbf{M}_s = \begin{cases} -2\hat{\mathbf{n}} \times \mathbf{E}_a & \rho' \leq a \\ 0 & \text{elsewhere} \end{cases}$ $\mathbf{J}_s = 0 \quad \text{everywhere}$
<i>Far-zone fields</i> $Z = ka \sin \theta$ $C_1 = j \frac{ka^2 E_0 e^{-jkr}}{r}$ $C_2 = j \frac{ka E_0 J_1(\chi'_{11}) e^{-jkr}}{r}$ $\chi'_{11} = 1.841$	$E_r = H_r = 0$ $E_\theta = j C_1 \sin \phi \frac{J_1(Z)}{Z}$ $E_\phi = j C_1 \cos \theta \cos \phi \frac{J_1(Z)}{Z}$ $H_\theta = -E_\phi / \eta$ $H_\phi = E_\theta / \eta$	$E_r = H_r = 0$ $E_\theta = C_2 \sin \phi \frac{J_1(Z)}{Z}$ $E_\phi = C_2 \cos \theta \cos \phi \frac{J_1'(Z)}{1 - (Z/\chi'_{11})^2}$ $H_\theta = -E_\phi / \eta$ $H_\phi = E_\theta / \eta$ $J_1'(Z) = J_0(Z) - J_1(Z)/Z$

Half-power beamwidth (degrees)	$E$ -plane $a \gg \lambda$	$\frac{29.2}{a/\lambda}$	$\frac{29.2}{a/\lambda}$
	$H$ -plane $a \gg \lambda$	$\frac{29.2}{a/\lambda}$	$\frac{37.0}{a/\lambda}$
First null beamwidth (degrees)	$E$ -plane $a \gg \lambda$	$\frac{69.9}{a/\lambda}$	$\frac{69.9}{a/\lambda}$
	$H$ -plane $a \gg \lambda$	$\frac{69.9}{a/\lambda}$	$\frac{98.0}{a/\lambda}$
First side lobe max. (to main max.) (dB)	$E$ -plane	$-17.6$	$-17.6$
	$H$ -plane	$-17.6$	$-26.2$
Directivity $D_0$ (dimensionless)		$\frac{4\pi}{\lambda^2}(\text{area}) = \frac{4\pi}{\lambda^2}(\pi a^2) = \left(\frac{2\pi a}{\lambda}\right)^2$	$0.836\left(\frac{2\pi a}{\lambda}\right)^2 = 10.5\pi\left(\frac{a}{\lambda}\right)^2$

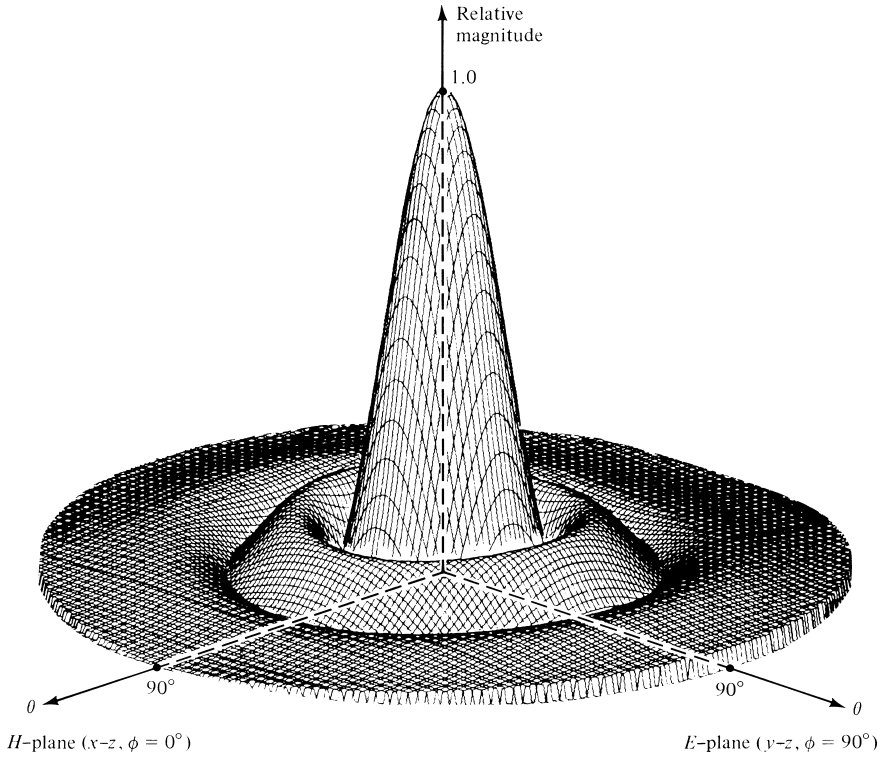


**Figure 12.17** Three-dimensional field pattern of a constant field circular aperture mounted on an infinite ground plane ( $a = 1.5\lambda$ ).

### 12.6.2 TE<sub>11</sub>-Mode Distribution on an Infinite Ground Plane

A very practical antenna is a circular waveguide of radius  $a$  mounted on an infinite ground plane, as shown in Figure 12.16. However, the field distribution over the aperture is usually that of the dominant TE<sub>11</sub>-mode for a circular waveguide given by

$$\left. \begin{aligned} E_{\rho} &= \frac{E_0}{\rho'} J_1 \left( \frac{\chi'_{11}}{a} \rho' \right) \sin \phi' \\ E_{\phi} &= E_0 \frac{\partial}{\partial \rho'} \left[ J_1 \left( \frac{\chi'_{11}}{a} \rho' \right) \right] \cos \phi' \\ E_z &= 0 \\ \chi'_{11} &= 1.841 \end{aligned} \right\} \quad (12-57)$$

The analysis of this problem is assigned at the end of this chapter as an exercise to the reader (Problem 12.35). However, a three-dimensional pattern for  $a = 1.5\lambda$  was calculated, and it is shown in Figure 12.18. This pattern should be compared with that of Figure 12.17 for the constant aperture field distribution.

The beamwidths and the side lobe levels in the  $E$ - and  $H$ -planes are different, and exact closed-form expressions cannot be obtained. However, they can be calculated

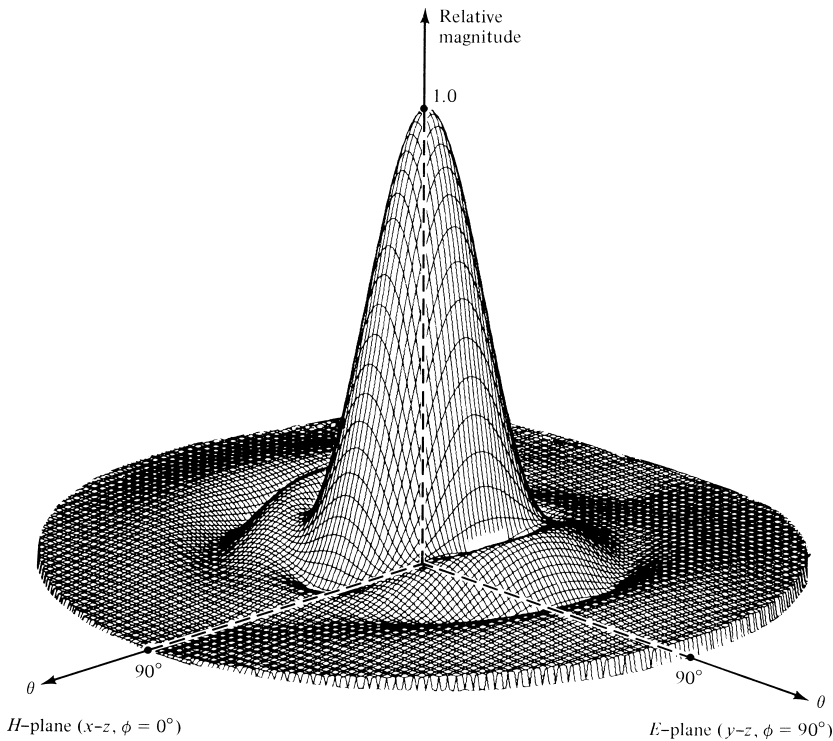


**Figure 12.18** Three-dimensional field pattern of a  $TE_{11}$ -mode circular waveguide mounted on an infinite ground plane ( $a = 1.5\lambda$ ).

using iterative methods, and the data are shown in Figure 12.19 and 12.20 for the  $E$ - and  $H$ -planes, respectively.

A summary of all the radiation characteristics is included in Table 12.2. When the same apertures of Table 12.2 are not mounted on a ground plane, the far-zone fields do not have to be re-derived but rather can be written by inspection. This is accomplished by introducing appropriately, in each of the field components ( $E_\theta$  and  $E_\phi$ ) of the second and third columns of Table 12.2, a  $(1 + \cos\theta)/2$  factor, as was done for the fields of the two apertures in the second and third columns of Table 12.1.

### 12.6.3 Beam Efficiency

Beam efficiency, as defined by (2-53) and calculated by (2-54), for circular apertures not mounted on infinite ground planes is shown in Figure 12.21 [11]. The lower abscissa scale (in degrees) is in terms of the half-cone angle  $\theta_1$  (in degrees), and it should be used only when the radius of the aperture is  $20\lambda$  ( $a = 20\lambda$ ). The upper abscissa scale is in terms of  $u$  ( $u = ka \sin\theta_1$ ), and it should be used for any radius circular aperture.

The procedure for finding the beam efficiency of a circular aperture is similar to that of a rectangular aperture as discussed in Section 12.5.4, illustrated in Figure 12.15, and demonstrated by Example 12.4.

A MATLAB computer program, designated as **Aperture**, has been developed to compute and display different radiation characteristics of rectangular and circular apertures.

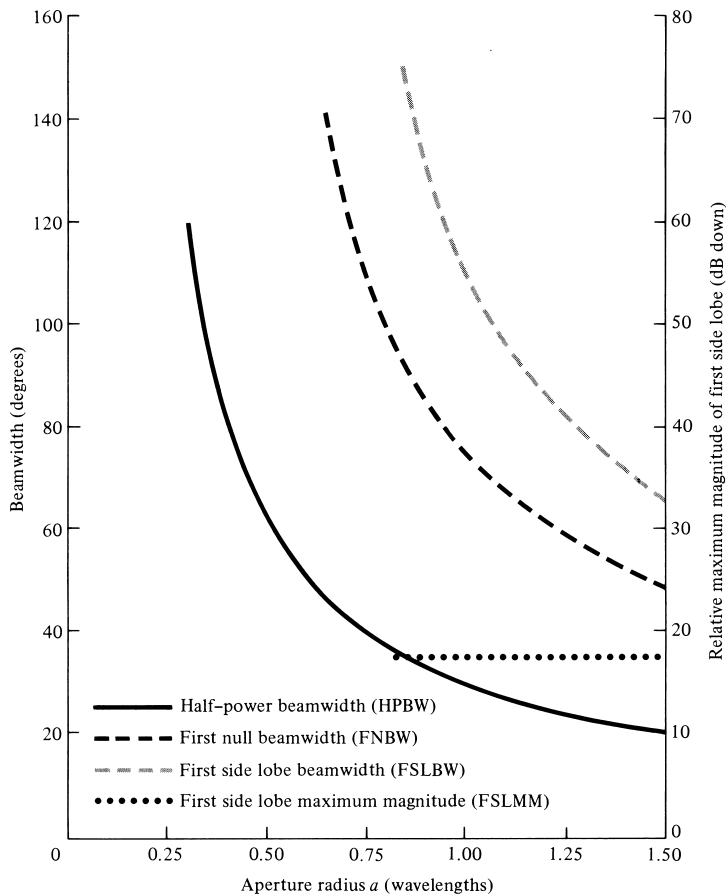


**Figure 12.19**  $E$ -plane beamwidths and first side lobe relative maximum magnitude for  $TE_{11}$ -mode circular aperture mounted on an infinite ground plane.

The description of the program is found in the corresponding READ ME file included in the CD attached to the book.

## 12.7 DESIGN CONSIDERATIONS

As is the case for arrays, aperture antennas can be designed to control their radiation characteristics. Typically the level of the minor lobes can be controlled by tapering the distribution across the aperture; the smoother the taper from the center of the aperture toward the edge, the lower the side lobe level and the larger the half-power beamwidth, and conversely. Therefore a very smooth taper, such as that represented by a binomial distribution or others, would result in very low side lobes but larger half-power beamwidths. In contrast, an abrupt distribution, such as that of uniform illumination, exhibits the smaller half-power beamwidth but the highest side lobe level (about - 13.5 dB). Therefore if it is desired to achieve simultaneously both a very low sidelobe level, as well as a small half-power beamwidth, a compromise has to be made. Typically an intermediate taper, such as that of a Tschebscheff distribution or



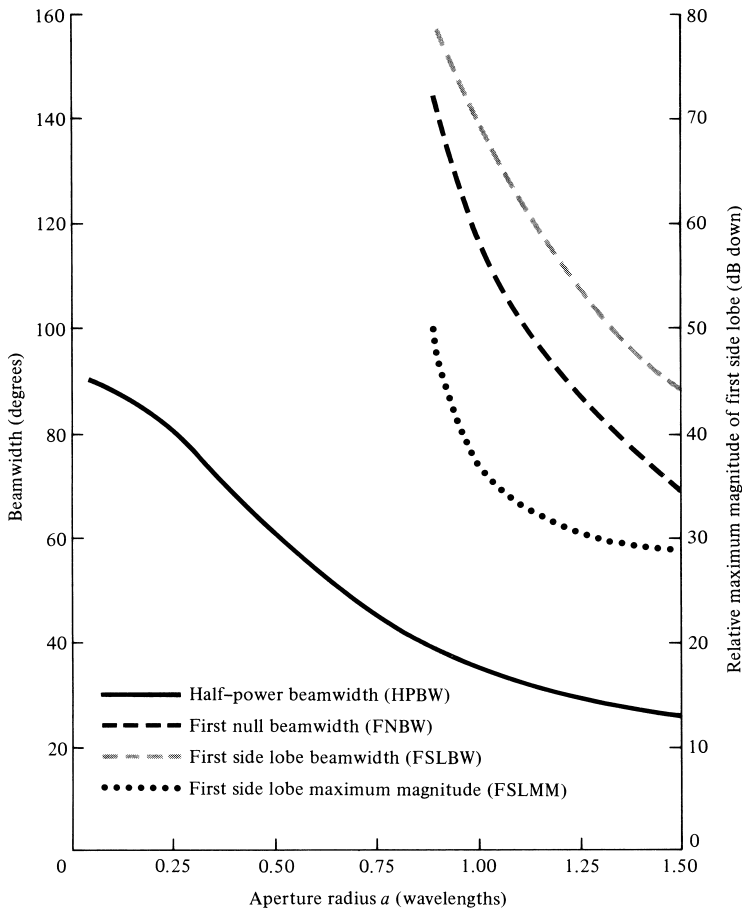


**Figure 12.20** *H*-plane beamwidths and first side lobe relative maximum magnitude for  $TE_{11}$ -mode circular waveguide mounted on an infinite ground plane.

any other similar one, will have to be selected. This has been discussed in detail both in Chapter 6 for arrays and in Chapter 7 for continuous sources. These can be used to design continuous distributions for apertures.

Aperture antennas, both rectangular and circular, can also be designed for satellite applications where the beamwidth can be used to determine the “footprint” area of the coverage. In such designs, it is important to relate the beamwidth to the size of the aperture. In addition, it is also important to maximize the directivity of the antennas within a desired angular sector defined by the beamwidth, especially at the edge of coverage (EOC) [12]. This can be accomplished, using approximate closed-form expressions, as outlined in [12]. This procedure was used in Section 6.11 of Chapter 6 for arrays, and it is applicable for apertures, both rectangular and circular.

### 12.7.1 Rectangular Aperture

For a rectangular aperture, of dimensions  $a$  and  $b$ , and with a uniform distribution, the procedure to determine the optimum aperture dimensions  $a, b$  to maximize the

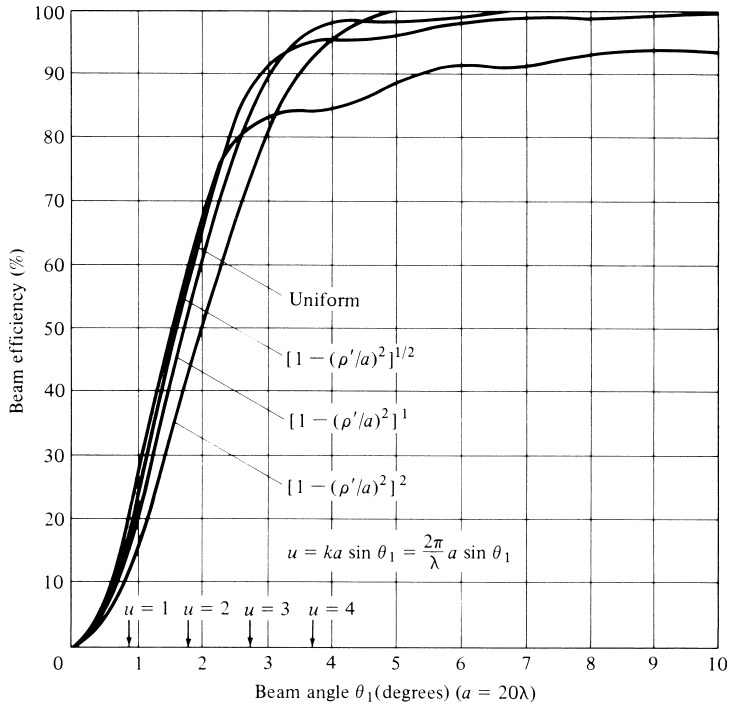


**Figure 12.21** Beam efficiency versus half-cone angle  $\theta_1$ , for a circular aperture with different field distributions. The aperture is not mounted on an infinite ground plane. (SOURCE: D. G. Fink (ed.), *Electronics Engineers' Handbook*, Section 18 (by W. F. Croswell), McGraw-Hill, New York, 1975)

directivity at an edge angle  $\theta_c$  of a given angular sector ( $0 \leq \theta \leq \theta_c$ ) is identical to that outlined in Section 6.11. Thus to determine the optimum dimension  $b$  of the aperture so that the directivity is maximum at an edge-of-coverage angle  $\theta_{ce}$  of an angular sector  $0 \leq \theta \leq \theta_{ce}$  in the  $E$ -plane is given by (6-105a), or

$$E\text{-Plane: } b = \frac{\lambda}{2 \sin \theta_{ce}} \quad (12-58a)$$

Similarly for the  $H$ -plane, the optimum dimension  $a$  is determined by

$$H\text{-Plane: } a = \frac{\lambda}{2 \sin \theta_{ch}} \quad (12-58b)$$

where  $\theta_{ch}$  is the angle, in the  $H$ -plane, at the edge-of-coverage (EOC) angular sector where the directivity needs to be maximized.

Since the aperture antenna is uniformly illuminated, the directivity of (6-103) based on the optimum dimensions of (12-58a) and (12-58b) is

$$D_0 = \frac{4\pi}{\lambda^2} A_{em} = \frac{4\pi}{\lambda^2} A_p = \frac{4\pi}{\lambda^2} \left( \frac{\lambda}{2 \sin \theta_{ce}} \right) \left( \frac{\lambda}{2 \sin \theta_{ch}} \right) \quad (12-59)$$

### 12.7.2 Circular Aperture

A procedure similar to that for the rectangular aperture can be used for the circular aperture. In fact, it can be used for circular apertures with uniform distributions as well as tapered (parabolic or parabolic with a pedestal) [12].

For a circular aperture with uniform distribution, the normalized power pattern multiplied by the maximum directivity can be written as

$$P(\theta) = (2\pi a)^2 \left\{ \frac{2J_1(ka \sin \theta)}{ka \sin \theta} \right\}^2 \quad (12-60)$$

The maximum value of (12-60) occurs when  $\theta = 0$ . However, for any other angle  $\theta = \theta_c$ , the maximum of the pattern occurs when

$$ka \sin \theta_c = 1.841 \quad (12-61)$$

or

$$a = \frac{1.841\lambda}{2\pi \sin \theta_c} = \frac{\lambda}{3.413 \sin \theta_c} \quad (12-61a)$$

Therefore to maximize the directivity at the edge  $\theta = \theta_c$  of a given angular sector  $0 \leq \theta \leq \theta_c$ , the optimum radius of the uniformly illuminated circular aperture must be chosen according to (12-61a).

The maximum value of (12-60), which occurs at  $\theta = 0$ , is equal to

$$P(\theta = 0)|_{\max} = (2\pi a)^2 \quad (12-62)$$

while at the edge of the angular sector ( $\theta = \theta_c$ ) is equal to

$$P(\theta = \theta_c) = (2\pi a)^2 \left\{ \frac{2(0.5818)}{1.841} \right\}^2 = (2\pi a)^2 (0.3995) \quad (12-63)$$

Therefore the value of the directivity at the edge of the desired coverage ( $\theta = \theta_c$ ), relative to its maximum value at  $\theta = 0$ , is

$$\frac{P(\theta = \theta_c)}{P(\theta = 0)} = 0.3995 = -3.985 \text{ dB} \quad (12-64)$$

Since the aperture is uniformly illuminated, the directivity based on the optimum radius of (12-61a) is

$$D_0 = \frac{4\pi}{\lambda^2} A_p = \frac{4\pi}{\lambda^2} \pi \left( \frac{1.841\lambda}{2\pi \sin \theta_c} \right)^2 = \frac{3.3893}{\sin^2 \theta_c} = \frac{1.079\pi}{\sin^2 \theta_c} \quad (12-65)$$

A similar procedure can be followed for circular apertures with radial taper (parabolic) and radial taper squared of Table 7.2, as well as radial taper (parabolic) with pedestal. The characteristics of these, along with those of the uniform, are listed in Table 12.3.

**TABLE 12.3 Edge-of-Coverage (EOC) Designs for Square and Circular Apertures**

Aperture	Distribution	Size Square: Side Circular: Radius	Directivity	EOC Directivity (relative to peak)
Square	Uniform	$\frac{\lambda}{2 \sin(\theta_c)}$	$\frac{\pi}{\sin^2(\theta_c)}$	−3.920 dB
Circular	Uniform	$\frac{\lambda}{3.413 \sin(\theta_c)}$	$\frac{1.086\pi}{\sin^2(\theta_c)}$	−3.985 dB
Circular	Parabolic taper	$\frac{\lambda}{2.732 \sin(\theta_c)}$	$\frac{1.263\pi}{\sin^2(\theta_c)}$	−4.069 dB
Circular	Parabolic taper with −10 dB pedestal	$\frac{\lambda}{3.064 \sin(\theta_c)}$	$\frac{1.227\pi}{\sin^2(\theta_c)}$	−4.034 dB

(SOURCE: K. Praba, “Optimal Aperture for Maximum Edge-of-Coverage (EOC) Directivity,” *IEEE Antennas & Propagation Magazine*, Vol. 36, No. 3, pp. 72–74, June 1994. © (1994) IEEE)

### Example 12.5

It is desired to design an aperture antenna, with uniform illumination, so that the directivity is maximized at an angle  $30^\circ$  from the normal to the aperture. Determine the optimum dimension and its associated directivity when the aperture is

- Square
- Circular

**Solution:** For a square aperture  $\theta_{ce} = \theta_{ch}$ . Therefore the optimum dimension, according to (12-58a) or (12-58b), is

$$a = b = \frac{\lambda}{2 \sin(30^\circ)} = \lambda$$

while the directivity, according to (12-59), is

$$D_0 = \frac{\pi}{\sin^2 \theta_c} = \frac{\pi}{\sin^2(30^\circ)} = 12.5664 = 10.992 \text{ dB}$$

The directivity at  $\theta = 30^\circ$  is −3.920 dB from the maximum at  $\theta = 0^\circ$ , or 7.072 dB.

For a circular aperture the optimum radius, according to (12-61a), is

$$a = \frac{\lambda}{3.413 \sin(30^\circ)} = \frac{\lambda}{3.413(0.5)} = 0.586\lambda$$

while the directivity, according to (12-65), is

$$D_0 = \frac{1.079\pi}{\sin^2 \theta_c} = \frac{1.079\pi}{\sin^2(30^\circ)} = 13.559 = 11.32 \text{ dB}$$

The directivity at  $\theta = 30^\circ$  is −3.985 dB from the maximum at  $\theta = 0^\circ$ , or 7.365 dB.

## 12.8 BABINET'S PRINCIPLE

Now that wire and aperture antennas have been analyzed, one may inquire as to whether there is any relationship between them. This can be answered better by first introducing *Babinet's principle* which in optics states that *when the field behind a screen with an opening is added to the field of a complementary structure, the sum is equal to the field when there is no screen*. Babinet's principle in optics does not consider polarization, which is so vital in antenna theory; it deals primarily with absorbing screens. An extension of Babinet's principle, which includes polarization and the more practical conducting screens, was introduced by Booker [13], [14]. Referring to Figure 12.22(a), let us assume that an electric source  $\mathbf{J}$  radiates into an unbounded medium of intrinsic impedance  $\eta = (\mu/\epsilon)^{1/2}$  and produces at point  $P$  the fields  $\mathbf{E}_0, \mathbf{H}_0$ . The same fields

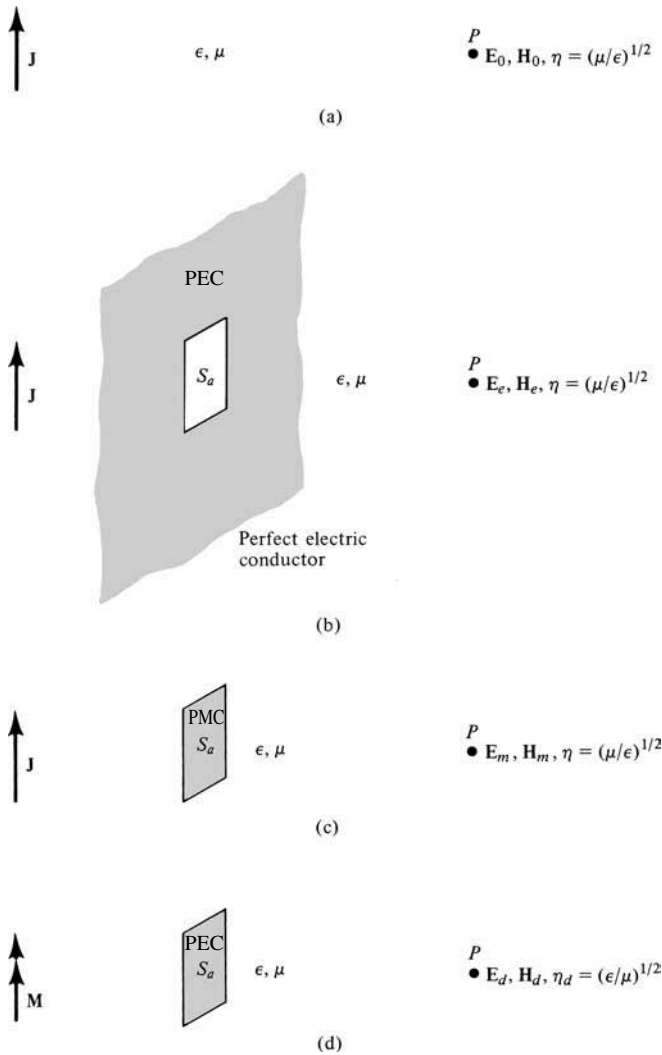


**Figure 12.22** Electric source in an unbounded medium and Babinet's principle equivalents.

can be obtained by combining the fields when the electric source radiates in a medium with intrinsic impedance  $\eta = (\mu/\epsilon)^{1/2}$  in the presence of

1. an infinite, planar, very thin, perfect electric conductor with an opening  $S_a$ , which produces at  $P$  the fields  $\mathbf{E}_e, \mathbf{H}_e$  [Figure 12.22(b)]
2. a flat, very thin, perfect magnetic conductor  $S_a$ , which produces at  $P$  the fields  $\mathbf{E}_m, \mathbf{H}_m$  [Figure 12.22(c)].

That is,

$$\begin{aligned}\mathbf{E}_0 &= \mathbf{E}_e + \mathbf{E}_m \\ \mathbf{H}_0 &= \mathbf{H}_e + \mathbf{H}_m\end{aligned}\tag{12-66a}$$

The field produced by the source in Figure 12.22(a) can also be obtained by combining the fields of

1. an electric source  $\mathbf{J}$  radiating in a medium with intrinsic impedance  $\eta = (\mu/\epsilon)^{1/2}$  in the presence of an infinite, planar, very thin, perfect electric conductor  $S_a$ , which produces at  $P$  the fields  $\mathbf{E}_e, \mathbf{H}_e$  [Figure 12.22(b)]
2. a magnetic source  $\mathbf{M}$  radiating in a medium with intrinsic impedance  $\eta_d = (\epsilon/\mu)^{1/2}$  in the presence of a flat, very thin, perfect electric conductor  $S_a$ , which produces at  $P$  the fields  $\mathbf{E}_d, \mathbf{H}_d$  [Figure 12.22(d)]

That is,

$$\begin{aligned}\mathbf{E}_0 &= \mathbf{E}_e + \mathbf{H}_d \\ \mathbf{H}_0 &= \mathbf{H}_e - \mathbf{E}_d\end{aligned}\tag{12-66b}$$

The dual of Figure 12.22(d) is more easily realized in practice than that of Figure 12.22(c).

To obtain Figure 12.22(d) from Figure 12.22(c),  $\mathbf{J}$  is replaced by  $\mathbf{M}$ ,  $\mathbf{E}_m$  by  $\mathbf{H}_d$ ,  $\mathbf{H}_m$  by  $-\mathbf{E}_d$ ,  $\epsilon$  by  $\mu$ , and  $\mu$  by  $\epsilon$ . This is a form of duality often used in electromagnetics (see Section 3.7, Table 3.2). The electric screen with the opening in Figure 12.22(b) and the electric conductor of Figure 12.22(d) are also dual. They are usually referred to as *complementary structures*, because when combined they form a single solid screen with no overlaps. A proof of Babinet's principle and its extension can be found in the literature [5].

Using Booker's extension it can be shown [13], [14] by referring to Figure 12.23, that if a screen and its complement are immersed in a medium with an intrinsic impedance  $\eta$  and have terminal impedances of  $Z_s$  and  $Z_c$ , respectively, the impedances are related by

$$\boxed{Z_s Z_c = \frac{\eta^2}{4}}\tag{12-67}$$

To obtain the impedance  $Z_c$  of the complement (dipole) in a practical arrangement, a gap must be introduced to represent the feed points. In addition, the far-zone fields

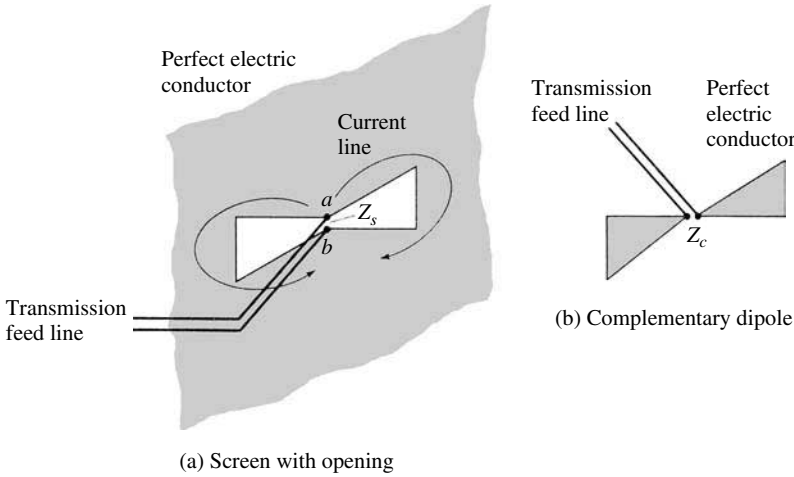


**Figure 12.23** Opening on a screen and its complementary dipole.

radiated by the opening on the screen ( $E_{\theta s}$ ,  $E_{\phi s}$ ,  $H_{\theta s}$ ,  $H_{\phi s}$ ) are related to the far-zone fields of the complement ( $E_{\theta c}$ ,  $E_{\phi c}$ ,  $H_{\theta c}$ ,  $H_{\phi c}$ ) by

$$E_{\theta s} = H_{\theta c}, \quad E_{\phi s} = H_{\phi c}, \quad H_{\theta s} = -\frac{E_{\theta c}}{\eta_0^2}, \quad H_{\phi s} = -\frac{E_{\phi c}}{\eta_0^2} \quad (12-68)$$

Infinite, flat, very thin conductors are not realizable in practice but can be closely approximated. If a slot is cut into a plane conductor that is large compared to the wavelength and the dimensions of the slot, the behavior predicted by Babinet's principle can be realized to a high degree. The impedance properties of the slot may not be affected as much by the finite dimensions of the plane as would be its pattern. The slot of Figure 12.23(a) will also radiate on both sides of the screen. Unidirectional radiation can be obtained by placing a backing (box or cavity) behind the slot, forming a so-called *cavity-backed slot* whose radiation properties (impedance and pattern) are determined by the dimensions of the cavity.

To demonstrate the application of Babinet's principle, an example is considered.

### Example 12.6

A very thin half-wavelength slot is cut on an infinite, planar, very thin, perfectly conducting electric screen as shown in Figure 12.24(a). Find its input impedance. Assume it is radiating into free-space.

**Solution:** From Babinet's principle and its extension we know that a very thin half-wavelength dipole, shown in Figure 12.24(b), is the complementary structure to the slot. From Chapter 4, the terminal (input) impedance of the dipole is  $Z_c = 73 + j42.5$ . Thus the

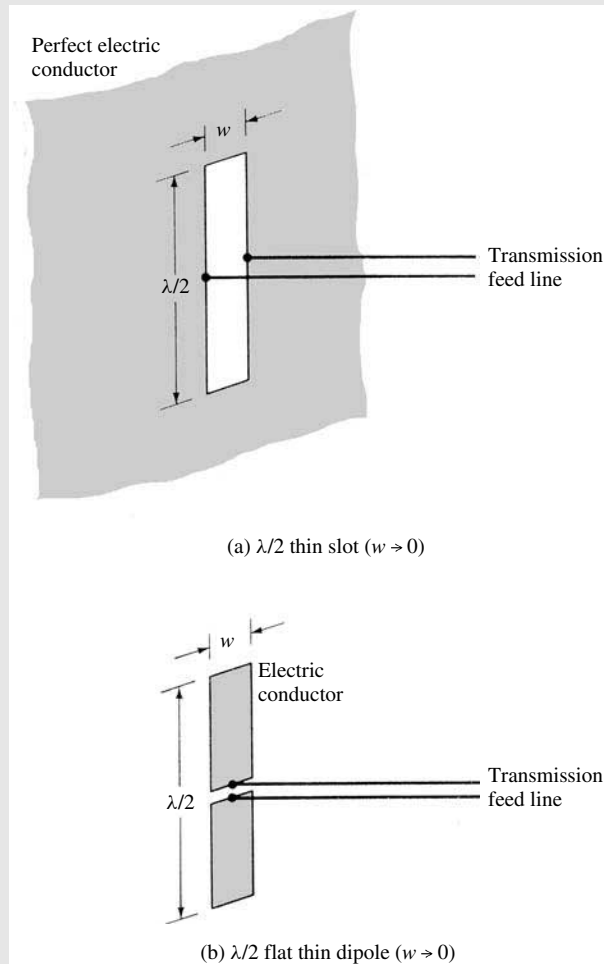


**Figure 12.24** Half-wavelength thin slot on an electric screen and its complement.

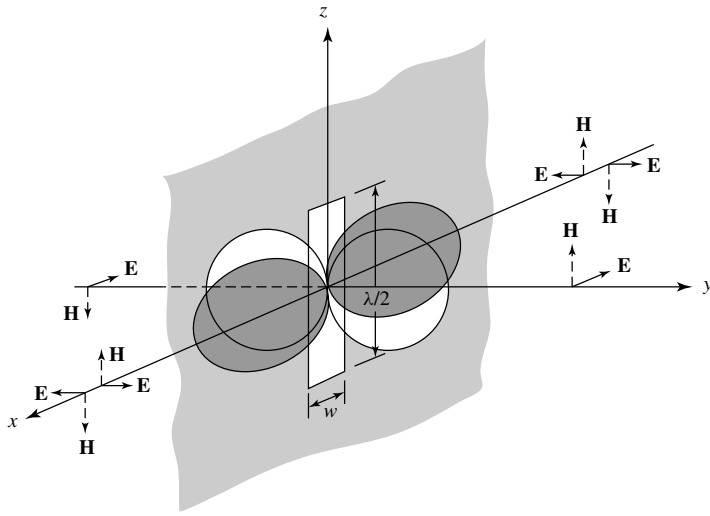
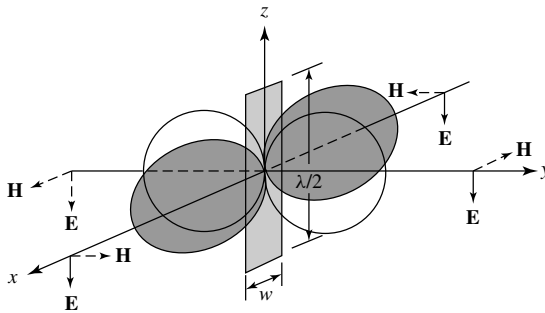
terminal (input) impedance of the slot, using (12-67), is given by

$$Z_s = \frac{\eta_0^2}{4Z_c} \simeq \frac{(376.7)^2}{4(73 + j42.5)} \simeq \frac{35,475.72}{73 + j42.5}$$

$$Z_s \simeq 362.95 - j211.31$$

The slot of Figure 12.24(a) can be made to resonate by choosing the dimensions of its complement (dipole) so that it is also resonant. The pattern of the slot is identical in shape to that of the dipole except that the  $\mathbf{E}$ - and  $\mathbf{H}$ -fields are interchanged. When a vertical slot is mounted on a vertical screen, as shown in Figure 12.25(a), its electric field is horizontally polarized while that of the dipole is vertically polarized



(a)  $\lambda/2$  slot on a screen(b)  $\lambda/2$  flat dipole

**Figure 12.25** Radiation fields of a  $\lambda/2$  slot on a screen and of a  $\lambda/2$  flat dipole. (SOURCE: J. D. Kraus, *Antennas*, McGraw-Hill, New York, 1988, Chapter 13)

[Fig. 12.25(b)]. Changing the angular orientation of the slot or screen will change the polarization.

The slot antenna, as a cavity-backed design, has been utilized in a variety of law enforcement applications. Its main advantage is that it can be fabricated and concealed within metallic objects, and with a small transmitter it can provide covert communications. There are various methods of feeding a slot antenna [15]. For proper operation, the cavity depth must be equal to odd multiples of  $\lambda_g/4$ , where  $\lambda_g$  is the guide wavelength.

## 12.9 FOURIER TRANSFORMS IN APERTURE ANTENNA THEORY

Previously the spatial domain analysis of aperture antennas was introduced, and it was applied to rectangular and circular apertures radiating in an infinite, homogeneous,

lossless medium. The analysis of aperture antennas mounted on infinite ground planes, covered with lossless and/or lossy dielectric media, becomes too complex when it is attempted in the spatial domain. Considerable simplification can result with the utility of the frequency (*spectral*) domain.

### 12.9.1 Fourier Transforms-Spectral Domain

From Fourier series analysis, any periodic function  $f(x)$  with a period  $T$  can be represented by a Fourier series of cosine and sine terms. If the function  $f(x)$  is aperiodic and exists only in the interval of  $0 < x < T$ , a Fourier series can be formed by constructing, in a number of ways, a periodic function. The Fourier series for the constructed periodic function represents the actual aperiodic function  $f(x)$  only in the interval  $0 < x < T$ . Outside this space, the aperiodic function  $f(x)$  is zero and the series representation is not needed. A Fourier series for  $f(x)$  converges to the values of  $f(x)$  at each point of continuity and to the midpoint of its values at each discontinuity.

In addition,  $f(x)$  can also be represented as a superposition of discrete complex exponentials of the form

$$f(x) = \sum_{n=-\infty}^{+\infty} c_n e^{-j(2n\pi/T)x} \quad (12-69)$$

$$c_n = \frac{1}{T} \int_0^T f(x) e^{+j(2n\pi/T)x} dx \quad (12-69a)$$

or of continuous complex exponentials of the form

$$f(x) = \frac{1}{2\pi} \int_{-\infty}^{+\infty} \mathcal{F}(\omega) e^{-jx\omega} d\omega \quad -\infty < \omega < +\infty \quad (12-70a)$$

whose inverse is given by

$$\mathcal{F}(\omega) = \int_{-\infty}^{+\infty} f(x) e^{+j\omega x} dx \quad -\infty < x < +\infty \quad (12-70b)$$

The integral operation in (12-70a) is referred to as the *direct transformation* and that of (12-70b) as the *inverse transformation* and both form a *transform pair*.

Another useful identity is *Parseval's theorem*, which for the transform pair, can be written as

$$\int_{-\infty}^{+\infty} f(x) g^*(x) dx = \frac{1}{2\pi} \int_{-\infty}^{+\infty} \mathcal{F}(\omega) \mathcal{G}^*(\omega) d\omega \quad (12-71)$$

where  $*$  indicates complex conjugate.

From the definitions of (12-70a), (12-70b) and (12-71), the Fourier transforms can be expanded to two dimensions and can be written as

$$f(x, y) = \frac{1}{4\pi^2} \int_{-\infty}^{+\infty} \int_{-\infty}^{+\infty} \mathcal{F}(\omega_1, \omega_2) e^{-j(\omega_1 x + \omega_2 y)} d\omega_1 d\omega_2 \quad (12-72a)$$

$$\mathcal{F}(\omega_1, \omega_2) = \int_{-\infty}^{+\infty} \int_{-\infty}^{+\infty} f(x, y) e^{+j(\omega_1 x + \omega_2 y)} dx dy \quad (12-72b)$$

$$\begin{aligned}
 & \int_{-\infty}^{+\infty} \int_{-\infty}^{+\infty} f(x, y) g^*(x, y) dx dy \\
 &= \frac{1}{4\pi^2} \int_{-\infty}^{+\infty} \int_{-\infty}^{+\infty} \mathcal{F}(\omega_1, \omega_2) \mathcal{G}^*(\omega_1, \omega_2) d\omega_1 d\omega_2
 \end{aligned} \tag{12-72c}$$

The process can be continued to  $n$  dimensions.

The definitions, theorems, and principles introduced will be utilized in the sections that follow to analyze the radiation characteristics of aperture antennas mounted on infinite ground planes.

### 12.9.2 Radiated Fields

To apply Fourier transforms (*spectral techniques*) to the analysis of aperture antennas, let us consider a rectangular aperture of dimensions  $a$  and  $b$  mounted on an infinite ground plane, as shown in Figure 12.26. In the source-free region ( $z > 0$ ), the field  $\mathbf{E}(x, y, z)$  of a monochromatic wave radiated by the aperture can be written as a superposition of plane waves (all of the same frequency, different amplitudes, and traveling in different directions) of the form  $\mathbf{f}(k_x, k_y)e^{-j\mathbf{k}\cdot\mathbf{r}}$  [16], [17]. The function  $\mathbf{f}(k_x, k_y)$  is the vector amplitude of the wave, and  $k_x$  and  $k_y$  are the spectral frequencies which extend over the entire frequency spectrum ( $-\infty \leq k_x, k_y \leq \infty$ ). Thus the field  $\mathbf{E}(x, y, z)$  can be written as

$$\mathbf{E}(x, y, z) = \frac{1}{4\pi^2} \int_{-\infty}^{+\infty} \int_{-\infty}^{+\infty} \mathbf{f}(k_x, k_y) e^{-j\mathbf{k}\cdot\mathbf{r}} dk_x dk_y \tag{12-73}$$

according to the definition of (12-72a). The object of a plane wave expansion is to determine the unknown amplitudes  $\mathbf{f}(k_x, k_y)$  and the direction of propagation of the plane waves. Since

$$\mathbf{r} = \hat{\mathbf{a}}_x x + \hat{\mathbf{a}}_y y + \hat{\mathbf{a}}_z z \tag{12-74}$$

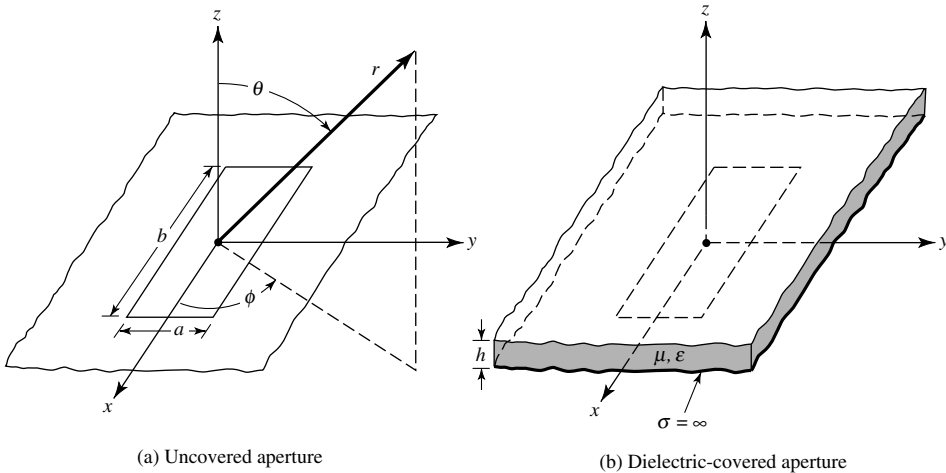


**Figure 12.26** Rectangular apertures mounted on infinite ground planes.

and the propagation factor  $\mathbf{k}$  (often referred to as the *vector wavenumber*) can be defined as

$$\mathbf{k} = \hat{\mathbf{a}}_x k_x + \hat{\mathbf{a}}_y k_y + \hat{\mathbf{a}}_z k_z \quad (12-75)$$

(12-73) can be written as

$$\mathbf{E}(x, y, z) = \frac{1}{4\pi^2} \int_{-\infty}^{+\infty} \int_{-\infty}^{+\infty} [\mathbf{f}(k_x, k_y) e^{-jk_z z}] e^{-j(k_x x + k_y y)} dk_x dk_y. \quad (12-76)$$

The part of the integrand within the brackets can be regarded as the transform of  $\mathbf{E}(x, y, z)$ . This allows us to write the transform pair as

$$\mathbf{E}(x, y, z) = \frac{1}{4\pi^2} \int_{-\infty}^{+\infty} \int_{-\infty}^{+\infty} \mathcal{E}(k_x, k_y, z) e^{-j(k_x x + k_y y)} dk_x dk_y \quad (12-77a)$$

$$\mathcal{E}(k_x, k_y, z) = \int_{-\infty}^{+\infty} \int_{-\infty}^{+\infty} \mathbf{E}(x, y, z) e^{+j(k_x x + k_y y)} dx dy \quad (12-77b)$$

where

$$\mathcal{E}(k_x, k_y, z) = \mathbf{f}(k_x, k_y) e^{-jk_z z} \quad (12-77c)$$

In principle then, according to (12-77a) and (12-77b) the fields radiated by an aperture  $\mathbf{E}(x, y, z)$  can be found provided its transform  $\mathcal{E}(k_x, k_y, z)$  is known. To this point the transform field  $\mathcal{E}(k_x, k_y, z)$  can only be found provided the actual field  $\mathbf{E}(x, y, z)$  is known *a priori*. In other words, the answer must be known beforehand! However, as it will be seen from what follows, if the transform field at  $z = 0$

$$\mathcal{E}(k_x, k_y, z = 0) = \mathbf{f}(k_x, k_y) \quad (12-78)$$

is formed, it will be sufficient to determine  $\mathbf{E}(x, y, z)$ . To form the transform  $\mathcal{E}(k_x, k_y, z = 0) = \mathbf{f}(k_x, k_y)$ , it will be necessary and sufficient to know only the tangential components of the  $\mathbf{E}$ -field at  $z = 0$ . For the problem of Figure 12.26(a), the tangential components of the  $\mathbf{E}$ -field at  $z = 0$  exist only over the bounds of the aperture (they vanish outside it because of the presence of the infinite ground plane).

In general

$$\mathbf{f}(k_x, k_y) = \hat{\mathbf{a}}_x f_x(k_x, k_y) + \hat{\mathbf{a}}_y f_y(k_x, k_y) + \hat{\mathbf{a}}_z f_z(k_x, k_y) \quad (12-79)$$

which can also be written as

$$\mathbf{f}(k_x, k_y) = \mathbf{f}_t(k_x, k_y) + \hat{\mathbf{a}}_z f_z(k_x, k_y) \quad (12-79a)$$

$$\mathbf{f}_t(k_x, k_y) = \hat{\mathbf{a}}_x f_x(k_x, k_y) + \hat{\mathbf{a}}_y f_y(k_x, k_y) \quad (12-79b)$$

For aperture antennas positioned along the  $x$ - $y$  plane, the only components of  $\mathbf{f}(k_x, k_y)$  that need to be found are  $f_x$  and  $f_y$ . As will be shown in what follows,

$f_z$  can be found once  $f_x$  and  $f_y$  are known. This is a further simplification of the problem. The functions  $f_x$  and  $f_y$  are found, using (12-77a) and (12-77b), provided the tangential components of the  $\mathbf{E}$ -field over the aperture ( $E_{xa}$  and  $E_{ya}$ ) are specified. The solution of (12-77c) is valid provided the  $z$  variations of  $\mathbf{E}(k_x, k_y, z)$  are separable. In addition, in the source-free region the field  $\mathbf{E}(x, y, z)$  of (12-77a) must satisfy the homogeneous vector wave equation. These allow us to relate the propagation constant  $k_z$  to  $k_x, k_y$  and  $k = (\omega\sqrt{\mu\epsilon})$ , by

$$k_z^2 = k^2 - (k_x^2 + k_y^2) \quad (12-80)$$

or

$$k_z = \begin{cases} +[k^2 - (k_x^2 + k_y^2)]^{1/2} & \text{when } k^2 \geq k_x^2 + k_y^2 \\ -j[(k_x^2 + k_y^2) - k^2]^{1/2} & \text{when } k^2 < k_x^2 + k_y^2 \end{cases} \quad (12-80a)$$

$$(12-80b)$$

This is left as an exercise to the reader. The form of  $k_z$  as given by (12-80a) contributes to the propagating waves (radiation field) of (12-76) and (12-77a) whereas that of (12-80b) contributes to the evanescent waves. Since the field in the far zone of the antenna is of the radiation type, its contribution comes from the part of the  $k_x, k_y$  spectrum which satisfies (12-80a). The values of  $k_x$  and  $k_y$  in (12-80)–(12-80b) are analogous to the eigenvalues for the fields inside a rectangular waveguide [12]. In addition,  $k_z$  is analogous to the propagation constant for waveguides which is used to define cutoff.

To find the relation between  $f_z$  and  $f_x, f_y$ , we proceed as follows. In the source-free region ( $z > 0$ ) the field  $\mathbf{E}(x, y, z)$ , in addition to satisfying the vector wave equation, must also be solenoidal so that

$$\nabla \cdot \mathbf{E}(x, y, z) = \nabla \cdot \left\{ \frac{1}{4\pi^2} \int_{-\infty}^{+\infty} \int_{-\infty}^{+\infty} \mathbf{f}(k_x, k_y) e^{-j\mathbf{k}\cdot\mathbf{r}} dk_x dk_y \right\} = 0 \quad (12-81)$$

Interchanging differentiation with integration and using the vector identity

$$\nabla \cdot (\alpha \mathbf{A}) = \alpha \nabla \cdot \mathbf{A} + \mathbf{A} \cdot \nabla \alpha \quad (12-82)$$

reduces (12-81) to

$$\frac{1}{4\pi^2} \int_{-\infty}^{+\infty} \int_{-\infty}^{+\infty} [\mathbf{f} \cdot \nabla (e^{-j\mathbf{k}\cdot\mathbf{r}})] dk_x dk_y = 0 \quad (12-83)$$

since  $\nabla \cdot \mathbf{f}(k_x, k_y) = 0$ . Equation (12-83) is satisfied provided that

$$\mathbf{f} \cdot \nabla e^{-j\mathbf{k}\cdot\mathbf{r}} = -j\mathbf{f} \cdot \mathbf{k} e^{-j\mathbf{k}\cdot\mathbf{r}} = 0 \quad (12-84)$$

or

$$\mathbf{f} \cdot \mathbf{k} = (\mathbf{f}_t + \hat{\mathbf{a}}_z f_z) \cdot \mathbf{k} = 0 \quad (12-84a)$$

or

$$f_z = -\frac{\mathbf{f}_t \cdot \mathbf{k}}{k_z} = -\frac{(f_x k_x + f_y k_y)}{k_z} \quad (12-84b)$$

From (12-84b) it is evident that  $f_z$  can be formed once  $f_x$  and  $f_y$  are known.

All three components of  $\mathbf{f}$  ( $f_x$ ,  $f_y$  and  $f_z$ ) can be found, using (12-77b) and (12-78), provided the two components of  $\mathbf{E}$  ( $E_x$ ,  $E_y$ ) at  $z = 0$ , which is the plane of the aperture and ground plane of Figure 12.26(a), are known. Because  $E_x$  and  $E_y$  along the  $z = 0$  plane are zero outside the bounds of the aperture ( $|x| > a/2$ ,  $|y| > b/2$ ), (12-77b) and (12-78) reduce for  $f_x$  and  $f_y$  to

$$f_x(k_x, k_y) = \int_{-b/2}^{+b/2} \int_{-a/2}^{+a/2} E_{xa}(x', y', z' = 0) e^{+j(k_x x' + k_y y')} dx' dy' \quad (12-85a)$$

$$f_y(k_x, k_y) = \int_{-b/2}^{+b/2} \int_{-a/2}^{+a/2} E_{ya}(x', y', z' = 0) e^{+j(k_x x' + k_y y')} dx' dy' \quad (12-85b)$$

where primes indicate source points.  $E_{xa}(x', y', z' = 0)$  and  $E_{ya}(x', y', z' = 0)$ , which represent the tangential components of the electric field over the aperture, are the only fields that need to be known. Once  $f_x$  and  $f_y$  are found by using (12-85a) and (12-85b),  $f_z$  and  $\mathcal{E}(k_x, k_y, z)$  can be formed using (12-84a) and (12-77c), respectively. Thus, the solution for  $\mathbf{E}(x, y, z)$  for the aperture in Figure 12.26(a) is given by

$$\mathbf{E}(x, y, z) = \frac{1}{4\pi^2} \left\{ \iint_{\substack{k_x^2 + k_y^2 \leq k^2 \\ k_z = [k^2 - (k_x^2 + k_y^2)]^{1/2}}} \mathcal{E}(k_x, k_y, z) e^{-j(k_x x + k_y y)} dk_x dk_y + \iint_{\substack{k_x^2 + k_y^2 > k^2 \\ k_z = -j[(k_x^2 + k_y^2) - k^2]^{1/2}}} \mathcal{E}(k_x, k_y, z) e^{-j(k_x x + k_y y)} dk_x dk_y \right\} \quad (12-86)$$

$$\mathcal{E}(k_x, k_y, z) = \left[ \hat{\mathbf{a}}_x f_x + \hat{\mathbf{a}}_y f_y - \hat{\mathbf{a}}_z \left( \frac{f_x k_x + f_y k_y}{k_z} \right) \right] e^{-jk_z z} \quad (12-86a)$$

where  $f_x$  and  $f_y$  are given by (12-85a) and (12-85b).

In summary, the field radiated by the aperture of Figure 12.26(a) can be found by the following procedure:

1. Specify the tangential components of the  $\mathbf{E}$ -field ( $E_{xa}$  and  $E_{ya}$ ) over the bounds of the aperture.
2. Find  $f_x$  and  $f_y$  using (12-85a) and (12-85b), respectively.
3. Find  $f_z$  using (12-84b).
4. Find  $\mathcal{E}(k_x, k_y, z)$  using (12-86a).
5. Formulate  $\mathbf{E}(x, y, z)$  using (12-86).

This completes the solution for  $\mathbf{E}(x, y, z)$ . However, as is evident from (12-86), the integration is quite difficult even for the simplest of problems. However, if the observations are restricted in the far-field region, many simplifications in performing the integrations can result. This was apparent in Chapters 4, 5 and in others. In many practical problems, the far zone is usually the region of greatest importance. Since

it is also known that for all antennas the fields in the far zone are primarily of the radiated type (*propagating waves*), then only the first integral in (12-86) contributes in that region.

In the next section, our attention is directed toward the evaluation of (12-86a) or (12-73) in the far-zone region (large values of  $kr$ ). This is accomplished by evaluating (12-73) asymptotically for large values of  $kr$  by the method of *Stationary Phase* [18], [19].

To complete the formulation of the radiated fields in all regions, let us outline the procedure to find  $\mathbf{H}(x, y, z)$ . From Maxwell's equations

$$\begin{aligned}\mathbf{H}(x, y, z) &= -\frac{1}{j\omega\mu} \nabla \times \mathbf{E}(x, y, z) \\ &= -\frac{1}{j\omega\mu} \nabla \times \left[ \frac{1}{4\pi^2} \int_{-\infty}^{+\infty} \int_{-\infty}^{+\infty} \mathbf{f}(k_x, k_y) e^{-j\mathbf{k}\cdot\mathbf{r}} dk_x dk_y \right]\end{aligned}\quad (12-87)$$

Interchanging integration with differentiation and using the vector identity

$$\nabla \times (\alpha \mathbf{A}) = \alpha \nabla \times \mathbf{A} + (\nabla \alpha) \times \mathbf{A} \quad (12-88)$$

reduces (12-87) to

$$\mathbf{H}(x, y, z) = -\frac{1}{4\pi^2 k \eta} \int_{-\infty}^{+\infty} \int_{-\infty}^{+\infty} (\mathbf{f} \times \mathbf{k}) e^{-j\mathbf{k}\cdot\mathbf{r}} dk_x dk_y \quad (12-89)$$

since  $\nabla \times \mathbf{f}(k_x, k_y) = 0$  and  $\nabla(e^{-j\mathbf{k}\cdot\mathbf{r}}) = -j\mathbf{k}e^{-j\mathbf{k}\cdot\mathbf{r}}$  from (12-84).

### 12.9.3 Asymptotic Evaluation of Radiated Field

The main objective in this section is the evaluation of (12-73) or (12-86a) for observations made in the far-field. For most practical antennas, the field distribution on the aperture is such that an exact evaluation of (12-73) in closed form is not possible. However, if the observations are restricted to the far-field region (large  $kr$ ), the integral evaluation becomes less complex. This was apparent in Chapters 4, 5, and others. The integral of (12-73) will be evaluated asymptotically for large values of  $kr$  using the method of *Stationary Phase* (Appendix VIII) [18], [19].

The stationary phase method assumes that the main contribution to the integral of (12-73) comes from values of  $k_x$  and  $k_y$  where  $\mathbf{k} \cdot \mathbf{r}$  does not change for first order changes in  $k_x$  and  $k_y$ . That is to say  $\mathbf{k} \cdot \mathbf{r}$  remains stationary at those points. For the other values of  $k_x$  and  $k_y$ ,  $\mathbf{k} \cdot \mathbf{r}$  changes very rapidly and the function  $e^{-j\mathbf{k}\cdot\mathbf{r}}$  oscillates very rapidly between the values of  $+1$  and  $-1$ . Assuming that  $\mathbf{f}(k_x, k_y)$  is a slowly varying function of  $k_x$  and  $k_y$ , the integrand of (12-73) oscillates very rapidly outside the stationary points so that the contribution to the integral from that region is negligible. As the observation point approaches infinity, the contributions to the integral from the region outside the stationary points is zero. For practical applications, the observation point cannot be at infinity. However, it will be assumed to be far enough such that the major contributions come from the stationary points.

The first task in the asymptotic evaluation of (12-73) is to find the stationary points of  $\mathbf{k} \cdot \mathbf{r}$ . For that,  $\mathbf{k} \cdot \mathbf{r}$  is written as

$$\mathbf{k} \cdot \mathbf{r} = (\hat{\mathbf{a}}_x k_x + \hat{\mathbf{a}}_y k_y + \hat{\mathbf{a}}_z k_z) \cdot \hat{\mathbf{a}}_r r \quad (12-90)$$

Using the inverse transformation of (4-5), (12-90) can be written as

$$\mathbf{k} \cdot \mathbf{r} = r(k_x \sin \theta \cos \phi + k_y \sin \theta \sin \phi + k_z \cos \theta) \quad (12-91)$$

which reduces, using (12-80a) to

$$\mathbf{k} \cdot \mathbf{r} = r[k_x \sin \theta \cos \phi + k_y \sin \theta \sin \phi + \sqrt{k^2 - k_x^2 - k_y^2} \cos \theta] \quad (12-92)$$

The stationary points can be found by

$$\frac{\partial(\mathbf{k} \cdot \mathbf{r})}{\partial k_x} = 0 \quad (12-93a)$$

$$\frac{\partial(\mathbf{k} \cdot \mathbf{r})}{\partial k_y} = 0 \quad (12-93b)$$

Using (12-92) and (12-80), (12-93a) and (12-93b) reduce to

$$\frac{\partial(\mathbf{k} \cdot \mathbf{r})}{\partial k_x} = r \left( \sin \theta \cos \phi - \frac{k_x}{k_z} \cos \theta \right) = 0 \quad (12-94a)$$

$$\frac{\partial(\mathbf{k} \cdot \mathbf{r})}{\partial k_y} = r \left( \sin \theta \sin \phi - \frac{k_y}{k_z} \cos \theta \right) = 0 \quad (12-94b)$$

whose solutions are given, respectively, by

$$k_x = k_z \frac{\sin \theta \cos \phi}{\cos \theta} \quad (12-95a)$$

$$k_y = k_z \frac{\sin \theta \sin \phi}{\cos \theta} \quad (12-95b)$$

Using (12-95a) and (12-95b), (12-80) can be written as

$$k^2 = k_z^2 + k_x^2 + k_y^2 = k_z^2 \left( 1 + \frac{\sin^2 \theta}{\cos^2 \theta} \right) \quad (12-96)$$

which reduces for  $k_z$  to

$$k_z = k \cos \theta \quad (12-97)$$

With the aid of (12-97), the stationary point of (12-95a) and (12-95b) simplify to

$$k_x = k \sin \theta \cos \phi = k_1 \quad (12-98a)$$

$$k_y = k \sin \theta \sin \phi = k_2 \quad (12-98b)$$



The function  $\mathbf{k} \cdot \mathbf{r}$  can be expanded into a Taylor series, about the stationary point  $k_1, k_2$ , and it can be approximated by the zero, first, and second order terms. That is,

$$\begin{aligned} \mathbf{k} \cdot \mathbf{r} \simeq & \left. \mathbf{k} \cdot \mathbf{r} \right|_{k_1, k_2} + \left. \frac{\partial(\mathbf{k} \cdot \mathbf{r})}{\partial k_x} \right|_{k_1, k_2} (k_x - k_1) + \left. \frac{\partial(\mathbf{k} \cdot \mathbf{r})}{\partial k_y} \right|_{k_1, k_2} (k_y - k_2) \\ & + \frac{1}{2} \left. \frac{\partial^2(\mathbf{k} \cdot \mathbf{r})}{\partial k_x^2} \right|_{k_1, k_2} (k_x - k_1)^2 + \frac{1}{2} \left. \frac{\partial^2(\mathbf{k} \cdot \mathbf{r})}{\partial k_y^2} \right|_{k_1, k_2} (k_y - k_2)^2 \\ & + \left. \frac{\partial^2(\mathbf{k} \cdot \mathbf{r})}{\partial k_x \partial k_y} \right|_{k_1, k_2} (k_x - k_1)(k_y - k_2) \end{aligned} \quad (12-99)$$

Since the second and third terms vanish at the stationary point  $k_x = k_1$  and  $k_y = k_2$ , (12-99) can be expressed as

$$\mathbf{k} \cdot \mathbf{r} = \left. \mathbf{k} \cdot \mathbf{r} \right|_{k_1, k_2} - A\xi^2 - B\eta^2 - C\xi\eta \quad (12-100)$$

where

$$A = -\frac{1}{2} \left. \frac{\partial^2(\mathbf{k} \cdot \mathbf{r})}{\partial k_x^2} \right|_{k_1, k_2} \quad (12-100a)$$

$$B = -\frac{1}{2} \left. \frac{\partial^2(\mathbf{k} \cdot \mathbf{r})}{\partial k_y^2} \right|_{k_1, k_2} \quad (12-100b)$$

$$C = -\left. \frac{\partial^2(\mathbf{k} \cdot \mathbf{r})}{\partial k_x \partial k_y} \right|_{k_1, k_2} \quad (12-100c)$$

$$\xi = (k_x - k_1) \quad (12-100d)$$

$$\eta = (k_y - k_2) \quad (12-100e)$$

Using (12-97)-(12-98b), (12-90) reduces to

$$\left. \mathbf{k} \cdot \mathbf{r} \right|_{k_1, k_2} = kr \quad (12-101)$$

Similarly, with the aid of (12-92),  $A$ ,  $B$ , and  $C$  can be written, after a few manipulations, as

$$A = -\frac{1}{2} \left. \frac{\partial^2(\mathbf{k} \cdot \mathbf{r})}{\partial k_x^2} \right|_{k_1, k_2} = \frac{r}{2k} \left( 1 + \frac{\sin^2 \theta \cos^2 \phi}{\cos^2 \theta} \right) \quad (12-102a)$$

$$B = -\frac{1}{2} \left. \frac{\partial^2(\mathbf{k} \cdot \mathbf{r})}{\partial k_y^2} \right|_{k_1, k_2} = \frac{r}{2k} \left( 1 + \frac{\sin^2 \theta \sin^2 \phi}{\cos^2 \theta} \right) \quad (12-102b)$$

$$C = -\left. \frac{\partial^2(\mathbf{k} \cdot \mathbf{r})}{\partial k_x \partial k_y} \right|_{k_1, k_2} = \frac{r}{k} \frac{\sin^2 \theta}{\cos^2 \theta} \cos \phi \sin \phi \quad (12-102c)$$

Thus (12-73) can be approximated around the stationary point  $k_x = k_1$  and  $k_y = k_2$ , which contributes mostly to the integral, by

$$\mathbf{E}(x, y, z) \simeq \frac{1}{4\pi^2} \iint_{S_{1,2}} \mathbf{f}(k_x = k_1, k_y = k_2) e^{-j(kr - A\xi^2 - B\eta^2 - C\xi\eta)} d\xi d\eta \quad (12-103)$$

or

$$\mathbf{E}(x, y, z) \simeq \frac{1}{4\pi^2} \mathbf{f}(k_1, k_2) e^{-jkr} \iint_{S_{1,2}} e^{+j(A\xi^2 + B\eta^2 + C\xi\eta)} d\xi d\eta \quad (12-103a)$$

where  $S_{1,2}$  is the surface near the stationary point.

The integral of (12-103a) can be evaluated with the method of *Stationary Phase*. That is, (see Appendix VIII)

$$\iint_{S_{1,2}} e^{j(A\xi^2 + B\eta^2 + C\xi\eta)} d\xi d\eta = j \frac{2\pi\delta}{\sqrt{|4AB - C^2|}} \quad (12-104)$$

$$\delta = \begin{cases} +1 & \text{if } 4AB > C^2 \text{ and } A > 0 \\ -1 & \text{if } 4AB > C^2 \text{ and } A < 0 \\ -j & \text{if } 4AB < C^2 \end{cases} \quad (12-104a)$$

With the aid of (12-102a)-(12-102c), the factor  $4AB - C^2$  is

$$4AB - C^2 = \left( \frac{r}{k \cos \theta} \right)^2 \quad (12-105)$$

Since  $4AB > C^2$  and  $A > 0$ , (12-103) reduces to

$$\iint_{S_{1,2}} e^{j(A\xi^2 + B\eta^2 + C\xi\eta)} d\xi d\eta = j \frac{2\pi k}{r} \cos \theta \quad (12-106)$$

and (12-103a) to

$$\mathbf{E}(r, \theta, \phi) \simeq j \frac{ke^{-jkr}}{2\pi r} [\cos \theta \mathbf{f}(k_1 = k \sin \theta \cos \phi, k_2 = k \sin \theta \sin \phi)] \quad (12-107)$$

In the far-field region, only the  $\theta$  and  $\phi$  components of the electric and magnetic fields are dominant. Therefore, the  $E_\theta$  and  $E_\phi$  components of (12-107) can be written in terms of  $f_x$  and  $f_y$ . With the aid of (12-84b),  $\mathbf{f}$  can be expressed as

$$\mathbf{f} = \hat{\mathbf{a}}_x f_x + \hat{\mathbf{a}}_y f_y + \hat{\mathbf{a}}_z f_z = \left[ \hat{\mathbf{a}}_x f_x + \hat{\mathbf{a}}_y f_y - \hat{\mathbf{a}}_z \frac{(f_x k_x + f_y k_y)}{k_z} \right] \quad (12-108)$$

At the stationary point ( $k_x = k_1 = k \sin \theta \cos \phi$ ,  $k_y = k_2 = k \sin \theta \sin \phi$ ,  $k_z = k \cos \theta$ ), (12-108) reduces to

$$\mathbf{f}(k_1, k_2) = \left[ \hat{\mathbf{a}}_x f_x + \hat{\mathbf{a}}_y f_y - \hat{\mathbf{a}}_z \frac{\sin \theta}{\cos \theta} (f_x \cos \phi + f_y \sin \phi) \right] \quad (12-109)$$

Using the inverse transformation of (4-5), the  $\theta$  and  $\phi$  components of  $\mathbf{f}$  can be written as

$$f_\theta = \frac{f_x \cos \phi + f_y \sin \phi}{\cos \theta} \quad (12-110a)$$

$$f_\phi = -f_x \sin \phi + f_y \cos \phi \quad (12-110b)$$

The  $\mathbf{E}$ -field of (12-107) reduces, for the  $\theta$  and  $\phi$  components, to

$$\mathbf{E}(r, \theta, \phi) \simeq j \frac{ke^{-jkr}}{2\pi r} [\hat{\mathbf{a}}_\theta (f_x \cos \phi + f_y \sin \phi) + \hat{\mathbf{a}}_\phi \cos \theta (-f_x \sin \phi + f_y \cos \phi)] \quad (12-111)$$

and the  $\mathbf{H}$ -field to

$$\mathbf{H}(r, \theta, \phi) = \sqrt{\frac{\epsilon}{\mu}} [\hat{\mathbf{a}}_r \times \mathbf{E}(r, \theta, \phi)] \quad (12-112)$$

where from (12-85a) and (12-85b)

$$f_x(k_x = k_1, k_y = k_2) = \int_{-b/2}^{+b/2} \int_{-a/2}^{+a/2} E_{xa}(x', y', z' = 0) e^{jk(x' \sin \theta \cos \phi + y' \sin \theta \sin \phi)} dx' dy' \quad (12-113a)$$

$$f_y(k_x = k_1, k_y = k_2) = \int_{-b/2}^{+b/2} \int_{-a/2}^{+a/2} E_{ya}(x', y', z' = 0) e^{jk(x' \sin \theta \cos \phi + y' \sin \theta \sin \phi)} dx' dy' \quad (12-113b)$$

To illustrate the frequency domain (*spectral*) techniques, the problem of a uniform illuminated aperture, which was previously analyzed in Section 12.5.1 using spatial methods, will be solved again using transform methods.

**Example 12.7**

A rectangular aperture of dimensions  $a$  and  $b$  is mounted on an infinite ground plane, as shown in Figure 12.26(a). Find the field radiated by it assuming that over the opening the electric field is given by

$$\mathbf{E}_a = \hat{\mathbf{a}}_y E_0, \quad \begin{aligned} -a/2 \leq x' \leq a/2 \\ -b/2 \leq y' \leq b/2 \end{aligned}$$

where  $E_0$  is a constant.

*Solution:* From (12-113a) and (12-113b)

$$\begin{aligned} f_x &= 0 \\ f_y &= E_0 \int_{-b/2}^{+b/2} e^{jky' \sin \theta \sin \phi} dy' \int_{-a/2}^{+a/2} e^{jkx' \sin \theta \cos \phi} dx' \end{aligned}$$

which, when integrated, reduces to

$$\begin{aligned} f_y &= abE_0 \left( \frac{\sin X}{X} \right) \left( \frac{\sin Y}{Y} \right) \\ X &= \frac{ka}{2} \sin \theta \cos \phi \\ Y &= \frac{kb}{2} \sin \theta \sin \phi \end{aligned}$$

The  $\theta$  and  $\phi$  components of (12-111) can be written as

$$\begin{aligned} E_\theta &= j \frac{abkE_0 e^{-jkr}}{2\pi r} \left\{ \sin \phi \left[ \frac{\sin X}{X} \right] \left[ \frac{\sin Y}{Y} \right] \right\} \\ E_\phi &= j \frac{abkE_0 e^{-jkr}}{2\pi r} \left\{ \cos \theta \cos \phi \left[ \frac{\sin X}{X} \right] \left[ \frac{\sin Y}{Y} \right] \right\} \end{aligned}$$

which are identical to those of (12-23b) and (12-23c), respectively.

**12.9.4 Dielectric-Covered Apertures**

The transform (*spectral*) technique can easily be extended to determine the field radiated by dielectric-covered apertures [20], [21]. For the sake of brevity, the details will not be included here. However, it can be shown that for a single lossless dielectric sheet cover of thickness  $h$ , dielectric constant  $\epsilon_r$ , unity relative permeability, and free-space phase constant  $k_0$ , the far-zone radiated field  $E_\theta$ ,  $E_\phi$  of the covered aperture of Figure 12.26(b) are related to  $E_\theta^0$ ,  $E_\phi^0$  of the uncovered aperture of Figure 12.26(a) by

$$E_\theta(r, \theta, \phi) = f(\theta) E_\theta^0(r, \theta, \phi) \quad (12-114a)$$

$$E_\phi(r, \theta, \phi) = g(\theta) E_\phi^0(r, \theta, \phi) \quad (12-114b)$$

where

$E_\theta, E_\phi$  = field components of dielectric-covered aperture [Fig. 12.26(b)]

$E_\theta^0, E_\phi^0$  = field components of uncovered aperture [Fig. 12.26(a)]

$$f(\theta) = \frac{e^{jk_0h \cos \theta}}{\cos \psi + jZ_h \sin \psi} \quad (12-114c)$$

$$g(\theta) = \frac{e^{jk_0h \cos \theta}}{\cos \psi + jZ_e \sin \psi} \quad (12-114d)$$

$$\psi = k_0h \sqrt{\epsilon_r - \sin^2 \theta} \quad (12-114e)$$

$$Z_e = \frac{\cos \theta}{\sqrt{\epsilon_r - \sin^2 \theta}} \quad (12-114f)$$

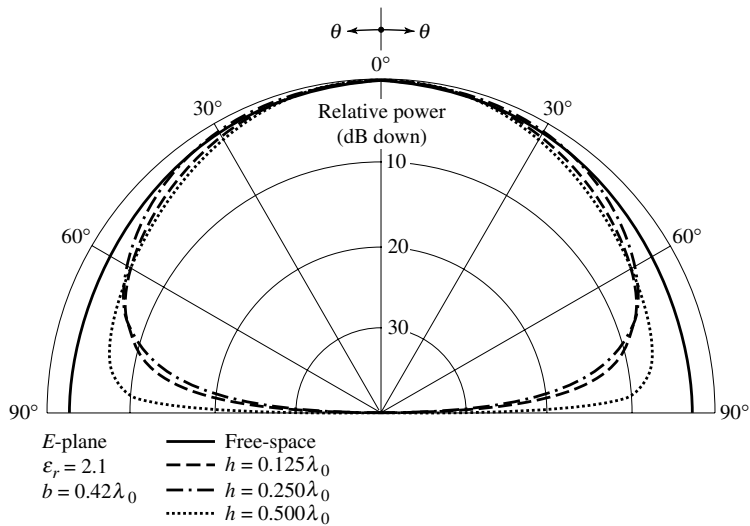
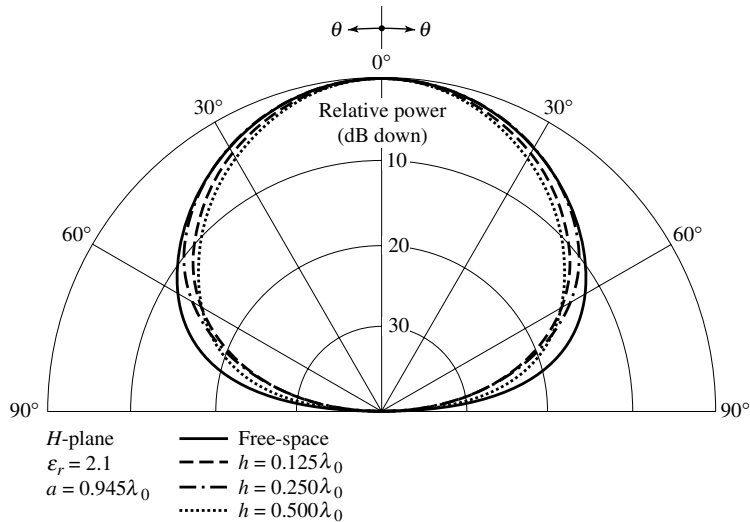
$$Z_h = \frac{\sqrt{\epsilon_r - \sin^2 \theta}}{\epsilon_r \cos \theta} \quad (12-114g)$$

The above relations do not include surface wave contributions which can be taken into account but are beyond the scope of this section [20].

To investigate the effect of the dielectric sheet, far-zone principal  $E$ - and  $H$ -plane patterns were computed for a rectangular waveguide shown in Figure 12.26(b). The waveguide was covered with a single dielectric sheet, was operating in the dominant  $TE_{10}$  mode, and was mounted on an infinite ground plane. The  $E$ - and  $H$ -plane patterns are shown in Figure 12.27(a) and 12.27(b), respectively. In the  $E$ -plane patterns, it is evident that the surface impedance of the modified ground plane forces the normal electric field component to vanish along the surface ( $\theta = \pi/2$ ). This is similar to the effects experienced by the patterns of the vertical dipole above ground shown in Figure 4.31. Since the  $H$ -plane patterns have vanishing characteristics when the aperture is radiating in free-space, the presence of the dielectric sheet has a very small overall effect. This is similar to the effects experienced by the patterns of a horizontal dipole above ground shown in Figure 4.32. However, both the  $E$ - and  $H$ -plane patterns become more broad near the surface, and more narrow elsewhere, as the thickness increases.

### 12.9.5 Aperture Admittance

Another parameter of interest, especially when the antenna is used as a diagnostic tool, is its terminating impedance or admittance. In this section, using Fourier transform

(a)  $E$ -plane(b)  $H$ -plane

**Figure 12.27** Amplitude radiation patterns of a dielectric-covered waveguide mounted on an infinite ground plane and with a  $TE_{10}$ -mode aperture field distribution.

(*spectral*) techniques, the admittance of an aperture antenna mounted on an infinite ground plane and radiating into free-space will be formulated. Computations will be presented for a parallel-plate waveguide. The techniques can best be presented by considering a specific antenna configuration and field distribution. Similar steps can be used for any other geometry and field distribution.

The geometrical arrangement of the aperture antenna under consideration is shown in Figure 12.26(a). It consists of a rectangular waveguide mounted on an infinite ground plane. It is assumed that the field distribution, *above cutoff*, is that given by the  $TE_{10}$

mode, or

$$\mathbf{E}_a = \hat{\mathbf{a}}_y E_0 \cos\left(\frac{\pi}{a} x'\right) \quad \begin{array}{l} -a/2 \leq x' \leq a/2 \\ -b/2 \leq y' \leq b/2 \end{array} \quad (12-115)$$

where  $E_0$  is a constant. The aperture admittance is defined as

$$Y_a = \frac{2P^*}{|V|^2} \quad (12-116)$$

where

$P^*$  = conjugate of complex power transmitted by the aperture

$V$  = aperture reference voltage.

The complex power transmitted by the aperture can be written as

$$P = \frac{1}{2} \iint_{S_a} [\mathbf{E}(x', y', z' = 0) \times \mathbf{H}^*(x', y', z' = 0)] \cdot \hat{\mathbf{a}}_z dx' dy' \quad (12-117)$$

where  $S_a$  is the aperture of the antenna.  $\mathbf{E}(x', y', z' = 0)$  and  $\mathbf{H}(x', y', z' = 0)$  represent the total electric and magnetic fields at the aperture including those of the modes which operate below cutoff and contribute to the imaginary power. For the field distribution given by (12-115), (12-117) reduces to

$$P = -\frac{1}{2} \iint_{S_a} [E_y(x', y', z' = 0) H_x^*(x', y', z' = 0)] dx' dy' \quad (12-117a)$$

The amplitude coefficients of all modes that can exist within the waveguide, propagating and nonpropagating, can be evaluated provided the total tangential  $\mathbf{E}$ - and/or  $\mathbf{H}$ -field at any point within the waveguide is known. Assuming that (12-115) represents the total tangential  $\mathbf{E}$ -field, it allows the determination of all mode coefficients. Even though this can be accomplished, the formulation of (12-117a) in the spatial domain becomes rather complex [22].

An alternate and simpler method in the formulation of the aperture admittance is to use Fourier transforms. By Parseval's theorem of (12-72c), (12-117a) can be written as

$$\begin{aligned} P &= -\frac{1}{2} \int_{-\infty}^{+\infty} \int_{-\infty}^{+\infty} E_y(x', y', z' = 0) H_x^*(x', y', z' = 0) dx' dy' \\ &= -\frac{1}{8\pi^2} \int_{-\infty}^{+\infty} \int_{-\infty}^{+\infty} \mathcal{E}_y(k_x, k_y) \mathcal{H}_x^*(k_x, k_y) dk_x dk_y \end{aligned} \quad (12-118)$$

where the limits of the first integral have been extended to infinity since  $E_y(x', y', z' = 0)$  vanishes outside the physical bounds of the aperture.  $\mathcal{E}_y(k_x, k_y)$  and  $\mathcal{H}_x(k_x, k_y)$  are the Fourier transforms of the aperture  $E$ - and  $H$ -fields, respectively.

The transform  $\mathcal{E}(k_x, k_y, z = 0)$  is obtained from (12-78) while  $\mathcal{H}(k_x, k_y, z = 0)$  can be written, by referring to (12-89), as

$$\mathcal{H}(k_x, k_y, z = 0) = -\frac{1}{k\eta} (\mathbf{f} \times \mathbf{k}) \quad (12-119)$$

For the problem at hand, the transforms  $\mathcal{E}_y$  and  $\mathcal{H}_x$  are given by

$$\mathcal{E}_y(k_x, k_y) = f_y(k_x, k_y) \quad (12-120)$$

$$\mathcal{H}_x(k_x, k_y) = -\frac{1}{k\eta} \left( k_z + \frac{k_y^2}{k_z} \right) f_y = -\frac{1}{k\eta} \left( \frac{k^2 - k_x^2}{k_z} \right) f_y \quad (12-121)$$

Using (12-77b) and (12-115), (12-120) reduces to

$$f_y(k_x, k_y) = E_0 \int_{-b/2}^{+b/2} \int_{-a/2}^{+a/2} \cos\left(\frac{\pi}{a}x'\right) e^{j(k_x x' + k_y y')} dx' dy' \quad (12-122)$$

$$f_y(k_x, k_y) = \left(\frac{\pi ab}{2}\right) E_0 \left[ \frac{\cos X}{(\pi/2)^2 - (X)^2} \right] \left[ \frac{\sin Y}{Y} \right]$$

where

$$X = \frac{k_x a}{2} \quad (12-122a)$$

$$Y = \frac{k_y b}{2} \quad (12-122b)$$

Substituting (12-120)–(12-122b) into (12-118) leads to

$$P = \frac{(\pi ab E_0)^2}{32\pi^2 k\eta} \int_{-\infty}^{+\infty} \int_{-\infty}^{+\infty} \left\{ \frac{(k^2 - k_x^2)}{k_z^*} \left[ \frac{\cos X}{(\pi/2)^2 - (X)^2} \right]^2 \left[ \frac{\sin Y}{Y} \right]^2 \right\} dk_x dk_y \quad (12-123)$$

If the reference aperture voltage is given by

$$V = \frac{ab}{\sqrt{2}} E_0 \quad (12-124)$$

the aperture admittance can be written as

$$Y_a = \frac{2P^*}{|V|^2} = \frac{1}{8k\eta} \int_{-\infty}^{+\infty} \left\{ \left[ \frac{\sin\left(\frac{k_y b}{2}\right)}{\frac{k_y b}{2}} \right]^2 \int_{-\infty}^{+\infty} \frac{(k^2 - k_x^2)}{k_z} \right. \\ \left. \times \left[ \frac{\cos\left(\frac{k_x a}{2}\right)}{\left(\frac{\pi}{2}\right)^2 - \left(\frac{k_x a}{2}\right)^2} \right]^2 dk_x \right\} dk_y \quad (12-125)$$



where  $k_z$  is given by (12-80a) and (12-80b). As stated before, the values of  $k_z$  as given by (12-80a) contribute to the radiated (real) power and those of (12-80b) contribute to the reactive (imaginary) power. Referring to Figure 12.28, values of  $k_x$  and  $k_y$  within the circle contribute to the aperture conductance, and the space is referred to as the *visible region*. Values of  $k_x$  and  $k_y$  outside the circle contribute to the aperture susceptance and constitute the *invisible region*. Thus (12-125) can be separated into its real and imaginary parts, and it can be written as

$$Y_a = G_a + jB_a \quad (12-126)$$

$$G_a = \frac{1}{4k\eta} \int_0^k \left[ \frac{\sin\left(\frac{k_y b}{2}\right)}{\frac{k_y b}{2}} \right]^2 \left\{ \int_0^{\sqrt{k^2 - k_y^2}} \frac{(k^2 - k_x^2)}{[k^2 - (k_x^2 + k_y^2)]^{1/2}} \right. \\ \times \left. \left[ \frac{\cos\left(\frac{k_x a}{2}\right)}{\left(\frac{\pi}{2}\right)^2 - \left(\frac{k_x a}{2}\right)^2} \right]^2 dk_x \right\} dk_y \quad (12-126a)$$

$$B_a = -\frac{1}{4k\eta} \left\{ \int_0^k \left[ \frac{\sin\left(\frac{k_y b}{2}\right)}{\frac{k_y b}{2}} \right]^2 \left\{ \int_{\sqrt{k^2 - k_y^2}}^{\infty} \frac{(k_x^2 - k^2)}{[(k_x^2 + k_y^2) - k^2]^{1/2}} \right. \right. \\ \times \left. \left[ \frac{\cos\left(\frac{k_x a}{2}\right)}{\left(\frac{\pi}{2}\right)^2 - \left(\frac{k_x a}{2}\right)^2} \right]^2 dk_x \right\} dk_y \\ + \int_k^{\infty} \left[ \frac{\sin\left(\frac{k_y b}{2}\right)}{\frac{k_y b}{2}} \right]^2 \left\{ \int_0^{\infty} \frac{(k_x^2 - k^2)}{[(k_x^2 + k_y^2) - k^2]^{1/2}} \right. \\ \times \left. \left[ \frac{\cos\left(\frac{k_x a}{2}\right)}{\left(\frac{\pi}{2}\right)^2 - \left(\frac{k_x a}{2}\right)^2} \right]^2 dk_x \right\} dk_y \right\} \quad (12-126b)$$

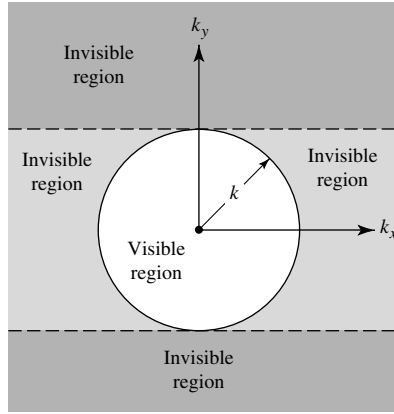


**Figure 12.28** Visible and invisible regions in  $k$ -space.

The first term in (12-126b) takes into account the contributions from the strip outside the circle for which  $k_y < k$ , and the second term includes the remaining space outside the circle.

The numerical evaluation of (12-126a) and (12-126b) is complex and will not be attempted here. Computations for the admittance of rectangular apertures radiating into lossless and lossy half spaces have been carried out and appear in the literature [23]–[27]. Various ingenious techniques have been used to evaluate these integrals.

Because of the complicated nature of (12-126a) and (12-126b) to obtain numerical data, a simpler configuration will be considered as an example.

### Example 12.8

A parallel plate waveguide (slot) is mounted on an infinite ground plane, as shown in Figure 12.29. Assuming the total electric field at the aperture is given by

$$\mathbf{E}_a = \hat{\mathbf{a}}_y E_0 \quad -b/2 \leq y' \leq b/2$$

where  $E_0$  is a constant, find the aperture admittance assuming the aperture voltage is given by  $V = bE_0$ .

*Solution:* This problem bears a very close similarity to that of Figure 12.26(a), and most of the results of this example can be obtained almost directly from the previous formulation. Since the problem is two-dimensional, (12-120)–(12-122) reduce to

$$\begin{aligned} \mathcal{E}_y(k_y) &= f_y(k_y) = bE_0 \frac{\sin\left(\frac{k_y b}{2}\right)}{\frac{k_y b}{2}} \\ \mathcal{H}_x(k_y) &= \frac{k}{\eta} \frac{f_y}{k_z} = \frac{kbE_0}{\eta k_z} \frac{\sin\left(\frac{k_y b}{2}\right)}{\frac{k_y b}{2}} \end{aligned}$$

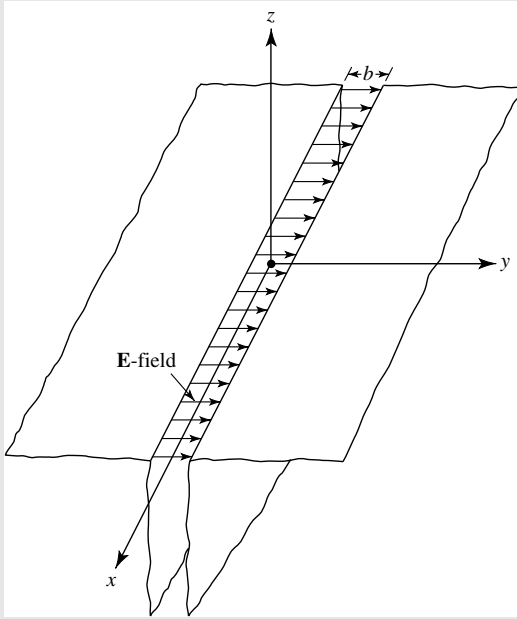


**Figure 12.29** Parallel-plate waveguide geometry and aperture field distribution.

and (12-123) to

$$P = \frac{(bE_0)^2 k}{4\pi\eta} \int_{-\infty}^{+\infty} \frac{1}{k_z^*} \left[ \frac{\sin\left(\frac{k_y b}{2}\right)}{\frac{k_y b}{2}} \right]^2 dk_y$$

Since the aperture voltage is given by  $V = bE_0$ , the aperture slot admittance (*per unit length along the  $x$  direction*) of (12-125) can be written as

$$Y_a = \frac{k}{2\pi\eta} \int_{-\infty}^{+\infty} \frac{1}{k_z} \left[ \frac{\sin\left(\frac{k_y b}{2}\right)}{\frac{k_y b}{2}} \right]^2 dk_y$$

and the aperture slot conductance and susceptance of (12-126a) and (12-126b) as

$$\begin{aligned} G_a &= \frac{k}{2\pi\eta} \int_{-k}^k \frac{1}{\sqrt{k^2 - k_y^2}} \left[ \frac{\sin\left(\frac{k_y b}{2}\right)}{\frac{k_y b}{2}} \right]^2 dk_y \\ &= \frac{k}{\pi\eta} \int_0^k \frac{1}{\sqrt{k^2 - k_y^2}} \left[ \frac{\sin\left(\frac{k_y b}{2}\right)}{\frac{k_y b}{2}} \right]^2 dk_y \end{aligned}$$

$$B_a = \frac{k}{2\pi\eta} \left\{ \int_{-\infty}^{-k} \frac{1}{\sqrt{k_y^2 - k^2}} \left[ \frac{\sin\left(\frac{k_y b}{2}\right)}{\frac{k_y b}{2}} \right]^2 dk_y + \int_k^{\infty} \frac{1}{\sqrt{k_y^2 - k^2}} \left[ \frac{\sin\left(\frac{k_y b}{2}\right)}{\frac{k_y b}{2}} \right]^2 dk_y \right\}$$

$$B_a = \frac{k}{\pi\eta} \int_k^{\infty} \frac{1}{\sqrt{k_y^2 - k^2}} \left[ \frac{\sin\left(\frac{k_y b}{2}\right)}{\frac{k_y b}{2}} \right]^2 dk_y$$

If

$$w = \frac{b}{2}k_y$$

the expressions for the slot conductance and susceptance reduce to

$$G_a = \frac{2}{\eta\lambda} \int_0^{kb/2} \frac{1}{\sqrt{(kb/2)^2 - w^2}} \left( \frac{\sin w}{w} \right)^2 dw$$

$$B_a = \frac{2}{\eta\lambda} \int_{kb/2}^{\infty} \frac{1}{\sqrt{w^2 - (kb/2)^2}} \left( \frac{\sin w}{w} \right)^2 dw$$

The admittance will always be capacitive since  $B_a$  is positive.

The expressions for the slot conductance and susceptance (*per unit length along the x direction*) reduce for small values of  $kb$  to [5]

$$\left. \begin{aligned} G_a &\simeq \frac{\pi}{\eta\lambda} \left[ 1 - \frac{(kb)^2}{24} \right] \\ B_a &\simeq \frac{\pi}{\eta\lambda} [1 - 0.636 \ln(kb)] \end{aligned} \right\} \frac{b}{\lambda} < \frac{1}{10}$$

and for large values of  $kb$  to

$$\left. \begin{aligned} G_a &\simeq \frac{1}{\eta b} \\ B_a &\simeq \frac{\lambda}{\eta} \left( \frac{1}{\pi b} \right)^2 \left[ 1 - \frac{1}{2} \sqrt{\frac{\lambda}{b}} \cos \left( \frac{2b}{\lambda} + \frac{1}{4} \right) \pi \right] \end{aligned} \right\} \frac{b}{\lambda} > 1$$

Normalized values of  $\lambda G_a$  and  $\lambda B_a$  as a function of  $b/\lambda$  for an aperture radiating into free space are shown plotted in Figure 12.30.

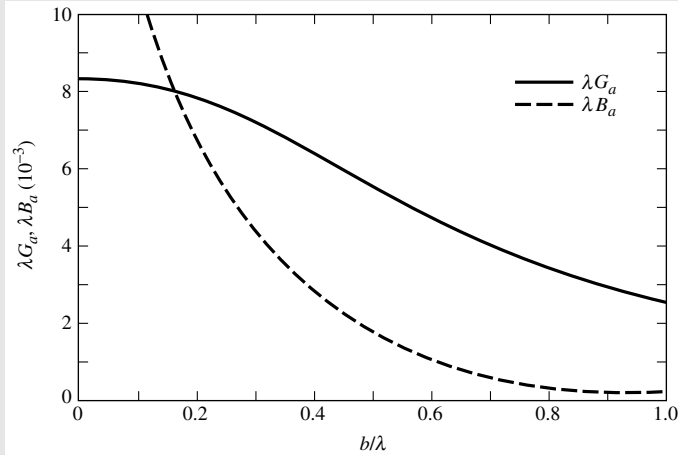


**Figure 12.30** Normalized values of conductance and susceptance of narrow slot.

## 12.10 GROUND PLANE EDGE EFFECTS: THE GEOMETRICAL THEORY OF DIFFRACTION

Infinite size (physically and/or electrically) ground planes are not realizable in practice, but they can be approximated closely by very large structures. The radiation characteristics of antennas (current distribution, pattern, impedance, etc.) mounted on finite size ground planes can be modified considerably, especially in regions of very low intensity, by the effects of the edges. The ground plane edge diffractions for an aperture antenna are illustrated graphically in Figure 12.31. For these problems, rigorous solutions do not exist unless the object's surface can be described by curvilinear coordinates. Presently there are two methods that can be used conveniently to account for the edge effects. One technique is the *Moment Method* (MM) [28] discussed in Chapter 8 and the other is the *Geometrical Theory of Diffraction* (GTD) [29].

The Moment Method describes the solution in the form of an integral, and it can be used to handle arbitrary shapes. It mostly requires the use of a digital computer for numerical computations and, because of capacity limitations of computers, it is most computationally efficient for objects that are small electrically. Therefore, it is usually referred to as a *low-frequency asymptotic method*.

When the dimensions of the radiating object are large compared to the wavelength, *high-frequency asymptotic techniques* can be used to analyze many otherwise not mathematically tractable problems. One such technique, which has received considerable attention in the past few years, is the *Geometrical Theory of Diffraction* (GTD) which was originally developed by Keller [29]. The GTD is an extension of the classical *Geometrical Optics* (GO; direct, reflected, and refracted rays), and it overcomes some of the limitations of GO by introducing a diffraction mechanism [2].

The diffracted field, which is determined by a generalization of Fermat's principle [2], [30], is initiated at points on the surface of the object where there is a discontinuity in the incident GO field (incident and reflected shadow boundaries). The

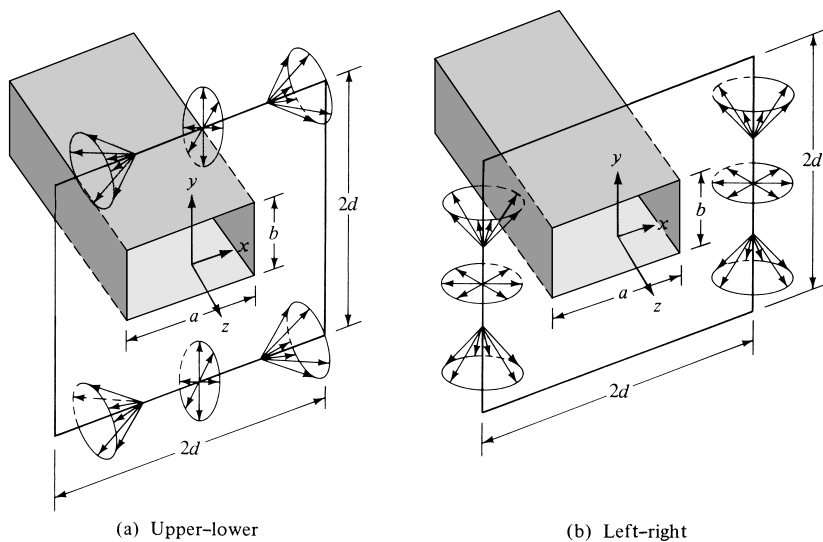


**Figure 12.31** Diffraction mechanisms for an aperture mounted on a finite size ground plane (diffractions at upper-lower and left-right edges of the ground plane).

phase of the field on a diffracted ray is assumed to be equal to the product of the optical length of the ray (from some reference point) and the phase constant of the medium. Appropriate phase jumps must be added as a ray passes through caustics.\* The amplitude is assumed to vary in accordance with the principle of conservation of energy in a narrow tube of rays. The initial value of the field on a diffracted ray is determined from the incident field with the aid of an appropriate diffraction coefficient (which, in general, is a dyadic for electromagnetic fields). The diffraction coefficient is usually determined from the asymptotic solutions of the simplest boundary-value problems which have the same local geometry at the points of diffraction as the object(s) of investigation. Geometries of this type are referred to as *canonical* problems. One of the simplest geometries is a conducting wedge [31], [32]. Another is that of a conducting, smooth, and convex surface [33]–[35].

The primary objective in using the GTD to solve complicated geometries is to resolve each such problem into smaller components [8]–[10], [35]. The partitioning is made so that each smaller component represents a canonical geometry of a known solution. These techniques have also been applied for the modeling and analysis of antennas on airplanes [36], and they have combined both wedge and smooth conducting surface diffractions [33], [35]. The ultimate solution is a superposition of the contributions from each canonical problem.

Some of the advantages of GTD are

1. It is simple to use.
2. It can be used to solve complicated problems that do not have exact solutions.

\*A caustic is a point or a line through which all the rays of a wave pass. Examples of it are the focal point of a paraboloid (parabola of revolution) and the focal line of a parabolic cylinder. The field at the caustic is infinite because, in principle, an infinite number of rays pass through it.

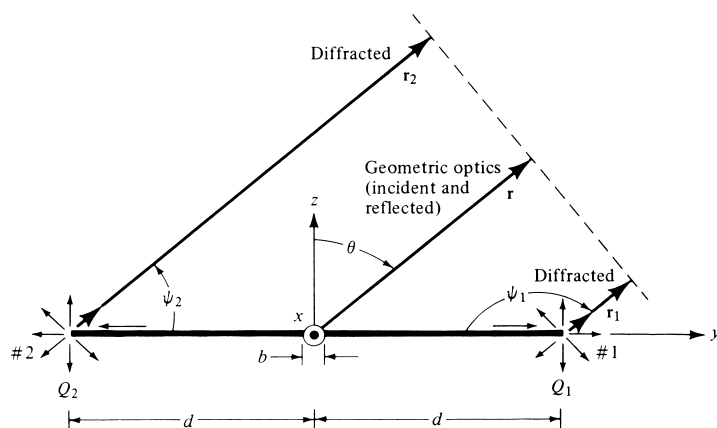


**Figure 12.32** Aperture geometry in principal  $E$ -plane ( $\phi = \pi/2$ ).

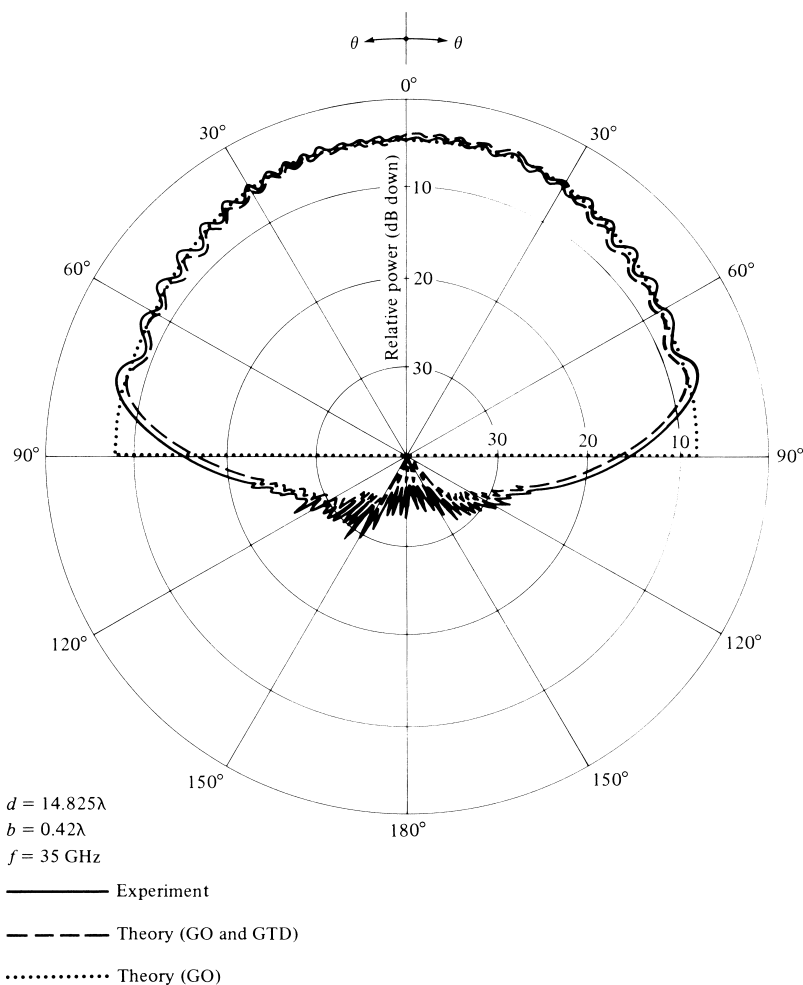


**Figure 12.33** Principal  $E$ -plane amplitude patterns of an aperture antenna mounted on a finite size ground plane.

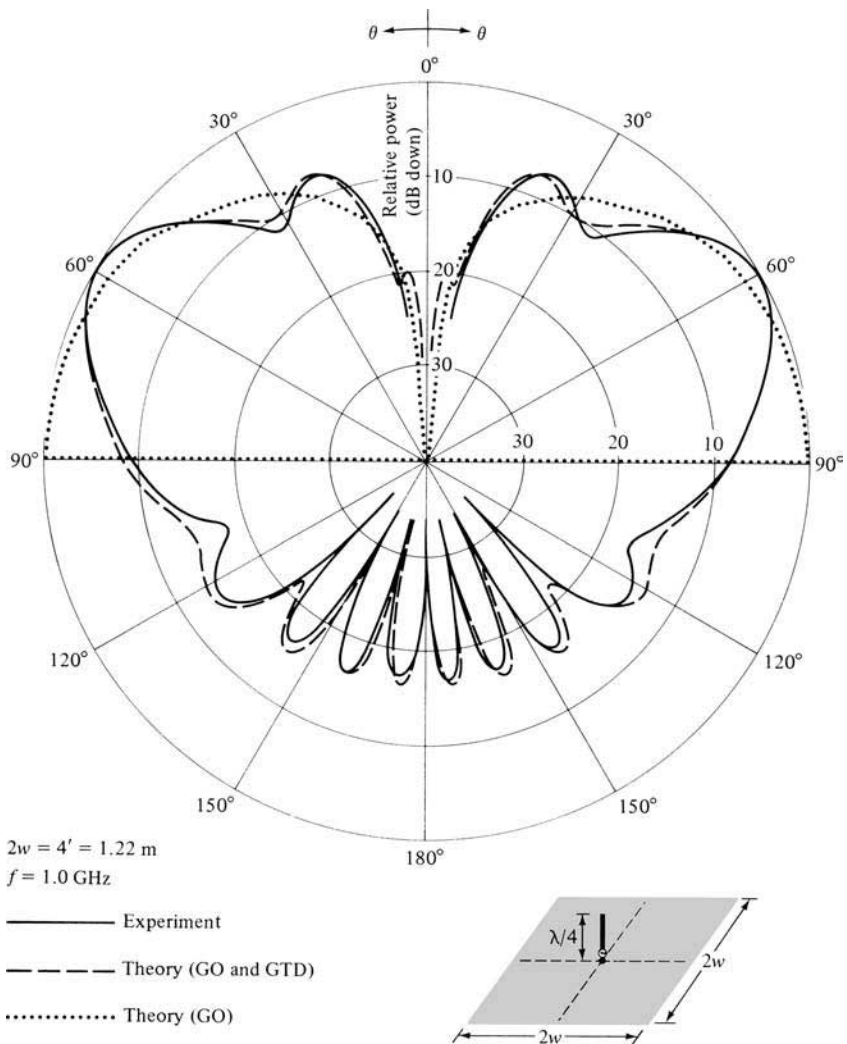


**Figure 12.34** Measured and computed principal elevation plane amplitude patterns of a  $\lambda/4$  monopole above infinite and finite square ground planes.

3. It provides physical insight into the radiation and scattering mechanisms from the various parts of the structure.
4. It yields accurate results which compare extremely well with experiments and other methods.
5. It can be combined with other techniques such as the Moment Method [37].

The derivation of the diffraction coefficients for a conducting wedge and their application are lengthy, and will not be repeated here. An extensive and detailed treatment of over 100 pages, for both antennas and scattering, can be found in [2]. However, to demonstrate the versatility and potential of the GTD, three examples are considered. The first is the  $E$ -plane pattern of a rectangular aperture of dimensions  $a, b$  mounted



on a finite size ground plane, as shown in Figure 12.31. The GTD formulation along the  $E$ -plane includes the direct radiation and the fields diffracted by the two edges of the ground plane, as shown in Figure 12.32. The computed  $E$ -plane pattern along with the measured one are shown in Figure 12.33; an excellent agreement is indicated.

The two other examples considered here are the elevation pattern of a  $\lambda/4$  monopole mounted on square and circular ground planes. The diffraction mechanism on the principal planes for these is the same as that of the aperture, which is shown in Figure 12.32. The corresponding principal elevation plane pattern of the monopole on the square ground plane is displayed in Figure 12.34 while that on the circular one is

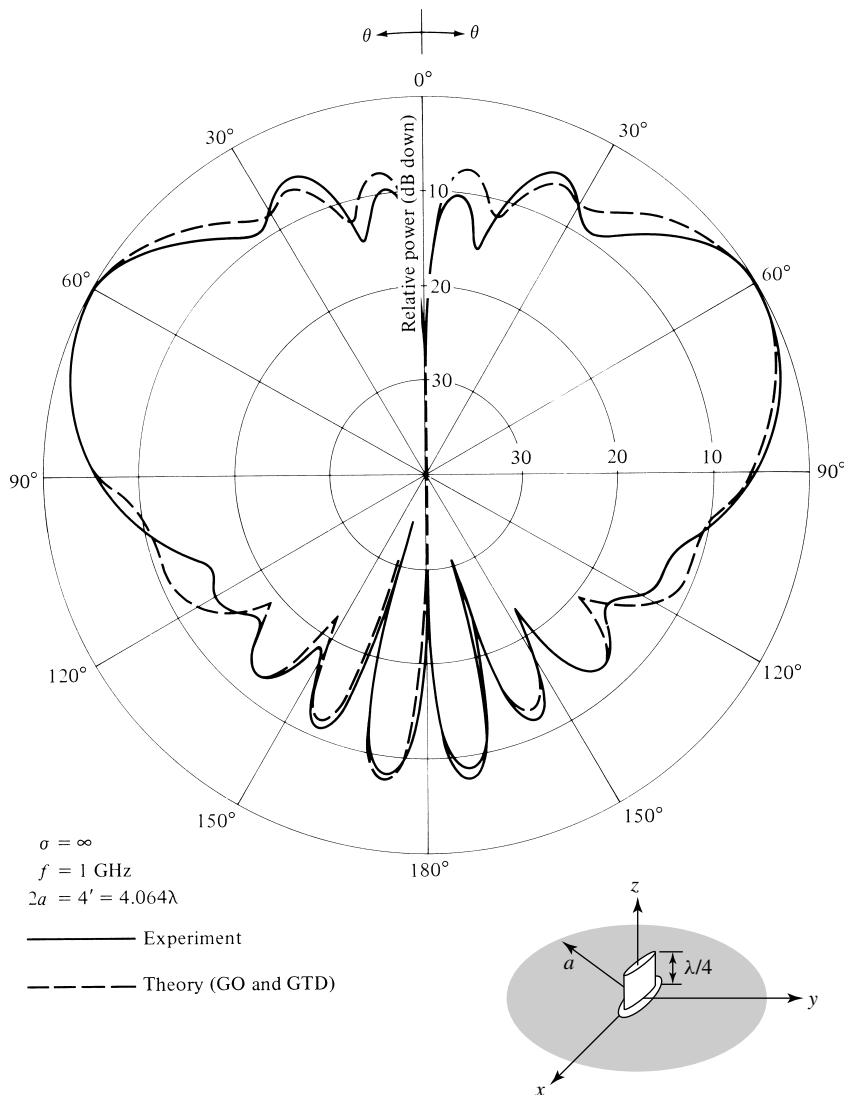


**Figure 12.35** Measured and computed principal elevation plane amplitude patterns of a  $\lambda/4$  monopole (blade) above a circular ground plane.

exhibited in Figure 12.35. For each case an excellent agreement is indicated with the measurements. It should be noted that the minor lobes near the symmetry axis ( $\theta = 0^\circ$  and  $\theta = 180^\circ$ ) for the circular ground plane of Figure 12.35 are more intense than the corresponding ones for the square ground plane of Figure 12.34. These effects are due to the ring-source radiation by the rim of the circular ground plane toward the symmetry axis [2], [10].

## 12.11 MULTIMEDIA

In the CD that is part of the book, the following multimedia resources are included for the review, understanding, and visualization of the material of this chapter:

- a. **Java-based interactive questionnaire**, with answers.
- b. **Matlab** computer program, designated *Aperture*, for computing and displaying the radiation characteristics of rectangular and circular apertures.
- c. **Power Point (PPT)** viewgraphs, in multicolor.

## REFERENCES

1. S. A. Schelkunoff, "Some Equivalence Theorems of Electromagnetics and Their Application to Radiation Problems," *Bell Syst. Tech. J.* Vol. 15, pp. 92–112, 1936.
2. C. A. Balanis, *Advanced Engineering Electromagnetics*, John Wiley and Sons, New York, 1989.
3. C. Huygens, *Traite de la Lumiere*, Leyden, 1690. Translated into English by S. P. Thompson, London, 1912, reprinted by The University of Chicago Press.
4. J. D. Kraus and K. R. Carver, *Electromagnetics* (second edition), McGraw-Hill, New York, 1973, pp. 464–467.
5. R. F. Harrington, *Time-Harmonic Electromagnetic Fields*, McGraw-Hill, New York, 1961, pp. 100–103, 143–263, 365–367.
6. A. E. H. Love, "The Integration of the Equations of Propagation of Electric Waves," *Philos. Trans. R. Soc. London, Ser. A*, Vol. 197, pp. 1–45, 1901.
7. R. Mittra (ed.), *Computer Techniques for Electromagnetics*, Pergamon Press, New York, 1973, pp. 9–13.
8. C. A. Balanis and L. Peters, Jr., "Equatorial Plane Pattern of an Axial-TEM Slot on a Finite Size Ground Plane," *IEEE Trans. Antennas Propagat.*, Vol. AP-17, No. 3, pp. 351–353, May 1969.
9. C. A. Balanis, "Pattern Distortion Due to Edge Diffractions," *IEEE Trans. Antennas Propagat.*, Vol. AP-18, No. 4, pp. 561–563, July 1970.
10. C. R. Cockrell and P. H. Pathak, "Diffraction Theory Techniques Applied to Aperture Antennas on Finite Circular and Square Ground Planes," *IEEE Trans. Antennas Propagat.*, Vol. AP-22, No. 3, pp. 443–448, May 1974.
11. D. G. Fink (ed.), *Electronics Engineers' Handbook*, Section 18 (Antennas by W. F. Croswell), McGraw-Hill, New York, 1975.
12. K. Praba, "Optimal Aperture for Maximum Edge-of-Coverage (EOC) Directivity," *IEEE Antennas Propagation Magazine*, Vol. 36, No. 3, pp. 72–74, June 1994.
13. H. G. Booker, "Slot Aerials and Their Relation to Complementary Wire Aerials," *J. Inst. Elect. Eng.*, part III A, pp. 620–626, 1946.

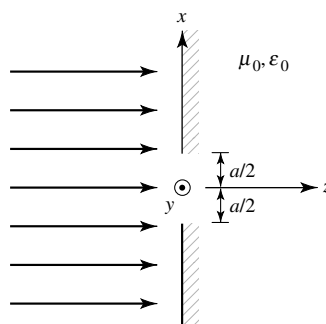
14. E. C. Jordan and K. G. Balmain, *Electromagnetic Waves and Radiating Systems*, Prentice-Hall, Inc., Englewood Cliffs, NJ, 1968.
15. J. D. Kraus, *Antennas*, Chapter 13, McGraw-Hill, New York, 1988.
16. H. G. Booker and P. C. Clemmow, "The Concept of an Angular Spectrum of Plane Waves, and its Relation to that of Polar Diagram and Aperture Distribution," *Proc. IEE (London)*, Vol. 97, part III, pp. 11–17, January 1950.
17. G. Borgiotti, "Fourier Transforms Method of Aperture Antennas," *Alta Freq.*, Vol. 32, pp. 196–204, November 1963.
18. L. B. Felsen and N. Marcuvitz, *Radiation and Scattering of Waves*, Prentice-Hall, Englewood Cliffs, NJ, 1973.
19. R. E. Collin and F. J. Zucker, *Antenna Theory: Part I*, Chapter 3, McGraw-Hill Book Co., New York, 1969.
20. C. M. Knop and G. I. Cohn, "Radiation from an Aperture in a Coated Plane," *Radio Sci. J. Res.*, Vol. 68D, No. 4, pp. 363–378, April 1964.
21. F. L. Whetten, "Dielectric Coated Meandering Leaky-Wave Long Slot Antennas," Ph.D. Dissertation, Arizona State University, May 1993.
22. M. H. Cohen, T. H. Crowley, and C. A. Lewis, "The Aperture Admittance of a Rectangular Waveguide Radiating Into Half-Space," Antenna Lab., Ohio State University, Rept. 339-22, Contract W 33-038 ac21114, November 14, 1951.
23. R. T. Compton, "The Admittance of Aperture Antennas Radiating Into Lossy Media," Antenna Lab., Ohio State University Research Foundation, Rept. 1691-5, March 15, 1964.
24. A. T. Villeneuve, "Admittance of a Waveguide Radiating into a Plasma Environment," *IEEE Trans. Antennas Propagat.*, Vol. AP-13, No. 1, pp. 115–121, January 1965.
25. J. Galejs, "Admittance of a Waveguide Radiating Into a Stratified Plasma," *IEEE Trans. Antennas Propagat.*, Vol. AP-13, No. 1, pp. 64–70, January 1965.
26. M. C. Bailey and C. T. Swift, "Input Admittance of a Circular Waveguide Aperture Covered by a Dielectric Slab," *IEEE Trans. Antennas Propagat.*, Vol. AP-16, No. 4, pp. 386–391, July 1968.
27. W. F. Croswell, W. C. Taylor, C. T. Swift, and C. R. Cockrell, "The Input Admittance of a Rectangular Waveguide-Fed Aperture Under an Inhomogeneous Plasma: Theory and Experiment," *IEEE Trans. Antennas Propagat.*, Vol. AP-16, No. 4, pp. 475–487, July 1968.
28. R. F. Harrington, *Field Computation by Moment Methods*, Macmillan Co., New York, 1968.
29. J. B. Keller, "Geometrical Theory of Diffraction," *Journal Optical Society of America*, Vol. 52, No. 2, pp. 116–130, February 1962.
30. R. G. Kouyoumjian, "The Geometrical Theory of Diffraction and Its Applications," in *Numerical and Asymptotic Techniques in Electromagnetics* (R. Mittra, ed.), Springer-Verlag, New York, 1975.
31. R. G. Kouyoumjian and P. H. Pathak, "A Uniform Geometrical Theory of Diffraction for an Edge in a Perfectly Conducting Surface," *Proc. IEEE*, Vol. 62, No. 11, pp. 1448–1461, November 1974.
32. D. L. Hutchins, "Asymptotic Series Describing the Diffraction of a Plane Wave by a Two-Dimensional Wedge of Arbitrary Angle," Ph.D. Dissertation, The Ohio State University, Dept. of Electrical Engineering, 1967.
33. P. H. Pathak and R. G. Kouyoumjian, "An Analysis of the Radiation from Apertures on Curved Surfaces by the Geometrical Theory of Diffraction," *Proc. IEEE*, Vol. 62, No. 11, pp. 1438–1447, November 1974.
34. G. L. James, *Geometrical Theory of Diffraction for Electromagnetic Waves*, Peter Peregrinus, Ltd., Stevenage, Herts., England, 1976.

35. C. A. Balanis and L. Peters, Jr., "Analysis of Aperture Radiation from an Axially Slotted Circular Conducting Cylinder Using GTD," *IEEE Trans. Antennas Propagat.*, Vol. AP-17, No. 1, pp. 93–97, January 1969.
36. C. A. Balanis and Y.-B. Cheng, "Antenna Radiation and Modeling for Microwave Landing System," *IEEE Trans. Antennas Propagat.*, Vol. AP-24, No. 4, pp. 490–497, July 1976.
37. W. D. Burnside, C. L. Yu, and R. J. Marhefka, "A Technique to Combine the Geometrical Theory of Diffraction and the Moment Method," *IEEE Trans. Antennas Propagat.*, Vol. AP-23, No. 4, pp. 551–558, July 1975.

## PROBLEMS

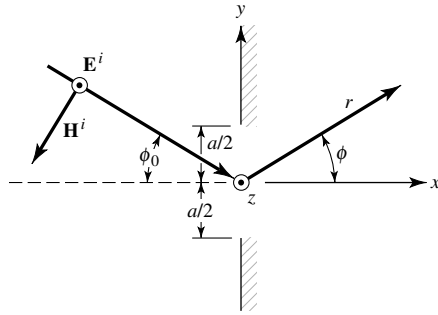
- 12.1.** A uniform plane wave traveling in the  $+z$  direction, whose magnetic field is expressed as

$$\mathbf{H}^i = \hat{\mathbf{a}}_y H_0 e^{-jkz} \quad z \leq 0$$



impinges upon an aperture on an infinite, flat, perfect electric conductor whose cross section is indicated in the figure.

- (a) State the equivalent that must be used to determine the field radiated by the aperture to the right of the conductor ( $z > 0$ ).
  - (b) Assuming the aperture dimension in the  $y$  direction is  $b$ , determine the far-zone fields for  $z > 0$ .
- 12.2.** Repeat Problem 12.1 when the incident magnetic field is polarized in the  $x$  direction.
- 12.3.** Repeat Problem 12.1 when the incident electric field is polarized in the  $y$  direction.
- 12.4.** Repeat Problem 12.1 when the incident electric field is polarized in the  $x$  direction.
- 12.5.** A perpendicularly polarized plane wave is obliquely incident upon an aperture, with dimension  $a$  and  $b$ , on a perfectly electric conducting ground plane of infinite extent, as shown in the figure. Assuming the field over the aperture is given by the incident field (ignore diffractions from the edges of the aperture), find the far-zone spherical components of the fields for  $x > 0$ .

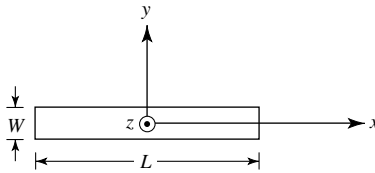


- 12.6.** Repeat Problem 12.5 for a parallelly polarized plane wave (when the incident magnetic field is polarized in the  $z$  direction, i.e., the incident magnetic field is perpendicular to the  $x$ - $y$  plane while the incident electric field is parallel to the  $x$ - $y$  plane).
- 12.7.** A narrow rectangular slot of size  $L$  by  $W$  is mounted on an infinite ground plane that covers the  $x$ - $y$  plane. The tangential field over the aperture is given by

$$\mathbf{E}_a = \hat{\mathbf{a}}_y E_0 e^{-jk_0 x' \sqrt{2}/2}$$

Using the equivalence principle and image theory, we can replace the aperture and infinite ground plane with an equivalent magnetic current radiating in free-space. Determine the

- appropriate equivalent
- far-zone spherical electric field components for  $z > 0$
- direction  $(\theta, \phi)$  in which the radiation intensity is maximum



- 12.8.** A rectangular aperture, of dimensions  $a$  and  $b$ , is mounted on an infinite ground plane, as shown in Figure 12.6(a). Assuming the tangential field over the aperture is given by

$$\mathbf{E}_a = \hat{\mathbf{a}}_z E_0 \quad -a/2 \leq y' \leq a/2, \quad -b/2 \leq z' \leq b/2$$

find the far-zone spherical electric and magnetic field components radiated by the aperture.

- 12.9.** Repeat Problem 12.8 when the same aperture is analyzed using the coordinate system of Figure 12.6(b). The tangential aperture field distribution is given by

$$\mathbf{E}_a = \hat{\mathbf{a}}_x E_0 \quad -b/2 \leq x' \leq b/2, \quad -a/2 \leq z' \leq a/2$$

**12.10.** Repeat Problem 12.8 when the aperture field is given by

$$\mathbf{E}_a = \hat{\mathbf{a}}_z E_0 \cos\left(\frac{\pi}{a} y'\right) \quad -a/2 \leq y' \leq a/2, \quad -b/2 \leq z' \leq b/2$$

**12.11.** Repeat Problem 12.9 when the aperture field distribution is given by

$$\mathbf{E}_a = \hat{\mathbf{a}}_x E_0 \cos\left(\frac{\pi}{a} z'\right) \quad -b/2 \leq x' \leq b/2, \quad -a/2 \leq z' \leq a/2$$

**12.12.** Find the fields radiated by the apertures of Problems

(a) 12.8 (b) 12.9

(c) 12.10 (d) 12.11

when each of the apertures with their associated field distributions are *not* mounted on a ground plane. Assume the tangential  $\mathbf{H}$ -field at the aperture is related to the  $\mathbf{E}$ -field by the intrinsic impedance.

**12.13.** Find the fields radiated by the rectangular aperture of Section 12.5.3 when it is not mounted on an infinite ground plane.

**12.14.** For the rectangular aperture of Section 12.5.3 (with  $a = 4\lambda$ ,  $b = 3\lambda$ ), compute the

(a)  $E$ -plane beamwidth (*in degrees*) between the maxima of the *second* minor lobe

(b)  $E$ -plane amplitude (*in dB*) of the maximum of the second minor lobe (relative to the maximum of the major lobe)

(c) approximate directivity of the antenna using Kraus' formula. Compare it with the value obtained using the expression in Table 12.1.

**12.15.** A rectangular  $X$ -band (8.2–12.4 GHz) waveguide (with inside dimensions of 0.9 in by 0.4 in) operating in the dominant  $\text{TE}_{10}$  mode at 10 GHz is mounted on an infinite ground plane and used as a receiving antenna. This antenna is connected to a matched lossless transmission line and a matched load is attached to the transmission line. Determine the:

(a) Directivity (*dimensionless* and *in dB*) using:

1. the most accurate formula that is available to you in class.

2. Kraus' formula.

(b) Maximum power (*in watts*) that can be delivered to the load when a uniform plane wave with a power density of  $10 \text{ mW/cm}^2$  is incident upon the antenna at normal incidence. Neglect any losses.

**12.16.** A lossless aperture antenna has a gain of 11 dB and overall physical area of  $2\lambda^2$ .

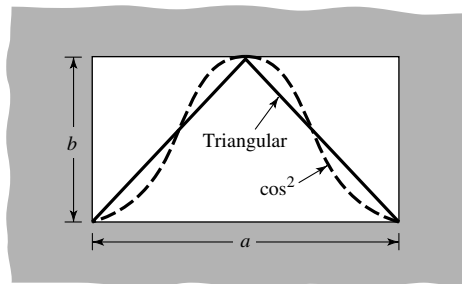
(a) What is the aperture efficiency of this antenna (*in %*)?

(b) Assuming the antenna is matched to a lossless transmission line that in turn is connected to a load that is also matched to the transmission line, what is the maximum power that can be delivered to the load if the incident power density at the antenna aperture is  $10 \times 10^{-3} \text{ watts/cm}^2$ ? The frequency of operation is 10 GHz.

- 12.17.** For the rectangular aperture of Section 12.5.1 with  $a = b = 3\lambda$ , compute the directivity using (12-37) and the *Aperture* computer program.
- 12.18.** For the rectangular aperture of Section 12.5.2 with  $a = b = 3\lambda$ , compute the directivity using (12-37) and the *Aperture* computer program.
- 12.19.** Compute the directivity of the aperture of Section 12.5.3, using the *Aperture* computer program, when  
 (a)  $a = 3\lambda, b = 2\lambda$  (b)  $a = b = 3\lambda$
- 12.20.** Repeat Problem 12.19 when the aperture is not mounted on an infinite ground plane.
- 12.21.** For the rectangular aperture of Section 12.5.3 with  $a = 3\lambda, b = 2\lambda$ , compute the  
 (a)  $E$ -plane half-power beamwidth  
 (b)  $H$ -plane half-power beamwidth  
 (c)  $E$ -plane first-null beamwidth  
 (d)  $H$ -plane first-null beamwidth  
 (e)  $E$ -plane first side lobe maximum (relative to main maximum)  
 (f)  $H$ -plane first side lobe maximum (relative to main maximum)  
 using the formulas of Table 12.1. Compare the results with the data from Figures 12.13 and 12.14. Verify using the computer program *Aperture*.
- 12.22.** A square waveguide aperture, of dimensions  $a = b$  and lying on the  $x$ - $y$  plane, is radiating into free-space. Assuming a  $\cos(\pi x'/a)$  by  $\cos(\pi y'/b)$  distribution over the aperture, find the dimensions of the aperture (in wavelengths) so that the beam efficiency within a  $37^\circ$  total included angle cone is 90%.
- 12.23.** Verify (12-39a), (12-39b), (12-39c), and (12-40).
- 12.24.** A rectangular aperture mounted on an infinite ground plane has aperture electric field distributions and corresponding efficiencies of

**FIELD DISTRIBUTION      APERTURE EFFICIENCY**

- |                   |        |
|-------------------|--------|
| (a) Triangular    | 75%    |
| (b) Cosine square | 66.67% |



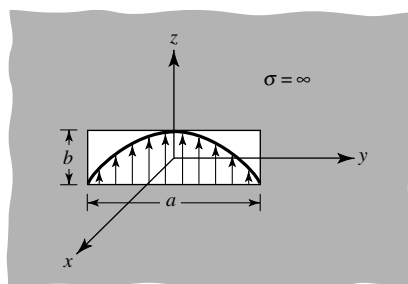
What are the corresponding directivities (in dB) if the dimensions of the aperture are  $a = \lambda/2$  and  $b = \lambda/4$ ?

- 12.25.** The physical area of an aperture antenna operating at 10 GHz is  $200 \text{ cm}^2$  while its directivity is 23 dB. Assuming the antenna has an overall radiation efficiency of 90% and it is perfectly matched to the input transmission line, find the aperture efficiency of the antenna.
- 12.26.** Two X-band (8.2–12.4 GHz) rectangular waveguides, each operating in the dominant  $\text{TE}_{10}$ -mode, are used, respectively, as transmitting and receiving antennas in a long distance communication system. The dimensions of each waveguide are  $a = 2.286 \text{ cm}$  (0.9 in.) and  $b = 1.016 \text{ cm}$  (0.4 in.) and the center frequency of operation is 10 GHz. Assuming the waveguides are separated by 10 kilometers and they are positioned for maximum radiation and reception toward each other, and the radiated power is 1 watt, find the:
- Incident power density at the receiving antenna
  - Maximum power that can be delivered to a matched load
- Assume the antennas are lossless, are polarization matched, and each is mounted on an infinite ground plane.
- 12.27.** The normalized far-zone electric field radiated in the  $E$ -plane ( $x$ - $z$  plane;  $\phi = 0^\circ$ ) by a waveguide aperture antenna of dimensions  $a$  and  $b$ , mounted on an infinite ground plane as shown in the figure, is given by

$$\mathbf{E} = -\hat{\mathbf{a}}_\theta j \frac{\omega \mu b I_0 e^{-jkr}}{4\pi r} \frac{\sin\left(\frac{kb}{2} \cos \theta\right)}{\frac{kb}{2} \cos \theta}$$

Determine in the  $E$ -plane the:

- Vector effective length of the antenna.
- Maximum value of the effective length.



State the value of  $\theta$  (in degrees) which maximizes the effective length.

- 12.28.** A uniform plane wave is incident upon an X-band rectangular waveguide, with dimensions of 2.286 cm and 1.016 cm, mounted on an infinite ground plane. Assuming the waveguide is operating in the dominant  $\text{TE}_{10}$  mode, determine the maximum power that can be delivered to a matched load. The frequency is 10 GHz and the power density of the incident plane wave is  $10^{-4} \text{ watts/m}^2$ .



- 12.29.** Compute the aperture efficiency of a rectangular aperture, mounted on an infinite ground plane as shown in Figure 12.7, with an **E**-field aperture distribution directed toward  $y$  but with variations
- triangular in the  $x$  and uniform in the  $y$
  - cosine-squared in the  $x$  and uniform in the  $y$
  - cosine in the  $x$  and cosine in the  $y$
  - cosine-squared in both the  $x$  and  $y$  directions.
- How do they compare with those of a cosine distribution?
- 12.30.** An X-band (8.2–12.4 GHz) WR 90 rectangular waveguide, with inner dimensions of 0.9 in. (2.286 cm) and 0.4 in. (1.016 cm), is mounted on an infinite ground plane. Assuming the waveguide is operating in the dominant  $TE_{10}$ -mode, find its directivity at  $f = 10$  GHz using the
- computer program *Aperture*
  - formula in Table 12.1
- Compare the answers.
- 12.31.** Repeat Problem 12.30 at  $f = 20$  GHz for a *K*-band (18–26.5 GHz) WR 42 rectangular waveguide with inner dimensions of 0.42 in. (1.067 cm) and 0.17 in. (0.432 cm).
- 12.32.** Four rectangular X-band waveguides of dimensions  $a = 0.9$  in. (2.286 cm) and  $b = 0.4$  in. (1.016 cm) and each operating on the dominant  $TE_{10}$ -mode, are mounted on an infinite ground plane so that their apertures and the ground plane coincide with the  $x$ - $y$  plane. The apertures form a linear array, are placed along the  $x$ -axis with a center-to-center separation of  $d = 0.85\lambda$  apart, and they are fed so that they form a broadside Dolph–Tschebyscheff array of  $-30$  dB minor lobes. Assuming a center frequency of 10 GHz, determine the overall directivity of the array in decibels.
- 12.33.** Sixty-four (64) X-band rectangular waveguides are mounted so that the aperture of each is mounted on an infinite ground plane that coincides with the  $x$ - $y$  plane, and all together form an  $8 \times 8 = 64$  planar array. Each waveguide has dimensions of  $a = 0.9$  in. (2.286 cm),  $b = 0.4$  in. (1.086 cm) and the center-to-center spacing between the waveguides is  $d_x = d_y = 0.85\lambda$ . Assuming a  $TE_{10}$ -mode operation for each waveguide, a center frequency of 10 GHz, and the waveguides are fed to form a *uniform* broadside planar array, find the directivity of the total array.
- 12.34.** Find the far-zone fields radiated when the circular aperture of Section 12.6.1 is not mounted on an infinite ground plane.
- 12.35.** Derive the far-zone fields when the circular aperture of Section 12.6.2
- is
  - is not
- mounted on an infinite ground plane.
- 12.36.** A circular waveguide (not mounted on a ground plane), operating in the dominant  $TE_{11}$  mode, is used as an antenna radiating in free-space. Write

in simplified form the normalized far-zone electric field components radiated by the waveguide antenna. You do not have to derive them.

- 12.37.** A circular waveguide of radius  $a = 1.125$  cm, NOT mounted on an infinite PEC ground plane and operating in the dominant  $TE_{11}$  mode at a frequency of 10 GHz, is used as a receiving antenna. On the basis of the *approximate equivalent*, determine the following:
- Far-zone electric and magnetic radiated fields (*you do not have to derive them*). Specify the angular limits (lower and higher *in degrees*) on the observation angles  $\theta$  and  $\phi$ .
  - Maximum power (*in watts*) that can be delivered to a receiver (load) assuming the receiver (load) is matched to the transmission line that connects the antenna and the receiver (load). Assume that the transmission line has a characteristic impedance of 300 ohms while the antenna has an input impedance of  $350 + j 400$  ohms. Assume no other losses. The maximum power density of the wave impinging upon the antenna is  $100 \text{ watts}/\text{m}^2$ .
- 12.38.** A lossless circular aperture antenna has a gain of 15 dB and overall physical area of  $25 \text{ cm}^2$ . The frequency of operation is 10 GHz.
- What is the aperture efficiency of the antenna (*in %*)?
  - What is the power  $P_L$  delivered to a matched load given that the power density of the incident wave at the antenna aperture is  $30 \text{ mW}/\text{cm}^2$ ? Assume ideal conditions (no losses).
- 12.39.** A *lossless* circular aperture antenna operating on the *dominant  $TE_{11}$ -mode* and mounted on an infinite ground plane has an overall *gain of 9 dB*. Determine the following:
- Physical area (*in  $\lambda^2$* ) of the antenna.
  - Maximum effective/equivalent area (*in  $\lambda^2$* ) of the antenna.
  - Aperture efficiency (*in percent*).
  - How much *more or less* efficient (*in percent*) is this antenna with a  *$TE_{11}$ -mode distribution* compared with the same antenna but with a *uniform field distribution* over its aperture. *State which one is more or less efficient.*
- 12.40.** For the circular aperture of Section 12.6.1, compute its directivity, using the *Aperture* computer program of this chapter, when its radius is
- $a = 0.5\lambda$
  - $a = 1.5\lambda$
  - $a = 3.0\lambda$
- Compare the results with data from Table 12.2.
- 12.41.** Repeat Problem 12.40 when the circular aperture of Section 12.6.1 is not mounted on an infinite ground plane. Compare the results with those of Problem 12.40.
- 12.42.** For the circular aperture of Problem 12.35, compute the directivity, using the *Aperture* computer program of this chapter, when its radius is
- $a = 0.5\lambda$
  - $a = 1.5\lambda$
  - $a = 3.0\lambda$
- Compare the results with data from Table 12.2.

- 12.43.** For the circular aperture of Section 12.6.2 with  $a = 1.5\lambda$ , compute the
- $E$ -plane half-power beamwidth
  - $H$ -plane half-power beamwidth
  - $E$ -plane first-null beamwidth
  - $H$ -plane first-null beamwidth
  - $E$ -plane first side lobe maximum (relative to main maximum)
  - $H$ -plane first side lobe maximum (relative to main maximum) using the formulas of Table 12.2. Compare the results with the data from Figures 12.19 and 12.20. Verify using the program *Aperture*.

- 12.44.** A circular aperture of radius  $a$  is mounted on an infinite electric ground plane. Assuming the opening is on the  $x$ - $y$  plane and its field distribution is given by

$$(a) \quad \mathbf{E}_a = \hat{\mathbf{a}}_y E_0 \left[ 1 - \left( \frac{\rho'}{a} \right)^2 \right], \quad \rho' \leq a$$

$$(b) \quad \mathbf{E}_a = \hat{\mathbf{a}}_y E_0 \left[ 1 - \left( \frac{\rho'}{a} \right)^2 \right]^2, \quad \rho' \leq a$$

find the far-zone electric and magnetic field components radiated by the antenna.

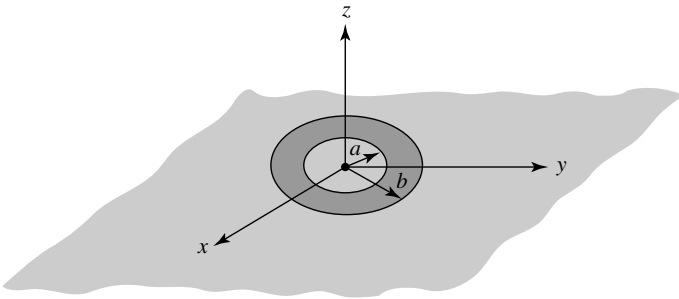
- 12.45.** Repeat Problem 12.44 when the electric field is given by

$$\mathbf{E}_a = \hat{\mathbf{a}}_y E_0 [1 - (\rho'/a)], \quad \rho' \leq a$$

Find only the radiation vectors  $\mathbf{L}$  and  $\mathbf{N}$ . Work as far as you can. If you find you cannot complete the solution in closed form, state clearly why you cannot. Simplify as much as possible.

- 12.46.** A coaxial line of inner and outer radii  $a$  and  $b$ , respectively, is mounted on an infinite electric ground plane. Assuming that the electric field over the aperture of the coax is

$$\mathbf{E}_a = -\hat{\mathbf{a}}_\rho \frac{V}{\epsilon \ln(b/a)} \frac{1}{\rho'}, \quad a \leq \rho' \leq b$$



where  $V$  is the applied voltage and  $\epsilon$  is the permittivity of the coax medium, find the far-zone spherical electric and magnetic field components radiated by the antenna.

- 12.47.** It is desired to design a circular aperture antenna with a field distribution over its opening of

$$E = C[1 - (\rho'/a)^2]$$

where  $C$  is a constant,  $a$  its radius, and  $\rho'$  any point on the aperture, such that its beam efficiency within a  $60^\circ$  total included angle cone is 90%. Find its radius in wavelengths.

- 12.48.** For the antenna of Problem 12.47, find its efficiency within a  $40^\circ$  total included angle cone when its radius is  $2\lambda$ .
- 12.49.** Design square apertures with uniform illumination so that the directivity at  $60^\circ$  from the normal is maximized relative to that at  $\theta = 0^\circ$ . Determine the:
- Dimensions of the aperture (*in  $\lambda$* )
  - Maximum directivity (*in dB*)
  - Directivity (*in dB*) at  $60^\circ$  from the maximum
- 12.50.** Design a circular aperture with uniform illumination so that the directivity at  $60^\circ$  from the normal is maximized relative to that at  $\theta = 0^\circ$ . Determine the
- Radius of the aperture (*in  $\lambda$* )
  - Maximum directivity (*in dB*)
  - Directivity (*in dB*) at  $60^\circ$  from the maximum
- 12.51.** Repeat Problem 12.50 for a circular aperture with a parabolic distribution.
- 12.52.** Repeat Problem 12.50 for a circular aperture with a parabolic taper on 10 dB pedestal.
- 12.53.** Derive the edge-of-coverage (EOC) design characteristics for a circular aperture with a parabolic taper.
- 12.54.** Design a rectangular aperture of uniform illumination so that its directivity in the  $E$ - and  $H$ -planes is maximized (relative to its maximum value), respectively, at angles of  $30^\circ$  and  $45^\circ$  from the normal to the aperture.
- Determine the optimum dimensions (*in  $\lambda$* ) of the aperture.
  - What is the *maximum* directivity (*in dB*) of the aperture and at what angle(s) (*in degrees*) will this occur?
  - What is the directivity (*in dB*) of the aperture along the  $E$ -plane at  $30^\circ$  from the normal to the aperture?
  - What is the directivity (*in dB*) of the aperture along the  $H$ -plane at  $45^\circ$  from the normal to the aperture?
- 12.55.** Design a circular aperture with *uniform* distribution so that its directivity at an angle  $\theta = 35^\circ$  from the normal to the aperture is maximized relative to its maximum value at  $\theta = 0^\circ$ . Specifically,

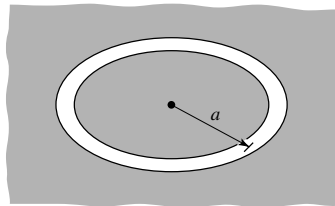
- (a) find the optimum radius (*in*  $\lambda$ ) of the aperture.
- (b) what is the maximum directivity (*in dB*) at  $\theta = 0^\circ$ ?
- (c) what is the directivity (*in dB*) at  $\theta = 35^\circ$ ?

**12.56.** A vertical dipole is radiating into a free-space medium and produces fields  $\mathbf{E}_0$  and  $\mathbf{H}_0$ . Illustrate alternate methods for obtaining the same fields using Babinet's principle and extensions of it.

**12.57.** (a) (1) Sketch the six principal-plane patterns, and (2) define the direction of  $\mathbf{E}$  and  $\mathbf{H}$  along the three principal axes and at  $45^\circ$  to the axes, for a thin slot one-half wavelength long, cut in a conducting sheet which has infinite conductivity and extending to infinity, and open on both sides. Inside dimensions of the slot are approximately  $0.5\lambda$  by  $0.1\lambda$ . Assume that the width ( $0.1\lambda$ ) of the slot is small compared to a wavelength. Assume a coordinate system such that the conducting plane lies on the  $x$ - $y$  plane with the larger dimension of the slot parallel to the  $y$ -axis.

(b) Sketch the six approximate principal-plane patterns  $E_\theta(\phi = 0^\circ)$ ,  $E_\phi(\phi = 0^\circ)$ ,  $E_\theta(\phi = 90^\circ)$ ,  $E_\phi(\phi = 90^\circ)$ ,  $E_\theta(\theta = 90^\circ)$ ,  $E_\phi(\theta = 90^\circ)$ .

**12.58.** A very thin circular annular slot with circumference of one wavelength is cut on a very thin, infinite, flat, perfectly electric conducting plate. The slot is radiating into free-space. What is the impedance (real and imaginary parts) of the slot?



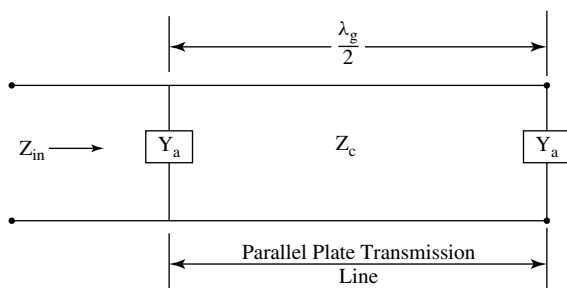
**12.59.** Repeat Example 12.7 for a rectangular aperture with an electric field distribution of

$$\mathbf{E}_a = \hat{\mathbf{a}}_y E_0 \cos\left(\frac{\pi}{a}x'\right), \quad \begin{array}{l} -a/2 \leq x' \leq a/2 \\ -b/2 \leq y' \leq b/2 \end{array}$$

**12.60.** Two identical very thin ( $b = \lambda/20$ ) parallel-plate waveguides (slots), *each mounted on an infinite ground plane*, as shown in Figure 12.29 of the book for one of them, are separated by a distance of  $\lambda_g/2$  where  $\lambda_g$  is the parallel-plate waveguide (transmission line) that is connecting the two slots. Assuming each slot is of width  $W = 10$  cm, the parallel-plate waveguide (transmission line) is filled with air, the slots are radiating in free-space and are operating at  $10$  GHz:

- (a) What is the admittance  $Y_a$  of *one slot in the absence of the other* (both real and imaginary parts)?

- (b) What is the total input impedance  $Z_{in}$  of both slots together when looking in at the input of one of them in the presence of the other (both real and imaginary parts)?



# CHAPTER 13



## Horn Antennas

### 13.1 INTRODUCTION

One of the simplest and probably the most widely used microwave antenna is the horn. Its existence and early use dates back to the late 1800s. Although neglected somewhat in the early 1900s, its revival began in the late 1930s from the interest in microwaves and waveguide transmission lines during the period of World War II. Since that time a number of articles have been written describing its radiation mechanism, optimization design methods, and applications. Many of the articles published since 1939 which deal with the fundamental theory, operating principles, and designs of a horn as a radiator can be found in a book of reprinted papers [1] and chapters in handbooks [2], [3].

The horn is widely used as a feed element for large radio astronomy, satellite tracking, and communication dishes found installed throughout the world. In addition to its utility as a feed for reflectors and lenses, it is a common element of phased arrays and serves as a universal standard for calibration and gain measurements of other high-gain antennas. Its widespread applicability stems from its simplicity in construction, ease of excitation, versatility, large gain, and preferred overall performance.

An electromagnetic horn can take many different forms, four of which are shown in Figure 13.1. The horn is nothing more than a hollow pipe of different cross sections, which has been tapered (flared) to a larger opening. The type, direction, and amount of taper (flare) can have a profound effect on the overall performance of the element as a radiator. In this chapter, the fundamental theory of horn antennas will be examined. In addition, data will be presented that can be used to understand better the operation of a horn and its design as an efficient radiator.

### 13.2 *E*-PLANE SECTORAL HORN

The *E*-plane sectoral horn is one whose opening is flared in the direction of the *E*-field, and it is shown in Figure 13.2(a). A more detailed geometry is shown in Figure 13.2(b).

\*Portions of this chapter on aperture-matched horns, multimode horns, and dielectric-loaded horns were first published by the author in [2], Copyright 1988, reprinted by permission of Van Nostrand Reinhold Co.

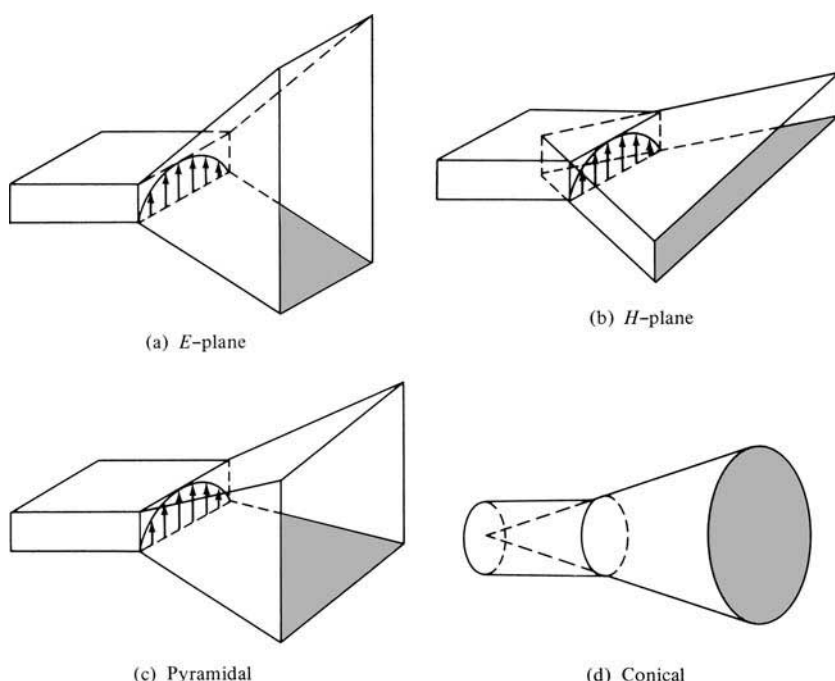


**Figure 13.1** Typical electromagnetic horn antenna configurations.

### 13.2.1 Aperture Fields

The horn can be treated as an aperture antenna. To find its radiation characteristics, the equivalent principle techniques developed in Chapter 12 can be utilized. To develop an exact equivalent of it, it is necessary that the tangential electric and magnetic field components over a closed surface are known. The closed surface that is usually selected is an infinite plane that coincides with the aperture of the horn. When the horn is not mounted on an infinite ground plane, the fields outside the aperture are not known and an exact equivalent cannot be formed. However, the usual approximation is to assume that the fields outside the aperture are zero, as was done for the aperture of Section 12.5.2.

The fields at the aperture of the horn can be found by treating the horn as a radial waveguide [4]–[6]. The fields within the horn can be expressed in terms of cylindrical TE and TM wave functions which include Hankel functions. This method finds the fields not only at the aperture of the horn but also within the horn. The process is straightforward but laborious, and it will not be included here. However, it is assigned as an exercise at the end of the chapter (Problem 13.1).

It can be shown that if the (1) fields of the feed waveguide are those of its dominant TE<sub>10</sub> mode and (2) horn length is large compared to the aperture dimensions, the lowest order mode fields at the aperture of the horn are given by

$$E'_z = E'_x = H'_y = 0 \quad (13-1a)$$

$$E'_y(x', y') \simeq E_1 \cos\left(\frac{\pi}{a}x'\right) e^{-j[ky'^2/(2\rho_1)]} \quad (13-1b)$$



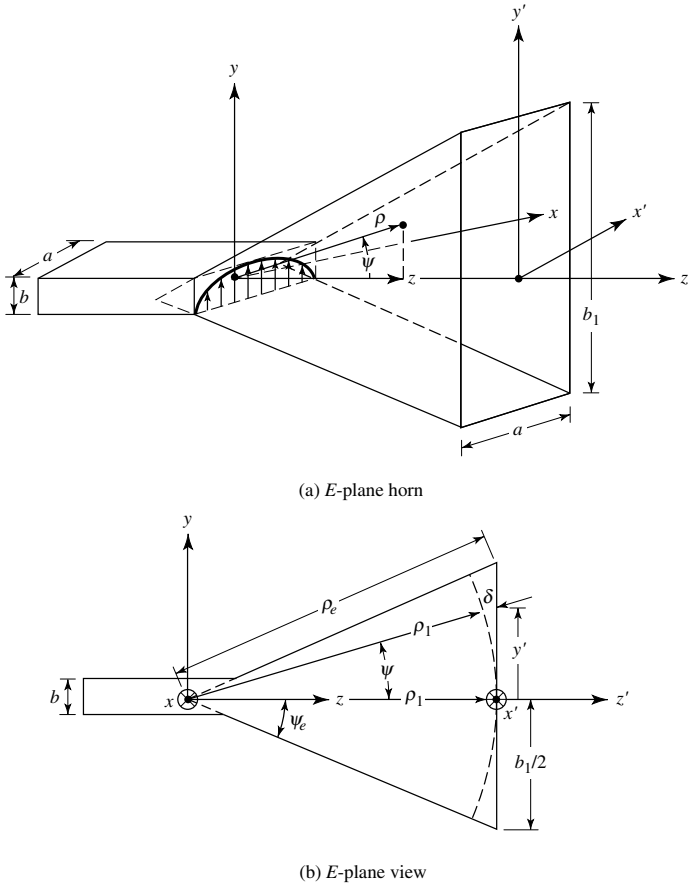


**Figure 13.2** E-plane horn and coordinate system.

$$H'_z(x', y') \simeq jE_1 \left( \frac{\pi}{kan\eta} \right) \sin \left( \frac{\pi}{a} x' \right) e^{-j[ky'^2/(2\rho_1)]} \quad (13-1c)$$

$$H'_x(x', y') \simeq -\frac{E_1}{\eta} \cos \left( \frac{\pi}{a} x' \right) e^{-j[ky'^2/(2\rho_1)]} \quad (13-1d)$$

$$\rho_1 = \rho_e \cos \psi_e \quad (13-1e)$$

where  $E_1$  is a constant. The primes are used to indicate the fields at the aperture of the horn. The expressions are similar to the fields of a  $TE_{10}$ -mode for a rectangular waveguide with aperture dimensions of  $a$  and  $b_1$  ( $b_1 > a$ ). The only difference is the complex exponential term which is used here to represent the quadratic phase variations of the fields over the aperture of the horn.

The necessity of the quadratic phase term in (13-1b)–(13-1d) can be illustrated geometrically. Referring to Figure 13.2(b), let us assume that at the imaginary apex of the horn (shown dashed) there exists a line source radiating cylindrical waves. As the waves travel in the outward radial direction, the constant phase fronts are cylindrical. At any point  $y'$  at the aperture of the horn, the phase of the field will not be the same as that at the origin ( $y' = 0$ ). The phase is different because the wave has traveled

different distances from the apex to the aperture. The difference in path of travel, designated as  $\delta(y')$ , can be obtained by referring to Figure 13.2(b). For any point  $y'$

$$[\rho_1 + \delta(y')]^2 = \rho_1^2 + (y')^2 \quad (13-2)$$

or

$$\delta(y') = -\rho_1 + [\rho_1^2 + (y')^2]^{1/2} = -\rho_1 + \rho_1 \left[ 1 + \left( \frac{y'}{\rho_1} \right)^2 \right]^{1/2} \quad (13-2a)$$

which is referred to as the *spherical* phase term.

Using the binomial expansion and retaining only the first two terms of it, (13-2a) reduces to

$$\delta(y') \simeq -\rho_1 + \rho_1 \left[ 1 + \frac{1}{2} \left( \frac{y'}{\rho_1} \right)^2 \right] = \frac{1}{2} \left( \frac{y'^2}{\rho_1} \right) \quad (13-2b)$$

when (13-2b) is multiplied by the phase factor  $k$ , the result is identical to the *quadratic* phase term in (13-1b)–(13-1d).

The quadratic phase variation for the fields of the dominant mode at the aperture of a horn antenna has been a standard for many years, and it has been chosen because it yields in most practical cases very good results. Because of its simplicity, it leads to closed form expressions, in terms of sine and cosine Fresnel integrals, for the radiation characteristics (far-zone fields, directivity, etc.) of the horn. It has been shown recently [7] that using the more accurate expression of (13-2a) for the phase, error variations and numerical integration yield basically the same directivities as using the approximate expression of (13-2b) for large aperture horns ( $b_1$  of Figures 13.2 or  $a_1$  of Figure 13.10 greater than  $50\lambda$ ) or small peak aperture phase error ( $S = \rho_e - \rho_1$  of Figure 13.2 or  $T = \rho_h - \rho_2$  of Figure 13.10 less than  $0.2\lambda$ ). However, for intermediate aperture sizes ( $5\lambda \leq b_1$  or  $a_1 \leq 8\lambda$ ) or intermediate peak aperture phase errors ( $0.2\lambda \leq S$  or  $T \leq 0.6\lambda$ ) the more accurate expression of (13-2a) for the phase variation yields directivities which are somewhat higher (by as much as a few tenths of a decibel) than those obtained using (13-2b). Also it has been shown using a full-wave Moment Method analysis of the horn [8] that as the horn dimensions become large the amplitude distribution at the aperture of the horn contains higher-order modes than the  $TE_{10}$  mode and the phase distribution at the aperture approaches the parabolic phase front.

### Example 13.1

Design an  $E$ -plane sectoral horn so that the maximum phase deviation at the aperture of the horn is  $56.72^\circ$ . The dimensions of the horn are  $a = 0.5\lambda$ ,  $b = 0.25\lambda$ ,  $b_1 = 2.75\lambda$ .

*Solution:* Using (13-2b)

$$\Delta\phi|_{\max} = k\delta(y')|_{y'=b_1/2} = \frac{k(b_1/2)^2}{2\rho_1} = 56.72 \left( \frac{\pi}{180} \right)$$

or

$$\rho_1 = \left( \frac{2.75}{2} \right)^2 \frac{180}{56.72} \lambda = 6\lambda$$

The total flare angle of the horn should be equal to

$$2\psi_e = 2 \tan^{-1} \left( \frac{b_1/2}{\rho_1} \right) = 2 \tan^{-1} \left( \frac{2.75/2}{6} \right) = 25.81^\circ$$

### 13.2.2 Radiated Fields

To find the fields radiated by the horn, only the tangential components of the **E**- and/or **H**-fields over a closed surface must be known. The closed surface is chosen to coincide with an infinite plane passing through the mouth of the horn. To solve for the fields, the approximate equivalent of Section 12.5.2 is used. That is,

$$\left. \begin{aligned} J_y &= -\frac{E_1}{\eta} \cos \left( \frac{\pi}{a} x' \right) e^{-jk\delta(y')} \\ M_x &= E_1 \cos \left( \frac{\pi}{a} x' \right) e^{-jk\delta(y')} \end{aligned} \right\} \begin{aligned} -a/2 \leq x' \leq a/2 \\ -b_1/2 \leq y' \leq b_1/2 \end{aligned} \quad (13-3)$$

and

$$\mathbf{J}_s = \mathbf{M}_s = 0 \quad \text{elsewhere} \quad (13-3a)$$

Using (12-12a)

$$N_\theta = -\frac{E_1}{\eta} \cos \theta \sin \phi I_1 I_2 \quad (13-4)$$

where

$$\begin{aligned} I_1 &= \int_{-a/2}^{+a/2} \cos \left( \frac{\pi}{a} x' \right) e^{jkx' \sin \theta \cos \phi} dx' \\ &= -\left( \frac{\pi a}{2} \right) \left[ \frac{\cos \left( \frac{ka}{2} \sin \theta \cos \phi \right)}{\left( \frac{ka}{2} \sin \theta \cos \phi \right)^2 - \left( \frac{\pi}{2} \right)^2} \right] \end{aligned} \quad (13-4a)$$

$$I_2 = \int_{-b_1/2}^{+b_1/2} e^{-jk[\delta(y') - y' \sin \theta \sin \phi]} dy' \quad (13-4b)$$

The integral of (13-4b) can also be evaluated in terms of cosine and sine Fresnel integrals. To do this,  $I_2$  can be written, by completing the square, as

$$I_2 = \int_{-b_1/2}^{+b_1/2} e^{-j[ky'^2/(2\rho_1) - k_y y']} dy' = e^{j(k_y^2 \rho_1 / 2k)} \int_{-b_1/2}^{+b_1/2} e^{-j[(ky' - k_y \rho_1)^2 / 2k\rho_1]} dy' \quad (13-5)$$

where

$$k_y = k \sin \theta \sin \phi \quad (13-5a)$$

Making a change of variable

$$\sqrt{\frac{\pi}{2}} t = \sqrt{\frac{1}{2k\rho_1}} (ky' - k_y \rho_1) \quad (13-6a)$$

$$t = \sqrt{\frac{1}{\pi k\rho_1}} (ky' - k_y \rho_1) \quad (13-6b)$$

$$dt = \sqrt{\frac{k}{\pi\rho_1}} dy' \quad (13-6c)$$

reduces (13-5) to

$$\begin{aligned} I_2 &= \sqrt{\frac{\pi\rho_1}{k}} e^{j(k_y^2 \rho_1 / 2k)} \int_{t_1}^{t_2} e^{-j(\pi/2)t^2} dt \\ &= \sqrt{\frac{\pi\rho_1}{k}} e^{j(k_y^2 \rho_1 / 2k)} \int_{t_1}^{t_2} \left[ \cos\left(\frac{\pi}{2}t^2\right) - j \sin\left(\frac{\pi}{2}t^2\right) \right] dt \end{aligned} \quad (13-7)$$

and takes the form of

$$I_2 = \sqrt{\frac{\pi\rho_1}{k}} e^{j(k_y^2 \rho_1 / 2k)} \{ [C(t_2) - C(t_1)] - j[S(t_2) - S(t_1)] \} \quad (13-8)$$

where

$$t_1 = \sqrt{\frac{1}{\pi k\rho_1}} \left( -\frac{kb_1}{2} - k_y \rho_1 \right) \quad (13-8a)$$

$$t_2 = \sqrt{\frac{1}{\pi k\rho_1}} \left( \frac{kb_1}{2} - k_y \rho_1 \right) \quad (13-8b)$$

$$C(x) = \int_0^x \cos\left(\frac{\pi}{2}t^2\right) dt \quad (13-8c)$$

$$S(x) = \int_0^x \sin\left(\frac{\pi}{2}t^2\right) dt \quad (13-8d)$$

$C(x)$  and  $S(x)$  are known as the cosine and sine Fresnel integrals and are well tabulated [9] (see Appendix IV). Computer subroutines are also available for efficient numerical evaluation of each [10], [11].

Using (13-4a) and (13-8), (13-4) can be written as

$$N_\theta = E_1 \frac{\pi a}{2} \sqrt{\frac{\pi \rho_1}{k}} e^{j(k_y^2 \rho_1 / 2k)} \times \left\{ \frac{\cos \theta \sin \phi}{\eta} \left[ \frac{\cos \left( \frac{k_x a}{2} \right)}{\left( \frac{k_x a}{2} \right)^2 - \left( \frac{\pi}{2} \right)^2} \right] F(t_1, t_2) \right\} \quad (13-9)$$

where

$$k_x = k \sin \theta \cos \phi \quad (13-9a)$$

$$k_y = k \sin \theta \sin \phi \quad (13-9b)$$

$$F(t_1, t_2) = [C(t_2) - C(t_1)] - j[S(t_2) - S(t_1)] \quad (13-9c)$$

In a similar manner,  $N_\phi$ ,  $L_\theta$ ,  $L_\phi$  of (12-12b)–(12-12d) reduce to

$$N_\phi = E_1 \frac{\pi a}{2} \sqrt{\frac{\pi \rho_1}{k}} e^{j(k_y^2 \rho_1 / 2k)} \left\{ \frac{\cos \phi}{\eta} \left[ \frac{\cos \left( \frac{k_x a}{2} \right)}{\left( \frac{k_x a}{2} \right)^2 - \left( \frac{\pi}{2} \right)^2} \right] F(t_1, t_2) \right\} \quad (13-10a)$$

$$L_\theta = E_1 \frac{\pi a}{2} \sqrt{\frac{\pi \rho_1}{k}} e^{j(k_y^2 \rho_1 / 2k)} \times \left\{ -\cos \theta \cos \phi \left[ \frac{\cos \left( \frac{k_x a}{2} \right)}{\left( \frac{k_x a}{2} \right)^2 - \left( \frac{\pi}{2} \right)^2} \right] F(t_1, t_2) \right\} \quad (13-10b)$$

$$L_\phi = E_1 \frac{\pi a}{2} \sqrt{\frac{\pi \rho_1}{k}} e^{j(k_y^2 \rho_1 / 2k)} \left\{ \sin \phi \left[ \frac{\cos \left( \frac{k_x a}{2} \right)}{\left( \frac{k_x a}{2} \right)^2 - \left( \frac{\pi}{2} \right)^2} \right] F(t_1, t_2) \right\} \quad (13-10c)$$

The electric field components radiated by the horn can be obtained by using (12-10a)–(12-10c), and (13-9)–(13-10c). Thus,

$$E_r = 0 \quad (13-11a)$$

$$E_\theta = -j \frac{a \sqrt{\pi k \rho_1} E_1 e^{-jkr}}{8r} \times \left\{ e^{j(k_y^2 \rho_1 / 2k)} \sin \phi (1 + \cos \theta) \left[ \frac{\cos \left( \frac{k_x a}{2} \right)}{\left( \frac{k_x a}{2} \right)^2 - \left( \frac{\pi}{2} \right)^2} \right] F(t_1, t_2) \right\} \quad (13-11b)$$

$$E_\phi = -j \frac{a\sqrt{\pi k \rho_1} E_1 e^{-jkr}}{8r} \times \left\{ e^{j(k_y^2 \rho_1 / 2k)} \cos \phi (\cos \theta + 1) \left[ \frac{\cos\left(\frac{k_x a}{2}\right)}{\left(\frac{k_x a}{2}\right)^2 - \left(\frac{\pi}{2}\right)^2} \right] F(t_1, t_2) \right\} \quad (13-11c)$$

where  $t_1$ ,  $t_2$ ,  $k_x$ ,  $k_y$ , and  $F(t_1, t_2)$  are given, respectively, by (13-8a), (13-8b), (13-9a), (13-9b), and (13-9c). The corresponding **H**-field components are obtained using (12-10d)–(12-10f).

In the principal  $E$ - and  $H$ -planes, the electric field reduces to

**$E$ -Plane ( $\phi = \pi/2$ )**

$$E_r = E_\phi = 0 \quad (13-12a)$$

$$E_\theta = -j \frac{a\sqrt{\pi k \rho_1} E_1 e^{-jkr}}{8r} \left\{ -e^{j(k \rho_1 \sin^2 \theta / 2)} \left( \frac{2}{\pi} \right)^2 (1 + \cos \theta) F(t'_1, t'_2) \right\} \quad (13-12b)$$

$$t'_1 = \sqrt{\frac{k}{\pi \rho_1}} \left( -\frac{b_1}{2} - \rho_1 \sin \theta \right) \quad (13-12c)$$

$$t'_2 = \sqrt{\frac{k}{\pi \rho_1}} \left( +\frac{b_1}{2} - \rho_1 \sin \theta \right) \quad (13-12d)$$

**$H$ -Plane ( $\phi = 0$ )**

$$E_r = E_\theta = 0 \quad (13-13a)$$

$$E_\phi = -j \frac{a\sqrt{\pi k \rho_1} E_1 e^{-jkr}}{8r} \left\{ (1 + \cos \theta) \left[ \frac{\cos\left(\frac{ka}{2} \sin \theta\right)}{\left(\frac{ka}{2} \sin \theta\right)^2 - \left(\frac{\pi}{2}\right)^2} \right] F(t''_1, t''_2) \right\} \quad (13-13b)$$

$$t''_1 = -\frac{b_1}{2} \sqrt{\frac{k}{\pi \rho_1}} \quad (13-13c)$$

$$t''_2 = +\frac{b_1}{2} \sqrt{\frac{k}{\pi \rho_1}} \quad (13-13d)$$

To better understand the performance of an  $E$ -plane sectoral horn and gain some insight into its performance as an efficient radiator, a three-dimensional normalized field pattern has been plotted in Figure 13.3 utilizing (13-11a)–(13-11c). As expected, the  $E$ -plane pattern is much narrower than the  $H$ -plane because of the flaring and larger

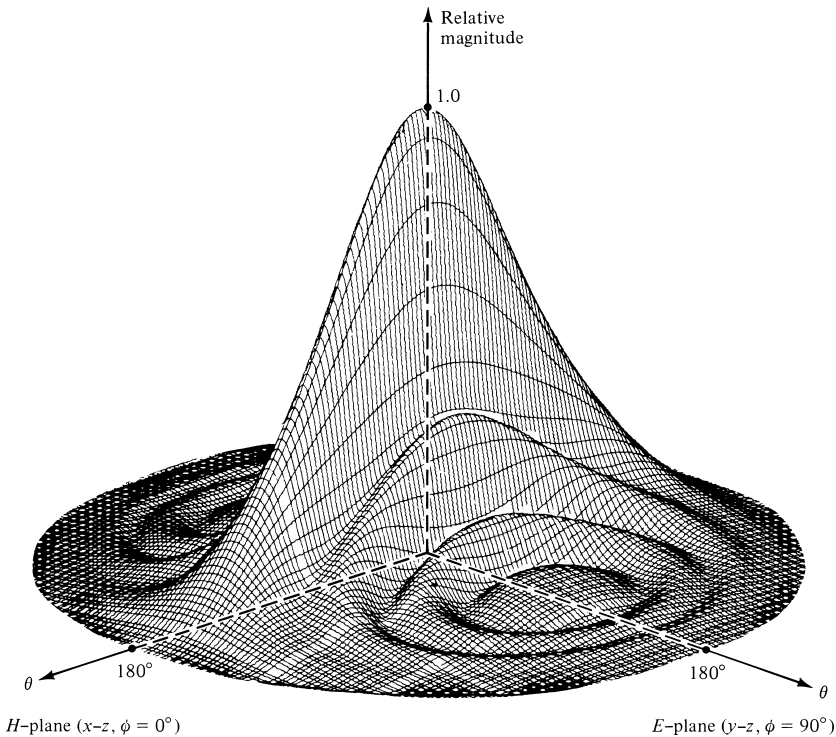


**Figure 13.3** Three-dimensional field pattern of *E*-plane sectoral horn ( $\rho_1 = 6\lambda$ ,  $b_1 = 2.75\lambda$ ,  $a = 0.5\lambda$ ).

dimensions of the horn in that direction. Figure 13.3 provides an excellent visual view of the overall radiation performance of the horn. To display additional details, the corresponding normalized *E*- and *H*-plane patterns (*in dB*) are illustrated in Figure 13.4. These patterns also illustrate the narrowness of the *E*-plane and provide information on the relative levels of the pattern in those two planes.

To examine the behavior of the pattern as a function of flaring, the *E*-plane patterns for a horn antenna with  $\rho_1 = 15\lambda$  and with flare angles of  $20^\circ \leq 2\psi_e \leq 35^\circ$  are plotted in Figure 13.5. A total of four patterns is illustrated. Since each pattern is symmetrical, only half of each pattern is displayed. For small included angles, the pattern becomes narrower as the flare increases. Eventually the pattern begins to widen, becomes flatter around the main lobe, and the phase tapering at the aperture is such that even the main maximum does not occur on axis. This is illustrated in Figure 13.5 by the pattern with  $2\psi_e = 35^\circ$ . As the flaring is extended beyond that point, the flatness (with certain allowable ripple) increases and eventually the main maximum returns again on axis. It is also observed that as the flaring increases, the pattern exhibits much sharper cutoff characteristics. In practice, to compensate for the phase taper at the opening, a lens is usually placed at the aperture making the pattern of the horn always narrower as its flare increases.

Similar pattern variations occur as the length of the horn is varied while the flare angle is held constant. As the length increases, the pattern begins to broaden and eventually becomes flatter (with a ripple). Beyond a certain length, the main maximum

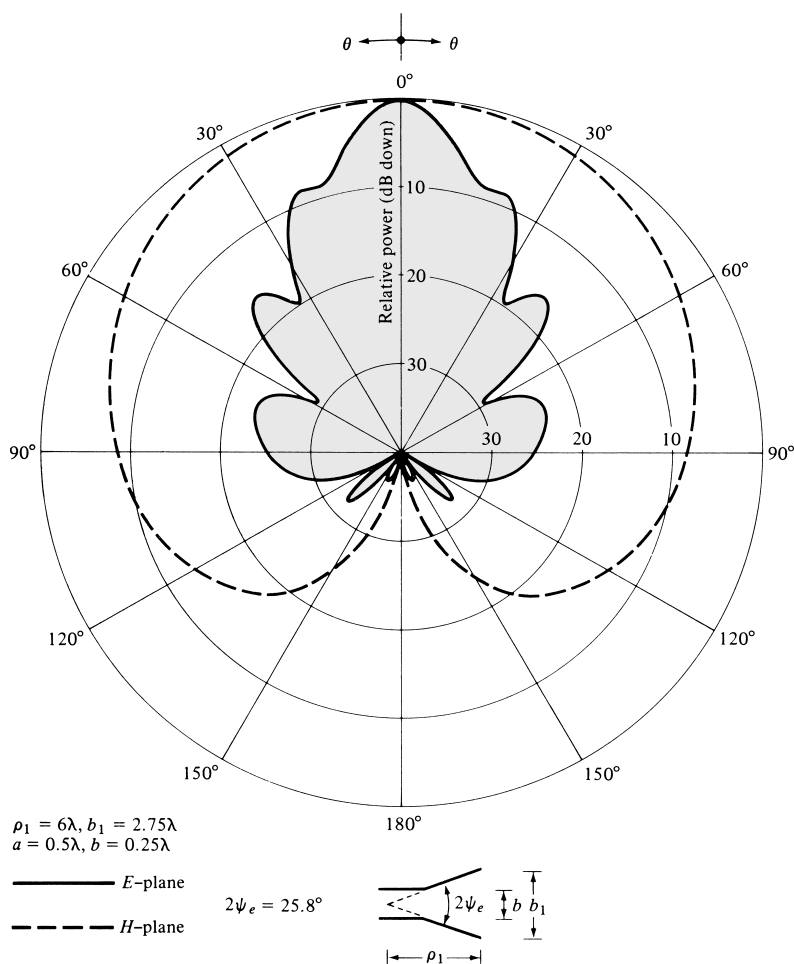


**Figure 13.4**  $E$ - and  $H$ -plane patterns of an  $E$ -plane sectoral horn.

does not even occur on axis, and the pattern continues to broaden and to become flatter (within an allowable ripple) until the maximum returns on axis. The process continues indefinitely.

An observation of the  $E$ -plane pattern, as given by (13-12a)–(13-12d), indicates that the *magnitude of the normalized pattern, excluding the factor  $(1 + \cos \theta)$* , can be written as

$$E_{\theta n} = F(t'_1, t'_2) = [C(t'_2) - C(t'_1)] - j[S(t'_2) - S(t'_1)] \quad (13-14a)$$

$$\begin{aligned}
 t'_1 &= \sqrt{\frac{k}{\pi \rho_1}} \left( -\frac{b_1}{2} - \rho_1 \sin \theta \right) = 2\sqrt{\frac{b_1^2}{8\lambda \rho_1}} \left[ -1 - \frac{1}{4} \left( \frac{8\rho_1 \lambda}{b_1^2} \right) \left( \frac{b_1}{\lambda} \sin \theta \right) \right] \\
 &= 2\sqrt{s} \left[ -1 - \frac{1}{4} \left( \frac{1}{s} \right) \left( \frac{b_1}{\lambda} \sin \theta \right) \right] \quad (13-14b)
 \end{aligned}$$



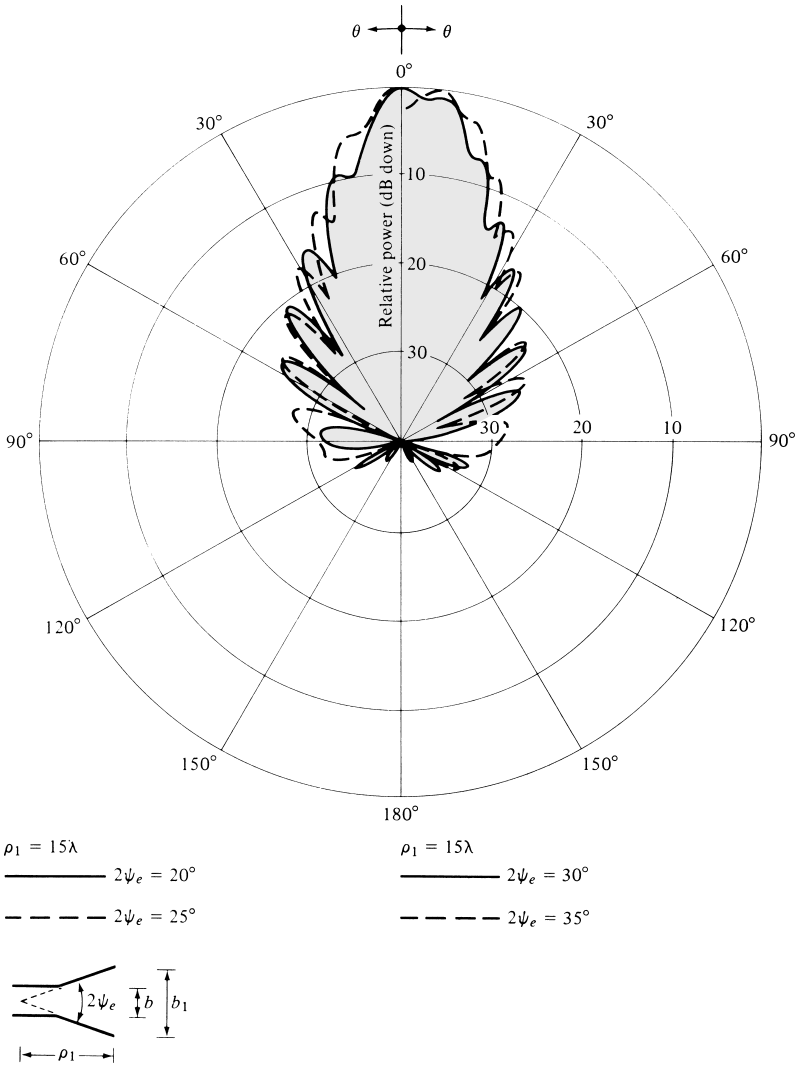


**Figure 13.5** E-plane patterns of E-plane sectoral horn for constant length and different included angles.

$$t'_2 = \sqrt{\frac{k}{\pi\rho_1}} \left( \frac{b_1}{2} - \rho_1 \sin \theta \right) = 2\sqrt{\frac{b_1^2}{8\lambda\rho_1}} \left[ 1 - \frac{1}{4} \left( \frac{8\rho_1\lambda}{b_1^2} \right) \left( \frac{b_1}{\lambda} \sin \theta \right) \right]$$

$$= 2\sqrt{s} \left[ 1 - \frac{1}{4} \left( \frac{1}{s} \right) \left( \frac{b_1}{\lambda} \sin \theta \right) \right] \quad (13-14c)$$

$$s = \frac{b_1^2}{8\lambda\rho_1} \quad (13-14d)$$

For a given value of  $s$ , the field of (13-14a) can be plotted as a function of  $b_1/\lambda \sin \theta$ , as shown in Figure 13.6 for  $s = \frac{1}{64}, \frac{1}{8}, \frac{1}{4}, \frac{1}{2}, \frac{3}{4}$ , and 1. These plots are usually referred to

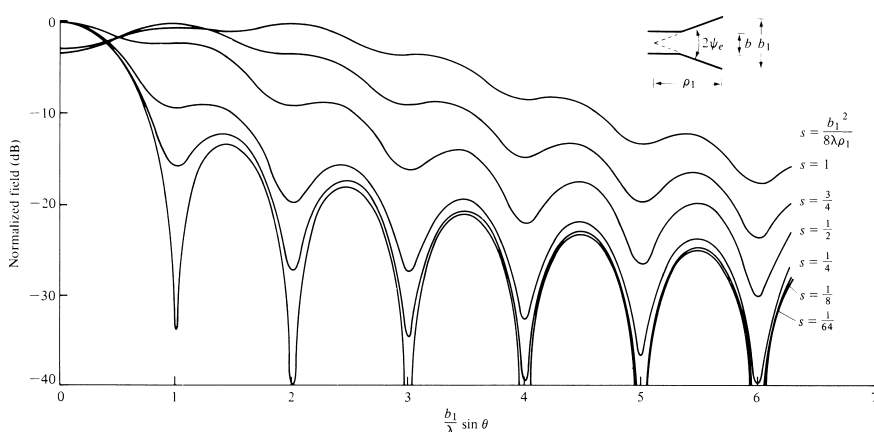


**Figure 13.6** *E*-plane universal patterns for *E*-plane sectoral and pyramidal horns.

as *universal curves*, because from them the normalized *E*-plane pattern of any *E*-plane sectoral horn can be obtained. This is accomplished by first determining the value of  $s$  from a given  $b_1$  and  $\rho_1$  by using (13-14d). For that value of  $s$ , the field strength (*in dB*) as a function of  $(b_1/\lambda) \sin \theta$  (or as a function of  $\theta$  for a given  $b_1$ ) is obtained from Figure 13.6. Finally the value of  $(1 + \cos \theta)$ , normalized to 0 dB and written as  $20 \log_{10}[(1 + \cos \theta)/2]$ , is added to that number to arrive at the required field strength.

### Example 13.2

An *E*-plane horn has dimensions of  $a = 0.5\lambda$ ,  $b = 0.25\lambda$ ,  $b_1 = 2.75\lambda$ , and  $\rho_1 = 6\lambda$ . Find its *E*-plane normalized field intensity (*in dB* and *as a voltage ratio*) at an angle of  $\theta = 90^\circ$  using the universal curves of Figure 13.6.

*Solution:* Using (13-14d)

$$s = \frac{b_1^2}{8\lambda\rho_1} = \frac{(2.75)^2}{8(6)} = 0.1575 \simeq \frac{1}{6.3}$$

None of the curves in Figure 13.6 represents  $s = \frac{1}{6.3}$ . Therefore interpolation will be used between the  $s = \frac{1}{4}$  and  $s = \frac{1}{8}$  curves.

At  $\theta = 90^\circ$

$$\frac{b_1}{\lambda} \sin(\theta) = 2.75 \sin(90^\circ) = 2.75$$

and at that point the field intensity between the  $s = \frac{1}{4}$  and  $s = \frac{1}{8}$  curves is about  $-20$  dB. Therefore the total field intensity at  $\theta = 90^\circ$  is equal to

$$E_\theta = -20 + 20 \log_{10} \left( \frac{1 + \cos 90^\circ}{2} \right) = -20 - 6 = -26 \text{ dB}$$

or as a normalized voltage ratio of

$$E_\theta = 0.05$$

which closely agrees with the results of Figure 13.4.

### 13.2.3 Directivity

The directivity is one of the parameters that is often used as a figure of merit to describe the performance of an antenna. To find the directivity, the maximum radiation is formed. That is,

$$U_{\max} = U(\theta, \phi)|_{\max} = \frac{r^2}{2\eta} |\mathbf{E}|_{\max}^2 \quad (13-15)$$

For most horn antennas  $|\mathbf{E}|_{\max}$  is directed nearly along the  $z$ -axis ( $\theta = 0^\circ$ ). Thus,

$$|\mathbf{E}|_{\max} = \sqrt{|E_\theta|_{\max}^2 + |E_\phi|_{\max}^2} = \frac{2a\sqrt{\pi k\rho_1}}{\pi^2 r} |E_1| |F(t)| \quad (13-16)$$

Using (13-11b), (13-11c), and (13-9c)

$$|E_\theta|_{\max} = \frac{2a\sqrt{\pi k\rho_1}}{\pi^2 r} |E_1 \sin \phi F(t)| \quad (13-16a)$$

$$|E_\phi|_{\max} = \frac{2a\sqrt{\pi k\rho_1}}{\pi^2 r} |E_1 \cos \phi F(t)| \quad (13-16b)$$

$$F(t) = [C(t) - jS(t)] \quad (13-16c)$$

$$t = \frac{b_1}{2} \sqrt{\frac{k}{\pi\rho_1}} = \frac{b_1}{\sqrt{2\lambda\rho_1}} \quad (13-16d)$$

since

$$k_x = k_y = 0 \quad (13-16e)$$

$$t_1 = -t = -\frac{b_1}{2} \sqrt{\frac{k}{\pi\rho_1}} = -\frac{b_1}{\sqrt{2\lambda\rho_1}} \quad (13-16f)$$

$$t_2 = +t = +\frac{b_1}{2} \sqrt{\frac{k}{\pi\rho_1}} = \frac{b_1}{\sqrt{2\lambda\rho_1}} \quad (13-16g)$$

$$C(-t) = -C(t) \quad (13-16h)$$

$$S(-t) = -S(t) \quad (13-16i)$$

Thus

$$\begin{aligned} U_{\max} &= \frac{r^2}{2\eta} |\mathbf{E}|_{\max}^2 = \frac{2a^2 k\rho_1}{\eta\pi^3} |E_1|^2 |F(t)|^2 \\ &= \frac{4a^2 \rho_1 |E_1|^2}{\eta\lambda\pi^2} |F(t)|^2 \end{aligned} \quad (13-17)$$

where

$$|F(t)|^2 = \left[ C^2 \left( \frac{b_1}{\sqrt{2\lambda\rho_1}} \right) + S^2 \left( \frac{b_1}{\sqrt{2\lambda\rho_1}} \right) \right] \quad (13-17a)$$

The total power radiated can be found by simply integrating the average power density over the aperture of the horn. Using (13-1a)–(13-1d)

$$P_{\text{rad}} = \frac{1}{2} \iint_{S_0} \text{Re}(\mathbf{E}' \times \mathbf{H}'^*) \cdot d\mathbf{s} = \frac{1}{2\eta} \int_{-b_1/2}^{+b_1/2} \int_{-a/2}^{+a/2} |E_1|^2 \cos^2\left(\frac{\pi}{a}x'\right) dx' dy' \quad (13-18)$$

which reduces to

$$P_{\text{rad}} = |E_1|^2 \frac{b_1 a}{4\eta} \quad (13-18a)$$

Using (13-17) and (13-18a), the directivity for the  $E$ -plane horn can be written as

$$\begin{aligned} D_E &= \frac{4\pi U_{\text{max}}}{P_{\text{rad}}} = \frac{64a\rho_1}{\pi\lambda b_1} |F(t)|^2 \\ &= \frac{64a\rho_1}{\pi\lambda b_1} \left[ C^2 \left( \frac{b_1}{\sqrt{2\lambda\rho_1}} \right) + S^2 \left( \frac{b_1}{\sqrt{2\lambda\rho_1}} \right) \right] \end{aligned} \quad (13-19)$$

The overall performance of an antenna system can often be judged by its beamwidth and/or its directivity. The half-power beamwidth (HPBW), as a function of flare angle, for different horn lengths is shown in Figure 13.7. In addition, the directivity (normalized with respect to the constant aperture dimension  $a$ ) is displayed in Figure 13.8. For a given length, the horn exhibits a monotonic decrease in half-power beamwidth and an increase in directivity up to a certain flare. Beyond that point a monotonic increase in beamwidth and decrease in directivity is indicated followed by rises and falls. The increase in beamwidth and decrease in directivity beyond a certain flare indicate the broadening of the main beam.

If the values of  $b_1$  (*in*  $\lambda$ ), which correspond to the maximum directivities in Figure 13.8, are plotted versus their corresponding values of  $\rho_1$  (*in*  $\lambda$ ), it can be shown that each optimum directivity occurs when

$$b_1 \simeq \sqrt{2\lambda\rho_1} \quad (13-19a)$$

with a corresponding value of  $s$  equal to

$$s|_{b_1} = \sqrt{2\lambda\rho_1} = s_{op} = \left. \frac{b_1^2}{8\lambda\rho_1} \right|_{b_1=\sqrt{2\lambda\rho_1}} = \frac{1}{4} \quad (13-19b)$$

The classic expression of (13-19) for the directivity of an  $E$ -plane horn has been the standard for many years. However, it has been shown that this expression may not always yield very accurate values for the on-axis directivity. A more accurate expression for the maximum on-axis directivity based on an exact open-ended parallel-plate waveguide analysis has been derived, and it yields a modification to the on-axis value of (13-19), which provides sufficient accuracy for most designs [12], [13]. Using (13-19a), the modified formula for the on-axis value of (13-19) can be written as [12], [13]

$$D_E(\text{max}) = \frac{16ab_1}{\lambda^2(1 + \lambda_g/\lambda)} \left[ C^2 \left( \frac{b_1}{\sqrt{2\lambda\rho_1}} \right) + S^2 \left( \frac{b_1}{\sqrt{2\lambda\rho_1}} \right) \right] e^{\frac{\pi a}{\lambda} \left( 1 - \frac{\lambda}{\lambda_g} \right)} \quad (13-19c)$$

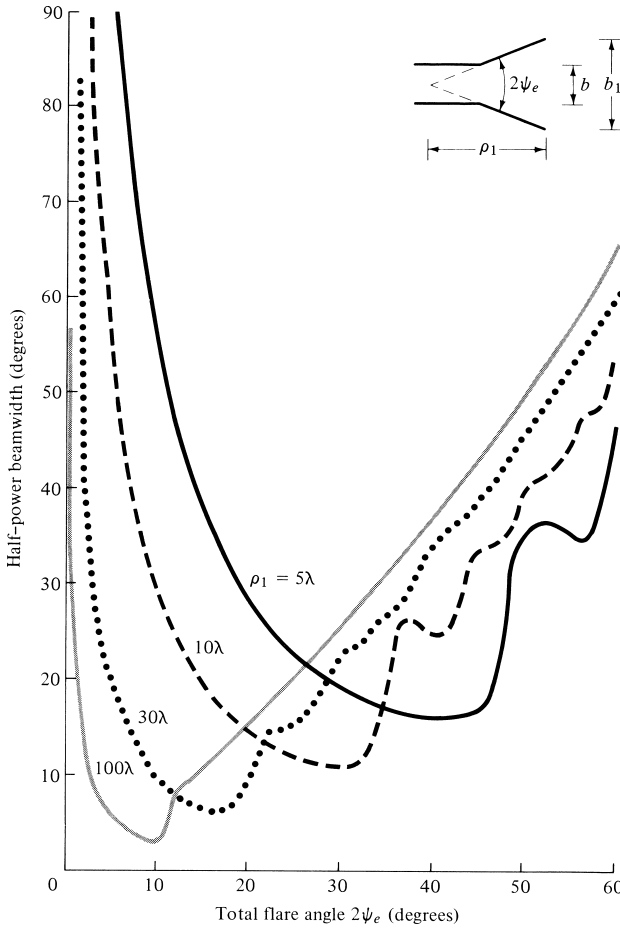


**Figure 13.7** Half-power beamwidth of *E*-plane sectoral horn as a function of included angle and for different lengths.

where  $\lambda_g$  is the guide wavelength in the feed waveguide for the dominant  $TE_{10}$  mode. Predicted values based on (13-19) and (13-19c) have been compared with measurements and it was found that (13-19c) yielded results which were closer to the measured values [12].

The directivity of an *E*-plane sectoral horn can also be computed by using the following procedure [14].

1. Calculate  $B$  by

$$B = \frac{b_1}{\lambda} \sqrt{\frac{50}{\rho_e/\lambda}} \quad (13-20a)$$

2. Using this value of  $B$ , find the corresponding value of  $G_E$  from Figure 13.9. If, however, the value of  $B$  is smaller than 2, compute  $G_E$  using

$$G_E = \frac{32}{\pi} B \quad (13-20b)$$

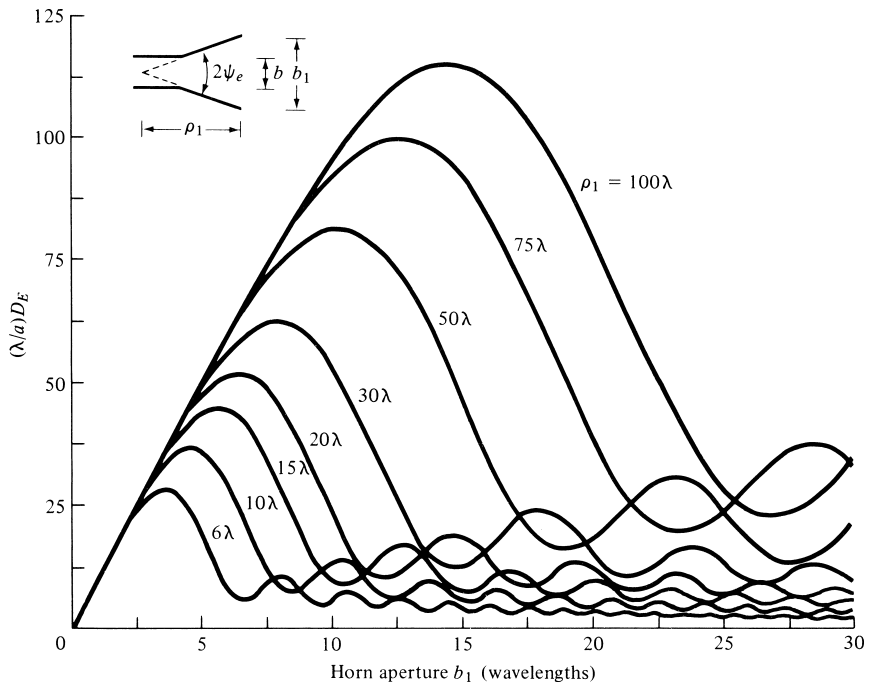


**Figure 13.8** Normalized directivity of  $E$ -plane sectoral horn as a function of aperture size and for different lengths.

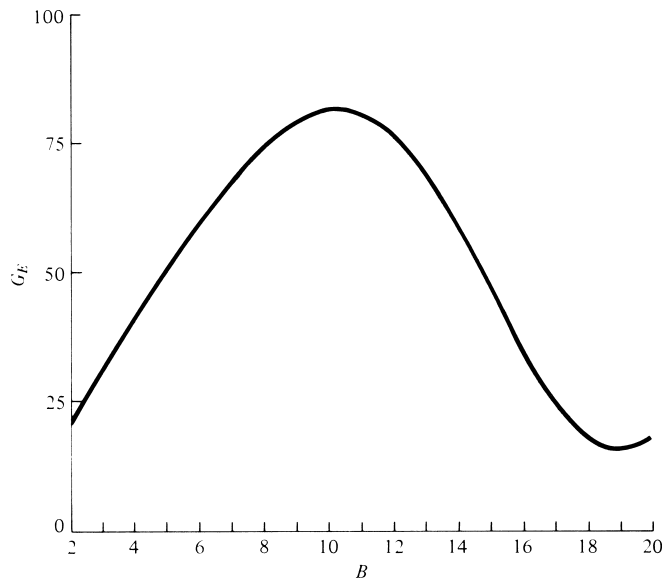


**Figure 13.9**  $G_E$  as a function of  $B$ . (SOURCE: Adopted from data by E. H. Braun, "Some Data for the Design of Electromagnetic Horns," *IRE Trans. Antennas Propagat.*, Vol. AP-4, No. 1, January 1956. © 1956 IEEE)

3. Calculate  $D_E$  by using the value of  $G_E$  from Figure 13.9 or from (13-20b). Thus

$$D_E = \frac{a}{\lambda} \frac{G_E}{\sqrt{\frac{50}{\rho_e/\lambda}}} \quad (13-20c)$$

### Example 13.3

An  $E$ -plane sectoral horn has dimensions of  $a = 0.5\lambda$ ,  $b = 0.25\lambda$ ,  $b_1 = 2.75\lambda$ , and  $\rho_1 = 6\lambda$ . Compute the directivity using (13-19) and (13-20c). Compare the answers.

*Solution:* For this horn

$$\frac{b_1}{\sqrt{2\lambda\rho_1}} = \frac{2.75}{\sqrt{2(6)}} = 0.794$$

Therefore (from Appendix IV)

$$[C(0.794)]^2 = (0.72)^2 = 0.518$$

$$[S(0.794)]^2 = (0.24)^2 = 0.0576$$

Using (13-19)

$$D_E = \frac{64(0.5)6}{2.75\pi}(0.518 + 0.0576) = 12.79 = 11.07 \text{ dB}$$

To compute the directivity using (13-20c), the following parameters are evaluated:

$$\rho_e = \lambda \sqrt{(6)^2 + \left(\frac{2.75}{2}\right)^2} = 6.1555\lambda$$

$$\sqrt{\frac{50}{\rho_e/\lambda}} = \sqrt{\frac{50}{6.1555}} = 2.85$$

$$B = 2.75(2.85) = 7.84$$

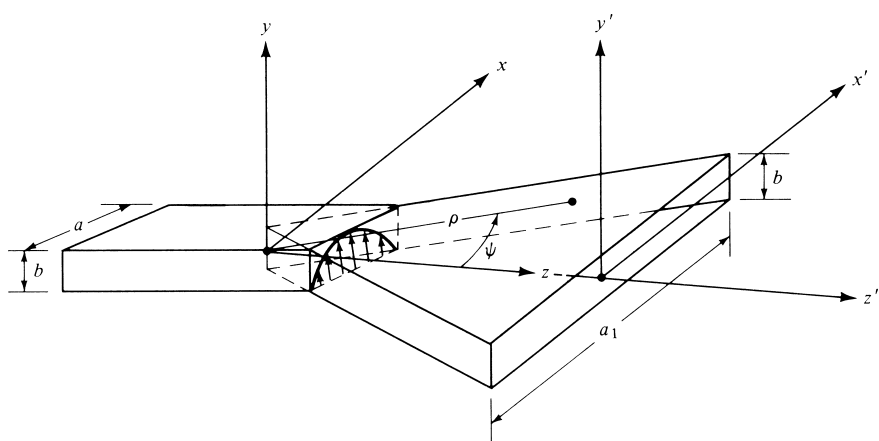
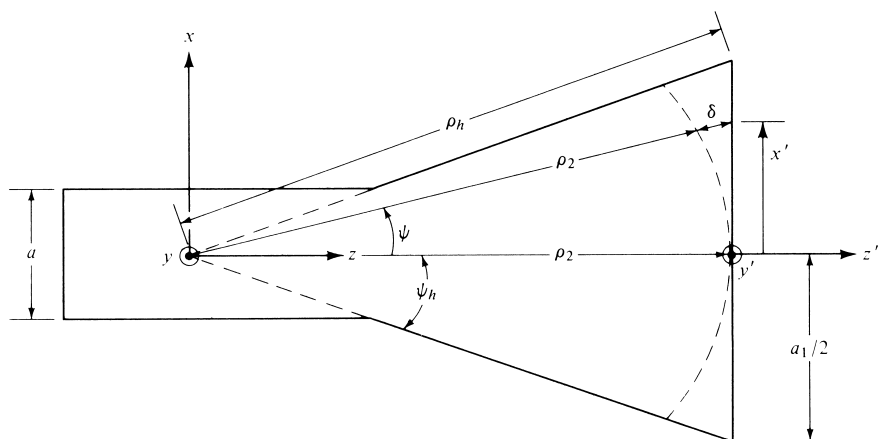
For  $B = 7.84$ ,  $G_E = 73.5$  from Figure 13.9. Thus, using (13-20c)

$$D_E = \frac{0.5(73.5)}{2.85} = 12.89 = 11.10 \text{ dB}$$

Obviously an excellent agreement between the results of (13-19) and (13-20c).

## 13.3 H-PLANE SECTORAL HORN

Flaring the dimensions of a rectangular waveguide in the direction of the  $\mathbf{H}$ -field, while keeping the other constant, forms an  $H$ -plane sectoral horn shown in Figure 13.1(b). A more detailed geometry is shown in Figure 13.10.

(a) *H*-plane sectoral horn(b) *H*-plane view**Figure 13.10** *H*-plane sectoral horn and coordinate system.

The analysis procedure for this horn is similar to that for the *E*-plane horn, which was outlined in the previous section. Instead of including all the details of the formulation, a summary of each radiation characteristic will be given.

### 13.3.1 Aperture Fields

The fields at the aperture of the horn can be found by treating the horn as a radial waveguide forming an imaginary apex shown dashed in Figure 13.10. Using this method, it can be shown that at the aperture of the horn

$$E'_x = H'_y = 0 \quad (13-21a)$$

$$E'_y(x') = E_2 \cos\left(\frac{\pi}{a_1}x'\right) e^{-jk\delta(x')} \quad (13-21b)$$



$$H'_x(x') = -\frac{E_2}{\eta} \cos\left(\frac{\pi}{a_1}x'\right) e^{-jk\delta(x')} \quad (13-21c)$$

$$\delta(x') = \frac{1}{2} \left( \frac{x'^2}{\rho_2} \right) \quad (13-21d)$$

$$\rho_2 = \rho_h \cos \psi_h \quad (13-21e)$$

### 13.3.2 Radiated Fields

The fields radiated by the horn can be found by first formulating the equivalent current densities  $\mathbf{J}_s$  and  $\mathbf{M}_s$ . Using (13-21a)–(13-21c), it can be shown that over the aperture of the horn

$$J_x = J_z = M_y = M_z = 0 \quad (13-22a)$$

$$J_y = -\frac{E_2}{\eta} \cos\left(\frac{\pi}{a_1}x'\right) e^{-jk\delta(x')} \quad (13-22b)$$

$$M_x = E_2 \cos\left(\frac{\pi}{a_1}x'\right) e^{-jk\delta(x')} \quad (13-22c)$$

and they are assumed to be zero elsewhere. Thus (12-12a) can be expressed as

$$N_\theta = \iint_S J_y \cos \theta \cos \phi e^{+jkr' \cos \psi} ds' = -\frac{E_2}{\eta} \cos \theta \sin \phi I_1 I_2 \quad (13-23)$$

where

$$I_1 = \int_{-b/2}^{+b/2} e^{+jky' \sin \theta \sin \phi} dy' = b \left[ \frac{\sin\left(\frac{kb}{2} \sin \theta \sin \phi\right)}{\frac{kb}{2} \sin \theta \sin \phi} \right] \quad (13-23a)$$

$$I_2 = \int_{-a_1/2}^{+a_1/2} \cos\left(\frac{\pi}{a_1}x'\right) e^{-jk[\delta(x') - x' \sin \theta \cos \phi]} dx' \quad (13-23b)$$

By rewriting  $\cos[(\pi/a_1)x']$  as

$$\cos\left(\frac{\pi}{a_1}x'\right) = \left[ \frac{e^{j(\pi/a_1)x'} + e^{-j(\pi/a_1)x'}}{2} \right] \quad (13-24)$$

(13-23b) can be expressed as

$$I_2 = I'_2 + I''_2 \quad (13-25)$$

where

$$I'_2 = \frac{1}{2} \sqrt{\frac{\pi \rho_2}{k}} e^{j(k_x^2 \rho_2 / 2k)} \{ [C(t'_2) - C(t'_1)] - j[S(t'_2) - S(t'_1)] \} \quad (13-26)$$

$$\boxed{t'_1 = \sqrt{\frac{1}{\pi k \rho_2}} \left( -\frac{ka_1}{2} - k'_x \rho_2 \right)} \quad (13-26a)$$

$$t'_2 = \sqrt{\frac{1}{\pi k \rho_2}} \left( +\frac{ka_1}{2} - k'_x \rho_2 \right) \quad (13-26b)$$

$$k'_x = k \sin \theta \cos \phi + \frac{\pi}{a_1} \quad (13-26c)$$

$$I''_2 = \frac{1}{2} \sqrt{\frac{\pi \rho_2}{k}} e^{j(k'^2_x \rho_2 / 2k)} \{ [C(t''_2) - C(t'_1)] - j[S(t''_2) - S(t'_1)] \} \quad (13-27)$$

$$t''_1 = \sqrt{\frac{1}{\pi k \rho_2}} \left( -\frac{ka_1}{2} - k''_x \rho_2 \right) \quad (13-27a)$$

$$t''_2 = \sqrt{\frac{1}{\pi k \rho_2}} \left( +\frac{ka_1}{2} - k''_x \rho_2 \right) \quad (13-27b)$$

$$k''_x = k \sin \theta \cos \phi - \frac{\pi}{a_1} \quad (13-27c)$$

$C(x)$  and  $S(x)$  are the cosine and sine Fresnel integrals of (13-8c) and (13-8d), and they are well tabulated (see Appendix IV).

With the aid of (13-23a), (13-25), (13-26), and (13-27), (13-23) reduces to

$$N_\theta = -E_2 \frac{b}{2} \sqrt{\frac{\pi \rho_2}{k}} \left\{ \frac{\cos \theta \sin \phi}{\eta} \frac{\sin Y}{Y} [e^{j f_1} F(t'_1, t'_2) + e^{j f_2} F(t''_1, t''_2)] \right\} \quad (13-28)$$

$$F(t_1, t_2) = [C(t_2) - C(t_1)] - j[S(t_2) - S(t_1)] \quad (13-28a)$$

$$f_1 = \frac{k'^2_x \rho_2}{2k} \quad (13-28b)$$

$$f_2 = \frac{k''^2_x \rho_2}{2k} \quad (13-28c)$$

$$Y = \frac{kb}{2} \sin \theta \sin \phi \quad (13-28d)$$

In a similar manner,  $N_\phi$ ,  $L_\theta$ , and  $L_\phi$  of (12-12b)–(12-12d) can be written as

$$N_\phi = -E_2 \frac{b}{2} \sqrt{\frac{\pi \rho_2}{k}} \left\{ \frac{\cos \phi \sin Y}{\eta} \frac{\sin Y}{Y} [e^{j f_1} F(t'_1, t'_2) + e^{j f_2} F(t''_1, t''_2)] \right\} \quad (13-29a)$$

$$L_\theta = E_2 \frac{b}{2} \sqrt{\frac{\pi \rho_2}{k}} \left\{ \cos \theta \cos \phi \frac{\sin Y}{Y} [e^{j\Gamma_1} F(t'_1, t'_2) + e^{j\Gamma_2} F(t''_1, t''_2)] \right\} \quad (13-29b)$$

$$L_\phi = -E_2 \frac{b}{2} \sqrt{\frac{\pi \rho_2}{k}} \left\{ \sin \phi \frac{\sin Y}{Y} [e^{j\Gamma_1} F(t'_1, t'_2) + e^{j\Gamma_2} F(t''_1, t''_2)] \right\} \quad (13-29c)$$

The far-zone electric field components of (12-10a)–(12-10c) can then be expressed as

$$\boxed{E_r = 0} \quad (13-30a)$$

$$\boxed{E_\theta = j E_2 \frac{b}{8} \sqrt{\frac{k \rho_2}{\pi}} \frac{e^{-jkr}}{r} \times \left\{ \sin \phi (1 + \cos \theta) \frac{\sin Y}{Y} [e^{j\Gamma_1} F(t'_1, t'_2) + e^{j\Gamma_2} F(t''_1, t''_2)] \right\}} \quad (13-30b)$$

$$\boxed{E_\phi = j E_2 \frac{b}{8} \sqrt{\frac{k \rho_2}{\pi}} \frac{e^{-jkr}}{r} \times \left\{ \cos \phi (\cos \theta + 1) \frac{\sin Y}{Y} [e^{j\Gamma_1} F(t'_1, t'_2) + e^{j\Gamma_2} F(t''_1, t''_2)] \right\}} \quad (13-30c)$$

The electric field in the principal  $E$ - and  $H$ -planes reduces to

### **$E$ -Plane ( $\phi = \pi/2$ )**

$$E_r = E_\phi = 0 \quad (13-31a)$$

$$E_\theta = j E_2 \frac{b}{8} \sqrt{\frac{k \rho_2}{\pi}} \frac{e^{-jkr}}{r} \times \left\{ (1 + \cos \theta) \frac{\sin Y}{Y} [e^{j\Gamma_1} F(t'_1, t'_2) + e^{j\Gamma_2} F(t''_1, t''_2)] \right\} \quad (13-31b)$$

$$Y = \frac{kb}{2} \sin \theta \quad (13-31c)$$

$$k'_x = \frac{\pi}{a_1} \quad (13-31d)$$

$$k''_x = -\frac{\pi}{a_1} \quad (13-31e)$$

### **$H$ -Plane ( $\phi = 0$ )**

$$E_r = E_\theta = 0 \quad (13-32a)$$

$$E_\phi = j E_2 \frac{b}{8} \sqrt{\frac{k \rho_2}{\pi}} \frac{e^{-jkr}}{r} \times \{ (\cos \theta + 1) [e^{j\Gamma_1} F(t'_1, t'_2) + e^{j\Gamma_2} F(t''_1, t''_2)] \} \quad (13-32b)$$

$$k'_x = k \sin \theta + \frac{\pi}{a_1} \quad (13-32c)$$

$$k''_x = k \sin \theta - \frac{\pi}{a_1} \quad (13-32d)$$

with  $f_1$ ,  $f_2$ ,  $F(t'_1, t'_2)$ ,  $F(t''_1, t''_2)$ ,  $t'_1$ ,  $t'_2$ ,  $t''_1$ , and  $t''_2$  as defined previously.

Computations similar to those for the  $E$ -plane sectoral horn were also performed for the  $H$ -plane sectoral horn. A three-dimensional field pattern of an  $H$ -plane sectoral horn is shown in Figure 13.11. Its corresponding  $E$ - and  $H$ -plane patterns are displayed in Figure 13.12. This horn exhibits narrow pattern characteristics in the flared  $H$ -plane.

Normalized  $H$ -plane patterns for a given length horn ( $\rho_2 = 12\lambda$ ) and different flare angles are shown in Figure 13.13. A total of four patterns is illustrated. Since each pattern is symmetrical, only half of each pattern is displayed. As the included angle is increased, the pattern begins to become narrower up to a given flare. Beyond that point the pattern begins to broaden, attributed primarily to the phase taper (phase error) across the aperture of the horn. To correct this, a lens is usually placed at the horn aperture, which would yield narrower patterns as the flare angle is increased. Similar pattern variations are evident when the flare angle of the horn is maintained fixed while its length is varied.

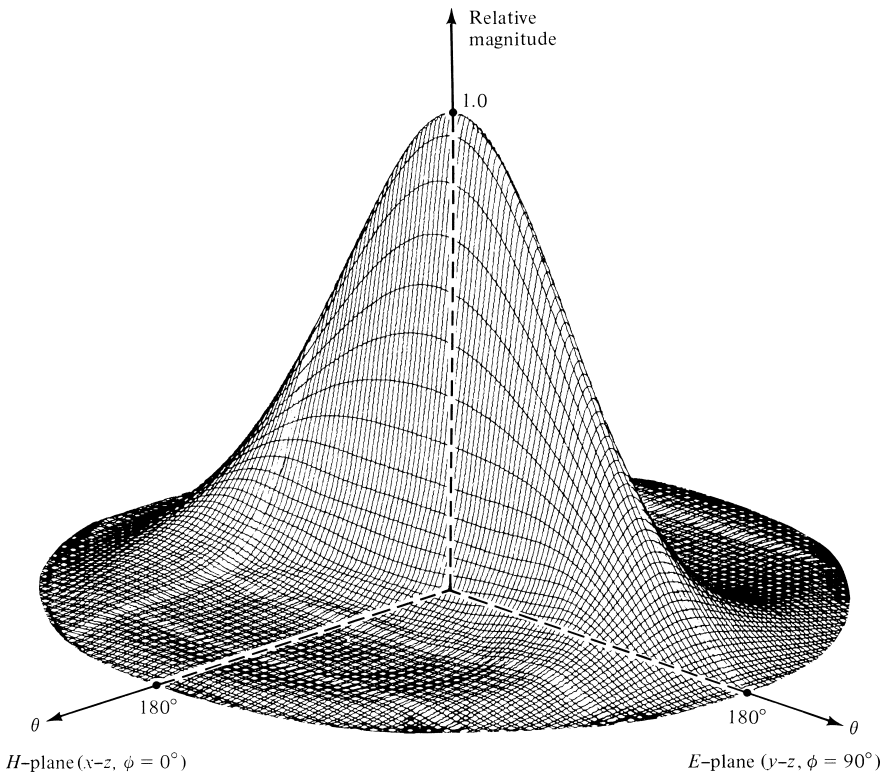


**Figure 13.11** Three-dimensional field pattern of an  $H$ -plane sectoral horn ( $\rho_2 = 6\lambda$ ,  $a_1 = 5.5\lambda$ ,  $b = 0.25\lambda$ ).

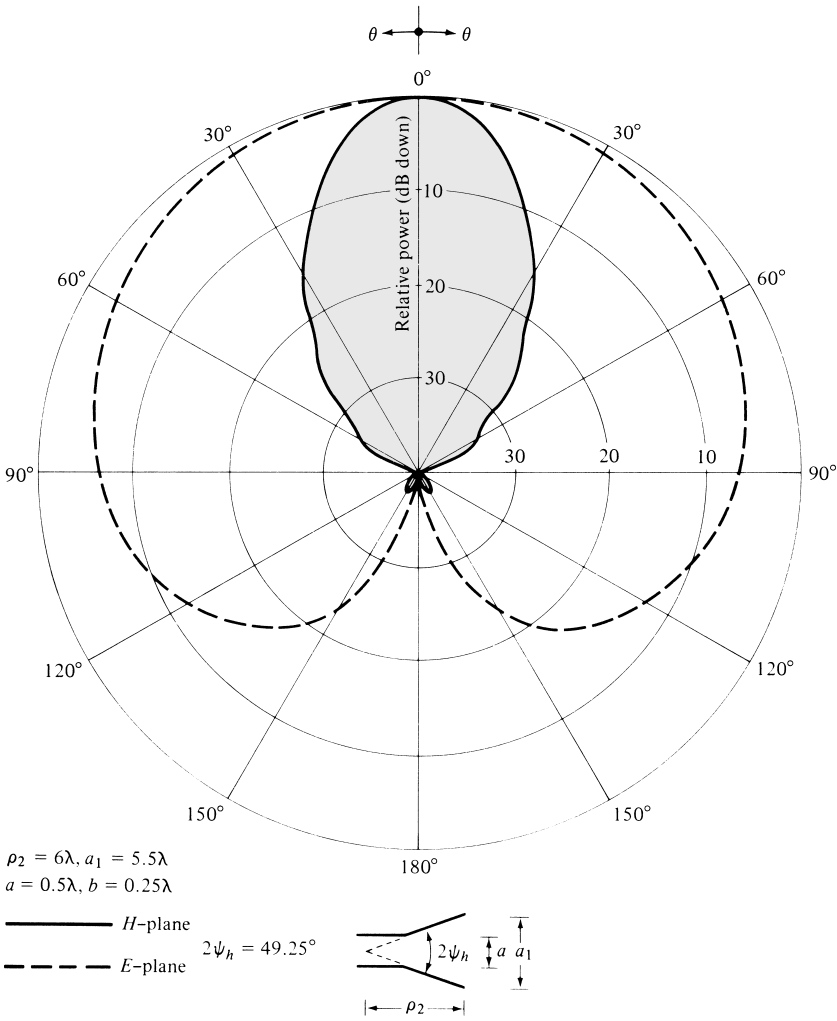


**Figure 13.12** E- and H-plane patterns of H-plane sectoral horn.

The *universal curves* for the H-plane sectoral horn are based on (13-32b), in the absence of the factor  $(1 + \cos \theta)$ . Neglecting the  $(1 + \cos \theta)$  factor, the normalized H-plane electric field of the H-plane sectoral horn can be written as

$$E_{\phi n} = [e^{jf_1} F(t'_1, t'_2) + e^{jf_2} F(t''_1, t''_2)] \quad (13-33)$$

$$F(t_1, t_2) = [C(t_2) - C(t_1)] - j[S(t_2) - S(t_1)] \quad (13-33a)$$

$$\begin{aligned}
 f_1 &= \frac{k_x'^2 \rho_2}{2k} = \frac{\rho_2}{2k} \left( k \sin \theta + \frac{\pi}{a_1} \right)^2 \\
 &= \frac{\pi}{8} \left( \frac{1}{t} \right) \left( \frac{a_1}{\lambda} \sin \theta \right)^2 \left[ 1 + \frac{1}{2} \left( \frac{\lambda}{a_1 \sin \theta} \right) \right]^2
 \end{aligned} \quad (13-33b)$$

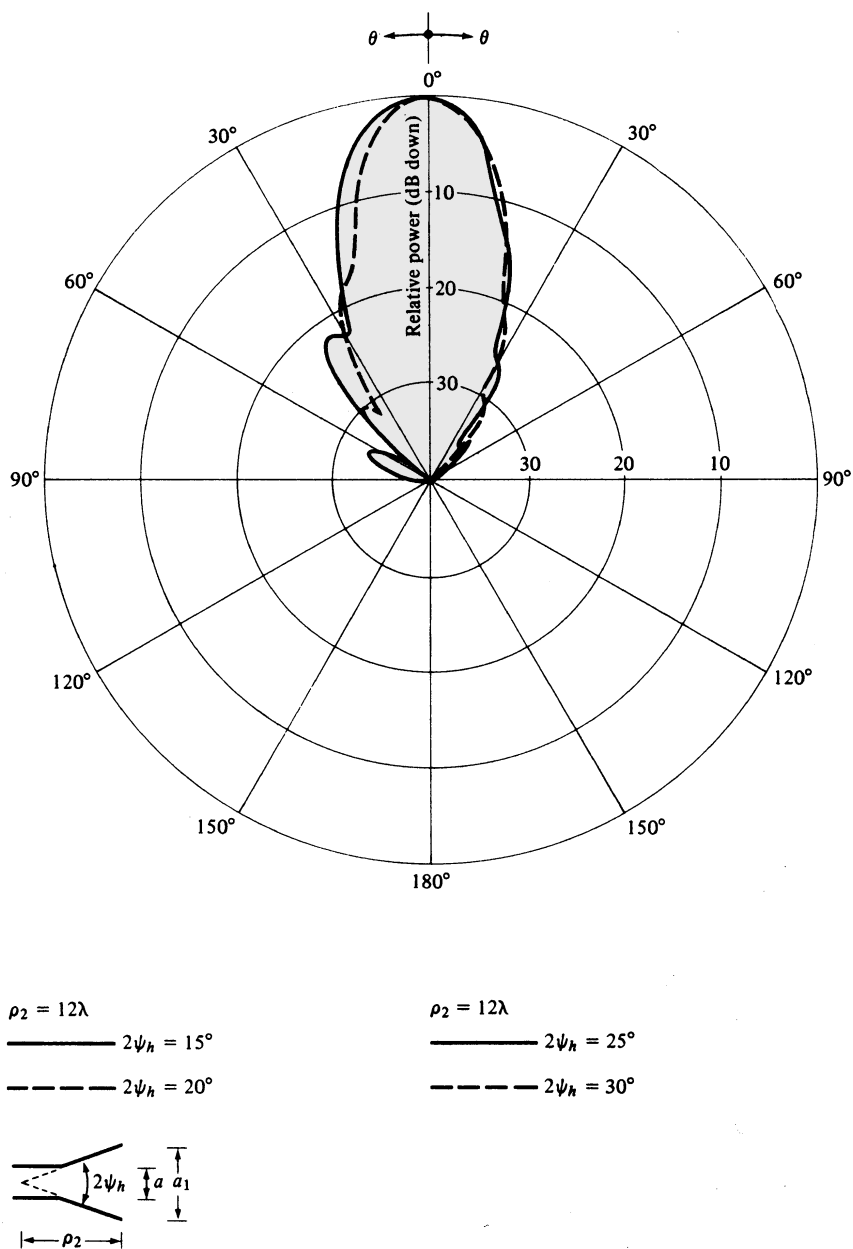


**Figure 13.13**  $H$ -plane patterns of  $H$ -plane sectoral horn for constant length and different included angles.

$$\begin{aligned}
 f_2 &= \frac{k_x'^2 \rho_2}{2k} = \frac{\rho_2}{2k} \left( k \sin \theta - \frac{\pi}{a_1} \right)^2 \\
 &= \frac{\pi}{8} \left( \frac{1}{t} \right) \left( \frac{a_1}{\lambda} \sin \theta \right)^2 \left[ 1 - \frac{1}{2} \left( \frac{\lambda}{a_1 \sin \theta} \right) \right]^2
 \end{aligned} \quad (13-33c)$$

$$\begin{aligned}
 t'_1 &= \sqrt{\frac{1}{\pi k \rho_2}} \left( -\frac{ka_1}{2} - k'_x \rho_2 \right) \\
 &= 2\sqrt{t} \left[ -1 - \frac{1}{4} \left( \frac{1}{t} \right) \left( \frac{a_1}{\lambda} \sin \theta \right) - \frac{1}{8} \left( \frac{1}{t} \right) \right] \quad (13-33d)
 \end{aligned}$$

$$\begin{aligned}
 t'_2 &= \sqrt{\frac{1}{\pi k \rho_2}} \left( +\frac{ka_1}{2} - k'_x \rho_2 \right) \\
 &= 2\sqrt{t} \left[ +1 - \frac{1}{4} \left( \frac{1}{t} \right) \left( \frac{a_1}{\lambda} \sin \theta \right) - \frac{1}{8} \left( \frac{1}{t} \right) \right] \quad (13-33e)
 \end{aligned}$$

$$\begin{aligned}
 t''_1 &= \sqrt{\frac{1}{\pi k \rho_2}} \left( -\frac{ka_1}{2} - k''_x \rho_2 \right) \\
 &= 2\sqrt{t} \left[ -1 - \frac{1}{4} \left( \frac{1}{t} \right) \left( \frac{a_1}{\lambda} \sin \theta \right) + \frac{1}{8} \left( \frac{1}{t} \right) \right] \quad (13-33f)
 \end{aligned}$$

$$\begin{aligned}
 t''_2 &= \sqrt{\frac{1}{\pi k \rho_2}} \left( +\frac{ka_1}{2} - k''_x \rho_2 \right) \\
 &= 2\sqrt{t} \left[ +1 - \frac{1}{4} \left( \frac{1}{t} \right) \left( \frac{a_1}{\lambda} \sin \theta \right) + \frac{1}{8} \left( \frac{1}{t} \right) \right] \quad (13-33g)
 \end{aligned}$$

$$t = \frac{a_1^2}{8\lambda\rho_2} \quad (13-33h)$$

For a given value of  $t$ , as given by (13-33h), the normalized field of (13-33) is plotted in Figure 13.14 as a function of  $(a_1/\lambda) \sin \theta$  for  $t = \frac{1}{64}, \frac{1}{8}, \frac{1}{4}, \frac{1}{2}, \frac{3}{4}$  and 1. Following a procedure identical to that for the  $E$ -plane sectoral horn, the  $H$ -plane pattern of any  $H$ -plane sectoral horn can be obtained from these curves. The normalized value of the  $(1 + \cos \theta)$  factor in dB, written as  $20 \log_{10}[(1 + \cos \theta)/2]$ , must also be included.

### 13.3.3 Directivity

To find the directivity of the  $H$ -plane sectoral horn, a procedure similar to that for the  $E$ -plane is used. As for the  $E$ -plane sectoral horn, the maximum radiation is directed nearly along the  $z$ -axis ( $\theta = 0^\circ$ ). Thus

$$\begin{aligned}
 |E_\theta|_{\max} &= |E_2| \frac{b}{4r} \sqrt{\frac{2\rho_2}{\lambda}} |\sin \phi \{ [C(t'_2) + C(t''_2) - C(t'_1) \\
 &\quad - C(t''_1)] - j[S(t'_2) + S(t''_2) - S(t'_1) - S(t''_1)] \}| \quad (13-34)
 \end{aligned}$$

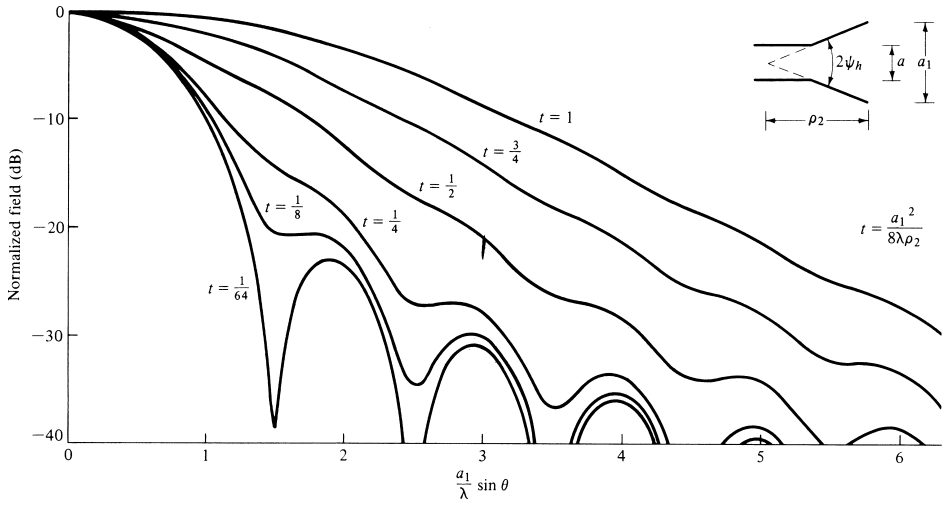


**Figure 13.14** *H*-plane universal patterns for *H*-plane sectoral and pyramidal horns.

$$t'_1 = \sqrt{\frac{1}{\pi k \rho_2}} \left( -\frac{ka_1}{2} - \frac{\pi}{a_1} \rho_2 \right) \quad (13-34a)$$

$$t'_2 = \sqrt{\frac{1}{\pi k \rho_2}} \left( +\frac{ka_1}{2} - \frac{\pi}{a_1} \rho_2 \right) \quad (13-34b)$$

$$t''_1 = \sqrt{\frac{1}{\pi k \rho_2}} \left( -\frac{ka_1}{2} + \frac{\pi}{a_1} \rho_2 \right) = -t'_2 = v \quad (13-34c)$$

$$t''_2 = \sqrt{\frac{1}{\pi k \rho_2}} \left( +\frac{ka_1}{2} + \frac{\pi}{a_1} \rho_2 \right) = -t'_1 = u \quad (13-34d)$$

Since

$$C(-x) = -C(x) \quad (13-35a)$$

$$S(-x) = -S(x) \quad (13-35b)$$

$$|E_\theta|_{\max} = |E_2| \frac{b}{r} \sqrt{\frac{\rho_2}{2\lambda}} \left| \sin \phi \{ [C(u) - C(v)] - j[S(u) - S(v)] \} \right| \quad (13-36)$$

$$u = t''_2 = -t'_1 = \sqrt{\frac{1}{\pi k \rho_2}} \left( +\frac{ka_1}{2} + \frac{\pi}{a_1} \rho_2 \right) = \frac{1}{\sqrt{2}} \left( \frac{\sqrt{\lambda} \rho_2}{a_1} + \frac{a_1}{\sqrt{\lambda} \rho_2} \right) \quad (13-36a)$$

$$v = t''_1 = -t'_2 = \sqrt{\frac{1}{\pi k \rho_2}} \left( -\frac{ka_1}{2} + \frac{\pi}{a_1} \rho_2 \right) = \frac{1}{\sqrt{2}} \left( \frac{\sqrt{\lambda} \rho_2}{a_1} - \frac{a_1}{\sqrt{\lambda} \rho_2} \right) \quad (13-36b)$$



Similarly

$$|E_\phi|_{\max} = |E_2| \frac{b}{r} \sqrt{\frac{\rho_2}{2\lambda}} \left| \cos \phi \{ [C(u) - C(v)] - j[S(u) - S(v)] \} \right| \quad (13-37)$$

Thus

$$|\mathbf{E}|_{\max} = \sqrt{|E_\theta|_{\max}^2 + |E_\phi|_{\max}^2} = |E_2| \frac{b}{r} \sqrt{\frac{\rho_2}{2\lambda}} \{ [C(u) - C(v)]^2 + [S(u) - S(v)]^2 \}^{1/2} \quad (13-38)$$

$$U_{\max} = |E_2|^2 \frac{b^2 \rho_2}{4\eta\lambda} \{ [C(u) - C(v)]^2 + [S(u) - S(v)]^2 \} \quad (13-39)$$

The total power radiated can be obtained by simply integrating the average power density over the mouth of the horn, and it is given by

$$P_{\text{rad}} = |E_2|^2 \frac{ba_1}{4\eta} \quad (13-40)$$

Using (13-39) and (13-40), the directivity for the  $H$ -plane sectoral horn can be written as

$$D_H = \frac{4\pi U_{\max}}{P_{\text{rad}}} = \frac{4\pi b \rho_2}{a_1 \lambda} \times \{ [C(u) - C(v)]^2 + [S(u) - S(v)]^2 \} \quad (13-41)$$

where

$$u = \frac{1}{\sqrt{2}} \left( \frac{\sqrt{\lambda \rho_2}}{a_1} + \frac{a_1}{\sqrt{\lambda \rho_2}} \right) \quad (13-41a)$$

$$v = \frac{1}{\sqrt{2}} \left( \frac{\sqrt{\lambda \rho_2}}{a_1} - \frac{a_1}{\sqrt{\lambda \rho_2}} \right) \quad (13-41b)$$

The half-power beamwidth (HPBW) as a function of flare angle is plotted in Figure 13.15. The normalized directivity (relative to the constant aperture dimension  $b$ ) for different horn lengths, as a function of aperture dimension  $a_1$ , is displayed in Figure 13.16. As for the  $E$ -plane sectoral horn, the HPBW exhibits a monotonic decrease and the directivity a monotonic increase up to a given flare; beyond that, the trends are reversed.

If the values of  $a_1$  (in  $\lambda$ ), which correspond to the maximum directivities in Figure 13.16, are plotted versus their corresponding values of  $\rho_2$  (in  $\lambda$ ), it can be shown that each optimum directivity occurs when

$$a_1 \simeq \sqrt{3\lambda \rho_2} \quad (13-41c)$$

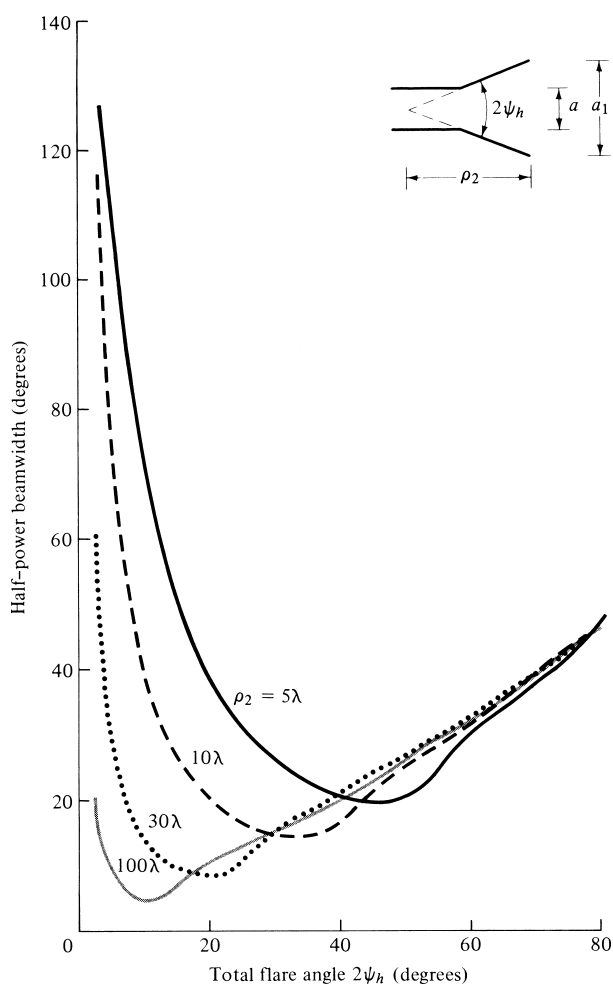


**Figure 13.15** Half-power beamwidth of *H*-plane sectoral horn as a function of included angle and for different lengths.

with a corresponding value of  $t$  equal to

$$t|_{a_1=\sqrt{3\lambda\rho_2}} = t_{op} = \frac{a_1^2}{8\lambda\rho_2} \Big|_{a_1=\sqrt{3\lambda\rho_2}} = \frac{3}{8} \quad (13-41d)$$

The directivity of an *H*-plane sectoral horn can also be computed by using the following procedure [14].

1. Calculate  $A$  by

$$A = \frac{a_1}{\lambda} \sqrt{\frac{50}{\rho_h/\lambda}} \quad (13-42a)$$

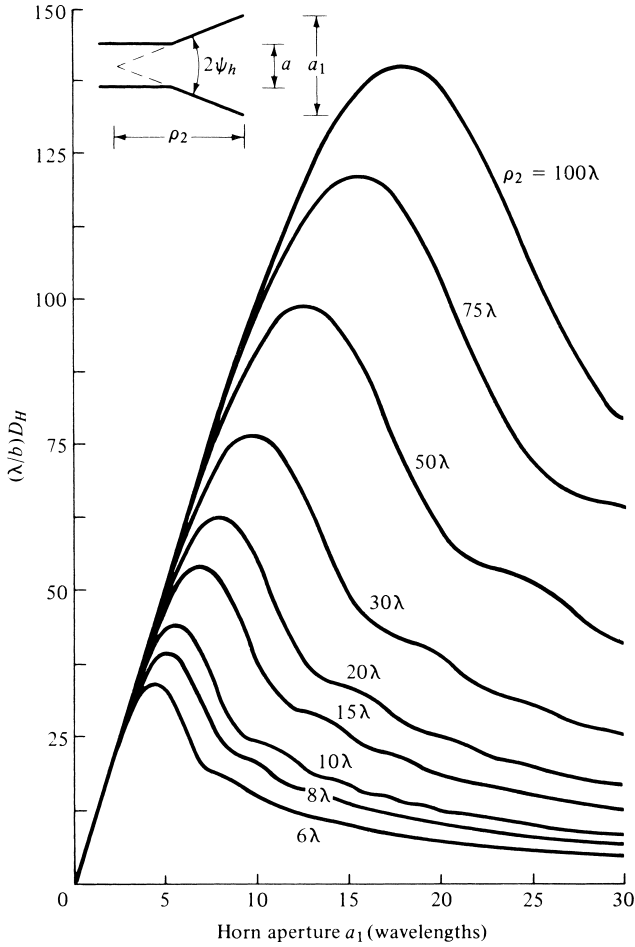


**Figure 13.16** Normalized directivity of  $H$ -plane sectoral horn as a function of aperture size and for different lengths.

- Using this value of  $A$ , find the corresponding value of  $G_H$  from Figure 13.17. *If the value of  $A$  is smaller than 2, then compute  $G_H$  using*

$$G_H = \frac{32}{\pi} A \quad (13-42b)$$

- Calculate  $D_H$  by using the value of  $G_H$  from Figure 13.17 or from (13-42b). Thus

$$\boxed{D_H = \frac{b}{\lambda} \frac{G_H}{\sqrt{\frac{50}{\rho_h/\lambda}}}} \quad (13-42c)$$

This is the actual directivity of the horn.

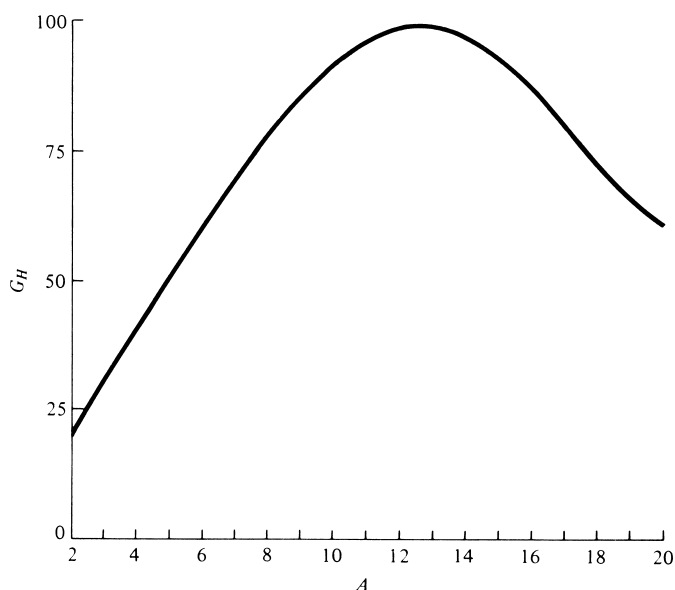


**Figure 13.17**  $G_H$  as a function of  $A$ . (SOURCE: Adopted from data by E. H. Braun, "Some Data for the Design of Electromagnetic Horns," *IRE Trans. Antennas Propagat.*, Vol. AP-4, No. 1, January 1956. © 1956 IEEE)

#### Example 13.4

An  $H$ -plane sectoral horn has dimensions of  $a = 0.5\lambda$ ,  $b = 0.25\lambda$ ,  $a_1 = 5.5\lambda$ , and  $\rho_2 = 6\lambda$ . Compute the directivity using (13-41) and (13-42c). Compare the answers.

*Solution:* For this horn

$$u = \frac{1}{\sqrt{2}} \left( \frac{\sqrt{6}}{5.5} + \frac{5.5}{\sqrt{6}} \right) = 1.9$$

$$v = \frac{1}{\sqrt{2}} \left( \frac{\sqrt{6}}{5.5} - \frac{5.5}{\sqrt{6}} \right) = -1.273$$

Therefore (from Appendix IV)

$$C(1.9) = 0.394$$

$$C(-1.273) = -C(1.273) = -0.659$$

$$S(1.9) = 0.373$$

$$S(-1.273) = -S(1.273) = -0.669$$

Using (13-41)

$$D_H = \frac{4\pi(0.25)6}{5.5} [(0.394 + 0.659)^2 + (0.373 + 0.669)^2]$$

$$D_H = 7.52 = 8.763 \text{ dB}$$

To compute the directivity using (13-42c), the following parameters are computed:

$$\begin{aligned}\rho_h &= \lambda \sqrt{(6)^2 + (5.5/2)^2} = 6.6\lambda \\ \sqrt{\frac{50}{\rho_h/\lambda}} &= \sqrt{\frac{50}{6.6}} = 2.7524 \\ A &= 5.5(2.7524) = 15.14\end{aligned}$$

For  $A = 15.14$ ,  $G_H = 91.8$  from Figure 13.17. Thus, using (13-42c)

$$D_H = \frac{0.25(91.8)}{2.7524} = 8.338 = 9.21 \text{ dB}$$

Although there is a good agreement between the results of (13-41) and (13-42c), they do not compare as well as those of Example 13.3.

## 13.4 PYRAMIDAL HORN

The most widely used horn is the one which is flared in both directions, as shown in Figure 13.18. It is widely referred to as a pyramidal horn, and its radiation characteristics are essentially a combination of the  $E$ - and  $H$ -plane sectoral horns.

### 13.4.1 Aperture Fields, Equivalent, and Radiated Fields

To simplify the analysis and to maintain a modeling that leads to computations that have been shown to correlate well with experimental data, the tangential components of the  $E$ - and  $H$ -fields over the aperture of the horn are approximated by

$$E'_y(x', y') = E_0 \cos\left(\frac{\pi}{a_1}x'\right) e^{-j[k(x'^2/\rho_2 + y'^2/\rho_1)/2]} \quad (13-43a)$$

$$H'_x(x', y') = -\frac{E_0}{\eta} \cos\left(\frac{\pi}{a_1}x'\right) e^{-j[k(x'^2/\rho_2 + y'^2/\rho_1)/2]} \quad (13-43b)$$

and the equivalent current densities by

$$J_y(x', y') = -\frac{E_0}{\eta} \cos\left(\frac{\pi}{a_1}x'\right) e^{-j[k(x'^2/\rho_2 + y'^2/\rho_1)/2]} \quad (13-44a)$$

$$M_x(x', y') = E_0 \cos\left(\frac{\pi}{a_1}x'\right) e^{-j[k(x'^2/\rho_2 + y'^2/\rho_1)/2]} \quad (3-44b)$$

The above expressions contain a cosinusoidal amplitude distribution in the  $x'$  direction and quadratic phase variations in both the  $x'$  and  $y'$  directions, similar to those of the sectoral  $E$ - and  $H$ -plane horns.

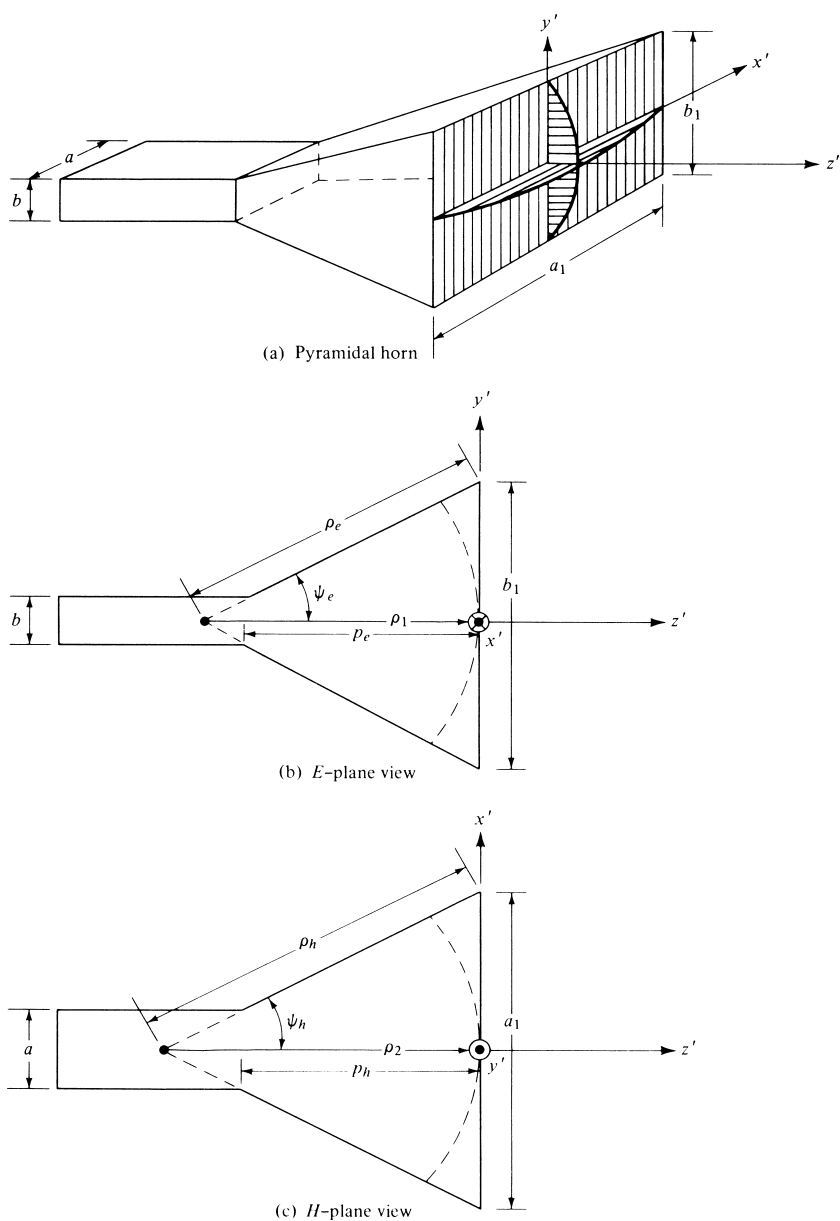


**Figure 13.18** Pyramidal horn and coordinate system.

The  $N_\theta$ ,  $N_\phi$ ,  $L_\theta$  and  $L_\phi$  can now be formulated as before, and it can be shown that they are given by

$$N_\theta = -\frac{E_0}{\eta} \cos \theta \sin \phi I_1 I_2 \quad (13-45a)$$

$$N_\phi = -\frac{E_0}{\eta} \cos \phi I_1 I_2 \quad (13-45b)$$

$$L_\theta = E_0 \cos \theta \cos \phi I_1 I_2 \quad (13-45c)$$

$$L_\phi = -E_0 \sin \phi I_1 I_2 \quad (13-45d)$$

where

$$I_1 = \int_{-a_1/2}^{+a_1/2} \cos\left(\frac{\pi}{a}x'\right) e^{-jk[x'^2/(2\rho_1) - x'\sin\theta\cos\phi]} dx' \quad (13-45e)$$

$$I_2 = \int_{-b_1/2}^{+b_1/2} e^{-jk[y'^2/(2\rho_1) - y'\sin\theta\sin\phi]} dy' \quad (13-45f)$$

Using (13-23b), (13-25), (13-26), and (13-27), (13-45e) can be expressed as

$$I_1 = \frac{1}{2} \sqrt{\frac{\pi\rho_2}{k}} (e^{j(k_x'^2\rho_2/2k)} \{[C(t'_2) - C(t'_1)] - j[S(t'_2) - S(t'_1)]\} \\ + e^{j(k_x''^2\rho_2/2k)} \{[C(t''_2) - C(t''_1)] - j[S(t''_2) - S(t''_1)]\}) \quad (13-46)$$

where  $t'_1, t'_2, k'_x, t''_1, t''_2$ , and  $k''_x$  are given by (13-26a)–(13-26c) and (13-27a)–(13-27c). Similarly, using (13-5)–(13-8d),  $I_2$  of (13-45f) can be written as

$$I_2 = \sqrt{\frac{\pi\rho_1}{k}} e^{j(k_y^2\rho_1/2k)} \{[C(t_2) - C(t_1)] - j[S(t_2) - S(t_1)]\} \quad (13-47)$$

where  $k_y, t_1$ , and  $t_2$  are given by (13-5a), (13-8a), and (13-8b).

Combining (13-45a)–(13-45d), the far-zone **E**- and **H**-field components of (12-10a)–(12-10c) reduce to

$$E_r = 0 \quad (13-48a)$$

$$E_\theta = -j \frac{ke^{jkr}}{4\pi r} [L_\phi + \eta N_\theta] \\ = j \frac{kE_0 e^{-jkr}}{4\pi r} [\sin \phi (1 + \cos \theta) I_1 I_2] \quad (13-48b)$$

$$E_\phi = +j \frac{ke^{-jkr}}{4\pi r} [L_\theta - \eta N_\phi] \\ = j \frac{kE_0 e^{-jkr}}{4\pi r} [\cos \phi (\cos \theta + 1) I_1 I_2] \quad (13-48c)$$

where  $I_1$  and  $I_2$  are given by (13-46) and (13-47), respectively.

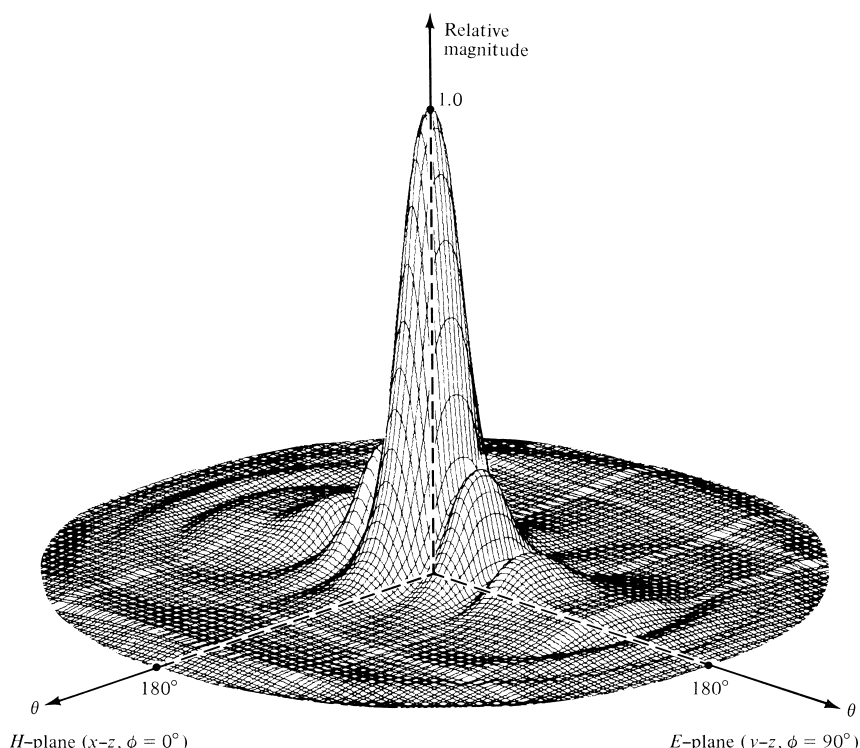


**Figure 13.19** Three-dimensional field pattern of a pyramidal horn ( $\rho_1 = \rho_2 = 6\lambda$ ,  $a_1 = 5.5\lambda$ ,  $b_1 = 2.75\lambda$ ,  $a = 0.5\lambda$ ,  $b = 0.25\lambda$ ).

The fields radiated by a pyramidal horn, as given by (13-48a)–(13-48c), are valid for all angles of observation. An examination of these equations reveals that the principal *E*-plane pattern ( $\phi = \pi/2$ ) of a pyramidal horn, aside from a normalization factor, is identical to the *E*-plane pattern of an *E*-plane sectoral horn. Similarly the *H*-plane ( $\phi = 0$ ) is identical to that of an *H*-plane sectoral horn. Therefore the pattern of a pyramidal horn is very narrow in both principal planes and, in fact, in all planes. This is illustrated in Figure 13.19. The corresponding *E*-plane pattern is shown in Figure 13.4 and the *H*-plane pattern in Figure 13.12.

To demonstrate that the maximum radiation for a pyramidal horn is not necessarily directed along its axis, the three-dimensional field pattern for a horn with  $\rho_1 = \rho_2 = 6\lambda$ ,  $a_1 = 12\lambda$ ,  $b_1 = 6\lambda$ ,  $a = 0.50\lambda$  and  $b = 0.25\lambda$  is displayed in Figure 13.20. The corresponding two-dimensional *E*- and *H*-plane patterns are shown in Figure 13.21. The maximum does not occur on axis because the phase error taper at the aperture is such that the rays emanating from the different parts of the aperture toward the axis are not in phase and do not add constructively.

To physically construct a pyramidal horn, the dimension  $p_e$  of Figure 13.18(b) given by

$$p_e = (b_1 - b) \left[ \left( \frac{\rho_e}{b_1} \right)^2 - \frac{1}{4} \right]^{1/2} \quad (13-49a)$$



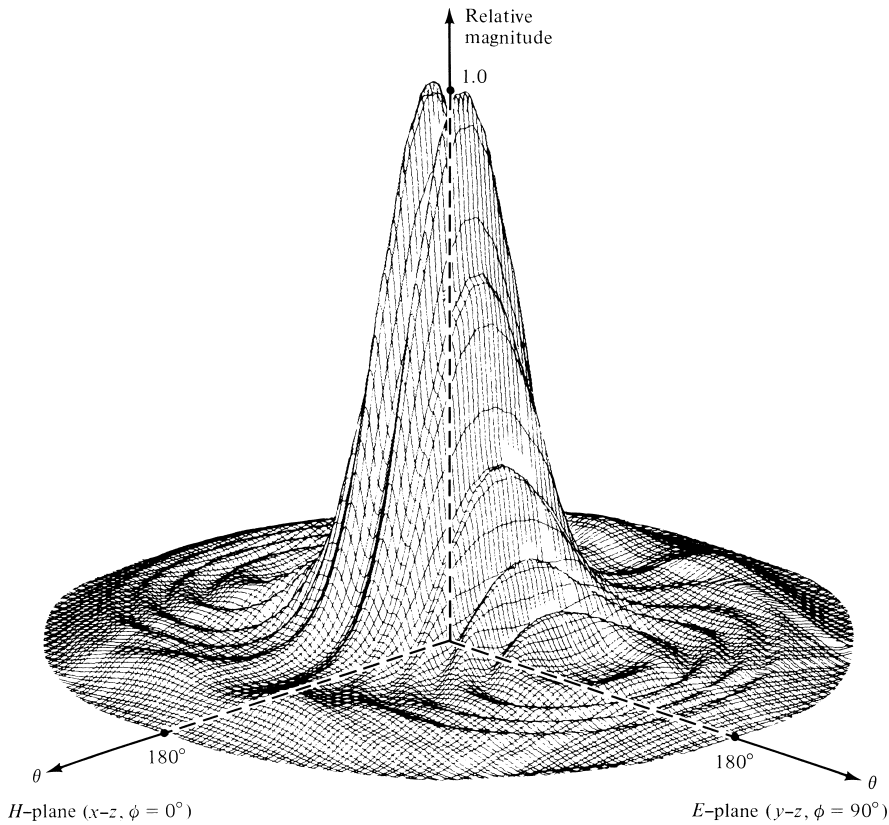


**Figure 13.20** Three-dimensional field pattern of a pyramidal horn with maximum not on axis ( $\rho_1 = \rho_2 = 6\lambda$ ,  $a_1 = 12\lambda$ ,  $b_1 = 6\lambda$ ,  $a = 0.5\lambda$ ,  $b = 0.25\lambda$ ).

should be equal to the dimension  $p_h$  of Figure 13.18(c) given by

$$p_h = (a_1 - a) \left[ \left( \frac{\rho_h}{a_1} \right)^2 - \frac{1}{4} \right]^{1/2} \quad (13-49b)$$

The dimensions chosen for Figures 13.19 and 13.20 do satisfy these requirements. For the horn of Figure 13.19,  $\rho_e = 6.1555\lambda$ ,  $\rho_h = 6.6\lambda$ , and  $\rho_e = \rho_h = 5.4544\lambda$ , whereas for that of Figure 13.20,  $\rho_e = 6.7082\lambda$ ,  $\rho_h = 8.4853\lambda$ , and  $\rho_e = \rho_h = 5.75\lambda$ . The fields of (13-48a)–(13-48c) provide accurate patterns for angular regions near the main lobe and its closest minor lobes. To accurately predict the field intensity of the pyramidal and other horns, especially in the minor lobes, diffraction techniques can be utilized [15]–[18]. These methods take into account diffractions that occur near the aperture edges of the horn. The diffraction contributions become more dominant in regions where the radiation of (13-48a)–(13-48c) is of very low intensity.

In addition to the previous methods, the horn antenna has been examined using full-wave analyses, such as the Method of Moments (MoM) [8] and the Finite-Difference Time-Domain (FDTD) [19]. These methods yield more accurate results in all regions,

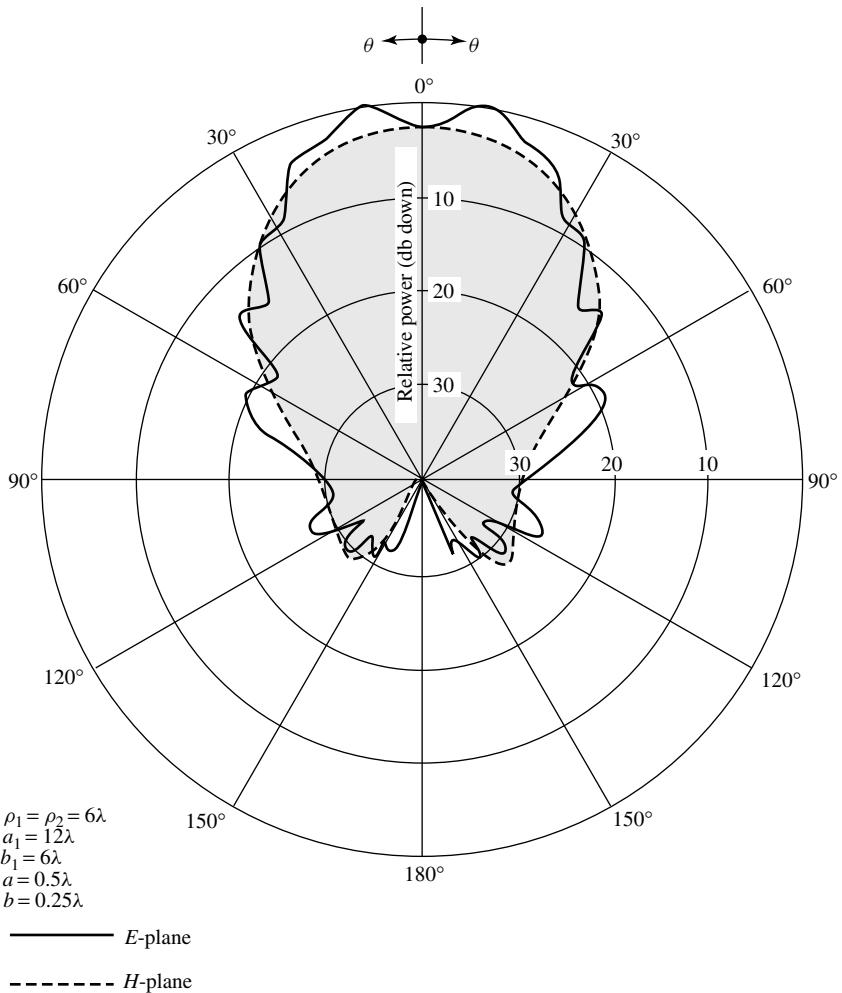


**Figure 13.21** *E*- and *H*-plane amplitude patterns of a pyramidal horn with maximum not on axis.

and they are able to include many of the other features of the horn, such as its wall thickness, etc. Predicted patterns based on these methods compare extremely well with measurements, even in regions of very low intensity (such as the back lobes). An example of such a comparison is made in Figure 13.22(a, b) for the *E*- and *H*-plane patterns of a 20-dB standard-gain horn whose Method of Moment predicted values are compared with measured patterns and with predicted values based on (13-48a) and (13-48c), which in Figure 13.22 are labeled as *approximate*. It is apparent that the MoM predicted patterns compare extremely well with the measured data.

All of the patterns presented previously represent the main polarization of the field radiated by the antenna (referred to as *copolarized* or *copol*). If the horn is symmetrical and it is excited in the dominant mode, ideally there should be no field component radiated by the antenna which is orthogonal to the main polarization (referred to as *cross polarization* or *cross-pol*), especially in the principal planes. However, in

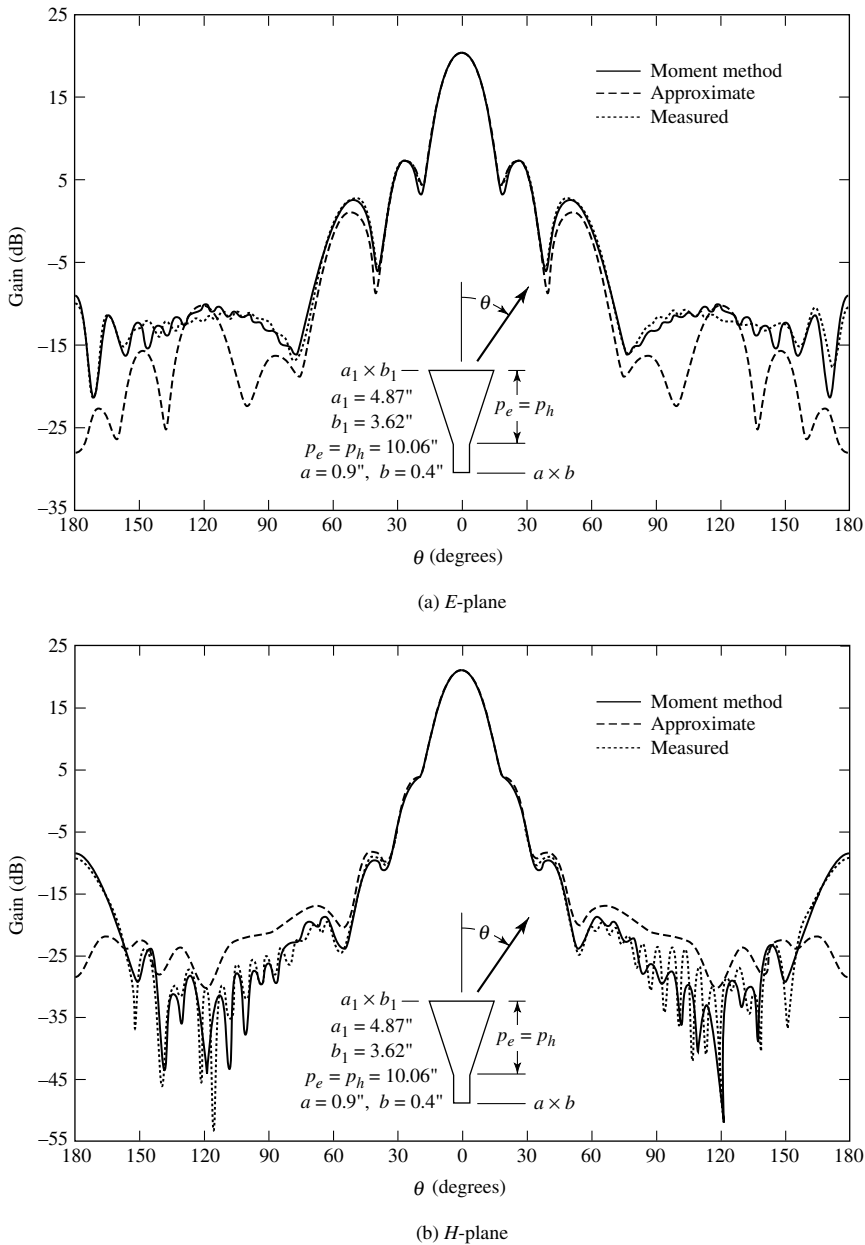


**Figure 13.22** Comparison of *E*- and *H*-plane patterns for 20-dB standard-gain horn at 10 GHz.

practice, either because of nonsymmetries, defects in construction and/or excitation of higher-order modes, all antennas exhibit cross-polarized components. These cross-pol components are usually of very low intensity compared to those of the primary polarization. For good designs, these should be 30 dB or more below the copolarized fields and are difficult to measure accurately or be symmetrical, as they should be in some cases.

### 13.4.2 Directivity

As for the  $E$ - and  $H$ -plane sectoral horns, the directivity of the pyramidal configuration is vital to the antenna designer. The maximum radiation of the pyramidal horn is directed nearly along the  $z$ -axis ( $\theta = 0^\circ$ ). It is a very simple exercise to show that  $|E_\theta|_{\max}$ ,  $|E_\phi|_{\max}$ , and in turn  $U_{\max}$  can be written, using (13-48b) and (13-48c), as

$$|E_\theta|_{\max} = |E_0 \sin \phi| \frac{\sqrt{\rho_1 \rho_2}}{r} \{ [C(u) - C(v)]^2 + [S(u) - S(v)]^2 \}^{1/2} \\ \times \left\{ C^2 \left( \frac{b_1}{\sqrt{2\lambda\rho_1}} \right) + S^2 \left( \frac{b_1}{\sqrt{2\lambda\rho_1}} \right) \right\}^{1/2} \quad (13-50a)$$

$$|E_\phi|_{\max} = |E_0 \cos \phi| \frac{\sqrt{\rho_1 \rho_2}}{r} \{ [C(u) - C(v)]^2 + [S(u) - S(v)]^2 \}^{1/2} \\ \times \left\{ C^2 \left( \frac{b_1}{\sqrt{2\lambda\rho_1}} \right) + S^2 \left( \frac{b_1}{\sqrt{2\lambda\rho_1}} \right) \right\}^{1/2} \quad (13-50b)$$

$$U_{\max} = \frac{r^2}{2\eta} |\mathbf{E}|_{\max}^2 = |E_0|^2 \frac{\rho_1 \rho_2}{2\eta} \{ [C(u) - C(v)]^2 + [S(u) - S(v)]^2 \} \\ \times \left\{ C^2 \left( \frac{b_1}{\sqrt{2\lambda\rho_1}} \right) + S^2 \left( \frac{b_1}{\sqrt{2\lambda\rho_1}} \right) \right\} \quad (13-50c)$$

where  $u$  and  $v$  are defined by (13-41a) and (13-41b).

Since

$$P_{\text{rad}} = |E_0|^2 \frac{a_1 b_1}{4\eta} \quad (13-51)$$

the directivity of the pyramidal horn can be written as

$$D_p = \frac{4\pi U_{\max}}{P_{\text{rad}}} = \frac{8\pi\rho_1\rho_2}{a_1 b_1} \{ [C(u) - C(v)]^2 + [S(u) - S(v)]^2 \} \\ \times \left\{ C^2 \left( \frac{b_1}{\sqrt{2\lambda\rho_1}} \right) + S^2 \left( \frac{b_1}{\sqrt{2\lambda\rho_1}} \right) \right\} \quad (13-52)$$

which reduces to

$$D_p = \frac{\pi\lambda^2}{32ab} D_E D_H \quad (13-52a)$$

where  $D_E$  and  $D_H$  are the directivities of the  $E$ - and  $H$ -plane sectoral horns as given by (13-19) and (13-41), respectively. This is a well-known relationship and has been used extensively in the design of pyramidal horns.

The directivity (*in dB*) of a pyramidal horn, over isotropic, can also be approximated by

$$D_p(\text{dB}) = 10 \left[ 1.008 + \log_{10} \left( \frac{a_1 b_1}{\lambda^2} \right) \right] - (L_e + L_h) \quad (13-53)$$

where  $L_e$  and  $L_h$  represent, respectively, the losses (*in dB*) due to phase errors in the  $E$ - and  $H$ -planes of the horn which are found plotted in Figure 13.23.

The directivity of a pyramidal horn can also be calculated by doing the following [14].

1. Calculate

$$A = \frac{a_1}{\lambda} \sqrt{\frac{50}{\rho_h/\lambda}} \quad (13-54a)$$

$$B = \frac{b_1}{\lambda} \sqrt{\frac{50}{\rho_e/\lambda}} \quad (13-54b)$$

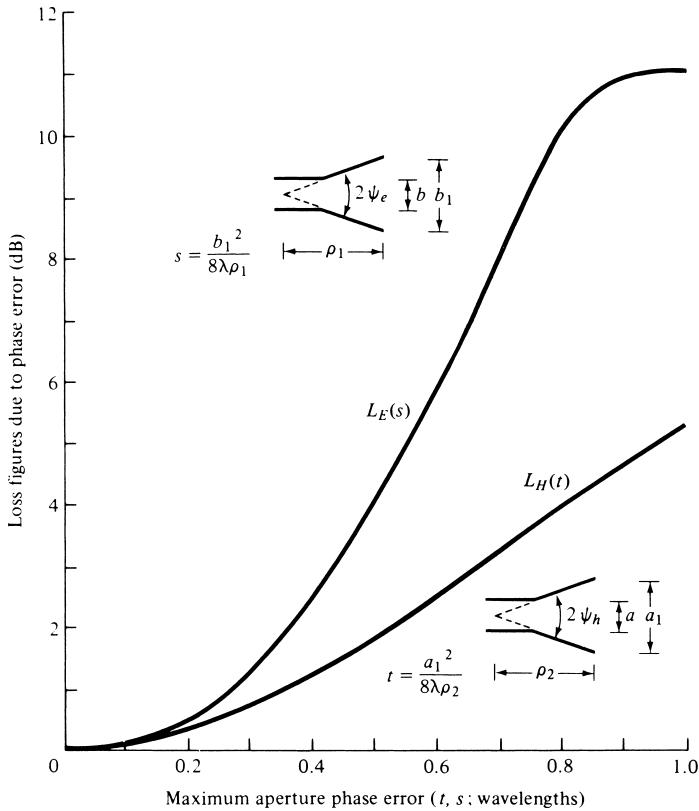


**Figure 13.23** Loss figures for  $E$ - and  $H$ -planes due to phase errors. (SOURCE: W. C. Jakes, in H. Jasik (ed.), *Antenna Engineering Handbook*, McGraw-Hill, New York, 1961).

2. Using  $A$  and  $B$ , find  $G_H$  and  $G_E$ , respectively, from Figures 13.17 and 13.9. If the values of either  $A$  or  $B$  or both are smaller than 2, then calculate  $G_E$  and/or  $G_H$  by

$$G_E = \frac{32}{\pi} B \quad (13-54c)$$

$$G_H = \frac{32}{\pi} A \quad (13-54d)$$

3. Calculate  $D_p$  by using the values of  $G_E$  and  $G_H$  from Figures 13.9 and 13.17 or from (13-54c) and (13-54d). Thus

$$\begin{aligned} D_p &= \frac{G_E G_H}{\frac{32}{\pi} \sqrt{\frac{50}{\rho_e/\lambda}} \sqrt{\frac{50}{\rho_h/\lambda}}} = \frac{G_E G_H}{10.1859 \sqrt{\frac{50}{\rho_e/\lambda}} \sqrt{\frac{50}{\rho_h/\lambda}}} \\ &= \frac{\lambda^2 \pi}{32ab} D_E D_H \end{aligned} \quad (13-54e)$$

where  $D_E$  and  $D_H$  are, respectively, the directivities of (13-20c) and (13-42c). This is the actual directivity of the horn. The above procedure has led to results accurate to within 0.01 dB for a horn with  $\rho_e = \rho_h = 50\lambda$ .

A commercial X-band (8.2–12.4 GHz) horn is that shown in Figure 13.24. It is a lightweight precision horn antenna, which is usually cast of aluminum, and it can be used as a

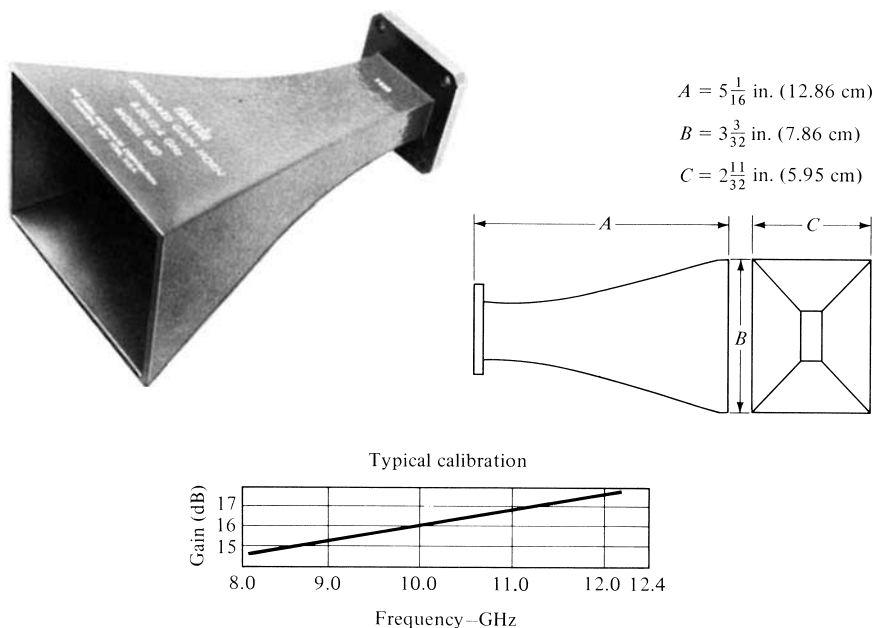


**Figure 13.24** Typical standard gain X-band (8.2–12.4 GHz) pyramidal horn and its gain characteristics. (Courtesy of The NARDA Microwave Corporation).

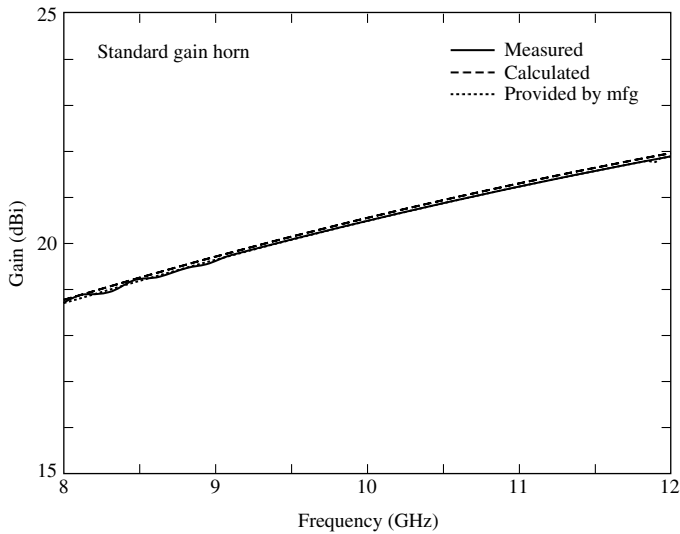


**Figure 13.25** Gains of the pyramidal horn which were measured, computed, and provided by the manufacturer. The amplitude patterns of the horn are shown in Figure 13.22.

1. standard for calibrating other antennas
2. feed for reflectors and lenses
3. pickup (probe) horn for sampling power
4. receiving and/or transmitting antenna.

It possesses an exponential taper, and its dimensions and typical gain characteristics are indicated in the figure. The half-power beamwidth in both the  $E$ - and  $H$ -planes is about  $28^\circ$  while the side lobes in the  $E$ - and  $H$ -planes are, respectively, about 13 and 20 dB down.

Gains of the horn antenna which were measured, predicted, and provided by the manufacturer, whose amplitude patterns are shown in Figure 13.22, are displayed in Figure 13.25. A very good agreement amongst all three sets is indicated.

### Example 13.5

A pyramidal horn has dimensions of  $\rho_1 = \rho_2 = 6\lambda$ ,  $a_1 = 5.5\lambda$ ,  $b_1 = 2.75\lambda$ ,  $a = 0.5\lambda$ , and  $b = 0.25\lambda$ .

- a. Check to see if such a horn can be constructed physically.
- b. Compute the directivity using (13-52a), (13-53), and (13-54e).

*Solution:* From Examples 13.3 and 13.4.

$$\rho_e = 6.1555\lambda$$

$$\rho_h = 6.6\lambda$$

Thus

$$p_e = (2.75 - 0.25)\lambda \sqrt{\left(\frac{6.1555}{2.75}\right)^2 - \frac{1}{4}} = 5.454\lambda$$

$$p_h = (5.5 - 0.5)\lambda \sqrt{\left(\frac{6}{5.5}\right)^2 - \frac{1}{4}} = 5.454\lambda$$

Therefore the horn can be constructed physically.

The directivity can be computed by utilizing the results of Examples 13.3 and 13.4. Using (13-52a) with the values of  $D_E$  and  $D_H$  computed using, respectively, (13-19) and (13-41) gives

$$D_p = \frac{\pi\lambda^2}{32ab} D_E D_H = \frac{\pi}{32(0.5)(0.25)} (12.79)(7.52) = 75.54 = 18.78 \text{ dB}$$

Utilizing the values of  $D_E$  and  $D_H$  computed using, respectively, (13-20c) and (13-42c), the directivity of (13-54e) is equal to

$$D_p = \frac{\pi\lambda^2}{32ab} D_E D_H = \frac{\pi}{32(0.5)0.25} (12.89)(8.338) = 84.41 = 19.26 \text{ dB}$$

For this horn

$$s = \frac{b_1^2}{8\lambda\rho_1} = \frac{(2.75)^2}{8(6)} = 0.1575$$

$$t = \frac{a_1^2}{8\lambda\rho_2} = \frac{(5.5)^2}{8(6)} = 0.63$$

For these values of  $s$  and  $t$

$$L_E = 0.20 \text{ dB}$$

$$L_H = 2.75 \text{ dB}$$

from Figure 13.23. Using (13-53)

$$D_p = 10\{1.008 + \log_{10}[5.5(2.75)]\} - (0.20 + 2.75) = 18.93 \text{ dB}$$

The agreement is best between the directivities of (13-52a) and (13-53).

A MATLAB and FORTRAN computer program entitled **Pyramidal Horn-Analysis** has been developed to analyze the radiation characteristics of a pyramidal horn and the directivities of the corresponding  $E$ - and  $H$ -plane sectoral horns. The program and the READ ME file are found in the CD attached to the book.

### 13.4.3 Design Procedure

The pyramidal horn is widely used as a standard to make gain measurements of other antennas (see Section 17.4, Chapter 17), and as such it is often referred to as a *standard gain horn*. To design a pyramidal horn, one usually knows the desired gain  $G_0$  and the dimensions  $a$ ,  $b$  of the rectangular feed waveguide. The objective of the design is



to determine the remaining dimensions ( $a_1$ ,  $b_1$ ,  $\rho_e$ ,  $\rho_h$ ,  $P_e$ , and  $P_h$ ) that will lead to an optimum gain. The procedure that follows can be used to accomplish this [2], [3].

The design equations are derived by first selecting values of  $b_1$  and  $a_1$  that lead, respectively, to optimum directivities for the  $E$ - and  $H$ -plane sectoral horns using (13-19a) and (13-41c). Since the overall efficiency (including both the antenna and aperture efficiencies) of a horn antenna is about 50% [2], [3], the gain of the antenna can be related to its physical area. Thus it can be written using (12-39c), (12-40), and (13-19a), (13-41c) as

$$G_0 = \frac{1}{2} \frac{4\pi}{\lambda^2} (a_1 b_1) = \frac{2\pi}{\lambda^2} \sqrt{3\lambda\rho_2} \sqrt{2\lambda\rho_1} \simeq \frac{2\pi}{\lambda^2} \sqrt{3\lambda\rho_h} \sqrt{2\lambda\rho_e} \quad (13-55)$$

since for long horns  $\rho_2 \simeq \rho_h$  and  $\rho_1 \simeq \rho_e$ . For a pyramidal horn to be physically realizable,  $P_e$  and  $P_h$  of (13-49a) and (13-49b) must be equal. Using this equality, it can be shown that (13-55) reduces to

$$\left( \sqrt{2\chi} - \frac{b}{\lambda} \right)^2 (2\chi - 1) = \left( \frac{G_0}{2\pi} \sqrt{\frac{3}{2\pi}} \frac{1}{\sqrt{\chi}} - \frac{a}{\lambda} \right)^2 \left( \frac{G_0^2}{6\pi^3} \frac{1}{\chi} - 1 \right) \quad (13-56)$$

where

$$\frac{\rho_e}{\lambda} = \chi \quad (13-56a)$$

$$\frac{\rho_h}{\lambda} = \frac{G_0^2}{8\pi^3} \left( \frac{1}{\chi} \right) \quad (13-56b)$$

Equation (13-56) is the horn-design equation.

1. As a first step of the design, find the value of  $\chi$  which satisfies (13-56) for a desired gain  $G_0$  (dimensionless). Use an iterative technique and begin with a trial value of

$$\chi(\text{trial}) = \chi_1 = \frac{G_0}{2\pi\sqrt{2\pi}} \quad (13-57)$$

2. Once the correct  $\chi$  has been found, determine  $\rho_e$  and  $\rho_h$  using (13-56a) and (13-56b), respectively.
3. Find the corresponding values of  $a_1$  and  $b_1$  using (13-19a) and (13-41c) or

$$a_1 = \sqrt{3\lambda\rho_2} \simeq \sqrt{3\lambda\rho_h} = \frac{G_0}{2\pi} \sqrt{\frac{3}{2\pi\chi}} \lambda \quad (13-58a)$$

$$b_1 = \sqrt{2\lambda\rho_1} \simeq \sqrt{2\lambda\rho_e} = \sqrt{2\chi\lambda} \quad (13-58b)$$

4. The values of  $p_e$  and  $p_h$  can be found using (13-49a) and (13-49b).

A MATLAB and FORTRAN computer program entitled **Pyramidal Horn-Design** has been developed to accomplish this, and it is included in the CD attached to the book.

**Example 13.6**

Design an optimum gain X-band (8.2–12.4 GHz) pyramidal horn so that its gain (above isotropic) at  $f = 11$  GHz is 22.6 dB. The horn is fed by a WR 90 rectangular waveguide with inner dimensions of  $a = 0.9$  in. (2.286 cm) and  $b = 0.4$  in. (1.016 cm).

*Solution:* Convert the gain  $G_0$  from dB to a dimensionless quantity. Thus

$$G_0(\text{dB}) = 22.6 = 10 \log_{10} G_0 \Rightarrow G_0 = 10^{2.26} = 181.97$$

Since  $f = 11$  GHz,  $\lambda = 2.7273$  cm and

$$a = 0.8382\lambda$$

$$b = 0.3725\lambda$$

1. The initial value of  $\chi$  is taken, using (13-57), as

$$\chi_1 = \frac{181.97}{2\pi\sqrt{2\pi}} = 11.5539$$

which does not satisfy (13-56) for the desired design specifications. After a few iterations, a more accurate value is  $\chi = 11.1157$ .

2. Using (13-56a) and (13-56b)

$$\rho_e = 11.1157\lambda = 30.316 \text{ cm} = 11.935 \text{ in.}$$

$$\rho_h = 12.0094\lambda = 32.753 \text{ cm} = 12.895 \text{ in.}$$

3. The corresponding values of  $a_1$  and  $b_1$  are

$$a_1 = 6.002\lambda = 16.370 \text{ cm} = 6.445 \text{ in.}$$

$$b_1 = 4.715\lambda = 12.859 \text{ cm} = 5.063 \text{ in.}$$

4. The values of  $p_e$  and  $p_h$  are equal to

$$p_e = p_h = 10.005\lambda = 27.286 \text{ cm} = 10.743 \text{ in.}$$

The same values are obtained using the computer program at the end of this chapter.

The derived design parameters agree closely with those of a commercial gain horn available in the market. As a check, the gain of the designed horn was computed using (13-52a) and (13-53), assuming an antenna efficiency  $e_t$  of 100%, and (13-55). The values were

$$G_0 \simeq D_0 = 22.4 \text{ dB} \quad \text{for (13-52a)}$$

$$G_0 \simeq D_0 = 22.1 \text{ dB} \quad \text{for (13-53)}$$

$$G_0 = 22.5 \text{ dB} \quad \text{for (13-55)}$$

All three computed values agree closely with the designed value of 22.6 dB.

The previous formulations for all three horn configurations ( $E$ -plane,  $H$ -plane, and pyramidal) are based on the use of the *quadratic* phase term of (13-2b) instead of the *spherical* phase term of (13-2a). This was necessary so that the integrations can be performed and expressed in terms of cosine and sine Fresnel integrals. In order to examine the differences using the *spherical* phase term instead of the *quadratic*, especially as it relates to the directivity, a numerical integration was used in [20]. It was found that the directivity of a *pyramidal* horn of Figure 13.18 using the spherical phase term, instead of the quadratic

- *is basically the same for*
  1. large aperture horns ( $a_1, b_1 > 50\lambda$ );
  2. small peak aperture phase errors ( $S = \rho_e - \rho_1 < 0.2\lambda$  or  $T = \rho_h - \rho_2 < 0.2\lambda$  of Figure 13.18).
- *is slightly higher (more improved) by as much as 0.6 dB for*
  1. intermediate apertures ( $5\lambda \leq a_1 \leq 8\lambda$  or  $5\lambda \leq b_1 \leq 8\lambda$ );
  2. intermediate peak aperture phase errors ( $0.2\lambda \leq S = \rho_e - \rho_1 \leq 0.6\lambda$  or  $0.2\lambda \leq T = \rho_h - \rho_2 \leq 0.6\lambda$  of Figure 13.18).
- *can be lower, especially for  $E$ -plane horns, for*
  1. large peak aperture phase errors ( $S = \rho_e - \rho_1 > 0.6\lambda$  or  $T = \rho_h - \rho_2 > 0.6\lambda$  of Figure 13.18).

### 13.5 CONICAL HORN

Another very practical microwave antenna is the conical horn shown in Figure 13.26. While the pyramidal,  $E$ -, and  $H$ -plane sectoral horns are usually fed by a rectangular waveguide, the feed of a conical horn is often a circular waveguide.

The first rigorous treatment of the fields radiated by a conical horn is that of Schorr and Beck [21]. The modes within the horn are found by introducing a spherical coordinate system and are in terms of spherical Bessel functions and Legendre polynomials. The analysis is too involved and will not be attempted here. However data, in the

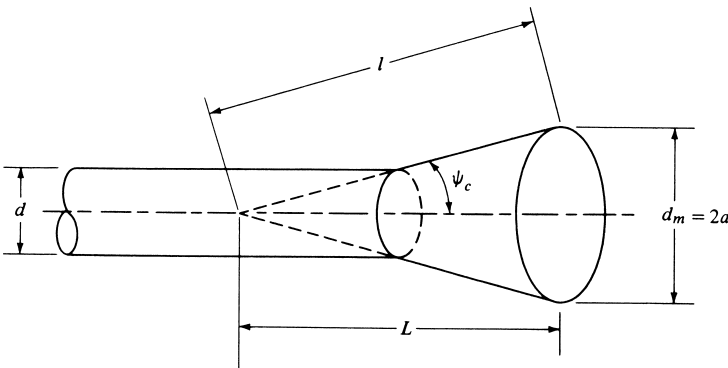


**Figure 13.26** Geometry of conical horn.

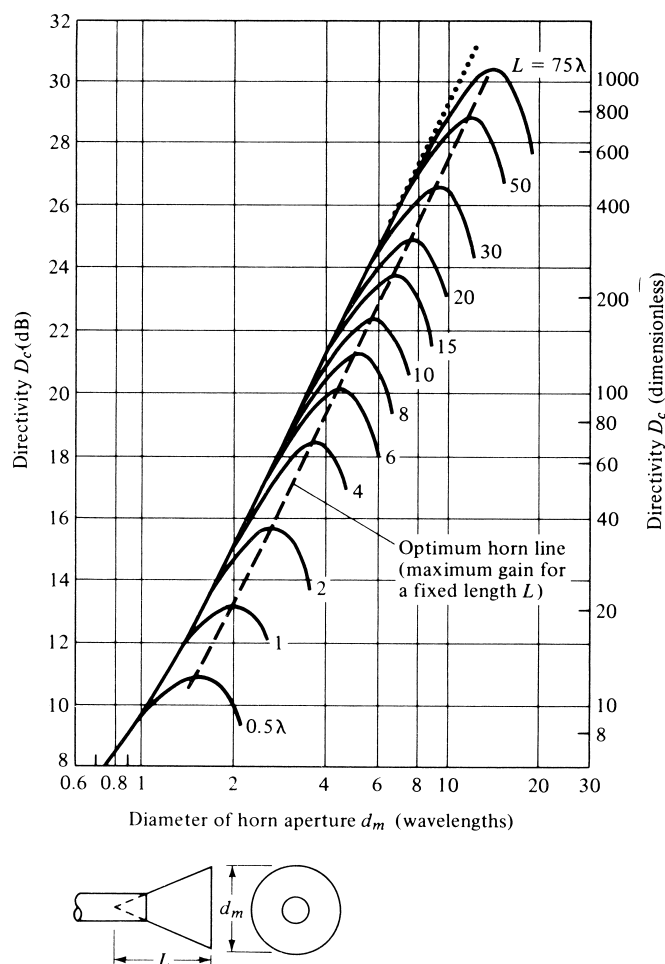


**Figure 13.27** Directivity of a conical horn as a function of aperture diameter and for different axial horn lengths. (SOURCE: A. P. King, "The Radiation Characteristics of Conical Horn Antennas," *Proc. IRE*, Vol. 38, pp. 249–251, March 1950. © 1950 IEEE)

form of curves [22], will be presented which give a qualitative description of the performance of a conical horn.

Referring to Figure 13.27, it is apparent that the behavior of a conical horn is similar to that of a pyramidal or a sectoral horn. As the flare angle increases, the directivity for a given length horn increases until it reaches a maximum beyond which it begins to decrease. The decrease is a result of the dominance of the quadratic phase error at the aperture. In the same figure, an optimum directivity line is indicated.

The results of Figure 13.27 behave as those of Figures 13.8 and 13.16. When the horn aperture ( $d_m$ ) is held constant and its length ( $L$ ) is allowed to vary, the maximum directivity is obtained when the flare angle is zero ( $\psi_c = 0$  or  $L = \infty$ ). This is equivalent to a circular waveguide of diameter  $d_m$ . As for the pyramidal and sectoral horns, a lens is usually placed at the aperture of the conical horn to compensate for its quadratic phase error. The result is a narrower pattern as its flare increases.

The directivity (*in dB*) of a conical horn, with an aperture efficiency of  $\epsilon_{ap}$  and aperture circumference  $C$ , can be computed using

$$D_c(\text{dB}) = 10 \log_{10} \left[ \epsilon_{ap} \frac{4\pi}{\lambda^2} (\pi a^2) \right] = 10 \log_{10} \left( \left( \frac{C}{\lambda} \right)^2 - L(s) \right) \quad (13-59)$$

where  $a$  is the radius of the horn at the aperture and

$$L(s) = -10 \log_{10}(\epsilon_{ap}) \quad (13-59a)$$

The first term in (13-59) represents the directivity of a uniform circular aperture whereas the second term, represented by (13-59a), is a correction figure to account for the loss in directivity due to the aperture efficiency. Usually the term in (13-59a) is referred to as *loss figure* which can be computed (*in decibels*) using [2], [3]

$$L(s) \simeq (0.8 - 1.71s + 26.25s^2 - 17.79s^3) \quad (13-59b)$$

where  $s$  is the maximum phase deviation (*in wavelengths*), and it is given by

$$s = \frac{d_m^2}{8\lambda l} \quad (13-59c)$$

The directivity of a conical horn is optimum when its diameter is equal to

$$d_m \simeq \sqrt{3l\lambda} \quad (13-60)$$

which corresponds to a maximum aperture phase deviation of  $s = 3/8$  (*wavelengths*) and a loss figure of about 2.9 dB (or an aperture efficiency of about 51%).

A summary of all the pertinent formulas and equation numbers that can be used to compute the directivity of *E*-plane, *H*-plane, pyramidal, and conical horns is listed in Table 13.1.

## 13.6 CORRUGATED HORN

The large emphasis placed on horn antenna research in the 1960s was inspired by the need to reduce spillover efficiency and cross-polarization losses and increase aperture efficiencies of large reflectors used in radio astronomy and satellite communications. In the 1970s, high-efficiency and rotationally symmetric antennas were needed in microwave radiometry. Using conventional feeds, aperture efficiencies of 50–60% were obtained. However, efficiencies of the order of 75–80% can be obtained with improved feed systems utilizing corrugated horns.

The aperture techniques introduced in Chapter 12 can be used to compute the pattern of a horn antenna and would yield accurate results only around the main lobe and the first few minor lobes. The antenna pattern structure in the back lobe region is strongly influenced by diffractions from the edges, especially from those that are perpendicular

**TABLE 13.1 Directivity Formulas and Equation Numbers For Horns**

Horn Type	Directivity	Equation Number
<i>E</i> -plane	$D_E = \frac{64a\rho_1}{\pi\lambda b_1} \left[ C^2 \left( \frac{b_1}{\sqrt{2\lambda\rho_1}} \right) + S^2 \left( \frac{b_1}{\sqrt{2\lambda\rho_1}} \right) \right]$	(13-19)
<i>E</i> -plane (alternate)	$D_E = \frac{a}{\lambda} \frac{G_E}{\sqrt{\frac{50}{\rho_e/\lambda}}}, \quad B = \frac{b_1}{\lambda} \sqrt{\frac{50}{\rho_e/\lambda}}$ $G_E = \frac{32}{\pi} B \quad \text{if } B < 2$ $G_E \text{ from Figure 13.9} \quad \text{if } B \geq 2$	(13-20c), (13-20a)  (13-20b) Figure 13.9
<i>H</i> -plane	$D_H = \frac{4\pi b\rho_2}{a_1\lambda} \{ [C(u) - C(v)]^2 + [S(u) - S(v)]^2 \}$ $u = \frac{1}{\sqrt{2}} \left( \frac{\sqrt{\lambda\rho_2}}{a_1} + \frac{a_1}{\sqrt{\lambda\rho_2}} \right), \quad v = \frac{1}{\sqrt{2}} \left( \frac{\sqrt{\lambda\rho_2}}{a_1} - \frac{a_1}{\sqrt{\lambda\rho_2}} \right)$	(13-41)  (13-41a), (13-41b)
<i>H</i> -plane (alternate)	$D_H = \frac{b}{\lambda} \frac{G_H}{\sqrt{\frac{50}{\rho_h/\lambda}}}, \quad A = \frac{a_1}{\lambda} \sqrt{\frac{50}{\rho_h/\lambda}}$ $G_H = \frac{32}{\pi} A \quad \text{if } A < 2$ $G_H \text{ from Figure 13.17} \quad \text{if } A \geq 2$	(13-42c), (13-42a)  (13-42b) Figure 13.17
Pyramidal	$D_P = \frac{\pi\lambda^2}{32ab} D_E D_H$	(13-52a), (13-19), (13-41)
Pyramidal (alternate)	$D_P(dB) = 10 \left[ 1.008 + \log_{10} \left( \frac{a_1 b_1}{\lambda^2} \right) \right] - (L_e + L_h)$ $L_e, L_h$	(13-53)  Figure 13.23
Pyramidal (alternate)	$D_P = \frac{G_E G_H}{\frac{32}{\pi} \sqrt{\frac{50}{\rho_e/\lambda}} \sqrt{\frac{50}{\rho_h/\lambda}}} = \frac{\lambda^2 \pi}{32ab} D_E D_H$	(13-54e), (13-52a) (13-20c), (13-42c)
Conical	$D_c(dB) = 10 \log_{10} \left[ \varepsilon_{ap} \frac{4\pi}{\lambda^2} (\pi a^2) \right] = 10 \log_{10} \left( \frac{C}{\lambda} \right)^2 - L(s)$ $L(s) = -10 \log_{10}(\varepsilon_{ap}) \simeq (0.8 - 1.71s + 26.25s^2 - 17.79s^3)$ $s = \frac{d_m^2}{8\lambda\ell}, \quad d_m \simeq \sqrt{3\ell\lambda}$	(13-59)  (13-59a), (13-59b)  (13-59c), (13-60)

to the  $E$ -field at the horn aperture. The diffractions lead to undesirable radiation not only in the back lobes but also in the main lobe and in the minor lobes. However, they dominate only in low-intensity regions.

In 1964, Kay [23] realized that grooves on the walls of a horn antenna would present the same boundary conditions to all polarizations and would taper the field distribution at the aperture in all the planes. The creation of the same boundary conditions on all four walls would eliminate the spurious diffractions at the edges of the aperture. For a square aperture, this would lead to an almost rotationally symmetric pattern with equal  $E$ - and  $H$ -plane beamwidths. A *corrugated (grooved)* pyramidal horn, with corrugations in the  $E$ -plane walls, is shown in Figure 13.28(a) with a side view in Figure 13.28(b). Since diffractions at the edges of the aperture in the  $H$ -plane are minimal, corrugations are usually not placed on the walls of that plane. Corrugations can also be placed in a conical horn forming a *conical corrugated* horn, also referred to in [23] as a *scalar horn*. However, instead of the corrugations being formed as shown in Figure 13.29(a), practically it is much easier to machine them to have the profile shown in Figure 13.29(b).

A photograph of a corrugated conical horn, often referred to as a *scalar* horn, is shown in Figure 13.30. This type of a horn is widely used as a feed of reflector antennas, especially of the Cassegrain (dual reflector) configuration of Figures 15.9 and 15.29.

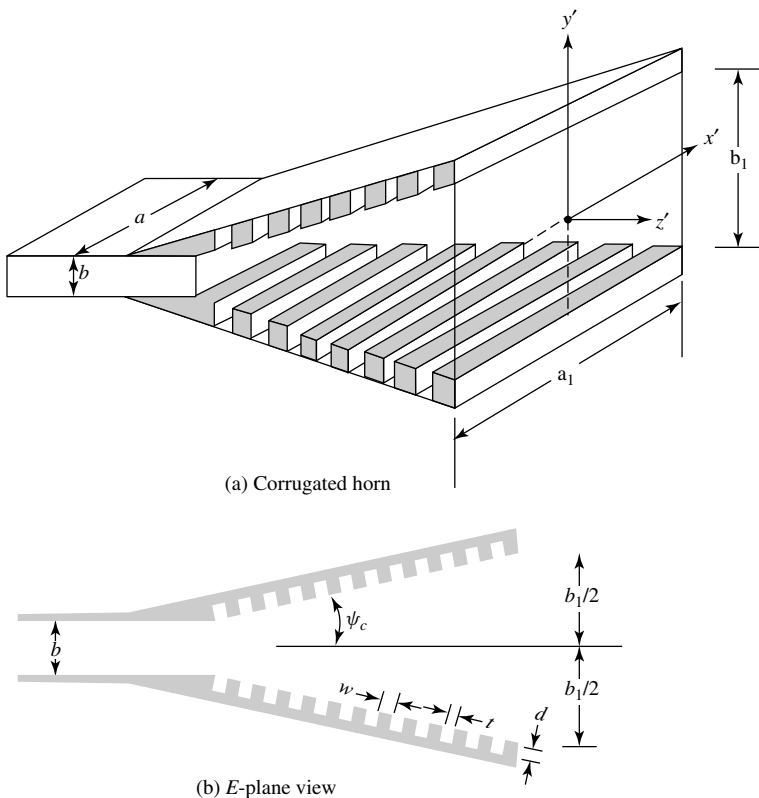


**Figure 13.28** Pyramidal horn with corrugations in the  $E$ -plane.

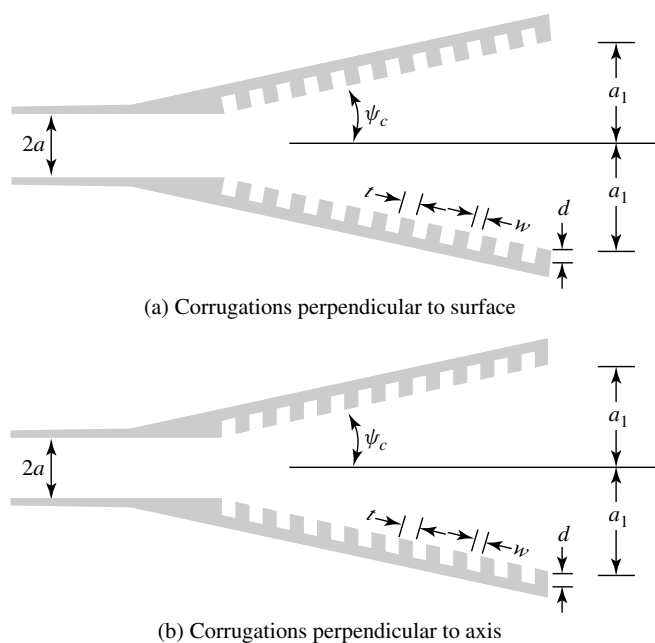


**Figure 13.29** Side view profiles of conical corrugated horns.



**Figure 13.30** Corrugated conical (scalar) horn. (COURTESY: March Microwave Systems, B.V., The Netherlands)



To form an effective corrugated surface, it usually requires 10 or more slots (corrugations) per wavelength [24]. To simplify the analysis of an infinite corrugated surface, the following assumptions are usually required:

1. The teeth of the corrugations are vanishingly thin.
2. Reflections from the base of the slot are only those of a TEM mode.

The second assumption is satisfied provided the width of the corrugation ( $w$ ) is small compared to the free-space wavelength ( $\lambda_0$ ) and the slot depth ( $d$ ) (usually  $w < \lambda_0/10$ ). For a corrugated surface satisfying the above assumptions, its approximate surface reactance is given by [25], [26]

$$X = \frac{w}{w + t} \sqrt{\frac{\mu_0}{\epsilon_0}} \tan(k_0 d) \quad (13-61)$$

when

$$\frac{w}{w + t} \simeq 1 \quad (13-61a)$$

which can be satisfied provided  $t \leq w/10$ .

The surface reactance of a corrugated surface, used on the walls of a horn, must be capacitive in order for the surface to force to zero the tangential magnetic field parallel to the edge at the wall. Such a surface will not support surface waves, will prevent illumination of the  $E$ -plane edges, and will diminish diffractions. This can be accomplished, according to (13-61), if  $\lambda_0/4 < d < \lambda_0/2$  or more generally when  $(2n + 1)\lambda_0/4 < d < (n + 1)\lambda_0/2$ . Even though the cutoff depth is also a function of the slot width  $w$ , its influence is negligible if  $w < \lambda_0/10$  and  $\lambda_0/4 < d < \lambda_0/2$ .

The effect of the corrugations on the walls of a horn is to modify the electric field distribution in the  $E$ -plane from uniform (at the waveguide-horn junction) to cosine (at the aperture). Through measurements, it has been shown that the transition from uniform to cosine distribution takes place almost at the onset of the corrugations. For a horn of about 45 corrugations, the cosine distribution has been established by the fifth corrugation (from the onset) and the spherical phase front by the fifteenth [27].

Referring to Figure 13.28(a), the field distribution at the aperture can be written as

$$E'_y(x', y') = E_0 \cos\left(\frac{\pi}{a_1}x'\right) \cos\left(\frac{\pi}{b_1}y'\right) e^{-j[k(x'^2/\rho_2 + y'^2/\rho_1)/2]} \quad (13-62a)$$

$$H'_x(x', y') = -\frac{E_0}{\eta} \cos\left(\frac{\pi}{a_1}x'\right) \cos\left(\frac{\pi}{b_1}y'\right) e^{-j[k(x'^2/\rho_2 + y'^2/\rho_1)/2]} \quad (13-62b)$$

corresponding to (13-43a) and (13-43b) of the uncorrugated pyramidal horn. Using the above distributions, the fields radiated by the horn can be computed in a manner analogous to that of the pyramidal horn of Section 13.4. Patterns have been computed and compare very well with measurements [27].

In Figure 13.31(a) the measured  $E$ -plane patterns of an uncorrugated square pyramidal horn (*referred to as the control horn*) and a corrugated square pyramidal horn

are shown. The aperture size on each side was 3.5 in. ( $2.96\lambda$  at 10 GHz) and the total flare angle in each plane was  $50^\circ$ . It is evident that the levels of the minor lobes and back lobes are much lower for the corrugated horn than those of the control horn. However the corrugated horn also exhibits a wider main beam for small angles; thus a larger 3-dB beamwidth (HPBW) but a lower 10-dB beamwidth. This is attributed to the absence of the diffracted fields from the edges of the corrugated horn which, for nearly on-axis observations, add to the direct wave contribution because of their in-phase relationship. The fact that the on-axis far-fields of the direct and diffracted fields are nearly in phase is also evident from the pronounced on-axis maximum of the control horn. The  $E$ - and  $H$ -plane patterns of the corrugated horn are almost identical to those of Figure 13.31(a) over the frequency range from 8 to 14 GHz. These suggest that the main beam in the  $E$ -plane can be obtained from known  $H$ -plane patterns of horn antennas.

In Figure 13.31(b) the measured  $E$ -plane patterns of larger control and corrugated square pyramidal horns, having an aperture of 9.7 in. on each side ( $8.2\lambda$  at 10 GHz) and included angles of  $34^\circ$  and  $31^\circ$  in the  $E$ - and  $H$ -planes, respectively, are shown. For this geometry, the pattern of the corrugated horn is narrower and its minor and back lobes are much lower than those of the corresponding control horn. The saddle formed on the main lobe of the control horn is attributed to the out-of-phase relations between the direct and diffracted rays. The diffracted rays are nearly absent from the corrugated horn and the minimum on-axis field is eliminated. The control horn is a thick-edged horn which has the same interior dimensions as the corrugated horn. The  $H$ -plane pattern of the corrugated horn is almost identical to the  $H$ -plane pattern of the corresponding control horn.

In Figures 13.31(c) and 13.31(d) the back lobe level and the 3-dB beamwidth for the smaller size control and corrugated horns, whose  $E$ -plane patterns are shown in Figure 13.31(a), are plotted as a function of frequency. All the observations made previously for that horn are well evident in these figures.

The presence of the corrugations, especially near the waveguide-horn junction, can affect the impedance and VSWR of the antenna. The usual practice is to begin the corrugations at a small distance away from the junction. This leads to low VSWR's over a broad band. Previously it was indicated that the width  $w$  of the corrugations must be small (usually  $w < \lambda_0/10$ ) to approximate a corrugated surface. This would cause corona and other breakdown phenomena. However the large corrugated horn, whose  $E$ -plane pattern is shown in Figure 13.31(b), has been used in a system whose peak power was 20 kW at 10 GHz with no evidence of any breakdown phenomena.

The design concepts of the pyramidal corrugated horn can be extended to include circumferentially corrugated conical horns, as shown in Figures 13.29 and 13.30. Several designs of conical corrugated horns were investigated in terms of pattern symmetry, low cross polarization, low side lobe levels, circular polarization, axial ratio, and phase center [28]–[37]. For small flare angles ( $\psi_c$  less than about  $20^\circ$  to  $25^\circ$ ) the slots can be machined perpendicular to the axis of the horn, as shown in Figure 13.29(b), and the grooves can be considered sections of parallel-plate TEM-mode waveguides of depth  $d$ . For large flare angles, however, the slots should be constructed perpendicular to the surface of the horn, as shown in Figure 13.29(a) and implemented in the design of Figure 13.30. The groove arrangement of Figure 13.29(b) is usually preferred because it is easier to fabricate.

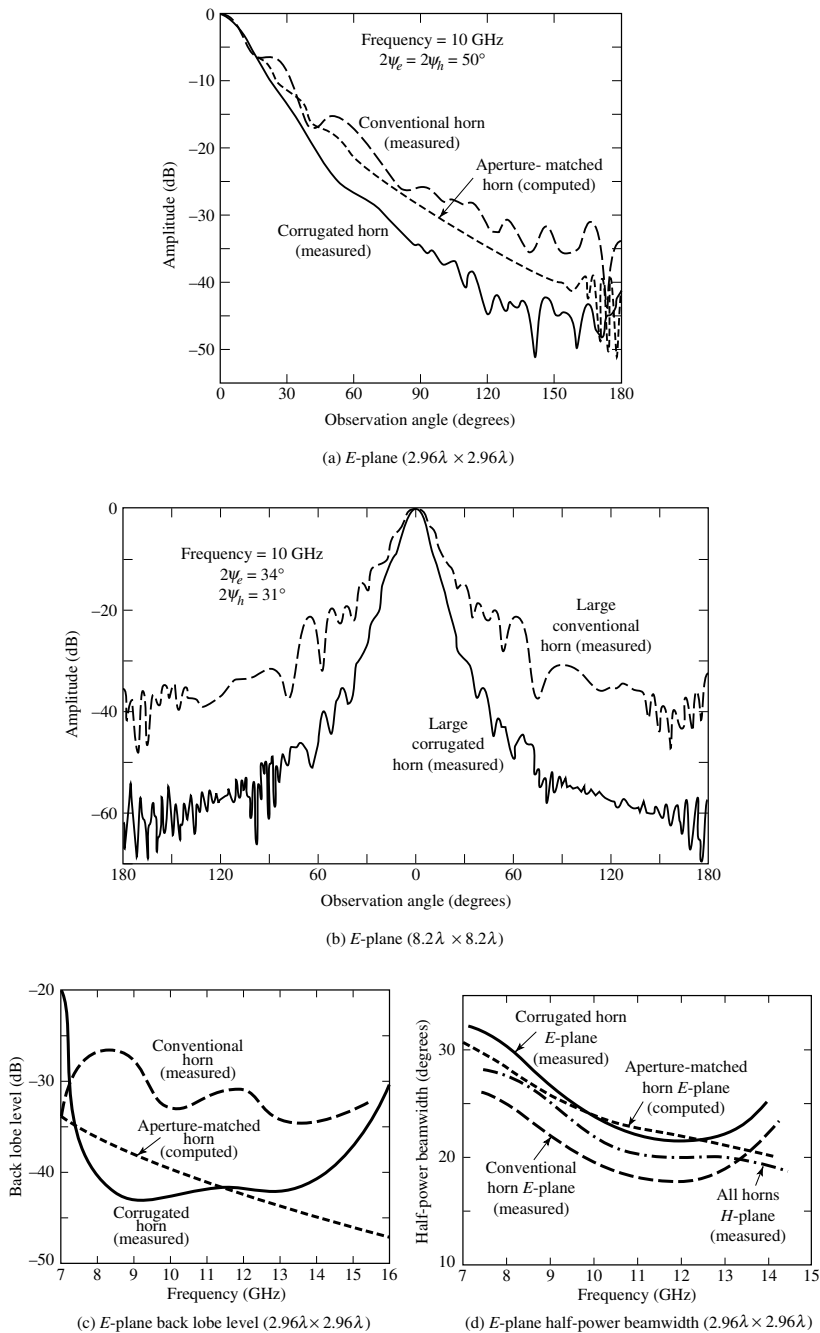
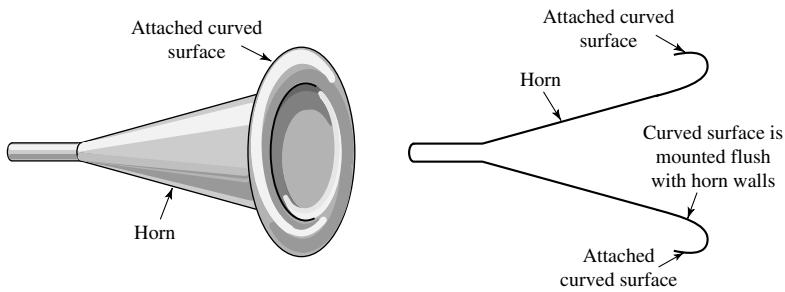


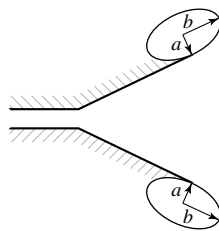
**Figure 13.31** Radiation characteristics of conventional (control), corrugated, and aperture-matched pyramidal horns. (SOURCE: (a), (c), (d). W. D. Burnside and C. W. Chuang, "An Aperture-Matched Horn Design," *IEEE Trans. Antennas Propagat.*, Vol. AP-30, No. 4, pp. 790–796, July 1982. © 1982 IEEE (b) R. E. Laurie and L. Peters, Jr., "Modifications of Horn Antennas for Low Side Lobe Levels," *IEEE Trans. Antennas Propagat.*, Vol. AP-14, No. 5, pp. 605–610, September 1966. © 1966 IEEE)

### 13.7 APERTURE-MATCHED HORNS

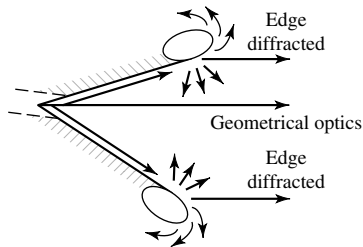
A horn which provides significantly better performance than an ordinary horn (in terms of pattern, impedance, and frequency characteristics) is that shown in Figure 13.32(a), which is referred to as an *aperture-matched* horn [38]. The main modification to the ordinary (conventional) horn, which we refer to here as the *control* horn, consists of



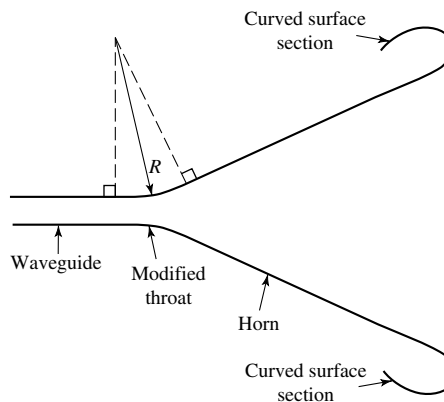
(a) Basic geometry



(b) Elliptical cylinder curved surface



(c) Diffraction mechanism



(d) Modified throat

**Figure 13.32** Geometry and diffraction mechanism of an aperture-matched horn. (SOURCE: W. D. Burnside and C. W. Chuang, "An Aperture-Matched Horn Design," *IEEE Trans. Antennas Propagat.*, Vol. AP-30, No. 4, pp. 790–796, July 1982. © 1982 IEEE)

the attachment of curved-surface sections to the outside of the aperture edges, which reduces the diffractions that occur at the sharp edges of the aperture and provides smooth matching sections between the horn modes and the free-space radiation.

In contrast to the corrugated horn, which is complex and costly and reduces the diffractions at the edges of the aperture by minimizing the incident field, the aperture-matched horn reduces the diffractions by modifying the structure (without sacrificing size, weight, bandwidth, and cost) so that the diffraction coefficient is minimized. The basic concepts were originally investigated using elliptic cylinder sections, as shown in Figure 13.32(b); however, other convex curved surfaces, which smoothly blend to the ordinary horn geometry at the attachment point, will lead to similar improvements. This modification in geometry can be used in a wide variety of horns, and includes *E*-plane, *H*-plane, pyramidal, and conical horns. Bandwidths of 2:1 can be attained easily with aperture-matched horns having elliptical, circular, or other curved surfaces. The radii of curvature of the curved surfaces used in experimental models [38] ranged over  $1.69\lambda \leq a \leq 8.47\lambda$  with  $a = b$  and  $b = 2a$ . Good results can be obtained by using circular cylindrical surfaces with  $2.5\lambda \leq a \leq 5\lambda$ .

The basic radiation mechanism of such a horn is shown in Figure 13.32(c). The introduction of the curved sections at the edges does not eliminate diffractions; instead it substitutes edge diffractions by curved-surface diffractions which have a tendency to provide an essentially undisturbed energy flow across the junction, around the curved surface, and into free-space. Compared with conventional horns, this radiation mechanism leads to smoother patterns with greatly reduced back lobes and negligible reflections back into the horn. The size, weight, and construction costs of the aperture-matched horn are usually somewhat larger and can be held to a minimum if half (one-half sections of an ellipse) or quadrant (one-fourth sections of an ellipse) sections are used instead of the complete closed surfaces.

To illustrate the improvements provided by the aperture-matched horns, the *E*-plane pattern, back lobe level, and half-power beamwidth of a pyramidal  $2.96\lambda \times 2.96\lambda$  horn were computed and compared with the measured data of corresponding control and corrugated horns. The data are shown in Figures 13.31(a,c,d). It is evident by examining the patterns of Figure 13.31(a) that the aperture-matched horn provides a smoother pattern and lower back lobe level than conventional horns (referred to here as control horn); however, it does not provide, for the wide minor lobes, the same reduction as the corrugated horn. To achieve nearly the same *E*-plane pattern for all three horns, the overall horn size must be increased. If the modifications for the aperture-matched and corrugated horns were only made in the *E*-plane edges, the *H*-plane patterns for all three horns would be virtually the same except that the back lobe level of the aperture-matched and corrugated horns would be greatly reduced.

The back lobe level of the same three horns (control, corrugated, and aperture matched) are shown in Figure 13.31(c). The corrugated horn has lower back lobe intensity at the lower end of the frequency band, while the aperture-matched horn exhibits superior performance at the high end. However, both the corrugated and aperture-matched horns exhibit superior back lobe level characteristics to the control (conventional) horn throughout almost the entire frequency band. The half-power beamwidth characteristics of the same three horns are displayed in Figure 13.31(d). Because the control (conventional) horn has uniform distribution across the complete aperture plane, compared with the tapered distributions for the corrugated and

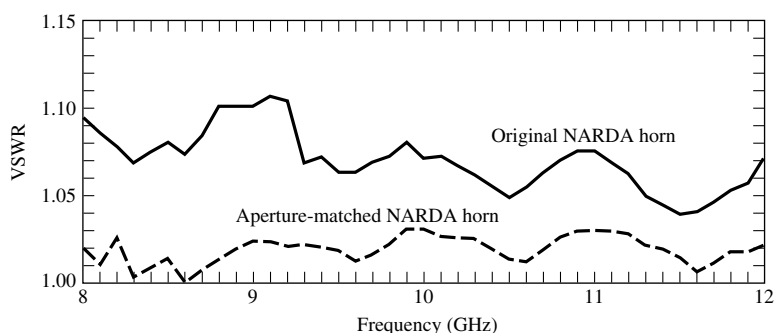


**Figure 13.33** Measured VSWR for exponentially tapered pyramidal horns (conventional and aperture matched). (SOURCE: W. D. Burnside and C. W. Chuang, "An Aperture-Matched Horn Design," *IEEE Trans. Antennas Propagat.*, Vol. AP-30, No. 4, pp. 790–796, July 1982. © 1982 IEEE)

aperture-matched horns, it possesses the smallest beamwidth almost over the entire frequency band.

In a conventional horn the VSWR and antenna impedance are primarily influenced by the throat and aperture reflections. Using the aperture-matched horn geometry of Figure 13.32(a), the aperture reflections toward the inside of the horn are greatly reduced. Therefore the only remaining dominant factors are the throat reflections. To reduce the throat reflections it has been suggested that a smooth curved surface be used to connect the waveguide and horn walls, as shown in Figure 13.32(d). Such a transition has been applied in the design and construction of a commercial X-band (8.2–12.4 GHz) pyramidal horn (see Figure 13.24), whose tapering is of an exponential nature. The VSWRs measured in the 8–12 GHz frequency band using the conventional exponential X-band horn (shown in Figure 13.24), with and without curved sections at its aperture, are shown in Figure 13.33.

The matched sections used to create the aperture-matched horn were small cylinder sections. The VSWR's for the conventional horn are very small (less than 1.1) throughout the frequency band because the throat reflections are negligible compared with the aperture reflections. It is evident, however, that the VSWR's of the corresponding aperture-matched horn are much superior to those of the conventional horn because both the throat and aperture reflections are very minimal.

The basic design of the aperture-matched horn can be extended to include corrugations on its inside surface [30]. This type of design enjoys the advantages presented by both the aperture-matched and corrugated horns with cross-polarized components of less than  $-45$  dB over a significant part of the bandwidth. Because of its excellent cross-polarization characteristics, this horn is recommended for use as a reference and for frequency reuse applications in both satellite and terrestrial applications.

### 13.8 MULTIMODE HORNS

Over the years there has been a need in many applications for horn antennas which provide symmetric patterns in all planes, phase center coincidence for the electric and magnetic planes, and side lobe suppression. All of these are attractive features

for designs of optimum reflector systems and monopulse radar systems. Side lobe reduction is a desired attribute for horn radiators utilized in antenna range, anechoic chamber, and standard gain applications, while pattern plane symmetry is a valuable feature for polarization diversity.

Pyramidal horns have traditionally been used over the years, with good success, in many of these applications. Such radiators, however, possess nonsymmetric beamwidths and undesirable side lobe levels, especially in the  $E$ -plane. Conical horns, operating in the dominant  $TE_{11}$  mode, have a tapered aperture distribution in the  $E$ -plane. Thus, they exhibit more symmetric electric- and magnetic-plane beamwidths and reduced side lobes than do the pyramidal horns. One of the main drawbacks of a conical horn is its relative incompatibility with rectangular waveguides.

To remove some of the deficiencies of pyramidal and conical horns and further improve some of their attractive characteristics, corrugations were introduced on the interior walls of the waveguides, which lead to the corrugated horns that were discussed in a previous section of this chapter. In some other cases designs were suggested to improve the beamwidth equalization in all planes and reduce side lobe levels by utilizing horn structures with multiple-mode excitations. These have been designated as *multimode* horns, and some of the designs will be discussed briefly here. For more information the reader should refer to the cited references.

One design of a multimode horn is the “diagonal” horn [39], shown in Figure 13.34, all of whose cross sections are square and whose internal fields consist of a superposition of  $TE_{10}$  and  $TE_{01}$  modes in a square waveguide. For small flare angles, the field structure within the horn is such that the  $\mathbf{E}$ -field vector is parallel to one of the diagonals. Although it is not a multimode horn in the true sense of the word, because it does not make use of higher-order TE and TM modes, it does possess the desirable attributes of the usual multimode horns, such as equal beamwidths and suppressed beamwidths

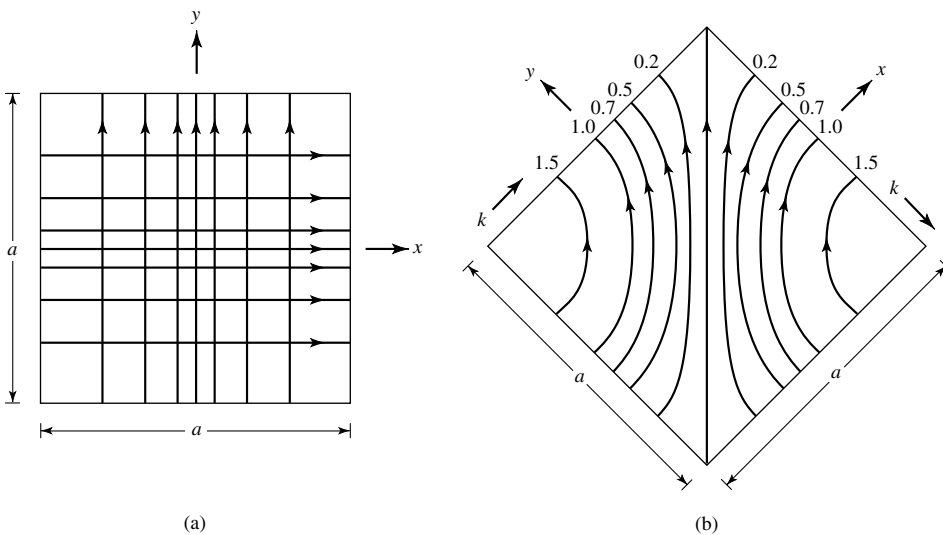


**Figure 13.34** electric field configuration inside square diagonal horn. (a) Two coexisting equal orthogonal modes. (b) Result of combining the two modes shown in (a). (After Love [39] reprinted with permission of *Microwave Journal*, Vol. V, No. 3, March 1962)

and side lobes in the  $E$ - and  $H$ -planes which are nearly equal to those in the principal planes. These attractive features are accomplished, however, at the expense of pairs of cross-polarized lobes in the intercardinal planes which make such a horn unattractive for applications where a high degree of polarization purity is required.

Diagonal horns have been designed, built, and tested [39] such that the 3-, 10-, and 30-dB beamwidths are nearly equal not only in the principal  $E$ - and  $H$ -planes, but also in the  $45^\circ$  and  $135^\circ$  planes. Although the theoretical limit of the side lobe level in the principal planes is 31.5 dB down, side lobes of at least 30 dB down have been observed in those planes. Despite a theoretically predicted level of  $-19.2$  dB in the  $\pm 45^\circ$  planes, side lobes with level of  $-23$  to  $-27$  dB have been observed. The principal deficiency in the side lobe structure appears in the  $\pm 45^\circ$ -plane cross-polarized lobes whose intensity is only 16 dB down; despite this, the overall horn efficiency remains high. Compared with diagonal horns, conventional pyramidal square horns have  $H$ -plane beamwidths which are about 35% wider than those in the  $E$ -plane, and side lobe levels in the  $E$ -plane which are only 12 to 13 dB down (although those in the  $H$ -plane are usually acceptable).

For applications which require optimum performance with narrow beamwidths, lenses are usually recommended for use in conjunction with diagonal horns. Diagonal horns can also be converted to radiate circular polarization by inserting a differential phase shifter inside the feed guide whose cross section is circular and adjusted so that it produces phase quadrature between the two orthogonal modes.

Another multimode horn which exhibits suppressed side lobes, equal beamwidths, and reduces cross polarization is the *dual-mode* conical horn [40]. Basically this horn is designed so that diffractions at the aperture edges of the horn, especially those in the  $E$ -plane, are minimized by reducing the fields incident on the aperture edges and consequently the associated diffractions. This is accomplished by utilizing a conical horn which at its throat region is excited in both the dominant  $TE_{11}$  and higher-order  $TM_{11}$  mode. A discontinuity is introduced at a position within the horn where two modes exist. The horn length is adjusted so that the superposition of the relative amplitudes of the two modes at the edges of the aperture is very small compared with the maximum aperture field magnitude. In addition, the dimensions of the horn are controlled so that the total phase at the aperture is such that, in conjunction with the desired amplitude distribution, it leads to side lobe suppression, beamwidth equalization, and phase center coincidence.

Qualitatively the pattern formation of a dual-mode conical horn operating in the  $TE_{11}$  and  $TM_{11}$  modes is accomplished by utilizing a pair of modes which have radiation functions with the same argument. However, one of the modes, in this case the  $TM_{11}$  mode, contains an additional envelope factor which varies very rapidly in the main beam region and remains relatively constant at large angles. Thus, it is possible to control the two modes in such a way that their fields cancel in all directions except within the main beam. The  $TM_{11}$  mode exhibits a null in its far-field pattern. Therefore a dual-mode conical horn possesses less axial gain than a conventional dominant-mode conical horn of the same aperture size. Because of that, dual-mode horns render better characteristics and are more attractive for applications where pattern plane symmetry and side lobe reduction are more important than maximum aperture efficiency. A most important application of a dual-mode horn is as a feed of Cassegrain reflector systems.

Dual-mode conical horns have been designed, built, and tested [40] with relatively good success in their performance. Generally, however, diagonal horns would be good



competitors for the dual-mode horns if it were not for the undesirable characteristics (especially the cross-polarized components) that they exhibit in the very important  $45^\circ$  and  $135^\circ$  planes. Improved performance can be obtained from dual-mode horns if additional higher-order modes (such as the  $TE_{12}$ ,  $TE_{13}$  and  $TM_{12}$ ) are excited [41] and if their relative amplitudes and phases can be properly controlled. Computed maximum aperture efficiencies of paraboloidal reflectors, using such horns as feeds, have reached 90% contrasted with efficiencies of about 76% for reflector systems using conventional dominant-mode horn feeds. In practice the actual maximum efficiency achieved is determined by the number of modes that can be excited and the degree to which their relative amplitudes and phases can be controlled.

The techniques of the dual-mode and multimode conical horns can be extended to the design of horns with rectangular cross sections. In fact a multimode pyramidal horn has been designed, built, and tested to be used as a feed in a low-noise Cassegrain monopulse system [42]. This rectangular pyramidal horn utilizes additional higher-order modes to provide monopulse capability, side lobe suppression in both the  $E$ - and  $H$ -planes, and beamwidth equalization. Specifically the various pattern modes for the monopulse system are formed in a single horn as follows:

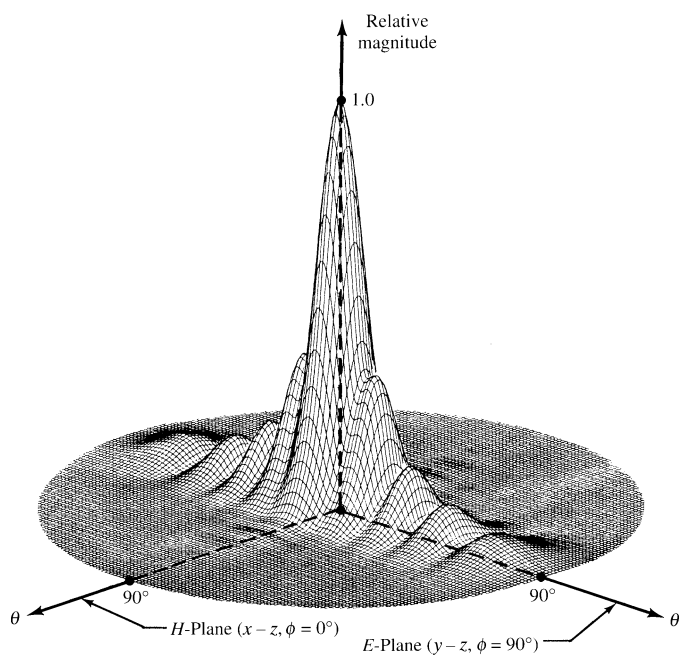
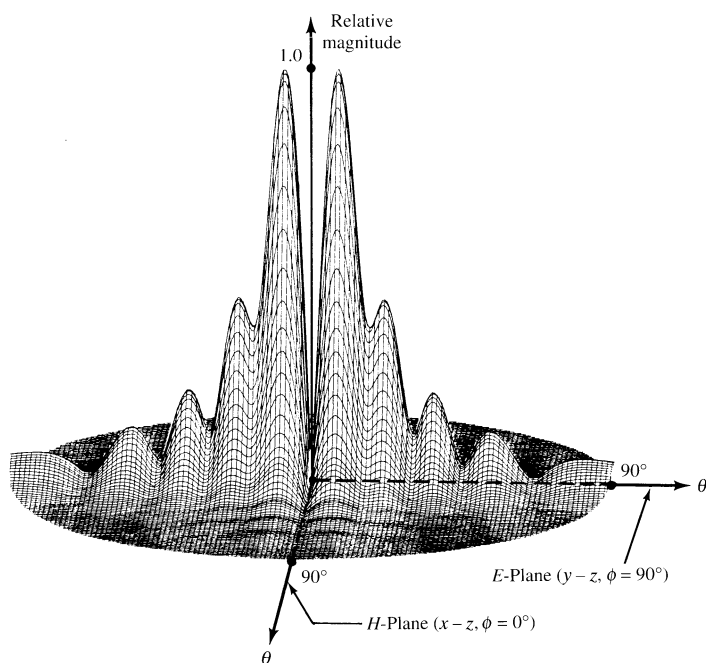
- a. *Sum*: Utilizes  $TE_{10} + TE_{30}$  instead of only  $TE_{10}$ . When the relative amplitude and phase excitations of the higher-order  $TE_{30}$  mode are properly adjusted, they provide side lobe cancellation at the second minor lobe of the  $TE_{10}$ -mode pattern
- b. *E-Plane Difference*: Utilizes  $TE_{11} + TM_{11}$  modes
- c. *H-Plane Difference*: Utilizes  $TE_{20}$  mode

In its input, the horn of [42] contained a four-guide monopulse bridge circuitry, a multimode matching section, a difference mode phasing section, and a sum mode excitation and control section. To illustrate the general concept, in Figure 13.35(a–c) are plots of three-dimensional patterns of the sum,  $E$ -plane difference, and  $H$ -plane difference modes which utilize, respectively, the  $TE_{10} + TE_{30}$ ,  $TE_{11} + TM_{11}$ , and  $TE_{20}$  modes. The relative excitation between the modes has been controlled so that each pattern utilizing multiple modes in its formation displays its most attractive features for its function.

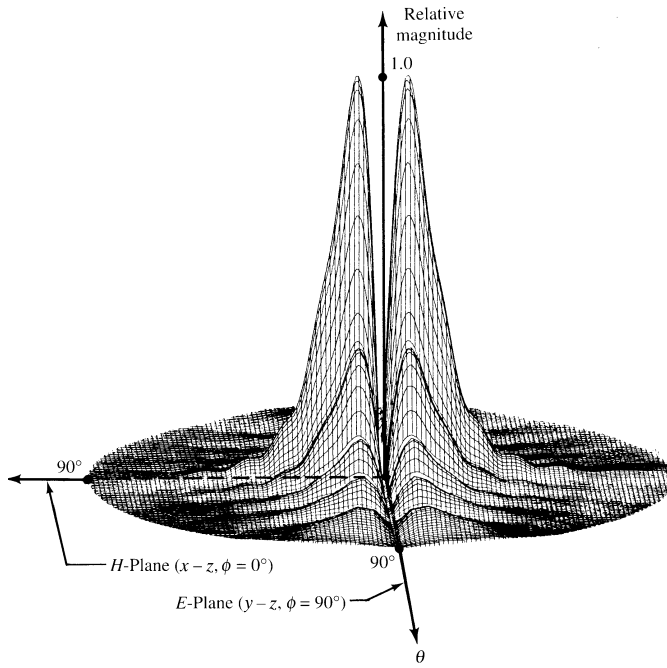
### 13.9 DIELECTRIC-LOADED HORNS

Over the years much effort has been devoted to enhance the antenna and aperture efficiencies of aperture antennas, especially for those that serve as feeds for reflectors (such as the horn). One technique that was proposed and then investigated was to use dielectric guiding structures, referred to as *Dielguides* [43], between the primary feed and the reflector (or subreflector). The technique is simple and inexpensive to implement and provides broadband, highly efficient, and low-noise antenna feeds. The method negates the compromise between taper and spillover efficiencies, and it is based on the principle of internal reflections, which has been utilized frequently in optics. Its role bears a very close resemblance to that of a lens, and it is an extension of the classical parabolic-shaped lens to other geometrical shapes.

Another method that has been used to control the radiation pattern of electromagnetic horns is to insert totally within them various shapes of dielectric material (wedges,

(a) Sum ( $TE_{10} + TE_{30}$  modes)(b)  $E$ -plane difference ( $TE_{11} + TM_{11}$  modes)

**Figure 13.35** Three-dimensional sum and difference ( $E$ - and  $H$ -planes) field patterns of a monopulse pyramidal horn. (SOURCE: C. A. Balanis, "Horn Antennas," in *Antenna Handbook* (Y. T. Lo and S. W. Lee, eds.), © 1988, Van Nostrand Reinhold Co., Inc.)


 (c) *H*-plane difference (TE<sub>20</sub> mode)

**Figure 13.35** (continued)

slabs, etc.) [44]–[52] to control in a predictable manner not only the phase distribution over the aperture, as is usually done by using the classical parabolic lenses, but also to change the power (amplitude) distribution over the aperture. The control of the amplitude and phase distributions over the aperture are essential in the design of very low side lobe antenna patterns.

Symmetrical loading of the *H*-plane walls has also been utilized, by proper parameter selection, to create a dominant longitudinal section electric (LSE) mode and to enhance the aperture efficiency and pattern-shaping capabilities of symmetrically loaded horns [44]. The method is simple and inexpensive, and it can also be utilized to realize high efficiency from small horns which can be used in limited scan arrays. Aperture efficiencies on the order of 92 to 96% have been attained, in contrast to values of 81% for unloaded horns.

A similar technique has been suggested to symmetrically load the *E*-plane walls of rectangular horns [46]–[52] and eventually to line all four of its walls with dielectric slabs. Other similar techniques have been suggested, and a summary of these and other classical papers dealing with dielectric-loaded horns can be found in [1].

## 13.10 PHASE CENTER

Each far-zone field component radiated by an antenna can be written, in general, as

$$\mathbf{E}_u = \hat{\mathbf{u}} E(\theta, \phi) e^{j\psi(\theta, \phi)} \frac{e^{-jkr}}{r} \quad (13-63)$$

where  $\hat{\mathbf{u}}$  is a unit vector. The terms  $E(\theta, \phi)$  and  $\psi(\theta, \phi)$  represent, respectively, the  $(\theta, \phi)$  variations of the amplitude and phase.

In navigation, tracking, homing, landing, and other aircraft and aerospace systems it is usually desirable to assign to the antenna a reference point such that for a given frequency,  $\psi(\theta, \phi)$  of (13-63) is independent of  $\theta$  and  $\phi$  (i.e.,  $\psi(\theta, \phi) = \text{constant}$ ). The reference point which makes  $\psi(\theta, \phi)$  independent of  $\theta$  and  $\phi$  is known as the *phase center* of the antenna [53]–[57]. When referenced to the phase center, the fields radiated by the antenna are spherical waves with ideal spherical wave fronts or equiphase surfaces. Therefore a phase center is a reference point from which radiation is said to emanate, and radiated fields measured on the surface of a sphere whose center coincides with the phase center have the same phase.

For practical antennas such as arrays, reflectors, and others, a single unique phase center valid for all values of  $\theta$  and  $\phi$  does not exist; for most, however, their phase center moves along a surface, and its position depends on the observation point. However, in many antenna systems a reference point can be found such that  $\psi(\theta, \phi) = \text{constant}$ , or nearly so, over most of the angular space, especially over the main lobe. When the phase center position variation is sufficiently small, that point is usually referred to as the *apparent phase center*.

The need for the phase center can best be explained by examining the radiation characteristics of a paraboloidal reflector (parabola of revolution). Plane waves incident on a paraboloidal reflector focus at a single point which is known as the *focal point*. Conversely, spherical waves emanating from the focal point are reflected by the paraboloidal surface and form plane waves. Thus in the receiving mode all the energy is collected at a single point. In the transmitting mode, ideal plane waves are formed if the radiated waves have spherical wavefronts and emanate from a single point.

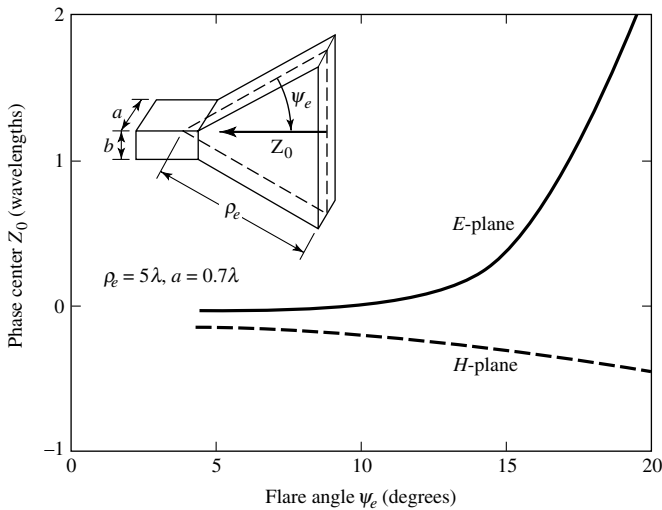
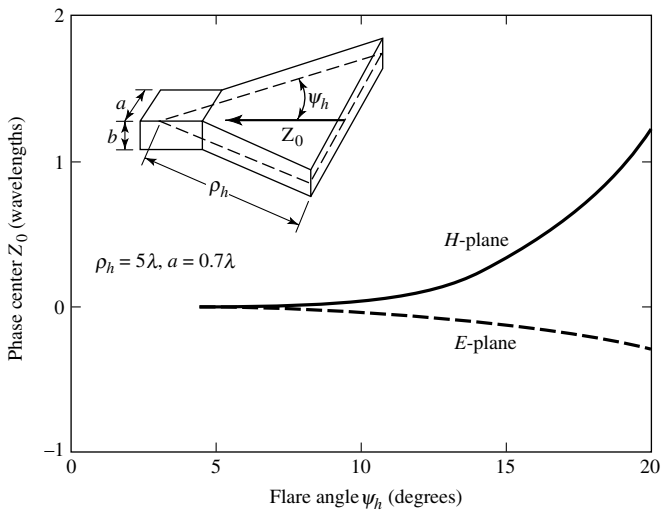
In practice, no antenna is a point source with ideal spherical equiphases. Many of them, however, contain a point from which their radiation, over most of the angular space, seems to have spherical wavefronts. When such an antenna is used as a feed for a reflector, its phase center must be placed at the focal point. Deviations of the feed from the focal point of the reflector lead to phase errors which result in significant gain reductions of the antenna, as illustrated in Section 15.4.1(G) of Chapter 15.

The analytical formulations for locating the phase center of an antenna are usually very laborious and exist only for a limited number of configurations [53]–[55]. Experimental techniques [56], [57] are available to locate the phase center of an antenna. The one reported in [56] is also discussed in some detail in [2], and it will not be repeated here. The interested reader is referred to [2] and [56].

The horn is a microwave antenna that is widely used as a feed for reflectors [58]. To perform as an efficient feed for reflectors, it is imperative that its phase center is known and it is located at the focal point of the reflector. Instead of presenting analytical formulations for the phase center of a horn, graphical data will be included to illustrate typical phase centers.

Usually the phase center of a horn is not located at its mouth (throat) or at its aperture but mostly between its imaginary apex point and its aperture. The exact location depends on the dimensions of the horn, especially on its flare angle. For large flare angles the phase center is closer to the apex. As the flare angle of the horn becomes smaller, the phase center moves toward the aperture of the horn.

Computed phase centers for an  $E$ -plane and an  $H$ -plane sectoral horn are displayed in Figure 13.36(a, b). It is apparent that for small flare angles the  $E$ - and  $H$ -plane phase


 (a)  $E$ -plane

 (b)  $H$ -plane

**Figure 13.36** Phase center location, as a function of flare angle, for  $E$ - and  $H$ -plane sectoral horns. (Adapted from Hu [53]).

centers are identical. Although each specific design has its own phase center, the data of Figure 13.36(a, b) are typical. If the  $E$ - and  $H$ -plane phase centers of a pyramidal horn are not identical, its phase center can be taken to be the average of the two.

Phase center nomographs for conical corrugated and uncorrugated ( $TE_{11}$ -mode) horns are available [55], and they can be found in [2] and [55]. The procedure to use these in order to locate a phase center is documented in [2] and [55], and it is not repeated here. The interested reader is referred to [2] where examples are also illustrated.

## 13.11 MULTIMEDIA

In the CD that is part of the book, the following multimedia resources are included for the review, understanding, and visualization of the material of this chapter:

- a. **Java-based interactive questionnaire**, with answers.
- b. **Matlab and Fortran** computer programs, designated
  - *Analysis*
  - *Design*
 for computing and displaying the analysis and design characteristics of a pyramidal horn.
- c. **Matlab-based animation-visualization** program, designated *te\_horn*, that can be used to animate and visualize the radiation of a two-dimensional horn. A detailed description of this program is provided in Section 1.3.4 and in the corresponding READ ME file of Chapter 1.
- d. **Power Point (PPT)** viewgraphs, in multicolor.

## REFERENCES

1. A. W. Love *Electromagnetic Horn Antennas*, IEEE Press, New York, 1976.
2. C. A. Balanis, "Horn Antennas," Chapter 8 in *Antenna Handbook: Theory, Applications and Design* (Y. T. Lo and S. W. Lee, eds.), Van Nostrand Reinhold Co., New York, 1988.
3. A. W. Love, "Horn Antennas," Chapter 15 in *Antenna Engineering Handbook* (R. C. Johnson and H. Jasik, eds.), New York, 1984.
4. R. F. Harrington, *Time-Harmonic Electromagnetic Fields*, McGraw-Hill, New York, 1961, pp. 208–213.
5. S. Silver (ed.), *Microwave Antenna Theory and Design*, MIT Radiation Laboratory Series, Vol. 12, McGraw-Hill, New York, 1949, pp. 349–376.
6. C. A. Balanis *Advanced Engineering Electromagnetics*, John Wiley and Sons, New York, 1989.
7. M. J. Maybell and P. S. Simon, "Pyramidal Horn Gain Calculation with Improved Accuracy," *IEEE Trans. Antennas Propagat.*, Vol. 41, No. 7, pp. 884–889, July 1993.
8. K. Liu, C. A. Balanis, C. R. Birtcher and G. C. Barber, "Analysis of Pyramidal Horn Antennas Using Moment Method," *IEEE Trans. Antennas Propagat.*, Vol. 41, No. 10, pp. 1379–1389, October 1993.
9. M. Abramowitz and I. A. Stegun (eds.), *Handbook of Mathematical Functions*, National Bureau of Standards, United States Dept. of Commerce, June 1964.
10. J. Boersma, "Computation of Fresnel Integrals," *Math. Comp.*, Vol. 14, p. 380, 1960.
11. Y.-B. Cheng, "Analysis of Aircraft Antenna Radiation for Microwave Landing System Using Geometrical Theory of Diffraction," MSEE Thesis, Dept. of Electrical Engineering, West Virginia University, 1976, pp. 208–211.
12. E. V. Jull, "Gain of an E-Plane Sectoral Horn—A Failure of the Kirchoff Theory and a New Proposal," *IEEE Trans. Antennas Propagat.*, Vol. AP-22, No. 2, pp. 221–226, March 1974.
13. E. V. Jull, *Aperture Antennas and Diffraction Theory*, Peter Peregrinus Ltd., London, United Kingdom, 1981, pp. 55–65.

14. E. H. Braun, "Some Data for the Design of Electromagnetic Horns," *IRE Trans. Antennas Propagat.*, Vol. AP-4, No. 1, pp. 29–31, January 1956.
15. P. M. Russo, R. C. Rudduck, and L. Peters, Jr., "A Method for Computing  $E$ -Plane Patterns of Horn Antennas," *IEEE Trans. Antennas Propagat.*, Vol. AP-13, No. 2, pp. 219–224, March 1965.
16. J. S. Yu, R. C. Rudduck, and L. Peters, Jr., "Comprehensive Analysis for  $E$ -Plane of Horn Antennas by Edge Diffraction Theory," *IEEE Trans. Antennas Propagat.*, Vol. AP-14, No. 2, pp. 138–149, March 1966.
17. M. A. K. Hamid, "Diffraction by a Conical Horn," *IEEE Trans. Antennas Propagat.*, Vol. AP-16, No. 5, pp. 520–528, September 1966.
18. M. S. Narasimhan and M. S. Shehadri, "GTD Analysis of the Radiation Patterns of Conical Horns," *IEEE Trans. Antennas Propagat.*, Vol. AP-26, No. 6, pp. 774–778, November 1978.
19. P. A. Tirkas and C. A. Balanis, "Contour Path FDTD Method for Analysis of Pyramidal Horns with Composite Inner  $E$ -Plane Walls," *IEEE Trans. Antennas Propagat.*, Vol. AP-42, No. 11, pp. 1476–1483, November 1994.
20. M. J. Maybell and P. S. Simon, "Pyramidal Horn Gain Calculation with Improved Accuracy," *IEEE Trans. Antennas Propagat.*, Vol. 41, No. 7, pp. 884–889, July 1993.
21. M. G. Schorr and F. J. Beck, Jr., "Electromagnetic Field of a Conical Horn," *J. Appl. Phys.*, Vol. 21, pp. 795–801, August 1950.
22. A. P. King, "The Radiation Characteristics of Conical Horn Antennas," *Proc. IRE*, Vol. 38, pp. 249–251, March 1950.
23. A. F. Kay, "The Scalar Feed," AFCRL Rep. 64–347, AD601609, March 1964.
24. R. E. Lawrie and L. Peters, Jr., "Modifications of Horn Antennas for Low Side Lobe Levels," *IEEE Trans. Antennas Propagat.*, Vol. AP-14, No. 5, pp. 605–610, September 1966.
25. R. S. Elliott, "On the Theory of Corrugated Plane Surfaces," *IRE Trans. Antennas Propagat.*, Vol. AP-2, No. 2, pp. 71–81, April 1954.
26. C. A. Mentzer and L. Peters, Jr., "Properties of Cutoff Corrugated Surfaces for Corrugated Horn Design," *IEEE Trans. Antennas Propagat.*, Vol. AP-22, No. 2, pp. 191–196, March 1974.
27. C. A. Mentzer and L. Peters, Jr., "Pattern Analysis of Corrugated Horn Antennas," *IEEE Trans. Antennas Propagat.*, Vol. AP-24, No. 3, pp. 304–309, May 1976.
28. M. J. Al-Hakkak and Y. T. Lo, "Circular Waveguides and Horns with Anisotropic and Corrugated Boundaries," *Antenna Laboratory Report No. 73-3*, Department of Electrical Engineering, University of Illinois, Urbana, January 1973.
29. B. MacA. Thomas, G. L. James and K. J. Greene, "Design of Wide-Band Corrugated Conical Horns for Cassegrain Antennas," *IEEE Trans. Antennas Propagat.*, Vol. AP-34, No. 6, pp. 750–757, June 1986.
30. B. MacA. Thomas, "Design of Corrugated Conical Horns," *IEEE Trans. Antennas Propagat.*, Vol. AP-26, No. 2, pp. 367–372, March 1978.
31. B. MacA. Thomas and K. J. Greene, "A Curved-Aperture Corrugated Horn Having Very Low Cross-Polar Performance," *IEEE Trans. Antennas Propagat.*, Vol. AP-30, No. 6, pp. 1068–1072, November 1982.
32. G. L. James, "TE<sub>11</sub>-to-HE<sub>11</sub> Mode Converters for Small-Angle Corrugated Horns," *IEEE Trans. Antennas Propagat.*, Vol. AP-30, No. 6, pp. 1057–1062, November 1982.
33. K. Tomiyasu, "Conversion of TE<sub>11</sub> mode by a Large-Diameter Conical Junction," *IEEE Trans. Microwave Theory Tech.*, Vol. MTT-17, No. 5, pp. 277–279, May 1969.
34. B. MacA. Thomas, "Mode Conversion Using Circumferentially Corrugated Cylindrical Waveguide," *Electron. Lett.*, Vol. 8, pp. 394–396, 1972.

35. J. K. M. Jansen and M. E. J. Jeuken, "Surface Waves in Corrugated Conical Horn," *Electronic Letters*, Vol. 8, pp. 342–344, 1972.
36. Y. Tacheichi, T. Hashimoto, and F. Takeda, "The Ring-Loaded Corrugated Waveguide," *IEEE Trans. Microwave Theory Tech.*, Vol. MTT-19, No. 12, pp. 947–950, December 1971.
37. F. Takeda and T. Hashimoto, "Broadbanding of Corrugated Conical Horns by Means of the Ring-Loaded Corrugated Waveguide Structure," *IEEE Trans. Antennas Propagat.*, Vol. AP-24, No. 6, pp. 786–792, November 1976.
38. W. D. Burnside and C. W. Chuang, "An Aperture-Matched Horn Design," *IEEE Trans. Antennas Propagat.*, Vol. AP-30, No. 4, pp. 790–796, July 1982.
39. A. W. Love, "The Diagonal Horn Antenna," *Microwave Journal*, Vol. V, pp. 117–122, March 1962.
40. P. D. Potter, "A New Horn Antenna with Suppressed Side Lobes and Equal Beamwidths," *Microwave Journal*, pp. 71–78, June 1963.
41. P. D. Potter and A. C. Ludwig, "Beamshaping by Use of Higher-Order Modes in Conical Horns," *Northeast Electron. Res. Eng. Mtg.*, pp. 92–93, November 1963.
42. P. A. Jensen, "A Low-Noise Multimode Cassegrain Monopulse with Polarization Diversity," *Northeast Electron. Res. Eng. Mtg.*, pp. 94–95, November 1963.
43. H. E. Bartlett and R. E. Moseley, "Dielguides—Highly Efficient Low-Noise Antenna Feeds," *Microwave Journal*, Vol. 9, pp. 53–58, December 1966.
44. L. L. Oh, S. Y. Peng, and C. D. Lunden, "Effects of Dielectrics on the Radiation Patterns of an Electromagnetic Horn," *IEEE Trans. Antennas Propagat.*, Vol. AP-18, No. 4, pp. 553–556, July 1970.
45. G. N. Tsandoulas and W. D. Fitzgerald, "Aperture Efficiency Enhancement in Dielectrically Loaded Horns," *IEEE Trans. Antennas Propagat.*, Vol. AP-20, No. 1, pp. 69–74, January 1972.
46. R. Baldwin and P. A. McInnes, "Radiation Patterns of Dielectric Loaded Rectangular Horns," *IEEE Trans. Antennas Propagat.*, Vol. AP-21, No. 3, pp. 375–376, May 1973.
47. C. M. Knop, Y. B. Cheng, and E. L. Osterlag, "On the Fields in a Conical Horn Having an Arbitrary Wall Impedance," *IEEE Trans. Antennas Propagat.*, Vol. AP-34, No. 9, pp. 1092–1098, September 1986.
48. J. J. H. Wang, V. K. Tripp, and R. P. Zimmer, "Magnetically Coated Horn for Low Side-lobes and Low Cross-Polarization," *IEE Proc.*, Vol. 136, pp. 132–138, April 1989.
49. J. J. H. Wang, V. K. Tripp, and J. E. Tehan, "The Magnetically Coated Conducting Surface as a Dual Conductor and Its Application to Antennas and Microwaves," *IEEE Trans. Antennas Propagat.*, Vol. AP-38, No. 7, pp. 1069–1077, July 1990.
50. K. Liu and C. A. Balanis, "Analysis of Horn Antennas with Impedance Walls," 1990 IEEE Antennas and Propagation Symposium Digest, Vol. I, pp. 1184–1187, May 7–11, 1990, Dallas, TX.
51. K. Liu and C. A. Balanis, "Low-Loss Material Coating for Horn Antenna Beam Shaping," 1991 IEEE Antennas and Propagation Symposium Digest, Vol. 3, pp. 1664–1667, June 24–28, 1991, London, Ontario, Canada.
52. P. A. Tirkas, "Finite-Difference Time-Domain for Aperture Antenna Radiation," PhD Dissertation, Dept. of Electrical Engineering, Arizona State University, December 1993.
53. Y. Y. Hu, "A Method of Determining Phase Centers and Its Applications to Electromagnetic Horns," *Journal of the Franklin Institute*, Vol. 271, pp. 31–39, January 1961.
54. E. R. Nagelberg, "Fresnel Region Phase Centers of Circular Aperture Antennas," *IEEE Trans. Antennas Propagat.*, Vol. AP-13, No. 3, pp. 479–480, May 1965.



55. I. Ohtera and H. Ujiie, "Nomographs for Phase Centers of Conical Corrugated and TE<sub>11</sub> Mode Horns," *IEEE Trans. Antennas Propagat.*, Vol. AP-23, No. 6, pp. 858–859, November 1975.
56. J. D. Dyson, "Determination of the Phase Center and Phase Patterns of Antennas," in *Radio Antennas for Aircraft and Aerospace Vehicles*, W. T. Blackband (ed.), AGARD Conference Proceedings, No. 15, Slough, England Technivision Services, 1967.
57. M. Teichman, "Precision Phase Center Measurements of Horn Antennas," *IEEE Trans. Antennas Propagat.*, Vol. AP-18, No. 5, pp. 689–690, September 1970.
58. W. M. Truman and C. A. Balanis, "Optimum Design of Horn Feeds for Reflector Antennas," *IEEE Trans. Antennas Propagat.*, Vol. AP-22, No. 4, pp. 585–586, July 1974.

## PROBLEMS

- 13.1. Derive (13-1a)–(13-1e) by treating the  $E$ -plane horn as a radial waveguide.
- 13.2. Design an  $E$ -plane horn such that the maximum phase difference between two points at the aperture, one at the center and the other at the edge, is  $120^\circ$ . Assuming that the maximum length along its wall ( $\rho_e$ ), measured from the aperture to its apex, is  $10\lambda$ , find the
  - (a) maximum total flare angle of the horn
  - (b) largest dimension of the horn at the aperture
  - (c) directivity of the horn (*dimensionless* and *in dB*)
  - (d) gain of the antenna (*in dB*) when the reflection coefficient within the waveguide feeding the horn is 0.2. Assume only mismatch losses. The waveguide feeding the horn has dimensions of  $0.5\lambda$  and  $0.25\lambda$
- 13.3. For an  $E$ -plane horn with  $\rho_1 = 6\lambda$ ,  $b_1 = 3.47\lambda$ , and  $a = 0.5\lambda$ ,
  - (a) compute (*in dB*) its pattern at  $\theta = 0^\circ$ ,  $10^\circ$ , and  $20^\circ$  using the results of Figure 13.6. Show all the steps for one angle.
  - (b) compute its directivity using (13-19) and (13-20c). Compare the answers.
- 13.4. Repeat Problem 13.3 for  $\rho_1 = 6\lambda$ ,  $b_1 = 6\lambda$ , and  $a = 0.5\lambda$ .
- 13.5. For an  $E$ -plane sectoral horn, plot  $b_1$  (*in  $\lambda$* ) versus  $\rho_1$  (*in  $\lambda$* ) using (13-19a). Verify, using the data of Figure 13.8, that the maximum directivities occur when (13-19a) is satisfied.
- 13.6. For an  $E$ -plane sectoral horn with  $\rho_1 = 20\lambda$ ,  $a = 0.5\lambda$ 
  - (a) find its optimum aperture dimensions for maximum normalized directivity
  - (b) compute the total flare angle of the horn
  - (c) compute its directivity, using (13-19), and compare it with the graphical answer
  - (d) find its half-power beamwidth (*in degrees*)
  - (e) compute the directivity using (13-20c)
- 13.7. An  $E$ -plane horn is fed by an X-band WR 90 rectangular waveguide with inner dimensions of 0.9 in. (2.286 cm) and  $b = 0.4$  in. (1.016 cm). Design the horn so that its maximum directivity at  $f = 11$  GHz is 30 (14.77 dB).

- 13.8.** Design an optimum directivity  $E$ -plane sectoral horn whose axial length is  $\rho_1 = 10\lambda$ . The horn is operating at  $X$ -band with a desired center frequency equal to  $f = 10$  GHz. The dimensions of the feed waveguide are  $a = 0.9$  in. (2.286 cm) and  $b = 0.4$  in. (1.016 cm). Assuming a 100% efficient horn ( $e_0 = 1$ ), find the
- horn aperture dimensions  $b_1$  and  $\rho_e$  (in  $\lambda$ ), and flare half-angle  $\psi_e$  (in degrees)
  - directivity  $D_E$  (in dB) using (13-20c)
  - aperture efficiency
  - largest phase difference (in degrees) between center of horn at the aperture and any point on the horn aperture along the principal  $E$ -plane.
- 13.9.** Derive (13-21a)–(13-21e) by treating the  $H$ -plane horn as a radial waveguide.
- 13.10.** For an  $H$ -plane sectoral horn with  $\rho_2 = 6\lambda$ ,  $a_1 = 6\lambda$ , and  $b = 0.25\lambda$  compute the
- directivity (in dB) using (13-41), (13-42c) and compare the answers
  - normalized field strength (in dB) at  $\theta = 30^\circ$ ,  $45^\circ$ , and  $90^\circ$ . Approximate it using linear interpolation.
- 13.11.** For an  $H$ -plane sectoral horn, plot  $a_1$  (in  $\lambda$ ) versus  $\rho_2$  (in  $\lambda$ ) using (13-41c). Verify, using the data of Figure 13.16, that the maximum directivities occur when (13-41c) is satisfied.
- 13.12.** Design an  $H$ -plane horn so that its maximum directivity at  $f = 10$  GHz is 13.25 dB. The horn is fed with a standard  $X$ -band waveguide with dimensions  $a = 2.286$  cm and  $b = 1.016$  cm. Determine:
- the horn aperture dimension  $a_1$  (in cm).
  - the axial length  $\rho_2$  of the horn (in cm).
  - the flare angle of the horn (in degrees).
- 13.13.** An  $H$ -plane sectoral horn is fed by an  $X$ -band WR 90 rectangular waveguide with dimensions of  $a = 0.9$  in. (2.286 cm) and  $b = 0.4$  in. (1.016 cm). Design the horn so that its maximum directivity at  $f = 11$  GHz is 16.3 (12.12 dB).
- 13.14.** Repeat the design of Problem 13.8 for an  $H$ -plane sectoral horn where axial length is also  $\rho_2 = 10\lambda$ . The feed waveguide dimensions and center frequency of operation are the same as in Problem 13.8. Assuming an 100% efficient horn ( $e_0 = 1$ ), find the
- horn aperture dimensions  $a_1$  and  $\rho_h$  (in  $\lambda$ ), and the flare half-angle  $\psi_h$  (in degrees)
  - directivity  $D_H$  (in dB) using (13-42c)
  - aperture efficiency
  - largest phase difference (in degrees) between the center of the horn at the aperture and any point on the horn aperture along the principal  $H$ -plane.

- 13.15.** Show that (13-49a) and (13-49b) must be satisfied in order for a pyramidal horn to be physically realizable.
- 13.16.** A standard-gain X-band (8.2–12.4 GHz) pyramidal horn has dimensions of  $\rho_1 \simeq 13.5$  in. (34.29 cm),  $\rho_2 \simeq 14.2$  in. (36.07 cm),  $a_1 = 7.65$  in. (19.43 cm),  $b_1 = 5.65$  in. (14.35 cm),  $a = 0.9$  in. (2.286 cm), and  $b = 0.4$  in. (1.016 cm).  
 (a) Check to see if such a horn can be constructed physically.  
 (b) Compute the directivity (in dB) at  $f = 8.2, 10.3, 12.4$  GHz using for each (13-52a), (13-53), and (13-54e). Compare the answers. Verify with the computer program *Pyramidal Horn-Analysis* of this chapter.
- 13.17.** A standard-gain X-band (8.2–12.4 GHz) pyramidal horn has dimensions of  $\rho_1 \simeq 5.3$  in. (13.46 cm),  $\rho_2 \simeq 6.2$  in. (15.75 cm),  $a_1 = 3.09$  in. (7.85 cm),  $b_1 = 2.34$  in. (5.94 cm),  $a = 0.9$  in. (2.286 cm), and  $b = 0.4$  in. (1.016 cm).  
 (a) Check to see if such a horn can be constructed physically.  
 (b) Compute the directivity (in dB) at  $f = 8.2, 10.3, 12.4$  GHz using for each (13-52a), (13-53), and (13-54e). Compare the computed answers with the gains of Figure 13.24. Verify with the computer program *Pyramidal Horn-Analysis* of this chapter.
- 13.18.** A *lossless linearly polarized* pyramidal horn antenna is used as a receiver in a microwave communications system operating at 10 GHz. Over the aperture of the horn, the incident wave of the communications system is uniform and *circularly polarized* with a total power density of  $10 \text{ mW}/\lambda^2$ . The pyramidal horn has been designed for optimum gain. The dimensions of the horn at the aperture are  $4\lambda_0$  by  $2.5\lambda_0$ . Determine the:  
 (a) Approximate aperture efficiency of the optimum gain horn (in %).  
 (b) Maximum directivity of the horn (in dB).  
 (c) Maximum power (in mW) that can be delivered to the receiver that is assumed to be matched to the transmission line that connects the antenna to the receiver. Assume no other losses.
- 13.19.** Repeat the design of the optimum X-band pyramidal horn of Example 13.6 so that the gain at  $f = 11$  GHz is 17.05 dB.
- 13.20.** It is desired to design an optimum directivity pyramidal horn antenna. The length of the horn from its interior apex is  $\rho_1 = \rho_2 = 9\lambda$ . The horn is fed by an X-band waveguide whose interior dimensions are  $0.5\lambda$  by  $0.22\lambda$ .  
 (a) To accomplish this, what should the aperture dimensions (in  $\lambda$ ) of the horn be?  
 (b) What is the directivity (in dB) of the horn?
- 13.21.** Design a pyramidal horn antenna with optimum gain at a frequency of 10 GHz. The overall length of the antenna from the imaginary vertex of the horn to the center of the aperture is  $10\lambda$  and is nearly the same in both planes. Determine the  
 (a) Aperture dimensions of the horn (in cm).  
 (b) Gain of the antenna (in dB)

- (c) Aperture efficiency of the antenna (*in %*). Assume the reflection, conduction, and dielectric losses of the antenna are negligible.
- (d) Power delivered to a matched load when the incident power density is  $10 \mu\text{watts/m}^2$ .
- 13.22.** Design an optimum gain C-band (3.95–5.85 GHz) pyramidal horn so that its gain at  $f = 4.90$  GHz is 20.0 dBi. The horn is fed by a WR 187 rectangular waveguide with inner dimensions of  $a = 1.872$  in. (4.755 cm) and  $b = 0.872$  in. (2.215 cm). Refer to Figure 13.18 for the horn geometry. Determine in cm, the remaining dimensions of the horn:  $\rho_e$ ,  $\rho_h$ ,  $a_1$ ,  $b_1$ ,  $p_e$ , and  $p_h$ . Verify using the computer program *Pyramidal Horn Design* of this chapter.
- 13.23.** For a conical horn, plot  $d_m$  (*in  $\lambda$* ) versus  $l$  (*in  $\lambda$* ) using (13-60). Verify, using the data of Figure 13.27, that the maximum directivities occur when (13-60) is satisfied.
- 13.24.** A conical horn has dimensions of  $L = 19.5$  in. (49.53 cm),  $d_m = 15$  in. (38.10 cm), and  $d = 2.875$  in. (7.3025 cm).
- (a) Find the frequency (*in GHz*) which will result in maximum directivity for this horn. What is that directivity (*in dB*)?
- (b) Find the directivity (*in dB*) at 2.5 and 5 GHz.
- (c) Compute the cutoff frequency (*in GHz*) of the  $\text{TE}_{11}$ -mode which can exist inside the circular waveguide that is used to feed the horn.
- 13.25.** It is desired to design an *optimum directivity* conical horn antenna of circular cross section whose overall *slanted* length  $l$  is  $10\lambda$ . Determine the
- (a) geometrical dimensions of the conical horn [*radius (in  $\lambda$ )*, *diameter (in  $\lambda$ )*, *total flare angle (in degrees)*].
- (b) aperture efficiency of the horn (*in %*).
- (c) directivity of the horn (*dimensionless* and *in dB*).
- 13.26.** Design an optimum directivity conical horn, using (13-59)–(13-60), so that its directivity (*above isotropic*) at  $f = 11$  GHz is 22.6 dB. Check your design with the data in Figure 13.27. Compare the design dimensions with those of the pyramidal horn of Example 13.6.
- 13.27.** Design an optimum directivity conical horn so that its directivity at 10 GHz (*above a standard-gain horn of 15 dB directivity*) is 5 dB. Determine the horn diameter (*in cm*) and its flare angle (*in degrees*).
- 13.28.** As part of a 10-GHz microwave communication system, you purchase a horn antenna that is said to have a directivity of 75 (dimensionless). The conduction and dielectric losses of the antenna are negligible, and the horn is polarization matched to the incoming signal. A standing wave meter indicates a voltage reflection coefficient of 0.1 at the antenna-waveguide junction.
- (a) Calculate the maximum effective aperture of the horn.
- (b) If an impinging wave with a uniform power density of  $1 \mu\text{watts/m}^2$  is incident upon the horn, what is the maximum power delivered to a load which is connected and matched to the lossless waveguide?

- 13.29.** For an  $X$ -band pyramidal corrugated horn operating at 10.3 GHz, find the
- (a) smallest lower and upper limits of the corrugation depths (*in cm*)
  - (b) width  $w$  of each corrugation (*in cm*)
  - (c) width  $t$  of each corrugation tooth (*in cm*)
- 13.30.** Find the  $E$ - and  $H$ -plane phase centers (*in  $\lambda$* ) of
- (a) an  $E$ -plane ( $\rho_e = 5\lambda$ ,  $a = 0.7\lambda$ )
  - (b) an  $H$ -plane ( $\rho_h = 5\lambda$ ,  $a = 0.7\lambda$ )
- sectoral horn with a total included angle of  $30^\circ$ .